Su-Il Pyun
Heon-Cheol Shin
Jong-Won Lee
Joo-Young Go

Electrochemistry of Insertion Materials for Hydrogen and Lithium

Springer

Electrochemistry of Insertion Materials for Hydrogen and Lithium

Monographs in Electrochemistry

Surprisingly, a large number of important topics in electrochemistry is not covered by up-to-date monographs and series on the market, some topics are even not covered at all. The series Monographs in Electrochemistry fills this gap by publishing indepth monographs written by experienced and distinguished electrochemists, covering both theory and applications. The focus is set on existing as well as emerging methods for researchers, engineers, and practitioners active in the many and often interdisciplinary fields, where electrochemistry plays a key role. These fields will range – among others – from analytical and environmental sciences to sensors, materials sciences and biochemical research.

Information about published and forthcoming volumes is available at
http://www.springer.com/series/7386

Series Editor: Fritz Scholz, University of Greifswald, Germany

Su-Il Pyun • Heon-Cheol Shin • Jong-Won Lee • Joo-Young Go

Electrochemistry of Insertion Materials for Hydrogen and Lithium

Springer

Su-Il Pyun
Dept. Materials Science & Eng.
Korea Adv. Inst. of Science and Techn.
Jeju National University
Daejeon
Republic of Korea

Jong-Won Lee
Fuel Cell Research Center
Korea Inst. of Energy Research
Daejon
Republic of Korea

Heon-Cheol Shin
School of Materials Science & Eng.
Pusan National Univ.
Busan, Geumjeong-gu
Republic of Korea

Joo-Young Go
SB LiMotive Co., Ltd
Gyeonggi-do
Republic of Korea

Preface

The electrochemical insertion of hydrogen and lithium into various materials is of utmost importance for modern energy storage systems, and the scientific literature abounds in treatise on the applied and technological aspects. However, there is a serious lack with respect to a fundamental treatment of the underlying electrochemistry. The respective literature is scattered across the scientific journals. The authors of this monograph have undertaken the commendable task of describing both the theory of hydrogen and lithium insertion electrochemistry, the experimental techniques to study it, and the results of various specific studies. The lifelong experience and enthusiasm of the senior author (Su-Il Pyun) and his coauthors (Heon-Cheol Shin, Jong-Won Lee, Joo-Young Go) form the solid basis for a monograph that will keep its value for a long time to come. This monograph specifically addresses the question of the rate-determining step of insertion reactions, and it gives a detailed discussion of the anomalous behavior of hydrogen and lithium transport, taking into account the effects of trapping, insertion-induced stress, interfacial boundary condition, cell impedance, and irregular/partially inactive interfaces (or fractal interfaces). It is primarily written for graduate students and other scientists and engineers entering the field for the first time as well as those active in the area of electrochemical systems where insertion electrochemistry is critical. Materials scientists, electrochemists, solid-state physicists, and chemists involved in the areas of energy storage systems and electrochromic devices and, generally, everybody working with hydrogen, lithium, and other electrochemical insertion systems will use this monograph as a reliable and detailed guide.

February, 2012

Fritz Scholz
Editor of the series
Monographs in Electrochemistry

Contents

Chapter 1
Introduction

1.1 Introductory Words to Mixed Diffusion and Interface Control

One of our research concerns is to determine the rate-determining step (*RDS*) for the overall lithium and hydrogen insertion into and desertion from lithium/hydrogen insertion compounds. The "slowest" reaction step among the series of reaction steps of the overall reaction is often referred to as the *RDS*, which is the most strongly disturbed (hindered) from the equilibrium for the *RDS*. In the same sense, other reaction steps are called relatively "fast" reactions for which the equilibria are practically undisturbed. Therefore, the *RDS* is quantitatively evaluated in terms of the overpotential (overvoltage) η, which is defined as the difference in potential between the instantaneous actual and equilibrium values and/or "relaxation (time)" delineated by the time lag between the electrical voltage (potential) and current. The overpotential and relaxation time are namely measured relative to the electrochemical equilibrium values of a "linear system," which is effective for the constraint of electrical energy $|zFE| \ll$ thermal energy RT. Here, z means the oxidation number, F the Faradaic constant (96,485 C mol^{-1}), E the electrode potential, R the gas constant, and T the absolute temperature.

Thus, the linear system shows linear Ohmic behavior between the voltage and current. In particular, the overpotential (overvoltage) η and the time lag imply a deviation from the equilibrium potential and an irreversible degradation (dissipation) of the Gibbs free energy (G) stored during the previous insertion (charge), respectively. The partial reaction step is the *RDS* when it satisfies the general condition that the overpotential and relaxation simultaneously have the maximum values among all of the partial reaction steps in question.

The overvoltage for all reaction steps corresponds simply to the product of the electrochemical equivalent rate (current) and "impedance" for all reaction steps at steady state. It can sometimes be conveniently expressed as being proportional to

the "impedance," since the respective equivalent rate is the same at steady state and, hence, it acts as a proportionality constant. The impedance is defined in particular in the linear system as the ratio of the complex voltage to the complex current and is generally referred to as a transfer function. By definition, the impedance [Ohm cm^2] for such reaction steps as the interfacial reaction and diffusion in the linear system is again in general inversely proportional to the specific current density [A cm^{-2}] spontaneously produced (generated) for charge transfer or adsorption/desorption at equilibrium (zero overpotential) and to the specific current density for diffusion or migration at infinite overpotential, respectively. The specific current density for the interfacial reaction and diffusion is referred to as the exchange current density i_o and maximum limiting diffusion current density (diffusion-limited maximum current density) i_{DL}, respectively.

The former is best thought of as the charge-transfer rate constant (the rate constant of electron transfer $k_{el} = i_o/zF$)/adsorption rate constant at equilibrium (zero overpotential), similarly to the way in which the engine of a stationary car ticks over in the idle state. In particular, the value of k_{el} here is related to the rate at zero overpotential. The value of k_{el} is generally a function of the applied potential E_{app} in the same way that the current density i resulting during charge transfer depends upon E_{app}. In the relatively high E_{app} region satisfying the constraint $|zFE| \gg$ thermal energy RT as a limiting case for instance, the logarithmic dependence of E_{app} or η on i, that is, "Butler-Volmer (Tafel) behavior" is effective. Practically, i_o means the migration rate of Li$^+$/H$^+$ ions through the double layer or charge-transfer rate by electron tunneling, which is regarded as a measure of the electrocatalytic effects. The latter is abbreviated as the maximum diffusion current density or simply diffusion current density at infinite (maximum) overpotential, similar to the rate of water flowing out of a reservoir when it is full of water under the maximum water height (level) gradient.

Regarding i_o, one speaks about the interfacial reaction impedance in general and the charge-transfer resistance R_{ct} in particular and regarding i_{DL} one speaks about the transport impedance in general and the diffusion resistance R_D in particular. From the above arguments about i_o (nonzero value) and i_{DL}, we can easily say that the charge-transfer current density ranges between i_o and infinity depending upon the impressed (applied) anodic (positive) or cathodic (negative) overpotential, whereas the diffusion current density varies from zero to i_{DL} depending upon the positive (anodic) or negative (cathodic) difference in concentration of the diffusing species between the electrode and bulk electrolyte, but it remains nearly constant, regardless of the applied anodic and cathodic potential. This is the reason why we can imagine the *RDS* to be diffusion controlled when the potential step is applied theoretically to infinite (extremely large) value, as described below. Similarly the former and latter overvoltages are simply termed the overpotential by charge transfer and overpotential by diffusion, respectively.

Starting from the pure diffusion-controlled mechanism, there are various kinds of mixed diffusion and interfacial reaction controls that have been suggested and experimentally substantiated so far [1]. All of the diffusion controls mixed with the charge-transfer reaction for lithium and hydrogen insertion, which deviate to a

lesser or greater extent from pure diffusion control, have been grouped together under the collective term, "anomalous behavior" in the literature. Pure diffusion control is theoretically thought to be valid for an electrode with an ideally "homogeneous clean" structure. One usually thinks of the mechanism of hydrogen and lithium insertion as being then fixed if the electrode (insertion compounds)/electrolyte system is specified. The mechanism represents which of either interfacial reaction such as adsorption, absorption, and charge-transfer reaction or subsequent diffusion or subsequent "transport" (a collective concept of diffusion and migration) becomes just the *RDS* among all reaction steps.

However, our series of investigations [1] taught us that the boundary condition at the electrode surface regarding the *RDS* during lithium and hydrogen insertion is not fixed at the specific electrode/electrolyte system by itself, but is simultaneously determined for any electrode/electrolyte system by external and internal parameters such as the temperature, the potential step, and the nature of the electrode surface roughness, depending upon, for example, the presence or absence of surface oxide scales, the presence of multiple phases, pores, structural defects acting as lithium and hydrogen trap sites, and pore fractals as well as surface fractals, etc.

1.2 Glossarial Explanation of Terminologies Relevant to Interfacial Reaction and Diffusion

Now we need then to choose in particular first the charge-transfer reaction at the electrode/electrolyte interface (through the electrical double layer), among all of the partial reaction steps, in order to characterize it in terms of a simple equivalent circuit element. As an example of the simple circuit element the arrangement of *RC* couple in parallel can serve which is found in electrochemistry so common and useful, for example, for the first approximation to the electrical double layer or other thin films. The charge-transfer reaction through the double layer will be activated under the applied potential (the force of the electric field). This goes on until the movement of charge counteracts the charge retention by the electrons or Li$^+$/H$^+$ ions being stuck like a glue to the electrical double layer, on the one hand, and simultaneously the resistance (impediment) to charge transfer by the electrons or Li$^+$/H$^+$ ions, on the other hand, regardless of whether it occurs by electron transfer or ion transfer. Stated another way, the charge transfer is then restricted, that is, there are both capacitive and resistive components.

Thus, the moving electrons or Li$^+$/H$^+$ ions sense the electrostatic double-layer capacitance C_{dl} as well as the charge-transfer resistance R_{ct} during the charge-transfer reaction across the electrode/electrolyte interface to a greater or lesser extent, depending upon the frequency, ω. Charge transfer across the double layer, as well as many other layers, behaves just like an *RC* element (a capacitor and resistor in parallel) within the equivalent circuit, generating a trace consisting of a semicircular arc as a function of frequency ω and, hence, it appears as one semicircular arc of radius R_{ct} on the complex impedance plane of the Nyquist

plot. The charge generally moves via more conductive paths. In extremely limiting cases, electrons or Li^+/H^+ ions move purely via the pure Ohmic resistance R_{ct} with Faradaic current and a pure electrostatic double-layer capacitance C_{dl} with capacitive current at zero frequency and infinite frequency, respectively.

The former current of course senses the Ohmic Faradaic resistance as the charge-transfer resistance, while the latter current does not sense the capacitive impedance at all. The latter current does not mean the flow of charge, but rather the charge retention, by alternatively changing the sign of the charge on both sides of the pure plate capacitor. At the equilibrium potential (zero overpotential), RC gives the minimum relaxation time τ_{min} required for electrons/Li^+/H^+ ions to completely move across the double layer, from one side of the layer to the other. Here, τ_{min} means the time constant of the arc caused by the RC element, that is, the reciprocal of the frequency at the maximum apex of the semicircle in the Nyquist plot. The frequency at the maximum apex, ω_{max}, is related to the RC element by the Maxwell relationship: $\omega_{max}R_{ct}C_{dl} = 1$.

Thus, τ_{min} and, hence, ω_{max}, can be used to experimentally determine the magnitude of i_o conveniently using the linear proportional relationship between ω_{max} and i_o. As an empirical and theoretical rule, C_{dl} has a value of 10 to 40 $\mu F\,cm^{-2}$. Taking both R_{ct} per unit length of the bulk medium [Ohm cm^{-1}] and C_{dl} per unit length of the interface [F cm^{-1}], the inverse of the RC time constant corresponds exactly to diffusivity [$cm^2\,s^{-1}$] in value being defined in the mass transport. The charge-transfer resistance and the double-layer capacitance at the maximum frequency in the Nyquist plot yield the rate constant of electron transfer and, hence, the exchange current density at equilibrium (zero overpotential).

It is worthwhile noting that the temperature dependence of the charge-transfer resistance exactly follows that of the electronic resistivity in a semiconductor, thus essentially differing from that in a metal by the term $\exp(-E_g/kT)$ (E_g = band gap energy required to make the electrons move across the double layer). This RC element in parallel, representing the charge transfer by electrons/ions across the double layer, is conceptually analogous to the oil drop experiment performed by Robert Andrew Millikan in 1909–1913 in Chicago to determine the elementary charge. The balance between the sum of the electrical field force in [N], $|eE/d|$ (d = distance between two parallel plates of capacitors in [m], E = potential difference between two parallel plates in [V]) and buoyant force (viscous force), and the gravitational force, mg (m = mass in [kg]; g = gravitational acceleration in [$m^2\,s^{-1}$]), of the oil drops permits us to experimentally quantify the electronic charge, e. Here, the counteracting electrical force and viscous force resemble the capacitive and resistive impedances, respectively. The gravitational force can then provide a good analog of the resulting force of the applied electric field.

Finally we consider diffusion through homogeneous medium (bulk electrode or electrolyte), among all of the partial reaction steps. In contrast to the charge transfer at the interface, the conductivity or diffusivity of charged ions or neutral atoms through an aqueous/solid medium can, in general, best be studied using a driving force/frictional force balance model. The diffusing species in the aqueous/solid medium will be accelerated under the force of the electric field/chemical potential

gradient until the frictional drag exactly counterbalances the electrical field force or the force induced by the concentration gradient, regardless of whether they are charged ions or neutral atoms. Equating these two kinds of forces allows us to quantitatively determine the (electrical) mobility in $[\mathrm{m^2\ s^{-1}\ V^{-1}}]$ of the diffusing species, which is defined as the ratio of the drift velocity of the species in question to the applied electrical field/concentration gradient and is related to the diffusivity and hence finally to i_{DL}. The diffusivity corresponds to the inverse of the RC time constant, which is defined based on the charge-transfer kinetics.

Estimating diffusion through homogeneous medium from another viewpoint in analogy to a simple equivalent circuit element, the diffusion process can be accounted for in terms of the ladder network which is composed of an infinite or a finite connection of R and C in series. The diffusing species, $\mathrm{Li^+/H^+}$ ions or neutral Li/H atoms, repeatedly sense (experience or feel, if you prefer) the electrostatic double-layer capacitance C_{d} for migration/diffusion per unit length of the interface $[\mathrm{F\ cm^{-1}}]$ and resistance R_{d} to migration/diffusion per unit length of the bulk medium $[\mathrm{Ohm\ cm^{-1}}]$ in series or sense (dwell in the thermally activated location between one equilibrium site to the next equilibrium site) the chemical capacitance C_{d} and resistance R_{d} to diffusion in series temporally and spatially during the whole diffusion reaction across the bulk medium. The capacitance C can be originally defined as the ability to retain or store charge or neutral chemical species. So the capacitive element C_{d} for migration/diffusion per unit length of the interface $[\mathrm{F\ cm^{-1}}]$ implies an instantaneous mass retention which acts as a glue when the diffusing species adhere to an instantaneous layer perpendicular to the flow direction or they dwell in the thermally activated location, irrespective of whether it is an electrostatic or chemical capacitance. By contrast, the resistance R_{d} to migration/diffusion per unit length of the bulk medium $[\mathrm{Ohm\ cm^{-1}}]$ refers to an instantaneous impediment to the mass transport preventing the diffusing species from jumping from one equilibrium site to the next equilibrium site (moving in the flow direction).

The frequency-dependent resistive and capacitive elements can be commonly described as appearing in a horizontal line just on the real impedance axis and straight-line perpendicular to the real axis, respectively, on the complex impedance plane of the Nyquist plots. In contrast to one R and C couple in parallel characterized by the charge-transfer reaction, the R and C components are completely separated from each other to exclusively go into the contribution to the real and imaginary parts of diffusion impedances, respectively. For this reason, the infinite sum of the ladder network of RC couple in series conceivably gives a straight line inclined to an angle of $45°$ with respect to the real axis of complex impedance plane.

Alternatively we can conceive of the diffusion process through homogeneous medium as though the diffusing medium were composed of an infinite or a finite sandwich of many millions of layers, each with a slightly different concentration of the species. Each of these layers resembles an RC element (a capacitor and resistor in parallel). The respective values of R_{k} and C_{k} for the k-th layer will be unique to each RC element, since each layer has a distinct value of concentration of the diffusing species. In order to simplify the equivalent circuit model, the infinite or

finite sum of RC elements is termed the Warburg impedance within the equivalent circuit. In contrast to the semicircular arc represented by the charge-transfer reaction, the ideal Warburg impedance represents in general the straight line inclined at an angle of exactly 45° in the Nyquist plot that always implies diffusion or migration with the same magnitude of the frequency-dependent resistive and capacitive impedances, R_k and C_k in absolute value, at a given frequency, ω. This is the same result as that obtained from the transmission line model with ladder network and mentioned above. The frequency-dependent resistive and capacitive impedances, R_k and C_k depend upon the common factor, $\omega^{-1/2}$, and simultaneously upon the frequency-independent term, the Warburg coefficient, as well. Therefore, R_k and C_k are termed the series resistance and pseudo-capacitance, respectively, in contrast to the frequency-independent pure Ohmic resistance and double-layer capacitance.

By converting the Nyquist plot into the time domain, the Warburg impedance including the common factor $\omega^{-1/2}$ becomes simplified to the Cottrell equation including $t^{-1/2}$ ($t =$ time) usually used in chronoamperometric experiments (potentiostatic current transient curve). The linear run of both formulae is characterized and identified as pure diffusion control. The Warburg coefficient obviously includes the diffusion coefficient by nature. Alternatively, the diffusivity can be readily estimated from either the linear part of the frequency dependence of the Warburg impedance or from the linear part of the time dependence of the diffusion current following the Cottrell equation.

1.3 Remarks for Further Consideration

Let us consider the question of which criteria need to be met to determine the RDS of the overall lithium and hydrogen insertion in the case where the charge transfer and subsequent diffusion are connected in series. We briefly discuss here some critical points which have not been so clearly understood until now. According to our series of investigations [2–9] there are several intrinsic parameters, such as the ratio of the diffusion resistance R_D to the sum of the charge-transfer resistance R_{ct} and electrolytic solution resistance R_s, as well as the extrinsic parameters, such as the potential step ΔE and temperature T, over a narrow range of which the transition from mixed diffusion and charge-transfer control to pure diffusion control appears. Taking ΔE as an external parameter, it is expected that the condition for $R_{ct} \approx R_D$ and $i_o \approx i_{DL}$ is valid at relatively low potential steps, that is, below a certain transition potential step, ΔE_{tr}, while the condition for $R_{ct} \ll R_D$ and $i_o \gg i_{DL}$ is effective at relatively high potential steps, that is, above a certain ΔE_{tr}. The above pairs of conditions are in good agreement with each other, because the respective resistance is inversely proportional to the respective current density.

The experimental treatment of the potentiostatic current transient and ac-impedance spectroscopy explained quite well the expected transition of $R_{ct} \approx R_D$ and $i_o \approx i_{DL}$ to $R_{ct} \ll R_D$ and $i_o \gg i_{DL}$ and thus confirmed the transition from mixed control to pure diffusion control over a relatively large potential step. It is

further inferred that the two curves corresponding to the dependence of i_o on the potential step ΔE and less dependence of i_{DL} on ΔE should intersect over a narrow range of ΔE_{tr}. The marked dependence of i_o on ΔE is at variance with the common prediction that the exchange current density i_o does not depend upon ΔE, but is defined at equilibrium (zero overpotential $\eta = 0$). We are now faced with a disconcerting situation.

In order to solve this difficulty, let us introduce the screening factor into the charge-transfer resistance R_{ct}. Whenever one is trying to newly understand a phenomenon, it is usually sufficient to use a somewhat oversimplified model before establishing a more exact one. In order to escape from this dilemma mentioned above and understand the sharp transition of i_o or R_{ct} to a relatively large or small value as compared to i_{DL} or R_D, respectively, at the transition ΔE_{tr} rather than the dependence of i_o or R_{ct} on ΔE, we introduced the term $\exp(-\lambda\Delta E)$ to add to $R_{ct} = (RT)/(zFi_o)$ as follows:

$$R_{ct} = \frac{RT}{zFi_o} \exp(-\lambda\Delta E) \tag{1.1}$$

where λ is called the screening constant. The reciprocal of $\lambda(\lambda^{-1})$ is termed the screening potential step, ΔE. The redox electrons, which are in quasi-equilibrium with the cations of Li^+/H^+, contribute to the value, $R_{ct} = (RT)/(zFi_o)$. This is a situation in which the electrons are trapped by the Li^+/H^+ cations in a similar manner to that in which a small bird cannot fly out of its cage.

As the potential step ΔE is raised, more redox electrons are produced and the new factor $\exp(-\lambda\Delta E)$ enters the equation. These excess redox electrons begin to create a screen of negative charge around the cationic charge, so that R_{ct} is much reduced. R_{ct} in this case takes the form of Eq. 1.1. It follows that the screened cationic charge cannot be sensed (felt, seen, experienced, or attracted, if you prefer) by the excess redox electrons when the screening ΔE, λ^{-1}, is extremely small as compared to the large ΔE. Now, we consider two cases, a small ΔE from 5 to 10 mV and a large ΔE from 800 to 1,000 mV, taking $\lambda^{-1} = (kT)/(ze) = 26$ mV at 298°K (room temperature). At the small ΔE, the screening factor $\exp(-\lambda\Delta E)$ amounts to 0.68 to 0.83, indicating that the trapping effect still overcomes the screening effect. In contrast, at the large ΔE, the screening factor is 2.0×10^{-17} to 4.3×10^{-14}, indicating that the screening effect easily overcomes the trapping effect.

Similarly, if the temperature is high enough, it is possible that the number of such excess redox electrons will become great enough for the screening to far overweigh the trapping effect and again there will be a sharp transition of R_{ct} to a very low value. Once the screening effect begins to act, ΔE is then raised, which leads to more screening and to the generation of excess redox electrons, thus resulting in $R_{ct} = 0$ when ΔE theoretically reaches an infinite value. In this region of pure diffusion control, the semicircular arc representing charge transfer in the Nyquist plot degenerates into a point ($R_{ct} = 0$). This is the case where the redox electrons are ideally in reversible equilibrium with the cations of Li^+/H^+. This is not unlike the avalanche ("Alpenlawine") effect where a large mass of snow falls down

the side of a mountain. The factor $\exp(-\lambda\Delta E)$ in the avalanche effect is the same as an "infinitely thin and long δ-function," a special form of the Weibull distribution density function of any event x given by

$$f(x) = \frac{m}{n} x^{m-1} \exp\left(-\frac{x^m}{n}\right) \qquad (1.2)$$

where m is an extremely large constant value and n is nearly zero. Here, m means the shape parameter and n is the scale parameter.

The screening factor $\exp(-\lambda\Delta E)$ is in many ways similar to the screening term that Mott [10] and Debye-Hueckel [11] introduced into the same electrical potential $U = -e^2/r$ (where e = electronic charge; r = the distance of the electron from the nucleus and the distance of the central ion from the next neighboring ion; λ = the screening radius and the thickness of the ionic atmosphere or Debye length, respectively), in order to explain the sharp transition in the conductivity of a semiconductor to a metal at a certain transition interatomic distance in a solid medium and also to explain the appreciable change of the ionic strength (degree of electrical interaction between ions) at the transition interionic distance in a dilute strong electrolyte. The screening concept of R_{ct} (i_o) may also provide a clue to understanding the sharp transition of i_{DL} or R_D to a relatively small or large value as compared to i_o or R_{ct}, respectively, at the transition ΔE_{tr} rather than to the dependence of i_{DL} or R_D on ΔE.

1.4 Concluding Remarks

This whole monograph discussed in detail how to quantitatively determine the *RDS* at different applied potential steps and in the presence of multiple phases, pores, structural defects such as lithium and hydrogen trap sites and surface and pore fractals, etc. Then, we dealt with the question of what mechanism of anomalous behavior is operative during the overall lithium and hydrogen insertion into and desertion from lithium/hydrogen insertion compounds from the viewpoint of the overpotential (the respective impedance) of charge transfer and diffusion and/or exchange current density at zero overpotential and maximum diffusion current density at infinite applied potential (overpotential).

Specifically enumerating the contents of this book, it first presents the basic concepts of and problems relating to the *RDS* of the overall insertion and desertion reactions in Chap. 1 and continues to give a brief overview of the electrochemical techniques that are essential to characterize the electrochemical and transport properties of insertion materials (Chap. 2). Then, there are in-depth theoretical and practical discussions of hydrogen absorption into and subsequent diffusion through the metals and metal oxides under the permeable and impermeable boundary conditions (Chaps. 3 and 4). The following three chapters cover the conceptual

and phenomenological aspects of hydrogen trapping inside the materials, insertion-induced generation of internal stress, and interfacial reaction kinetics that cause abnormal hydrogen transport behavior (Chaps. 5, 6, and 7). In the last two chapters, the unusual transport phenomena observed in lithium insertion materials are discussed in terms of internal cell resistance and irregular/partially inactive interfaces of the active materials (Chaps. 8 and 9). We hope this book will at least partially answer some of the queries and difficulties raised herein and provide the incentive to solve them.

References

1. Pyun SI (2002/2007) Interfacial, fractal, and bulk electrochemistry at cathode and anode materials, vol 1–3: the 1st series of collected papers to celebrate his 60th birthday; vol 4–5: the 2nd series of collected papers on the occasion of his 65th birthday, published by Research Laboratory for interfacial electrochemistry and corrosion at Korea Advanced Institute of Sciences and Technology
2. Han JN, Seo M, Pyun SI (2001) Analysis of anodic current transient and beam deflection transient simultaneously measured from Pd foil electrode pre-charged with hydrogen. J Electroanal Chem 499:152–160
3. Lee JW, Pyun SI, Filipek S (2003) The kinetics of hydrogen transport through amorphous $Pd_{82-y}Ni_ySi_{18}$ alloys (y = 0−32) by analysis of anodic current transient. Electrochim Acta 48:1603–1611
4. Lee SJ, Pyun SI, Lee JW (2005) Investigation of hydrogen transport through Mm $(Ni_{3.6}Co_{0.7}Mn_{0.4}Al_{0.3})_{1.12}$ and $Zr_{0.65}Ti_{0.35}Ni_{1.2} V_{0.4}Mn_{0.4}$ hydride electrodes by analysis of anodic current transient. Electrochim Acta 50:1121–1130
5. Lee JW, Pyun SI (2005) Anomalous behavior of hydrogen extraction from hydride-forming metals and alloys under impermeable boundary conditions. Electrochim Acta 50:1777–1805
6. Lee SJ, Pyun SI (2007) Effect of annealing temperature on mixed proton transport and charge transfer-controlled oxygen reduction in gas diffusion electrode. Electrochim Acta 52:6525–6533
7. Lee SJ, Pyun SI (2008) Oxygen reduction kinetics in nafion-impregnated gas diffusion electrode under mixed control using EIS and PCT. J Electrochem Soc 155:B1274–B1280
8. Lee SJ, Pyun SI (2010) Kinetics of mixed-controlled oxygen reduction at nafion-impregnated Pt-alloy-dispersed carbon electrode by analysis of cathodic current transients. J Solid State Electrochem 14:775–786
9. Lee SJ, Pyun SI, Yoon YG (2011) Pathways of diffusion mixed with subsequent reactions with examples of hydrogen extraction from hydride-forming electrode and oxygen reduction at gas diffusion electrode. J Solid State Electrochem 15:2437–2445
10. Moore Walter J (1967) Seven solid states. W. A. Benjamin, Inc, New York, p 138, originating from Mott NF (1956) On the transition to metallic conduction in semiconductors. Can J Phys 34:1356
11. Crow DR (1994) Principles and applications of electrochemistry. Blackie Academic & Professional, An imprint of Chapman & Hall, London, p 271, originating from Debye P, Hueckel E (1923) Physik 24:311; Onsager L (1926) ibid 27:388

Chapter 2
Electrochemical Methods

2.1 Chronopotentiometry

In chronopotentiometry, a current pulse is applied to the working electrode and its resulting potential is measured against a reference electrode as a function of time. At the moment when the current is first applied, the measured potential is abruptly changed due to the iR loss, and after that it gradually changes, because a concentration overpotential is developed as the concentration of the reactant is exhausted at the electrode surface. If the current is larger than the limiting current, the required flux for the current cannot be provided by the diffusion process and, therefore, the electrode potential rapidly rises until it reaches the electrode potential of the next available reaction, and so on.

The different types of chronopotentiometric techniques are depicted in Fig. 2.1. In constant current chronopotentiometry, the constant anodic/cathodic current applied to the electrode causes the electroactive species to be oxidized/reduced at a constant rate. The electrode potential accordingly varies with time as the concentration ratio of reactant to product changes at the electrode surface. This process is sometimes used for titrating the reactant around the electrode, resulting in a potentiometric titration curve. After the concentration of the reactant drops to zero at the electrode surface, the reactant might be insufficiently supplied to the surface to accept all of the electrons being forced by the application of a constant current. The electrode potential will then sharply change to more anodic/cathodic values. The shape of the curve is governed by the reversibility of the electrode reaction.

The applied current can be varied with time, rather than being kept constant. For example, the current can be linearly increased or decreased (chronopotentiometry with linearly rising current in the figure) and can be reversed after some time (current reversal chronopotentiometry in the figure). If the current is suddenly changed from an anodic to cathodic one, the product formed by the anodic reaction (i.e., anodic product) starts to be reduced. Then, the potential moves in the cathodic direction as the concentration of the cathodic product increases. On the other hand, the current is repeatedly reversed in cyclic chronopotentiometry.
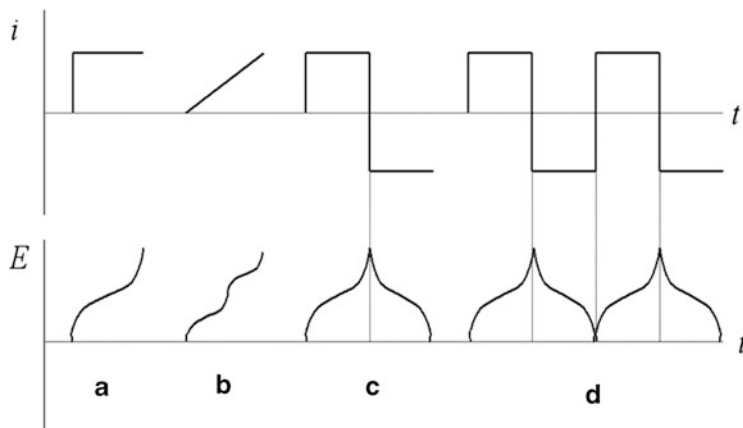
Fig. 2.1 Different types of chronopotentiometric experiments. (*a*) Constant current chronopotentiometry. (*b*) Chronopotentiometry with linearly rising current. (*c*) Current reversal chronopotentiometry. (*d*) Cyclic chronopotentiometry

The typical chronopotentiometric techniques can be readily extended to characterize the electrochemical properties of insertion materials. In particular, current reversal and cyclic chronopotentiometries are frequently used to estimate the specific capacity and to evaluate the cycling stability of the battery, respectively. Shown in Fig. 2.2a is a typical galvanostatic charge/discharge profile of $LiMn_2O_4$ powders at a rate of 0.2 C (In battery field, nC rate means the discharging/charging rate at which the battery is virtually fully discharged/charged for $1/n$ h.) [1]. The total quantity of electricity per mass available from a fully charged cell (or storable in a fully discharged cell) can be calculated at a specific C rate from the charge transferred during the discharging (or charging) process in terms of $C·g^{-1}$ or $mAh·g^{-1}$. Alternatively, the quantity of electricity can be converted to the number of moles of inserted atoms as long as the electrode potential is obtained in a (quasi-) equilibrium state (Fig. 2.2b [2]; for more details, please see the explanation below on the galvanostatic intermittent titration technique). The specific capacity is frequently measured at different discharging rates to evaluate the rate capability of the cell (Fig. 2.3) [3].

The voltage profile, obtained by current reversal or cyclic chronopotentiometry, can be effectively used to characterize the multi-step redox reactions during the insertion process. An example is given in Fig. 2.4 for Cu_6Sn_5 which is one of the anodic materials that can be used in rechargeable lithium batteries [4]. The differential capacity curve dC/dE (Fig. 2.4b), which is reproduced from the voltage versus specific capacity curve of Fig. 2.4a, clearly shows two reduction peaks and the corresponding oxidation peaks. The reduction peaks, R1 and R2, are caused by the phase transformation of Cu_6Sn_5–Li_2CuSn and the subsequent formation of $Li_{4.4}Sn$, while the oxidation peaks, O1 and O2, are ascribed to the corresponding reverse reactions for the formation of Li_2CuSn and Cu_6Sn_5, respectively [5, 6].

Fig. 2.2 (a) Galvanostatic charge/discharge curve of LiMn$_2$O$_4$ and (b) open-circuit potential versus lithium stoichiometry plot of LiCoO$_2$ (Reprinted from Zhang et al. [1], Copyright ©2004, and Shin and Pyun [2], Copyright ©2001, with permissions from Elsevier Science)
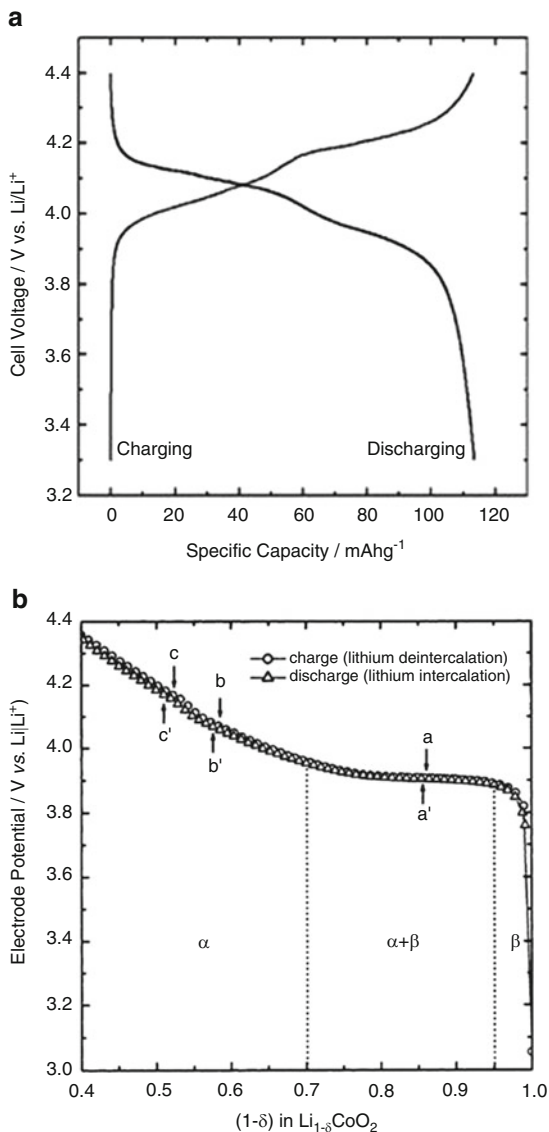
The galvanostatic intermittent titration technique (GITT) is considered to be one of the most useful techniques in chronopotentiometry. In the GITT, a constant current is applied for a given time to obtain a specific charge increment and then it is interrupted to achieve open circuit condition until the potential change is virtually zero. This process is repeated until the electrode potential reaches the cut-off voltage. Eventually, the equilibrium electrode potential is obtained as a function of lithium content, as shown in Fig. 2.5 [7]. Another important usage of the GITT is
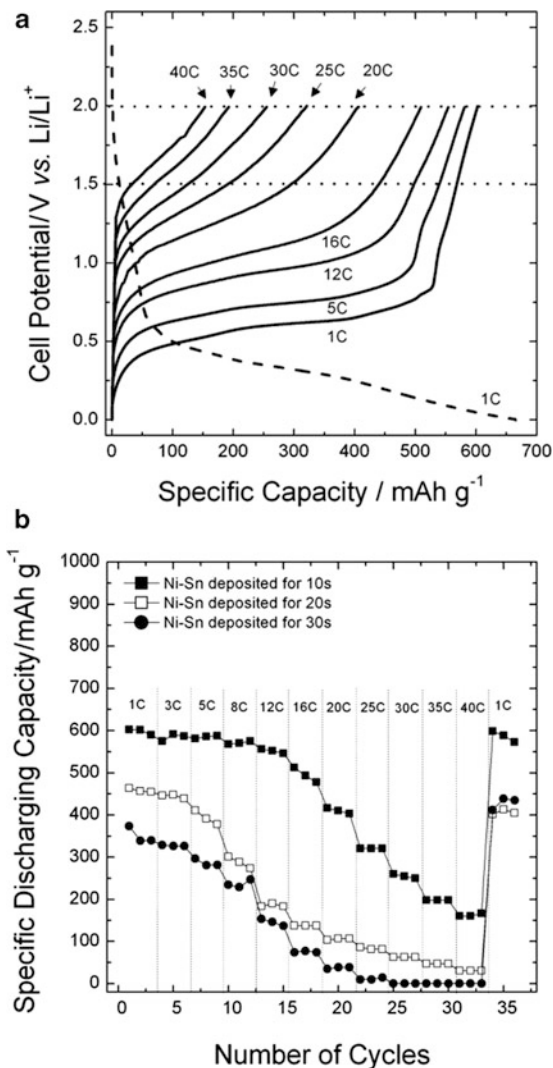
the estimation of the chemical diffusion coefficient of the species in the insertion
materials [8–10]. When the diffusion process in the material is assumed to obey
Fick's diffusion equations for a planar electrode, the chemical diffusion coefficient
can be expressed as follows [8]:

$$\tilde{D} = \frac{4}{\pi}\left(\frac{I_0 V_\mathrm{m}}{z_i F S}\right)^2 \left[\left(\frac{dE}{d\delta}\right)\middle/\left(\frac{dE}{d\sqrt{t}}\right)\right]^2 \text{ for } t << \frac{l^2}{\tilde{D}} \qquad (2.1)$$

Fig. 2.4 (**a**) Galvanostatic charge/discharge curves of the electrodeposited Cu_6Sn_5 porous film, and (**b**) the differential capacity dC/dE versus cell voltage plot, determined from (**a**) (Reprinted from Shin and Liu [4], Copyright ©2005 with permission from WILEY-VCH Verlag GmbH & Co)
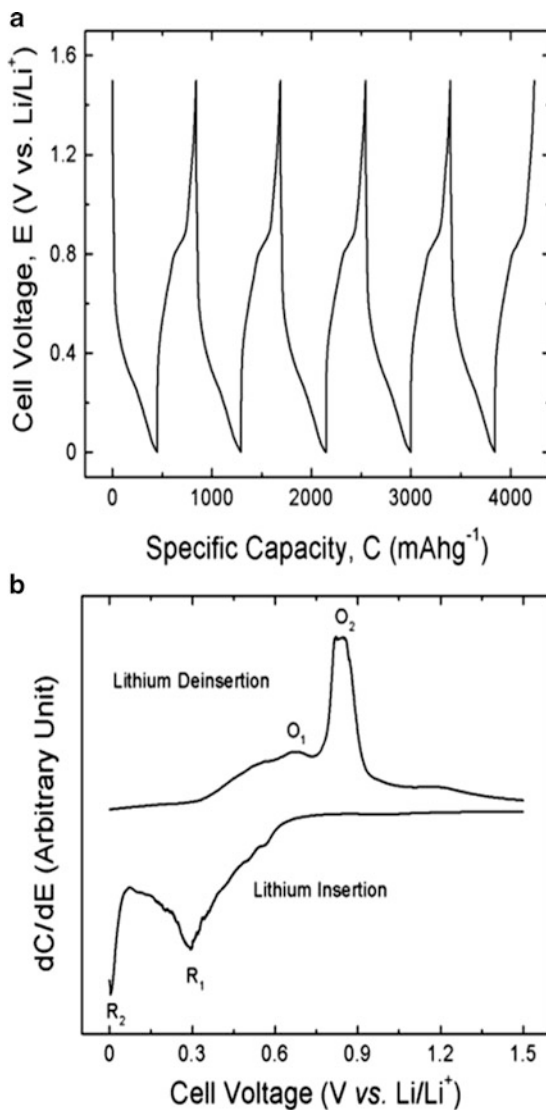
where V_m is the molar volume of the active material; z_i, the valence number of diffusing species; F, the Faraday constant; S, the surface area of the material; I_o, the applied constant current; $(dE/d\delta)$, the dependence of electrode potential on the stoichiometry of the inserted atoms; $(dE/d\sqrt{t})$, the dependence of the electrode potential on the square root of time; and l, the thickness of the electrode (or solid state-diffusion length).

Fig. 2.5 Typical
galvanostatic intermittent
charge–discharge curves of
the $Li_{1-\delta}NiO_2$ composite
electrode (Reprinted from
Choi et al. [7], Copyright
©1998 with permission from
Elsevier Science)
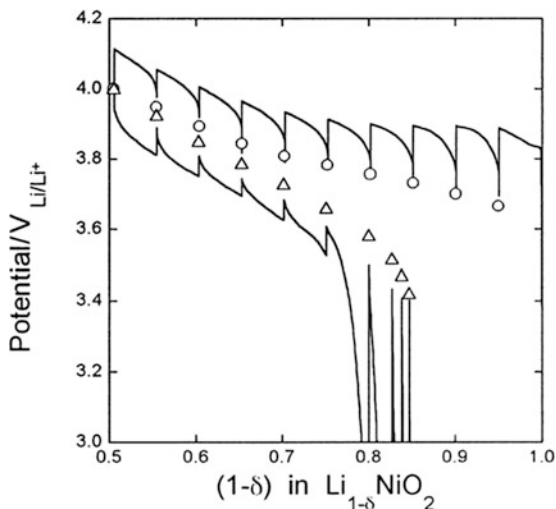
2.2 Chronoamperometry

The current transient technique is another name for chronoamperometry. In this technique, the electrode potential is abruptly changed from E_1 (the electrode is usually in the equilibrium state at this potential) to E_2 and the resulting current variation is recorded as a function of time. The interpretation of the results is typically based on a planar electrode in a stagnant solution and an extremely fast interfacial redox reaction as compared to mass transfer. Figure 2.6 shows the potential stepping in chronoamperometry, the resulting current variation with time, and the expected content profile of the active species in the electrolyte.

Chronoamperometry has been widely used to characterize the kinetic behavior of insertion materials. The typical assumption for the analysis of the chrono-amperometric curve (or current transient) of insertion materials is that the diffusion of the active species governs the rate of the whole insertion process. This means the following: The interfacial charge-transfer reaction is so kinetically fast that the equilibrium concentration of the active species is quickly reached at the electrode surface at the moment of potential stepping. The instantaneous depletion (or accumulation) of the concentration of active species at the surface caused by the chemical diffusion away from the surface to the bulk electrode (or to the interface away from the bulk electrode) is completely compensated by the supply from the electrolyte (or release into the electrolyte). This is referred to hereafter as the *potentiostatic* boundary condition. The interface between the electrode and current collector is typically under the *impermeable* boundary condition where the atom cannot penetrate into the back of the electrode. Conceptual illustrations of the *potentiostatic* and *impermeable* boundary conditions are presented in Fig. 2.7 along with their mathematical expressions.

Fig. 2.6 (a) Schematic illustration of the potential stepping in chronoamperometry, (b) the resulting current variation with time, and (c) the expected content profile of the active species O in the electrolyte. Bulk concentration of the species O is c_o^*. Species O is electrochemically inactive at E_1, but is reduced at E_2
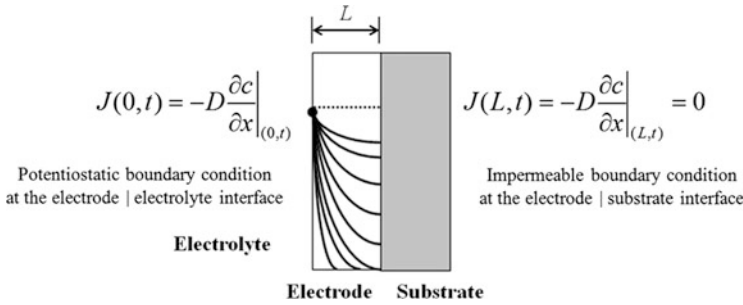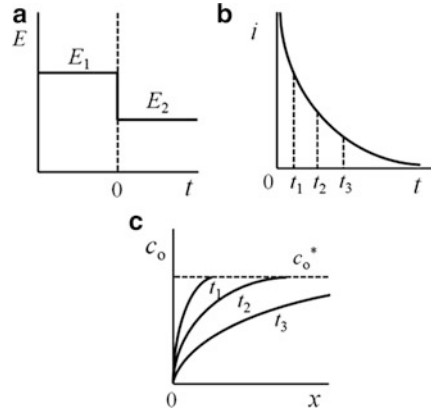
Fig. 2.7 Schematic illustration of concentration profile of the active species inserted into the electrode under the *potentiostatic* (at the electrode/electrolyte interface) and *impermeable* (at the electrode/substrate interface) boundary conditions, together with the mathematical expressions of the boundary conditions

When the atomic content is constant throughout the electrode before the application of the potential step, and the electrolyte/electrode and electrode/current collector interfaces are under *potentiostatic* and *impermeable* constraints, respectively, the normalized atomic content can be expressed as follows [11–13]:

$$\frac{c(x,t) - c_0}{c_s - c_0} = \sum_{n=0}^{\infty} \left[(-1)^n \left(\mathrm{erfc} \frac{(n+1)l - x}{\sqrt{\tilde{D}t}} + \mathrm{erfc} \frac{nl + x}{\sqrt{\tilde{D}t}} \right) \right]$$

$$\text{for } t \ll \frac{l^2}{\tilde{D}} \tag{2.2}$$

$$\frac{c(x,t) - c_0}{c_s - c_0} = -\frac{4}{\pi}\sum_{n=0}^{\infty}\left[\frac{1}{2n+1}\sin\frac{(2n+1)\pi x}{2l}\exp\left(-\frac{(2n+1)^2\pi^2\tilde{D}t}{4l^2}\right)\right]$$

$$\text{for } t \gg \frac{l^2}{\tilde{D}} \tag{2.3}$$

Equations 2.2 and 2.3 are useful to predict the atomic content in the electrode at the initial and later stages of the diffusion process, respectively. From the definition of the current given by

$$I(t) = -z_i FS\tilde{D}\left(\frac{\partial c(x,t)}{\partial x}\right)_{x=0} \tag{2.4}$$

Equations 2.2 and 2.3 become

$$I(t) = \frac{Q}{l}\left(\frac{\tilde{D}}{\pi}\right)^{1/2} t^{-1/2} \qquad\qquad \text{for } t << \frac{l^2}{\tilde{D}} \tag{2.5}$$

$$I(t) = \frac{2Q\tilde{D}^{1/2}}{l^2}\exp\left(-\frac{\pi^2\tilde{D}}{4l^2}t\right) \qquad\qquad \text{for } t >> \frac{l^2}{\tilde{D}} \tag{2.6}$$

where Q is the charge allocated to the atomic insertion/desertion process from $t = 0$ to $t \to \infty$.

Hence, the current transient shows a linear relation between the logarithmic current and logarithmic time with a slope of -0.5 in the initial stage of diffusion (Eq. 2.5), while it exhibits an exponential decay in the later stage (Eq. 2.6). In other words, the current transient shows a transition from semi-infinite diffusion behavior to finite-length diffusion behavior. The former is called Cottrell behavior.

Presented in Fig. 2.8a–c is the hypothetical open circuit potential curve with the potential drops chosen for the calculation, the resulting theoretically calculated current transients, and the time-dependent content profile across the electrode, respectively [14]. The Cottrell region and the transition time from semi-infinite diffusion to finite-length diffusion are explicitly indicated in figure (b). The content profile of figure (c) helps one understand the diffusion process during the chronoamperometric experiment: At the moment of potential stepping ($t = 0$), a new equilibrium content of the active species is imposed on the electrode surface. Then, the species diffuses into the electrode due to the content gradient. The resulting depletion of the species at the electrode surface is compensated by the continuous supply of the species from the electrolytic phase (although this process is not explicitly illustrated in the figure) and, as a result, the surface content of the species remains constant. As the diffusion time goes on, the content of the species in the electrode approaches the equilibrium composition of the final potential everywhere.
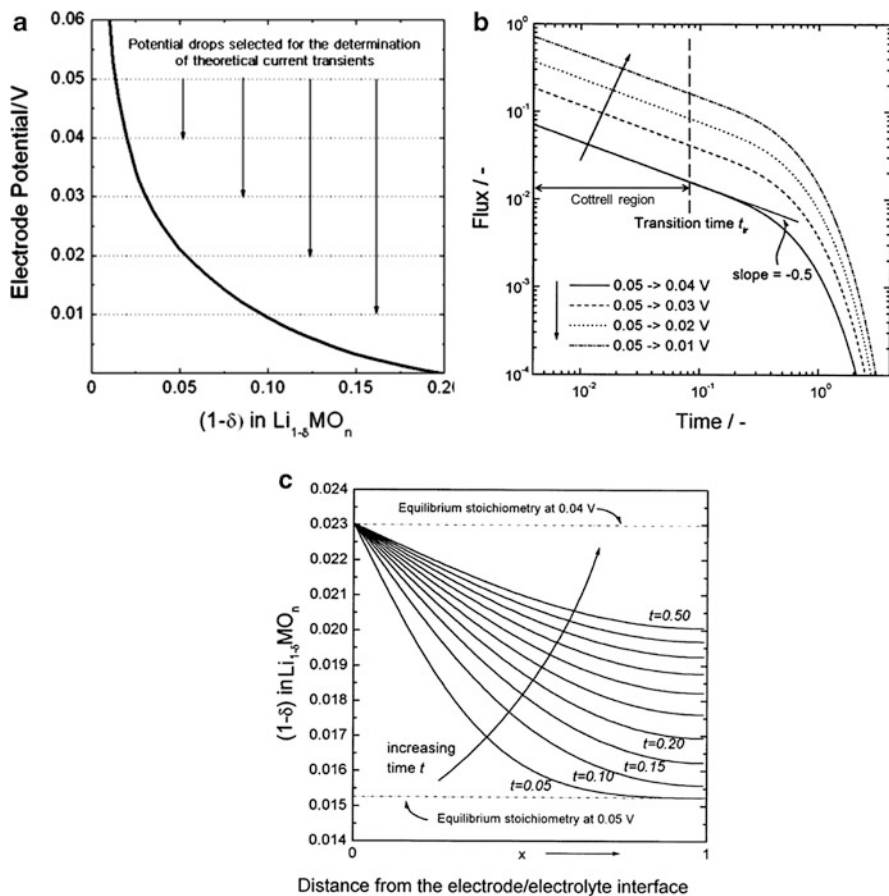
Fig. 2.8 (**a**) Hypothetic electrode potential curve, (**b**) the cathodic current transients at the potential drops of 0.05 V to different lithium insertion potentials, and (**c**) the change in lithium content profile across the electrode with time at the potential drop of 0.05–0.04 V. The *potentiostatic* and *impermeable* boundary conditions are assumed for the calculation (Reprinted from Shin and Pyun [14], Copyright ©1999 with permission from Elsevier Science)

The current transient for the insertion electrode can be classified into the following two types: The current buildup transient for the cathodic potential step and the current decay transient for the anodic potential step. It is expected that the active species is inserted into the electrode in the former, while it is extracted from the electrode in the latter. However, the current build-up transient occasionally includes the information of other (side) reaction than just the insertion of the active species. For example, when insertion materials such as Pd and LaNi$_5$ combine with hydrogen and form metal hydrides, hydrogen insertion (or hydride-forming process) accompanies sometimes the hydrogen evolution reaction. Accordingly, the current transient includes the information of both hydrogen insertion into the electrode and hydrogen evolution at the interface. Under the circumstances, the time-dependent hydrogen content in the electrode cannot be properly estimated

Fig. 2.9 Reduced current decay transients of PdH$_x$ electrode when the potential is jumped from 0.1 to 0.90 V$_{H/H+}$. Before potential jump, the hydrogen was injected to the Pd at 0.1 V$_{H/H+}$ for 2,000 s (Reprinted from Shin et al. [15], Copyright ©1998 with permission from Corrosion Science Society of Korea)
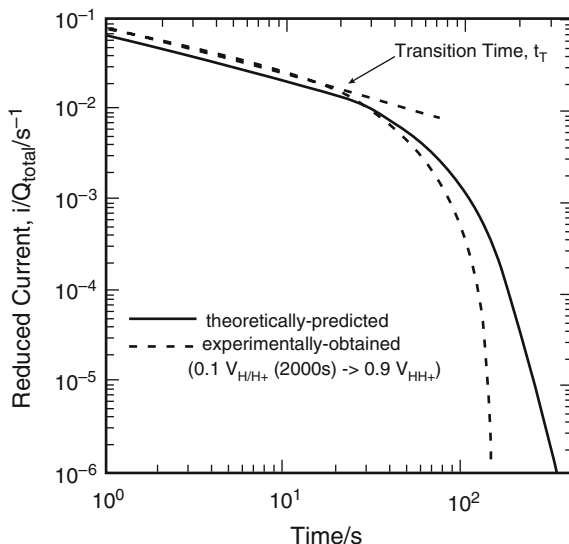
from the current transient. Consequently, in the case of a metal hydride electrode, Eqs. 2.5 and 2.6 are valid only for the current build-up transient obtained in the hydrogen-evolution-free region and current decay transient (Fig. 2.9) [15].

A number of current transients have been analyzed on the basis of Eqs. 2.5 and 2.6. Particularly, the slopes of $I(t)$ versus $t^{-1/2}$ (or the values of $I(t) \cdot t^{1/2}$) and ln $I(t)$ versus t curves have been determined in the initial and later stages of the diffusion process of the active species, respectively, to estimate its chemical diffusion coefficient in the electrode. However, it has been reported that the chemical diffusion coefficient determined from the current transient technique on the basis of the *diffusion control* process shows a large discrepancy from those values determined by other electrochemical techniques such as the GITT and electrochemical impedance spectroscopy (EIS) [16–19]. Furthermore, a number of anomalous shapes observed in current transients, which were never explained on the grounds of the *diffusion-controlled process*, have been reported for different insertion materials [20–23]. Several attempts have been made to explain these atypical behaviors of the current transient using modified *diffusion-controlled* concepts or completely new concepts. These considered the trapping/detrapping of the diffusing species [24], strain-induced diffusion [25], geometrical effect of the electrode surface [26, 27], phase transformation [28, 29], and internal cell-impedance [14, 30, 31].

2.3 Voltammetry

Voltammetry is basically referred to as techniques with the common characteristics that the potential of the working electrode is controlled and the resulting current flow is measured. One of the most general applications is "linear-sweep voltammetry
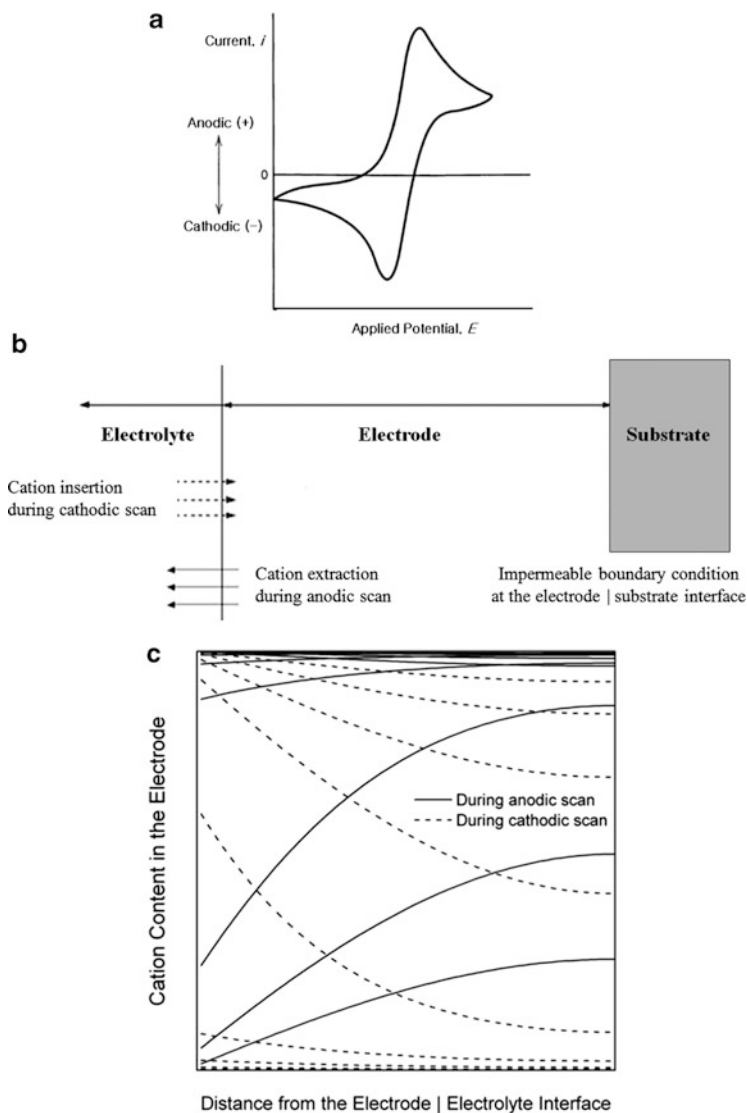
Fig. 2.10 (**a**) Typical shape of cyclic voltammogram, (**b**) the cation movement during potential scan, and (**c**) the expected potential (or time) dependence of the cation content profile

(LSV or LV)" where the potential is linearly scanned over time in either the negative or positive direction. "Cyclic voltammetry (CV)" is a set of LSV experiments in which anodic and cathodic scans are repeated alternately. That is, at the end of the first scan of LSV, the scan is continued in the reverse direction. This cycle can be repeated a number of times. Schematically shown in Fig. 2.10a–c are typical cyclic voltammogram, the cation movements during potential scans, and the expected voltage (or time) dependence of the cation content profile, respectively.

Fig. 2.11 The cyclic
voltammograms of (**a**) a
sputter-deposited LiCoO₂
film electrode and (**b**) multi-
walled carbon nanotubes
(MWNTs), tested as a
cathode and an anode,
respectively, in a
rechargeable lithium battery
(Reprinted from Shin and
Pyun [2], Copyright ©2001
and Shin et al. [32], Copyright
©2002, with permissions
from Elsevier Science)
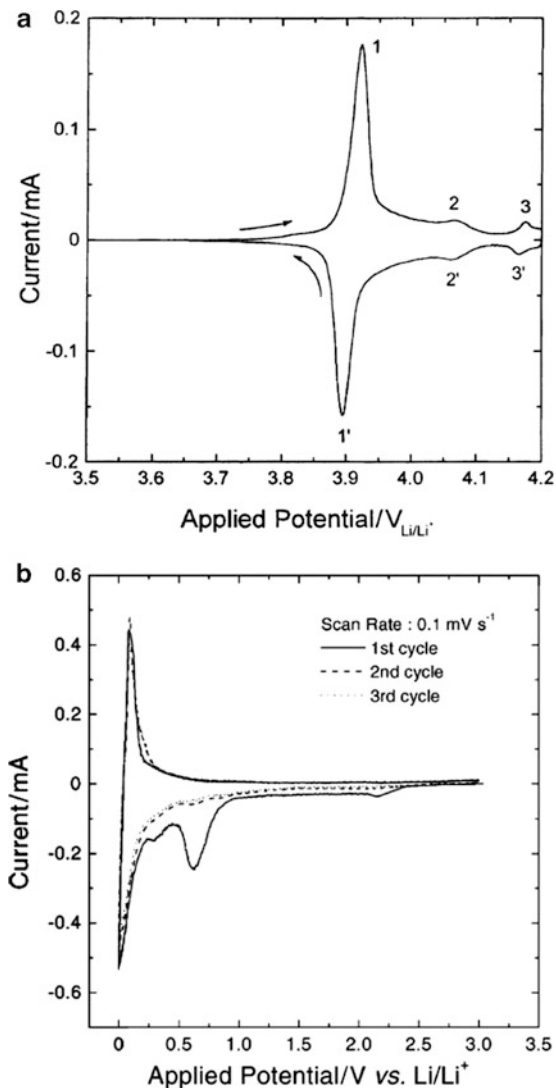
The voltammogram gives us information on the possible redox reactions of the
system, including the Faradaic insertion and extraction reaction. Figure 2.11a
presents the cyclic voltammogram of an LiCoO₂ film electrode as a cathode in
rechargeable lithium battery [2]. Three sets of anodic/cathodic current peaks are
observed. The first set of anodic/cathodic current peaks showing the largest value is
caused by the insertion/extraction-induced phase transformation from/to Li-diluted
hexagonal phase to/from Li-concentrated hexagonal phase. The second and third
sets are due to the insertion (extraction)-induced order–disorder phase transition.

Furthermore, the presence of a surface reaction and its reversibility during the atom insertion-extraction process can be successfully examined using voltammetry. Shown in Fig. 2.11b is the cyclic voltammograms for the first three cycles obtained from multi-walled carbon nanotubes (MWNTs) tested as an anode in a rechargeable lithium battery [32]. Aside from the reversible high-current redox signals below 0.5 V versus Li/Li^+, originating from the lithium insertion/extraction process, there are three irreversible peaks in the first cathodic scan. The two peaks below 1.0 V versus Li/Li^+ are caused by the formation of a solid electrolyte interphase (SEI) layer on the surface of the MWNT electrode, while the peak above 2.0 V versus Li/Li^+ is possibly due to the reduction of the oxygenated species.

Similar to chronoamperometry, the diffusion-controlled model has been usually used to analyze the voltammetric response of the insertion electrode. When an electrode initially holds at a potential E_i, where the electrode is in the equilibrium state, the linear or cyclic potential scanning is expressed at a scan rate v (V/s) as $E(t) = E_i \pm vt$. With the assumption of diffusion-controlled atomic transport, the flux balance based on Fick's law and the Nernst equation for voltammetry can be obtained in the same manner as the traditional equations for the combined process of liquid phase diffusion and the interfacial redox reaction. Nevertheless, the inability to use the Laplace transform procedure to figure out the equations greatly complicates the mathematics and makes it quite difficult to get a generalized expression for the potential-dependent current response during the voltammetric experiment.

The analytical solution of the peak current I_p on the assumption of the semi-infinite diffusion condition is known as the Sevčik equation and expressed as follows [33],

$$I_p = 2.69 \times 10^5 z_i^{3/2} S\tilde{D}^{1/2} v^{1/2} c_o \qquad (2.7)$$

In the case of finite-space diffusion, the reversible accumulation/consumption reaction can be characterized by the peak current.

$$I_p = \frac{z_i^2 F^2 v l S c_0}{2RT} \qquad (2.8)$$

Equation 2.7 indicates that the diffusion coefficient can be estimated from the intercept of the $\ln I_p$ versus v plot.

The approximate analytical solution for the generalized case has been derived by Aoki et al. for the dependence of the peak current, peak potential and half-peak width on the thickness of the electrode and the potential scan rate, in the whole range of scan rates. In particular, the relationship between the peak current and scan rate is given by [34]

$$I_p = 0.446 z_i FS(\tilde{D}/l)c_0 \beta^{0.5} \tanh(0.56\beta^{0.5} + 0.05\beta) \qquad (2.9)$$

where $\beta(= z_i Fv(l^2/D)/RT)$ is a dimensionless characteristic time parameter.

Fig. 2.12 (**a**) The cyclic
voltammograms at different
scan rates and (**b**) the plot of
cathodic peak current density
versus scan rate, reproduced
from (**a**)
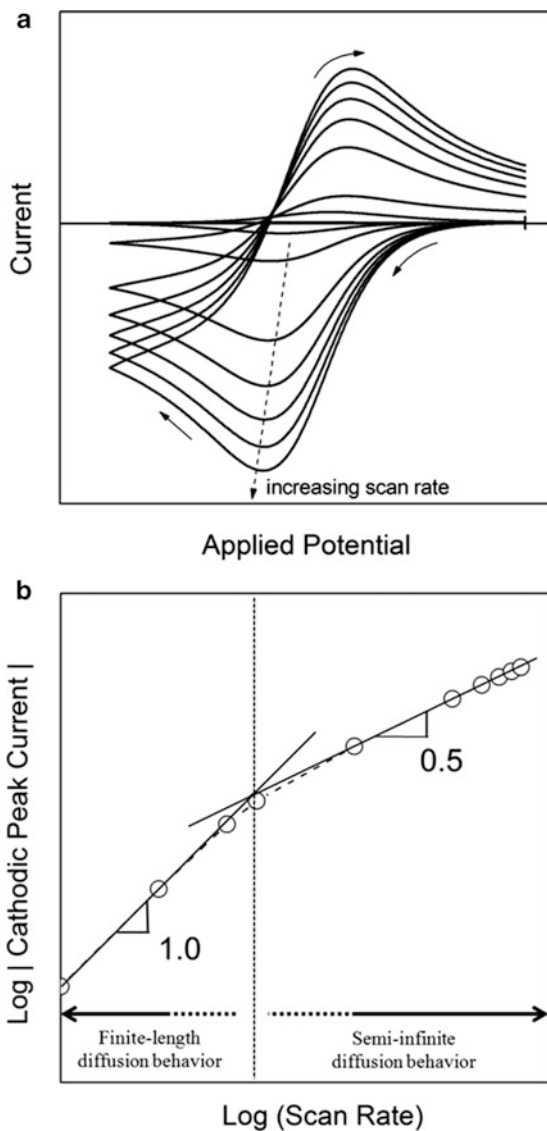
Presented in Fig. 2.12a are the cyclic voltammograms expected at different scan
rates. Two regions of finite-length diffusion and semi-infinite diffusion are
indicated at low- and high-rate potential scanning, respectively, in the reproduced
plot for the variation of the peak current with the scan rate (Fig. 2.12b).

2.4   Electrochemical Impedance Spectroscopy

In electrochemical impedance spectroscopy (EIS), the system under investigation (typically in the equilibrium state) is excited by a small amplitude ac sinusoidal signal of potential or current in a wide range of frequencies and the response of the current or voltage is measured. Since the amplitude of the excitation signal is small enough for the system to be in the (quasi-)equilibrium state, EIS measurements can be used to effectively evaluate the system properties without significantly disturbing them. Frequency sweeping in a wide range from high-to low-frequency enables the reaction steps with different rate constants, such as mass transport, charge transfer, and chemical reaction , to be separated.

For typical impedance measurements, a small excitation signal (e.g., <20 ~ 30 mV_{rms}) is used, so that the cell is considered as a (pseudo-)linear system. In this condition, a sinusoidal potential input to the system leads to a sinusoidal current output at the same frequency. As a matter of fact, the output current exponentially increases with the applied potential (or polarization, over-voltage), that is, the typical electrochemical system is not linear. When we take a closer look at a very small part of a current versus voltage curve, however, the relation might be regarded as (pseudo-)linear. If we use an excitation signal with a large amplitude and, in doing so, the system is deviated from linearity, the current output to the sinusoidal potential input contains the harmonics of the input frequency. Sometimes, the harmonic response is analyzed to estimate the non-linearity of the system, by intentionally applying an excitation potential with a large amplitude.

The system excitation caused by the time-dependent potential fluctuation has the form of

$$E(t) = E_0 \cos(\omega t) \tag{2.10}$$

where $E(t)$ is the applied potential at time t, E_o is the potential amplitude, and ω is the angular frequency that is defined as the number of vibrations per unit time (frequency, Hz) multiplied by 2π and expressed in rad/s. In a linear system, the output current signal $I(t)$ has amplitude I_0 and is shifted in phase by ϕ.

$$I(t) = I_0 \cos(\omega t - \phi) \tag{2.11}$$

Then, the impedance of the system $Z(t)$ is calculated from Ohm's law:

$$Z(t) = E(t)/I(t) = Z_0 \cos(\omega t)/\cos(\omega t - \phi) \tag{2.12}$$

When we plot the applied potential fluctuation $E(t)$ on the axis of the abscissa and the resulting current output $I(t)$ on the axis of the ordinate, we get an oval shape known as a "Lissajous figure" that can be displayed on an oscilloscope screen. By using Euler's relationship defined as $\exp(j\phi) = \cos\phi + j\sin\phi$, the system impedance is expressed as a complex function and a lot of useful information on it can be

Fig. 2.13 (a) Nyquist plot, representing absolute value of impedance vector (|Z|), phase angle (ϕ), and angular frequency (ω) dependence of the impedance, and (b) the corresponding equivalent circuit with RC parallel element
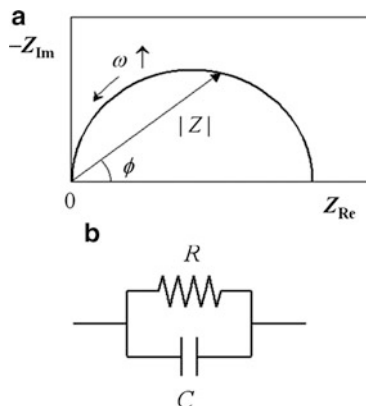
visualized in quite a simple manner. The excitation potential input and the resulting current output are described as

$$E(t) = E_0 \exp (j\omega t) \tag{2.13}$$

$$I(t) = I_0 \exp [j(\omega t - \phi)] \tag{2.14}$$

Based on Ohm's law, we get the expression for the impedance as a complex number,

$$Z(\omega) = Z_0 \exp (j\phi) = Z_0 (\cos \phi + j \sin \phi) \tag{2.15}$$

When the real part of the impedance is plotted on the axis of the abscissa and the imaginary part is plotted on the axis of the ordinate, we get a "Nyquist plot." The example presented in Fig. 2.13a is a graphical expression of the complex plane of the electrical equivalent circuit of Fig. 2.13b. In the Nyquist plot, a vector of length |Z| is the impedance and the angle between this vector and the real axis is a phase shift, ϕ.

In spite of the wide use of the Nyquist plot, it has a weakness that we cannot know the frequency at which a specific impedance point is recorded in the plot. The "Bode plot" might be useful, in that the frequency information is explicitly shown. In the "Bode plot," the axis of the abscissa is the logarithmic frequency (log ω) and the axis of the ordinate is either the absolute value of the logarithmic impedance (log |Z|) or phase shift (ϕ). The Bode plot for the equivalent circuit of Fig. 2.13b is shown in Fig. 2.14.

The Randles circuit is the simplest and most common electrical representation of an electrochemical cell. It includes a resistor (with a resistance of R_{ct}; an interfacial charge-transfer resistance) connected in parallel with a capacitor (with a capacitance of C_{dl}; a double layer-capacitance) and this RC electrical unit is connected in series with another resistor (with a resistance of R_s; a solution resistance), as shown in Fig. 2.15a. The total impedance of the Randles cell is then expressed by

Fig. 2.14 Bode plots for the
equivalent circuit with *RC*
parallel element (Fig. 2.13b)
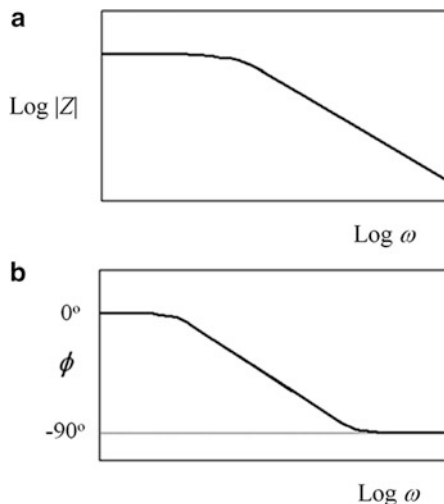
Fig. 2.15 (**a**) Randles circuit
and (**b**) its Nyquist plot
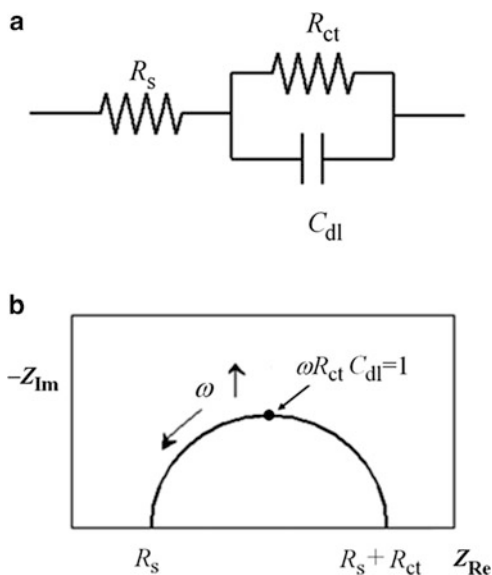
$$Z = R_s + \left(R_{ct}^{-1} + j\omega C_{dl}\right)^{-1} \tag{2.16}$$

From this equation, the real part $Z_{Re} (= R_s + R_{ct}/(1 + \omega^2 C_{dl}^2 R_{ct}^2))$ and imaginary part $Z_{Im} (= \omega C_{dl} R_{ct}^2/(1 + \omega^2 C_{dl}^2 R_{ct}^2))$ of the total impedance $Z(= Z_{Re} + jZ_{Im})$ can be separated. By eliminating the angular frequency, ω, we can get the following equation.
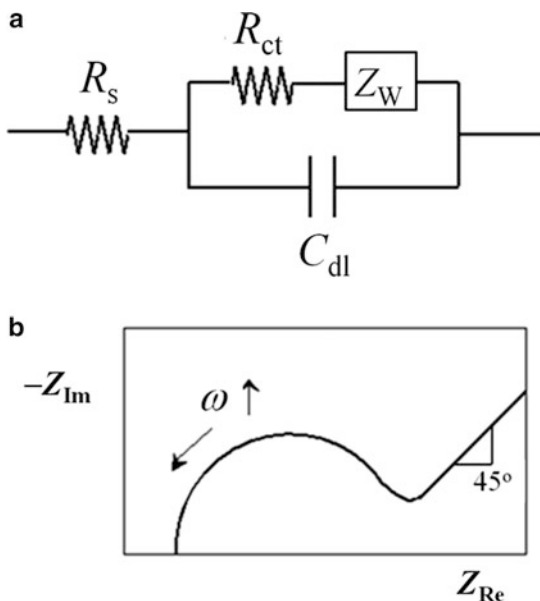
$$Z = \left[Z_{Re} - \left(R_s + \frac{R_{ct}}{2} \right) \right]^2 + R_{Im}^2 = \left(\frac{R_{ct}}{2} \right)^2 \qquad (2.17)$$

This indicates that the Nyquist plot for a Randles cell is a semicircle with two intercepts on the real axis in the high- and low-frequency regions (Fig. 2.15b). The former is the solution resistance, while the latter is the sum of the solution and charge-transfer resistances. The diameter of the semicircle is therefore equal to the charge-transfer resistance. In addition, the angular frequency is equal to the reciprocal of $R_{ct}C_{dl}$ at the minimum value of Z_{Im}.

It should be mentioned that the capacitor (e.g., the double-layer capacitor in the Randles cell) in an impedance experiment frequently does not show ideal behavior. Instead, it acts like an electrical element with constant phase called a constant phase element (CPE) and its impedance has the form of $Z = A(j\omega)^{-\alpha}(0.5 < \alpha \leqslant 1)$. A few theories have been proposed to explain the deviation of the capacitive behavior from ideality, including the surface roughness effect, but there is no general consensus on the origin of the CPE.

The equivalent circuit of insertion materials includes the diffusion impedance, originating from the solid-state diffusion of the active species. Assuming a semi-infinite diffusion process, the Warburg element with an impedance of Z_w is connected in series with the resistor representing the interfacial charge transfer, R_{ct}, as shown in Fig. 2.16a. The Nyquist plot for the equivalent circuit features an inclined line with a slope of 45 ° in the low-frequency region, due to the Warburg impedance (Fig. 2.16b).

Fig. 2.17 Impedance spectra of (**a**) the $Li_{1-\delta}CoO_2$ and (**b**) the graphite at a cell potential of 3.95 V (versus graphite) and different temperatures. The *solid* and *dotted* lines were determined from the CNLS fittings of the impedance spectra to the equivalent circuits presented in the insets. (Reprinted from Cho et al. [36], with permission from Elsevier Science)
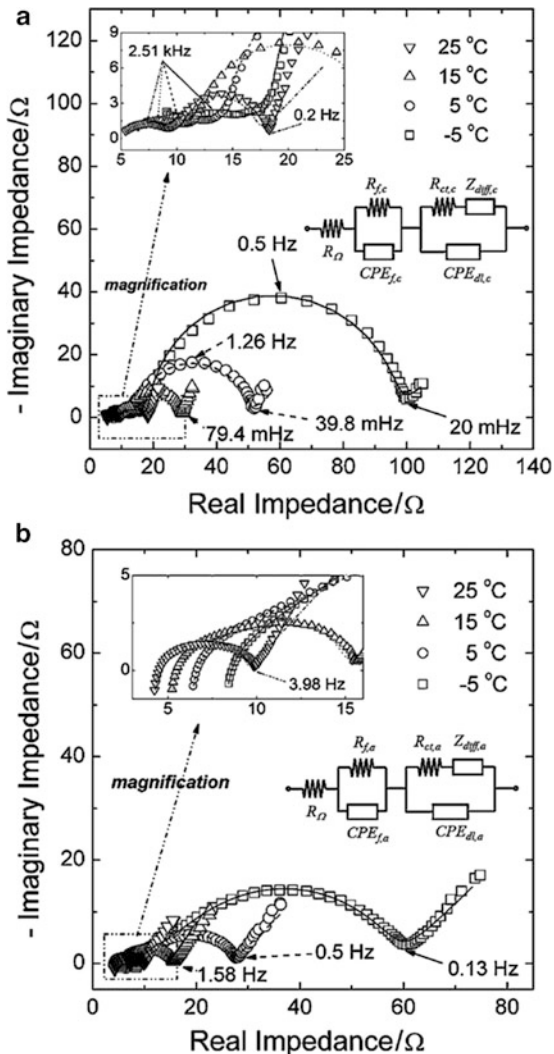
When an atom diffuses into the homogeneous single phase, the Warburg impedance Z_w is expressed as

$$Z_w = \frac{C}{\sqrt{j\omega}} = \frac{C}{\sqrt{2}}\omega^{-1/2}(1-j) \tag{2.18}$$

where $C/\sqrt{2}$ is a constant and is called the Warburg coefficient, σ_w. The Warburg coefficient has strong dependence on the chemical diffusion coefficient [35].

$$\sigma_w = \left[\frac{V_m}{F}\left(\frac{\partial E}{\partial \delta}\right)\frac{1}{\sqrt{2\tilde{D}}}\right]\frac{1}{S} \tag{2.19}$$

The real situation for the insertion process might be more complicated. Shown in Fig. 2.17a, b are the typical impedance spectra of the $Li_{1-\delta}CoO_2$ cathode and graphite anode, respectively, for a rechargeable lithium battery [36]. The first and second semicircles are attributed to the presence of the solid electrolyte interphase (or the particle-to-particle contact of the active materials) and charge-transfer resistance combined with double-layer charging/discharging, respectively [37, 38], while the inclined line (i.e., Warburg element) is due to solid-state lithium diffusion through the active materials.

The measured impedance spectra can be modeled in the simplified phenomenological equivalent circuit shown in the inset of the figure, although different circuit forms might be used according to the physical model employed to interpret the insertion process. The values of the resistance, capacitance, and the chemical diffusion coefficient of lithium into the active materials can be determined from the complex nonlinear least squares (CNLS) fitting method, by fitting the impedance spectra to the equivalent circuit [39–41].

References

1. Zhang Y, Shin HC, Dong J, Liu M (2004) Nanostructured $LiMn_2O_4$ prepared by a glycine-nitrate process for lithium-ion batteries. Solid State Ion 171:25–31
2. Shin HC, Pyun SI (2001) Investigation of lithium transport through lithium cobalt dioxide thin film sputter-deposited by analysis of cyclic voltammogram. Electrochim Acta 46:2477–2485
3. Jung HR, Kim EJ, Park YJ, Shin HC (2011) Nickel–tin foam with nanostructured walls for rechargeable lithium battery. J Power Sources 196:5122–5127
4. Shin HC, Liu M (2005) Three-dimensional porous copper-tin alloy electrodes for rechargeable lithium batteries. Adv Funct Mater 15:582–586
5. Larcher D, Beaulieu LY, MacNeil DD, Dahn JR (2000) In situ X-ray study of the electrochemical reaction of Li with η-Cu_6Sn_5. J Electrochem Soc 147:1658–1662
6. Fransson L, Nordstrom E, Edstrom K, Haggstrom L, Vaughey JT, Thackeray MM (2002) Structural transformations in Lithiated η-Cu_6Sn_5 electrodes probed by In situ Mössbauer spectroscopy and X-ray diffraction. J Electrochem Soc 149:A736–A742
7. Choi YM, Pyun SI, Moon SI, Hyung YE (1998) A study of the electrochemical lithium intercalation behavior of porous $LiNiO_2$ electrodes prepared by solid-state reaction and sol–gel methods. J Power Sources 72:83–90
8. Weppner W, Huggins RA (1977) Determination of the kinetic parameters of mixed-conducting electrodes and application to the system Li_3Sb. J Electrochem Soc 124:1569–1578
9. Choi YM, Pyun SI, Bae JS, Moon SI (1995) Effects of lithium content on the electrochemical lithium intercalation reaction into $LiNiO_2$ and $LiCoO_2$ electrodes. J Power Sources 56:25–30
10. Bae JS, Pyun SI (1995) Electrochemical lithium intercalation reaction of anodic vanadium oxide film. J Alloys Comp 217:52–58
11. Carslaw HS, Jaeger JC (1959) Conduction of heat in solids. Clarendon, Oxford
12. Crank J (1975) The mathematics of diffusion. Clarendon, Oxford
13. Wen CJ, Boukamp BA, Huggins RA, Weppner W (1979) Thermodynamic and mass transport properties of "LiAl". J Electrochem Soc 126:2258–2266
14. Shin HC, Pyun SI (1999) The kinetics of lithium transport through $Li_{1-\delta}CoO_2$ by theoretical analysis of current transient. Electrochim Acta 45:489–501
15. Shin HC, Han JN, Pyun SI (1998) Fundamentals of current transient technique and their applications to interfacial electrochemistry. J Corros Sci Soc Korea 27:232–245

16. Striebel KA, Deng CZ, Wen SJ, Cairns EJ (1996) Electrochemical behavior of $LiMn_2O_4$ and $LiCoO_2$ thin films produced with pulsed laser deposition. J Electrochem Soc 143:1821–1827

17. Uchida T, Morikawa Y, Ikuta H, Wakihara M, Suzuki K (1996) Chemical diffusion coefficient of lithium in carbon fiber. J Electrochem Soc 143:2606–2610

18. Sato H, Takahashi D, Nishina T, Uchida I (1997) Electrochemical characterization of thin-film $LiCoO_2$ electrodes in propylene carbonate solutions. J Power Sources 68:540–544

19. Zhang D, Popov BN, White RE (2000) Modeling lithium intercalation of a single spinel particle under potentiodynamic control. J Electrochem Soc 147:831–838

20. Choi YM, Pyun SI, Paulsen JM (1998) Lithium transport through porous $Li_{1-\delta}CoO_2$ electrode: analysis of current transient. Electrochim Acta 44:623–632

21. Bae JS, Pyun SI (1996) Electrochemical lithium intercalation into and deintercalation from vanadium oxide electrode by using potentiostatic current transient technique. Solid State Ionics 90:251–260

22. Pyun SI, Choi YM (1997) Electrochemical lithium intercalation into and de-intercalation from porous $LiCoO_2$ electrode by using potentiostatic current transient technique. J Power Sources 68:524–529

23. Pyun SI, Ryu YG (1998) Lithium transport through graphite electrodes that contain two stage phases. J Power Sources 70:34–39

24. Pyun SI, Yang TH (1998) Theoretical analysis of hydrogen transport through an electrode at the coexistence of two hydrogen-poor and -rich phases based upon the concept of hydrogen trapping. J Electroanal Chem 441:183–189

25. Kim DJ, Pyun SI (1998) Hydrogen transport through anodic WO_3 films. Electrochim Acta 43:2341–2347

26. Isidorsson J, Strømme M, Gahlin R, Niklasson GA, Granqvist CG (1996) Ion transport in porous Sn oxide films: cyclic voltammograms interpreted in terms of a fractal dimension. Solid State Commun 99:109–111

27. Mattsson MS, Niklasson GA, Granqvist CG (1996) Fractal dimension of Li insertion electrodes studied by diffusion-controlled voltammetry and impedance spectroscopy. Phys Rev B 54:2968–2971

28. Shin HC, Pyun SI (1999) An investigation of the electrochemical intercalation of lithium into a $Li_{1-\delta}CoO_2$ electrode based upon numerical analysis of potentiostatic current transients. Electrochim Acta 44:2235–2244

29. Funabiki A, Inaba M, Abe T, Ogumi Z (1999) Nucleation and phase-boundary movement upon stage transformation in lithium–graphite intercalation compounds. Electrochim Acta 45:865–871

30. Shin HC, Pyun SI, Kim SW, Lee MH (2001) Mechanisms of lithium transport through transition metal oxides studied by analysis of current transients. Electrochim Acta 46:897–906

31. Shin HC, Pyun SI (2003) Modern aspects of electrochemistry no. 36. In: Vayenas CG, Conway BE, White RE (eds) Chapter 5 Mechanisms of lithium transport through transition metal oxides and carbonaceous materials. Kluwer/Plenum, New York

32. Shin HC, Liu M, Sadanadan B, Rao AM (2002) Electrochemical insertion of lithium into multi-walled carbon nanotubes prepared by catalytic decomposition. J Power Sources 112:216–221

33. Bard AJ, Faulkner L (1980) Electrochemical methods. Wiley, New York

34. Aoki K, Tokuda K, Matsuda H (1983) Theory of linear sweep voltammetry with finite diffusion space. J Electroanal Chem 146:417–424

35. Ho C, Raistrick ID, Huggins RA (1980) Application of A-C techniques to the study of lithium diffusion in tungsten trioxide thin films. J Electrochem Soc 127:343–350

36. Cho HM, Choi WS, Go JY, Bae SE, Shin HC (2012) A study on time-dependent low temperature power performance of a lithium-ion battery. J Power Sources 198:273–280

37. Choi YM, Pyun SI (1997) Effects of intercalation-induced stress on lithium transport through porous $LiCoO_2$ electrode. Solid State Ionics 99:173–183

38. Aurbach D, Levi MD, Levi E, Teller H, Markovsky B, Salitra G, Heider U, Heider L (1998) Common electroanalytical behavior of Li intercalation processes into graphite and transition metal oxides. J Electrochem Soc 145:3024–3034
39. Macdonald JR, Garber JA (1977) Analysis of impedance and admittance data for solids and liquids. J Electrochem Soc 124:1022–1030
40. Macdonald JR (1987) Impedance spectroscopy. Wiley, New York
41. Bae JS, Pyun SI (1994) An a.c. impedance study of LiI-Al_2O_3 composite solid electrolyte. J Mater Sci Lett 13:573–576

Chapter 3
Hydrogen Absorption into and Subsequent Diffusion Through Hydride-Forming Metals

3.1 Introduction

In most theoretical and experimental investigations, it has been assumed that the rate-determining step (*RDS*) of hydrogen insertion (intercalation, ingress, cathodic charging/injection/introduction) into and desertion (deintercalation, egress, anodic extraction) from hydride-forming electrodes is hydrogen diffusion through the electrode. In practice, however, the rate of hydrogen insertion into and desertion from the electrode is simultaneously determined by the rates of two or more reaction steps, such as hydrogen ion transport through the electrolyte by diffusion and migration (ohmic potential drop), interfacial charge (electron) transfer (cathodic discharge of hydrogen ions), interfacial hydrogen transfer, and subsequent hydrogen diffusion through the electrode [1]. The *RDS* of the series-connected overall hydrogen insertion reaction is defined as the most strongly impeded/disturbed "slowest" step deviating far from its thermodynamic equilibrium state that represents the highest hydrogen overpotential and/or impedance pertaining to the step. In this respect, the mechanism of hydrogen insertion into and from a hydride-forming electrode has been extensively studied.

A detailed knowledge of the hydrogen insertion and desertion reactions has been acquired using various electrochemical techniques such as cyclic voltammetry [2–5], ac-impedance spectroscopy [6–17], the galvanostatic potential transient technique (chronopotentiometry) [18, 19], and potentiostatic current transient technique (chronoamperometry) [20–26]. Among these, ac-impedance spectroscopy has been widely used to identify the various reaction steps and to determine the rate-determining step, since it is an exceptionally powerful tool for separating the dynamics of several electrode processes with different relaxation times [27, 28].

In parallel with hydrogen insertion into hydride-forming electrodes, hydrogen absorption into and diffusion through metals has been widely studied in electrochemical permeation double cells with a metallic planar electrode [29–32] which

were first introduced by Devanathan and Starchurski [33]. The theoretical formulations for the potentiostatic or galvanostatic transient method [32–36], the steady-state stepwise method [37], and the steady-state galvanostatic pulse method [38] usually consider a constant concentration of absorbed hydrogen on (potentiostatic boundary condition) or constant flux (galvanostatic boundary condition) into the metal surface.

Furthermore, theoretical studies and experimental evidence of the hydrogen absorption reaction (*HAR*) using electrochemical impedance spectroscopy (*EIS*) have been presented for metal electrodes with symmetric (freestanding membrane electrode) and asymmetric (modified electrode) geometries by Pyun and coworkers [6, 7, 9–11, 39, 40]. The former and latter electrodes satisfy the permeable (transmissive) boundary (*PB*) and impermeable (reflective) boundary (*IPB*) conditions [41], respectively. The authors of this monograph extended the kinetic approach to the *HAR* into the metal which was first derived by Harrington and Conway [42]. These models consider both the hydrogen absorption into and subsequent diffusion through the metal membrane, which were disregarded in the model of Harrington and Conway [42]. Two models for the *HAR*, namely, the indirect *HAR* and direct *HAR*, were derived depending upon the presence or absence of an intermediate state of adsorbed hydrogen on entry. They showed that the hydrogen absorption mode into Pd is actually changed from the indirect *HAR* to direct *HAR*, based upon the derived models.

In order to find solutions to the problem of the Faradaic admittance which satisfy the two *PB* and *IPB* conditions established by experiment, let us first consider the "transmission line (*TL*) model." Before dealing in detail with the main topic of hydrogen insertion into the electrode, we should first discuss the *TL* model which is readily able to physically and mathematically express the two boundary conditions. The *TL* model is conveniently used as a powerful tool to generate these *PB* and *IPB* conditions in a quite arbitrary way, depending upon whether the final circuit element of the original *TL* network is replaced by pure resistance or pure capacitance, respectively. Therefore, the feature of the *TL* model is that it has versatile uses for adequately developing the *PB* and *IPB* conditions. Furthermore, the *TL* model can be modified and extended by replacing the capacitive element of the original *TL* network with an appropriate combination of resistance and capacitance/ constant phase element (*CPE*) or by taking quite different absolute values among themselves for the respective resistive and capacitive elements of the *TL* network.

This chapter covers hydrogen insertion into metals during electrochemical hydrogen charging and extraction, with particular attention to palladium as a model system. Following the discussion about the *TL* models under the *PB* and *IPB* conditions, the Faradaic admittance involving hydrogen absorption into and diffusion through the metal in the low hydrogen concentration range is theoretically derived under the *PB* and *IPB* boundary conditions that are experimentally accessible. All of the circuit parameters constituting the Faradaic admittance/impedance are quantitatively expressed in terms of the kinetic rate coefficients and constants. The kinetic parameters of hydrogen absorption coupled with its subsequent diffusion are determined and discussed.

3.2   Transmission Line Model Describing Overall Hydrogen Insertion

The conventional diffusion process in the electrode can be approximated by a transmission line (*TL*) network with the circuit parameters distributed throughout the line [27, 28, 43–52], since the basic differential equation involved in the *TL* network has formal mathematical similarity to the equation for a diffusion process [50]. From this point of view, the diffusion of hydrogen through hydride-forming electrodes can be conveniently described by a *TL* that has a network of distributed resistive and capacitive elements.

In general, *TL* networks are classified into two types depending on the boundary conditions. Figure 3.1a–c show the equivalent circuits of the *TL* networks which represent the diffusion process in the electrode under the permeable (transmissive) boundary (*PB*) condition, "one" impermeable (reflective) boundary(*IPB*) condition, and "another" impermeable (reflective) boundary(*IPB*) condition, respectively. In the *TL* model, as the diffusing atoms move in the forward direction toward the *PB* and *IPB*, they spatially and temporally sense (feel, see, or experience, if you prefer) their own instantaneous resistance to the movement as R_d in the forward direction and simultaneously experience (feel, see, or sense, if you prefer) their own instantaneous accumulation as C_d, downward perpendicular to the forward direction. In this way, a "right-angle-shaped" $R_d C_d$ series connection element is achieved.

Here, R_d [Ω cm^{-1}] designates the diffusion resistance per unit length, C_d [F cm^{-1}] the chemical capacitance for diffusion per unit length, and x is the distance from the electrode/electrolyte interface toward the *PB* and *IPB*. The finite diffusion processes are regarded as a *TL* network constituted of finite numbers of combined "right-angle-shaped" $R_d C_d$ elements achieved by successively welding the middle of one $R_d C_d$ element and the beginning of the next $R_d C_d$ element to each other, and so on, as illustrated in Fig. 3.1a, b. The beginning boundaries of the equivalent circuit bar ($x = 0$) serve as the electrolyte/electrode interfaces, as well for the *PB* and *IPB* conditions. In the case of hydrogen insertion, the electrolyte/electrode interface with $x = 0$ is subjected to an applied cathodic potential acting on the hydrogen entrance (insertion) side.

The only difference between the *PB* and *IPB* conditions is the capacitive element at the end of the equivalent circuit bar ($x = L$), which is replaced with the interfacial resistance R_{int} exposed to the electrolyte for the *PB* condition and with the interfacial capacitance C_{int} adjacent to the electrode interior for the *IPB* condition. Figure 3.1c shows that the alternative of the *IPB* can be generated by a mental experiment of sandwiching the two *IPBs* $x = L$ and $x = -L$ of one and the same finite bar with length L involving the *IPB* and simultaneously causing both ends of the equivalent bar $x = 0$ to be exposed to one and the same electrolyte as well [41]. In the case of hydrogen insertion, the *PB* with $x = L$ is subjected to an applied anodic potential serving as the hydrogen exit (desertion) side, while the two sandwiched *IPBs* with $x = L$ and $x = -L$ as well as the *IPB* with $x = L$ represent simply the interior of the
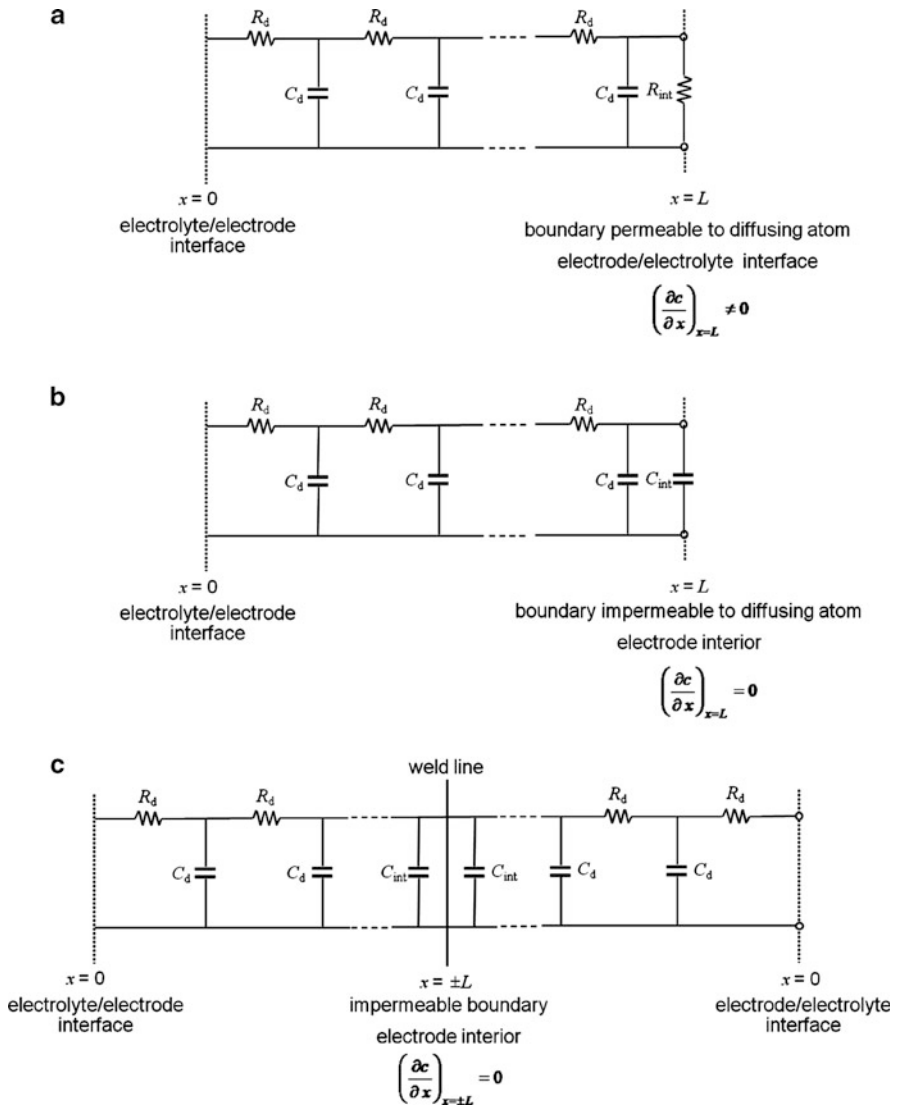
Fig. 3.1 Equivalent circuits of transmission line networks representing the diffusion process in the electrode under (**a**) permeable (transmissive) boundary (*PB*) condition, (**b**) "one" impermeable (reflective) boundary (*IPB*) condition and (**c**) "another" impermeable(reflective) boundary (*IPB*) condition

electrode which is impermeable to the diffusing hydrogen atoms. Hence, a zero concentration of the diffusing species at the *PB* $\left((c)_{x=L} = 0 \right)$ is indicative of the *PB*, whereas a zero concentration gradient at the *IPB* $\left(\left(\frac{\partial c}{\partial x} \right)_{x=\pm L} = 0 \right)$ is characteristic of the *IPB*, where c[mol cm^{-3}] means the concentration of the diffusing species in the electrode.

It is interesting to note that, on the one hand, both the first electrolyte/electrode interface with $x = 0$ and the opposite interface also with $x = 0$ involving the alternative *IPB* condition (Fig. 3.1c) need to be subjected to an applied cathodic potential acting as the hydrogen entrance (insertion) sides for the study of hydrogen insertion. On the other hand, both of these interfaces should be exposed to applied anodic potentials acting as the hydrogen exit (desertion) sides for the study of hydrogen desertion. This latter geometry is analogous to the case of the counter-diffusion [53] of tracer atoms and normal isotopic atoms involving a plane source such as a very thin disk film with a surface concentration of N^0 [mol cm^{-2}] located at the origin, $x = 0$, and satisfying the condition (constraint) $N^0 = \int_{-\infty}^{\infty} c \, \mathrm{d}x$ and the Fick's second law from $x = 0$ in one and opposite directions $x > 0$ and $x < 0$ toward infinity ∞ and $-\infty$. Such an infinite diffusion bar can easily be achieved by a mental experiment of intimately sandwiching the two semi-finite bars with $x = 0$ to ∞ and $x = 0$ to $-\infty$ together at the origin $x = 0$. Here $x = 0$ (reflection at the origin) of the semi-infinite bar exactly corresponds to the $x = L(IPB)$ and $x = +L$; $-L(IPB)$ in Fig. 3.1b, and Fig. 3.1c respectively.

Such a circuit configuration of the *TL* with *PB* can be adequately approximated by the almost symmetric interfaces of $x = 0$ (hydrogen entrance side) and $x = L$ (hydrogen exit side), both of which are exposed to the electrolyte. The equality of $R_\mathrm{d} = R_\mathrm{int}$ being the sum of the charge-transfer resistance and electrolyte resistance is characteristic of a symmetric electrode. By contrast, such a circuit configuration of the *TL* with *IPB* can be adequately approximated by the asymmetric interfaces of $x = 0$ (hydrogen entrance side) and $x = L$ (*IPB* impermeable to hydrogen atoms).

First, we will present the mathematical expressions for the transmission equivalent circuits describing hydrogen diffusion and/or transport through a homogeneous thin film electrode with thickness L. Using the Kirchhoff's voltage law for the circuits in Fig. 3.1a, b, the voltage and current are given as follows [46, 52]:

$$I = -\frac{\left(\dfrac{\partial E}{\partial x}\right)}{R_\mathrm{d}} \tag{3.1}$$

$$\left(\frac{\partial E}{\partial t}\right) = -\frac{\left(\dfrac{\partial I}{\partial x}\right)}{C_\mathrm{d}} \tag{3.2}$$

where E [V] is the electrode potential, I [A] the current, and t [s] is the diffusion time.

Combining Eqs. 3.1 and 3.2, we obtain:

$$\left(\frac{\partial E}{\partial t}\right) = \frac{\left(\dfrac{\partial^2 E}{\partial x^2}\right)}{R_\mathrm{d} C_\mathrm{d}} \tag{3.3}$$

When C_int and R_int are the same as C_d and R_d, respectively, the total finite diffusion impedance afforded by the Warburg circuit element Z_d [Ω] can be written in terms

of R_d [Ω cm^{-1}] and C_d [F cm^{-1}] by solving Eq. 3.3, depending upon the boundary conditions [52, 54] as follows:under the *PB* condition,

$$Z_d(\omega) = R_d \frac{\tanh\left[L(j\omega R_d C_d)^{1/2}\right]}{(j\omega R_d C_d)^{1/2}} \tag{3.4}$$

under the *IPB* condition [27, 28, 50],

$$Z_d(\omega) = R_d \frac{\coth\left[L(j\omega R_d C_d)^{1/2}\right]}{(j\omega R_d C_d)^{1/2}} = R_d L \frac{\coth(j\omega/\omega_c)^{1/2}}{(j\omega/\omega_c)^{1/2}}$$

with

$$\omega_c = \frac{1}{R_d C_d L^2} = \frac{\tilde{D}}{L^2} \tag{3.5}$$

where L [cm] is the thickness (diffusion layer thickness) of the whole electrode, j [$-$] the unit of the complex number, that is, $\sqrt{-1}$, $\sqrt{j} = \frac{1}{\sqrt{2}}(1+j)$, ω [Hz] the angular frequency, and ω_c [Hz] is the characteristic angular frequency of the transition from a straight line inclined at 45° to the real axis (Warburg line) in the high-frequency range $\omega \gg \omega_c = \frac{\tilde{D}}{L^2}$ to a capacitive line vertical to the real axis in the low-frequency range $\omega \ll \omega_c = \frac{\tilde{D}}{L^2}$ on the Nyquist plot. ω_c is conceptually equivalent to the reciprocal of the transition time t_{tr} in the potentiostatic current transient. It is noted that the solution for the diffusion impedance satisfying the two sandwiched *IPBs* with $x = L$ and $x = -L$ is the same as that given in Eq. 3.5.

Considering the appropriate driving forces and fluxes in the *TL* model and the diffusion reaction, the electric potential difference $\left(\frac{\partial E}{\partial x}\right)$ in the *TL* networks is basically analogous to the electrochemical potential difference in the case of one-dimensional diffusion, as follows:

$$\left(\frac{\partial E}{\partial x}\right) = \frac{RT}{zF} \frac{1}{c}\left(\frac{\partial c}{\partial x}\right) \tag{3.6}$$

where R is the gas constant, T the absolute temperature, $z[-]$ the charge(oxidation number) of the diffusing species, for instance hydrogen atoms, F the Faraday constant (96,485[C mol^{-1}]), and c[mol cm^{-3}] is the concentration of the diffusant in the electrode.

From Eq. 3.6, it is expected that Eqs. 3.4 and 3.5 derived from the circuit analysis of the *TL* model is analogous with the analytical solutions to the linear diffusion through the homogeneous thin film electrode. In fact, this can be verified by the following analytical approaches based upon the Fick's diffusion equation.

The diffusion/transport behavior of hydrogen atoms/hydrogen ions in the electrode can be described by the Fick's diffusion equation [55–58]:

$$\left(\frac{\partial c}{\partial t}\right) = \tilde{D}\left(\frac{\partial^2 c}{\partial x^2}\right) \tag{3.7}$$

Here, $\tilde{D}[\mathrm{cm}^2\ \mathrm{s}^{-1}]$ represents the chemical diffusivity [41] of any neutral diffusant, for instance hydrogen atoms.

By using the Laplace transform method, Eq. 3.7 can be solved under the oscillating concentration (or potential) perturbation at the electrode/electrolyte interface, depending on the boundary conditions, as follows:

$$\text{under } PB \text{ condition, } \ Z_{\mathrm{d}}(\omega) = \frac{RT}{z^2 F^2 A_{\mathrm{ea}} c \tilde{D}} \frac{\tanh \left(j\omega\, L^2/\tilde{D}\right)^{1/2}}{\left(j\omega/\tilde{D}\right)^{1/2}} \tag{3.8}$$

$$\text{under } IPB \text{ condition, } \ Z_{\mathrm{d}}(\omega) = \frac{RT}{z^2 F^2 A_{\mathrm{ea}} c \tilde{D}} \frac{\coth \left(j\omega\, L^2/\tilde{D}\right)^{1/2}}{\left(j\omega/\tilde{D}\right)^{1/2}} \tag{3.9}$$

Here, A_{ea} [cm^2] is the electrochemical active area. It is noticeable that the resulting Eqs. 3.8 and 3.9 determined from the diffusion equation are exactly the same functions as Eqs. 3.4 and 3.5 derived from the numerical approach based upon the *TL* networks, respectively.

There are extremely two limiting cases for a semi-infinite Warburg element under the *PB* condition as follows:

$$Z_{\mathrm{d}}(\omega) = \frac{\sigma_{\mathrm{W}}(1-j)}{\sqrt{\omega}} \ \ \text{with} \ \ \sigma_{\mathrm{W}} = \frac{RT}{z^2 F^2 A_{\mathrm{ea}} c \sqrt{2\tilde{D}}} \ \ \text{for} \ \ \omega \gg \omega_{\mathrm{c}} = \frac{\tilde{D}}{L^2}$$

$Z_{\mathrm{d}}^{\mathrm{re}}(\omega = 0) = L\sigma_{\mathrm{W}}\sqrt{\dfrac{2}{\tilde{D}}}$ (real impedance) and $Z_{\mathrm{d}}^{\mathrm{img}}(\omega = 0) = 0$ (imaginary

impedance) $\omega \ll \omega_{\mathrm{c}} = \dfrac{\tilde{D}}{L^2}$

Symmetrically, there are also the following two extremely limiting cases for a semi-infinite Warburg element under the *IPB* condition:

$$Z_{\mathrm{d}}(\omega) = \frac{\sigma_{\mathrm{W}}(1-j)}{\sqrt{\omega}} \ \ \text{with} \ \ \sigma_{\mathrm{W}} = \frac{RT}{z^2 F^2 A_{\mathrm{ea}} c \sqrt{2\tilde{D}}} \ \ \text{for} \ \ \omega \gg \omega_{\mathrm{c}} = \frac{\tilde{D}}{L^2}$$

which is common in the high-frequency range with *PB* condition.

$Z_{\mathrm{d}}^{\mathrm{re}}(\omega = 0) = \dfrac{1}{3}L\sigma_{\mathrm{W}}\sqrt{\dfrac{2}{\tilde{D}}}$ (real impedance) and $Z_{\mathrm{d}}^{\mathrm{img}}(\omega = 0) = -\infty$ (imaginary

impedance) $\omega \ll \omega_{\mathrm{c}} = \dfrac{\tilde{D}}{L^2}$

Fig. 3.2 Nyquist plot of the ac-impedance spectrum theoretically calculated for diffusion in the planar electrode in the permeable (transmissive) boundary (*PB*) condition from Eq. 3.4
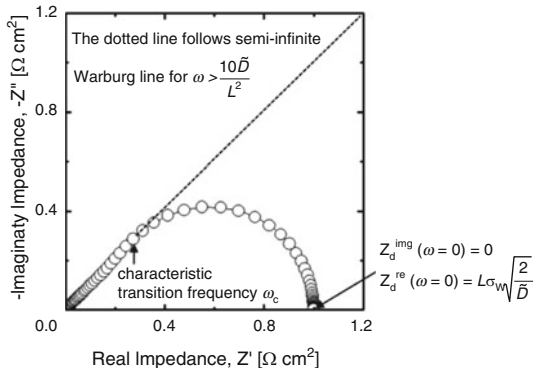
Here, $\sigma_W = \dfrac{RT}{z^2 F^2 A_{ea} c \sqrt{2\tilde{D}}}$ is termed the Warburg coefficient with dimensions of $[\Omega\ s^{-1/2}]$

According to Eqs. 3.4, 3.5, 3.8, and 3.9, R_d and C_d can be derived as follows [27, 28, 46, 49, 52]:

$$R_d = \frac{1}{zFA_{ea}\tilde{D}}\left(\frac{dE}{dc}\right) \tag{3.10}$$

$$C_d = zFA_{ea}\left(\frac{dc}{dE}\right) \tag{3.11}$$

The application of the *TL* model to hydrogen diffusion in the hydrogen insertion electrode provides us with R_d in $[\Omega\ cm^{-1}]$ and C_d in $[F\ cm^{-1}]$ which designate the resistance associated with hydrogen diffusion through the normal lattice sites and the intercalation capacitance for normal lattice sites, respectively. Both are taken per unit length. Thus, the reciprocal of the product of R_d and C_d yields the chemical diffusivity $\tilde{D}$ [41] which is by definition identical to the component diffusivity and Fickian diffusivity for ideal behavior.

The ac-impedance spectrum for diffusion under the transmissive *PB* conditions was simulated based upon Eq. 3.4, by assuming that $L = 1$ cm, $R_d = 1\ \Omega\ cm^{-1}$, and $C_d = 0.01\ F\ cm^{-1}$ which is given in Fig. 3.2. The high-frequency impedance follows the semi-infinite Warburg line for $\omega > \dfrac{10\tilde{D}}{L^2}$ and the zero-frequency impedance approaches the real impedance value of $Z_d^{re}(\omega = 0) = L\sigma_W\sqrt{\dfrac{2}{\tilde{D}}}$ and the imaginary impedance value of $Z_d^{img}(\omega = 0) = 0$. A characteristic difference in the low-frequency impedance was found in Fig. 3.2: The ac-impedance spectrum exhibits the ideal Warburg behavior with an inclined phase angle of $45°$ at high frequencies which is the same as that of the *IPB* condition, but a simple arc at low frequencies which is different from the *IPB* condition. The transition frequency ω_c appears less markedly in the transmissive *PB* condition than that in the reflective *IPB* condition (cf. Fig. 3.3).

Fig. 3.3 Nyquist plot of the ac-impedance spectrum theoretically determined for diffusion in the planar electrode in the impermeable (reflective) boundary (*IPB*) condition from Eq. 3.5
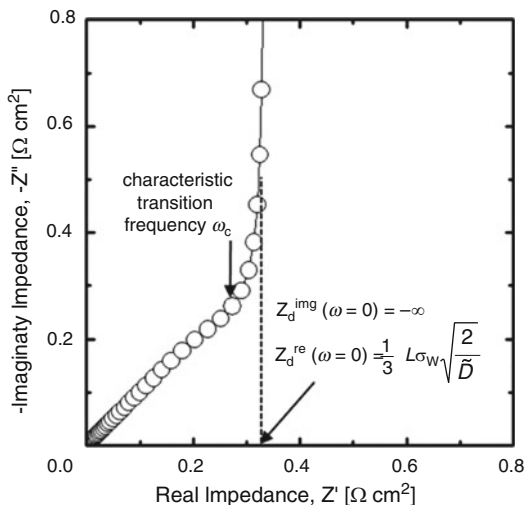
Obviously, this discrepancy in the low-frequency impedance between the *PB* and *IPB* conditions results from the different end elements of the equivalent circuit bar, either resistance or capacitance. Thus, it is recognized that the impedance behavior at low frequencies is highly dependent upon whether the mobile atoms (hydrogen) either pass through the electrolyte/electrode interface which is permeable to them or are accumulated at the *IPB* which is impermeable to them.

The *TL* model under the *PB* condition can be used to describe the Faradaic impedance (or admittance), which does not involve only the diffusion process, but also the subsequent interfacial reaction at the electrolyte/electrode interface that is permeable to the diffusing species. In other words, since the *TL* model under the *PB* condition includes the interfacial resistance, R_{int}, distributed at the end element of the equivalent circuit bar, the interfacial charge-transfer reaction mixed with subsequent diffusion can be effectively expressed in terms of this model.

Consequently, it can be reasonably stated that the *TL* model under the *PB* condition represents the Faradaic impedance/admittance rather than the non-Faradaic impedance, when R_{int} is regarded as the charge-transfer resistance, R_{ct}. In addition, the *TL* model can be modified by substituting the appropriate combination of resistance and/or capacitance elements for the capacitive element of the equivalent circuit bar, in order to describe the overall Faradaic impedances which are associated with hydrogen absorption, including adsorption and desorption, and even evolution coupled with subsequent diffusion. In this sense, the total Faradaic impedance does not represent the pure interfacial charge-transfer resistance, R_{int}.

Figure 3.3 illustrates the Nyquist plot of the ac-impedance spectrum under the reflective *IPB* condition theoretically calculated using Eq. 3.5, by assuming that $L = 1$ cm, $R_d = 1$ Ω cm^{-1}, and $C_d = 0.01$ F cm^{-1}. The ac-impedance spectrum given in Fig. 3.3 shows two characteristic features depending on the frequency range, that is, a straight Warburg line inclined at 45° to the real impedance axis in the high-frequency range above the characteristic (transition) frequency ω_c and a straight capacitive line with a phase angle of 90° (perpendicular) to the real axis in

the low-frequency range below ω_c. The transition appears more sharply in the reflective *IPB* condition than that in the transmissive *PB* condition (cf. Fig. 3.2).

In contrast to the *PB* condition, however, the *IPB* condition demonstrates that the *TL* model can effectively describe the non-Faradaic impedance for the diffusion process which is regarded as consisting of the ladder network of a finite connection of R_d and C_d in series. Alternatively we can conceive of the diffusion process as if the diffusing medium is composed of a finite sandwich of many millions layers, each with a slightly different concentration of the diffusing species. Each of these layers resembles just an $R_d C_d$ couple in parallel (see Chap. 1). Here R_d means instantaneous resistance to the movement of atoms per unit length through the electrode as a function of the position of the electrode and C_d implies instantaneous accumulation of atoms per unit length of the electrode as a function of the position of the electrode.

In fact, the *TL* model under the *IPB* condition is known to be the representative model explaining how the non-Faradaic impedance arises from the processes of hydrogen diffusion in the electrode. Nevertheless, in the special case where R_d is located at the electrolyte/electrode interface for the *IPB* condition and it is also regarded as the interfacial resistance R_{int} that is much greater than any other of the R_d s, the Faradaic admittances derived from both conditions are identical to each other, as can be seen from the conception of the hydrogen overpotential (see Sect. 3.3). Chapter 4 discusses the topic of the *IPB* condition in more detail.

Furthermore, the impedance analysis can also be readily extended to hydrogen diffusion which involves hydrogen trapping [27, 28] by modifying the diffusion capacitance in the *TL* network under the *IPB* condition. In the presence of reversible trap sites of one type, the original frequency-invariant diffusion capacitance C_d in Eq. 3.5 should be replaced by the complex capacitance, $C^*(\omega)$, which is the sum of the frequency-independent capacitance for the normal lattice sites C_d and the frequency-dependent capacitance for the reversible trap sites $C_t^*(\omega)$. Finally, we obtain the diffusion impedance formula Z_d which is the same as Eq. 3.5.

Thus, the impedance formula obtained for hydrogen diffusion with accompanying reversible trapping permits us to construct the equivalent circuit of a *TL* network which includes an additional series of resistive (R_t in $[\Omega \text{ cm}^{-1}]$) and capacitive (C_t in $[\text{F cm}^{-1}]$) elements related to reversible trapping. As a result, it is concluded that ac-impedance spectroscopy employing a *TL* network offers an exceptionally powerful tool for analyzing anomalous hydrogen diffusion through a hydride-forming electrode and also for separating the dynamics of two processes with different relaxation times. Especially, it is of special interest to study anomalous hydrogen diffusion with accompanying trapping in the frequency domain, which Chap. 5 will discuss in more detail.
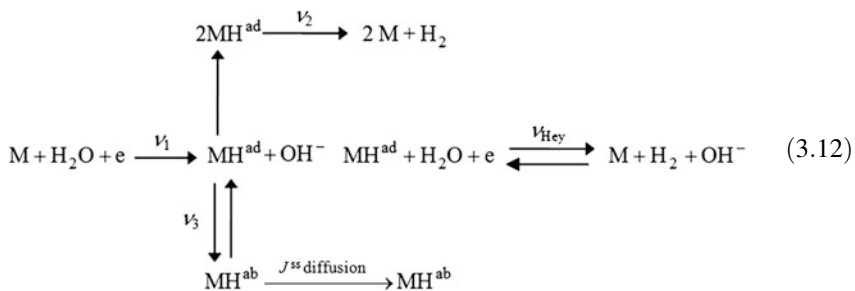
3.3 Faradaic Admittance Involving Hydrogen Absorption Reaction (*HAR*) into and Subsequent Diffusion Through Hydride-Forming Metals

From the late 1990s to the early 2000s, Pyun and coworkers [6, 7, 9–11, 39, 40] performed theoretical studies on the hydrogen absorption reaction (*HAR*) using electrochemical impedance spectroscopy (*EIS*) for planar metal electrodes with

symmetric and asymmetric geometries. With a small-amplitude signal, the electrochemical behavior is nearly linear, so electrode impedance measurements should provide correct values of the kinetic parameters for hydrogen insertion into the metal membrane at all hydrogen overpotentials. In fact, their models consider the complete sequence of water reduction, hydrogen adsorption, recombination, absorption, and diffusion through the planar metal electrode. Here, the models will be introduced along with the physical significance of the determined kinetic parameters.
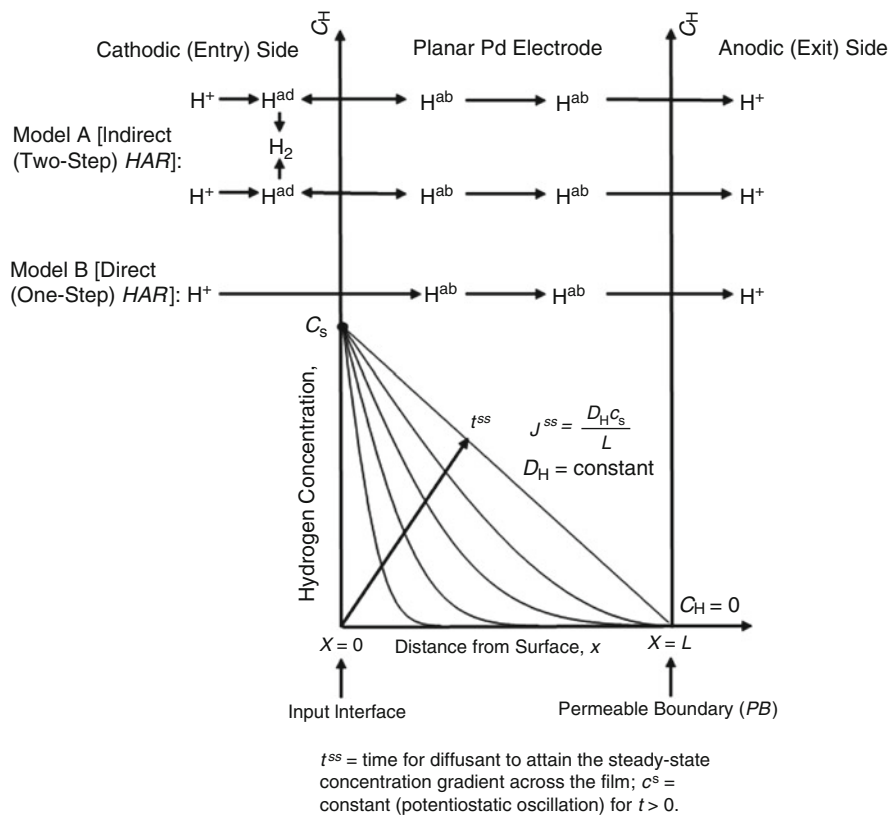
The hydrogen evolution reaction (*HER*) on a planar Pd electrode in alkaline solution is known to involve two successive steps [59–61]. The first step of the *HER* is the Volmer adsorption reaction of water electrolysis and the second step is the Tafel chemical desorption of the two adsorbed hydrogen atoms from the metal surface.

Hydride-forming materials, such as Pd, LaNi$_5$, and TiFe, can absorb a large amount of hydrogen, and the *HAR* provides an alternative reaction path which is parallel to the Tafel chemical or Heyrovsky electrochemical desorption of hydrogen atoms. The electrolytic hydrogen passes through the adsorbed state into the metal foil electrode. The adsorbed state is assumed to be identical to that which leads to the *HER* and *HAR*. The reaction sequence at the cathodic surface in alkaline solution is as follows:

$$
\begin{array}{c}
2MH^{ad} \xrightarrow{\ v_2\ } 2\,M + H_2 \\[2ex]
\uparrow \\[1ex]
M + H_2O + e \xrightarrow{\ v_1\ } MH^{ad} + OH^- \qquad MH^{ad} + H_2O + e \underset{}{\overset{v_{Hey}}{\rightleftharpoons}} M + H_2 + OH^- \\[2ex]
v_3 \updownarrow \\[1ex]
MH^{ab} \xrightarrow{\ J^{ss}\ diffusion\ } MH^{ab}
\end{array}
\qquad (3.12)
$$

where MH^{ad} is the adsorbed hydrogen on the surface, MH^{ab} the absorbed hydrogen just beneath the metal electrode subsurface, v_1 the rate of the Volmer adsorption, v_2 the rate of the Tafel desorption, v_3 the rate of the *HAR*, v_{Hey} the rate of the Heyrovsky electrochemical desorption, and J^{ss} [mol cm^{-2} s^{-1}] is the steady-state flux of hydrogen in the metal. v_i has in general dimensions of [mol cm^{-2} s^{-1}]. The Heyrovsky electrochemical reaction was not considered in this work, since the *HER* on Pd was reported [30, 62, 63] to follow the fast-discharge and slow-Tafel desorption (recombination) mechanism.

The boundary conditions (*BCs*) for hydrogen insertion into the metal can be divided into two categories, namely, the transmissive *PB* and reflective *IPB* conditions. In the former condition, hydrogen enters into the entry side of the planar metal electrode exposed to an applied cathodic potential, diffuses through the electrode, and finally escapes into the electrolyte from the exit side of the electrode exposed to an applied anodic potential, as shown in Fig. 3.4. The *PB*

Fig. 3.4 Schematic diagram of hydrogen evolution reaction *(HER)* on/from and hydrogen absorption reaction *(HAR)* into planar metal membrane electrode subjected to the two possible transmissive permeable boundary *(PB)* conditions with and without adsorbed intermediate state of hydrogen on the metal surface [6] (Reprinted from Lim and Pyun [6], Copyright ©1993 with permission from Elsevier Science)

condition is characterized by such typical quantities as t^{ss} (time for the diffusant to attain the steady-state concentration gradient across the planar film electrode) and constant (potentiostatic) values of the entry hydrogen concentration c_s (applied cathodic potential) at $x = 0$ and exit hydrogen concentration c (applied anodic potential) $= 0$ at $x = L$. This condition has been widely used in electrochemical hydrogen permeation studies [29–32] to determine the hydrogen diffusion coefficient in the metal, since Devanathan and Starchurski [33] first introduced this method.

The latter condition can be easily achieved by merely immersing the electrode in the electrolyte, as presented in Fig. 3.5, which is the same as that illustrated in Fig. 3.1c. The *IPB* conditions are experimentally realized for a zero hydrogen concentration gradient at the center of a thin Pd foil electrode and the same constant hydrogen concentration on both electrode surfaces, when hydrogen enters into both sides of the immersed foil electrode. The center of the electrode acts as a blocking
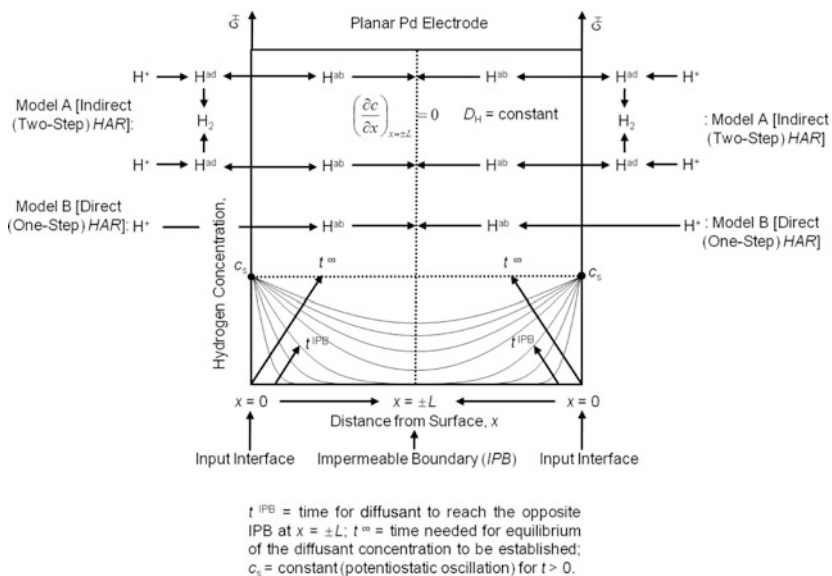
Fig. 3.5 Schematic diagram of hydrogen evolution reaction *(HER)* on/from and hydrogen absorption reaction *(HAR)* into planar metal membrane electrode subjected to reflective impermeable boundary *(IPB)* condition [10] (Reprinted from Yang and Pyun [10], Copyright © 1996 with permission from Elsevier Science)

plane against the diffusion of hydrogen. The *IPB* condition is characterized by such typical quantities as t^∞ (time for equilibrium of the diffusant concentration to be established across the planar film electrode), t^{ITB} (time for equilibrium of the diffusant to first reach the opposite *IPB* at $x = \pm L$) and such conditions as *IPB* at $x = \pm L$ ($\left(\dfrac{\partial c}{\partial x}\right)_{x=\pm L} = 0$). The *IPB* conditions have several advantages over the *PB* conditions in that the former can be applied to various systems comprising oxides and other compounds and that the obtained currents or potentials are close to the equilibrium values. Also, from a practical viewpoint, the electrode geometry satisfying the *IPB* conditions is in general used in electrochromic devices and batteries such as lithium ion and Ni/metal hydride secondary batteries [55, 64].

The Faradaic admittance based upon the above reaction scheme in Eq. 3.12 was first derived by Harrington and Conway [42] using an extension of Armstrong's kinetic approach to the Faradaic admittance associated with a two-step reaction [65], under the important assumption that the diffusion of the participating species within the electrolytic solution is not rate determining. However, they [42] disregarded the *HAR* step involved in the *HER* in determining the Faradaic admittance. Metals can in general absorb hydrogen to a greater or lesser extent, and the *HAR* provides an alternative reaction path which is in parallel to the chemical or electrochemical desorption(recombination) of hydrogen atoms. Two models have been suggested [59, 66, 67] to describe the *HAR* into the metal. One involves the concept that hydrogen, on discharging on the metal, passes through an adsorbed

state prior to entering into the metal (the indirect *HAR* "model A") [59]. The other is that hydrogen enters into the metal without passing through the adsorbed state in the same elementary act as that in which it is discharged (the direct *HAR* "model B") [66, 67]. The absorbed hydrogen diffuses toward the interior of the metal. Therefore, in deriving the Faradaic admittance involving the *HAR*, the absorption and diffusion steps should be taken into account in addition to the *HER*.

In this connection, the Faradaic admittance/impedance can also be understood as deduced from the general formulation of the diffusion impedance numerically simulated based upon the modified *TL* networks by substituting an appropriate specific equivalent circuit for the original *TL* networks, as discussed in Sect. 3.2.

3.3.1   Transmissive Permeable (PB) Boundary Condition

In this chapter, the Faradaic admittance involving the *HAR* into a hydride-forming electrode is theoretically derived on the basis of the two *HAR* models mentioned above under the *PB* condition which is experimentally accessible using the Armstrong's kinetic approach [65].

To explicitly express the Warburg impedance in terms of the ac diffusion of hydrogen, let us first determine the oscillating flux of hydrogen at the entry side of the metal membrane. Under small-signal ac conditions, the system variables may be separated into steady-state and time-dependent terms.

$$c = c^{\mathrm{ss}} + \tilde{c} \, \exp(j\omega t) \tag{3.13}$$

and

$$J = J^{\mathrm{ss}} + \tilde{J} \exp(j\omega t) \tag{3.14}$$

where c^{ss}[mol cm^{-3}] is the steady-state concentration of hydrogen in the metal, $\tilde{c}$ the perturbation (oscillation) in the concentration of hydrogen in the metal due to sinusoidal oscillations, J^{ss} [mol cm^{-2} s^{-1}] the steady-state flux of hydrogen in the metal, and $\tilde{J}$ is the perturbation (oscillation) in the flux of hydrogen in the metal due to sinusoidal oscillations.

Inserting Eqs. 3.13 and 3.14 into the equations of the Fick's first law of diffusion and equating the time-dependent terms with each other, one obtains

$$\tilde{J} = -D_{\mathrm{H}} \left(\frac{\partial \tilde{c}}{\partial x} \right) \tag{3.15}$$

where D_{H} means the Fickian diffusivity of hydrogen in the metal and x is the distance from the hydrogen entry surface of the metal to an arbitrary position in metal. The Fick's second law can then be written in small-signal form.

$$j\omega\tilde{c} = -D_H \left(\frac{\partial^2 \tilde{c}}{\partial x^2}\right) \tag{3.16}$$

where j is a complex number and ω the angular frequency.

The general solution of Eq. 3.16 is given by Franceschetti [68] as

$$\tilde{c} = A \, \sinh\!\left(\sqrt{\frac{j\omega}{D_H}}\, x\right) + B \, \cosh\!\left(\sqrt{\frac{j\omega}{D_H}}\, x\right), \tag{3.17}$$

where A and B are constants which must be suitably selected to satisfy the *BCs*. The transmissive permeable *BC* for the *HER* and *HAR* is schematically shown in Fig. 3.4. The initial (*IC*) and boundary (*BC*) permeable (*PB*) conditions are as follows:

$$t = 0(IC)\colon \; 0 \leqslant x \leqslant L(\text{finite diffusion bar})\, c = 0 \tag{3.18}$$

$$t > 0(BC)\colon x = 0 \;\; c = c_s^{ss} + \tilde{c}_s \exp(j\omega t) \;\; \text{(potentiostatic perturbation)}$$
$$x = L \;\; c = 0, \tag{3.19}$$

where c_s^{ss} is the steady-state concentration of hydrogen at the entry side, $\tilde{c}_s$ the perturbation in the concentration of hydrogen at the entry side of the planar metal electrode, and L is the thickness of the planar metal electrode. t^{ss} in Fig. 3.4 means the time needed to establish the steady-state concentration gradient across the planar electrode, which is called the "time-lag." The presence of t^{ss} is characteristic of the *PB* condition, while the existence of t^{IPB} and t^{∞} in Fig. 3.5 is typical of the *IPB* condition.

From the *BC* Eq. 3.19, apart from the perturbation, the Fick's first law also gives

$$c^{ss} = c_s^{ss}\left(1 - \frac{x}{L}\right) \tag{3.20}$$

where c^{ss} is the steady-state concentration of hydrogen at arbitrary x.

From Eq. 3.17 with the *BC* Eq. 3.19, the perturbation in the concentration of hydrogen within the planar electrode, $\tilde{c}$, is given by

$$\tilde{c} = \tilde{c}_s\left[\cosh\!\left(\sqrt{\frac{j\omega}{D_H}}\,L\right) - \coth\!\left(\sqrt{\frac{j\omega}{D_H}}\,L\right)\sinh\!\left(\sqrt{\frac{j\omega}{D_H}}\,x\right)\right] \tag{3.21}$$

Thus, the oscillating flux of hydrogen at the entry side of the electrode, $J_{x=0}$, gives as per the Fick's first law

$$J_{x=0} = -D_H\left(\frac{\partial\tilde{c}}{\partial x}\right)_{x=0} = \frac{D_H}{L}c_s^{ss} + \sqrt{j\omega D_H}\coth\!\left(\sqrt{\frac{j\omega}{D_H}}\,L\right)\tilde{c}_s \exp(j\omega t) \tag{3.22}$$
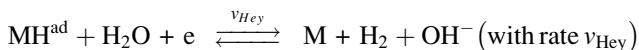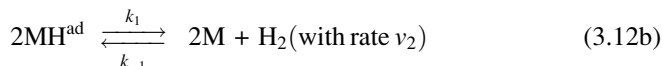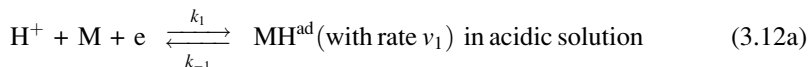
Based upon the indirect *HAR* model "A" and direct *HAR* model "B," the Faradaic admittances involving the *HAR* into the planar Pd electrode were theoretically derived [6, 7] in the permeable *BC*, where the activity of hydrogen at the exit side of the electrode is almost zero, by using Armstrong's kinetic approach [65] in conjunction with Eq. 3.22 which describes the hydrogen diffusion through the electrode. In the derivation of the Faradaic admittance, the Heyrovsky electrochemical desorption (recombination) is disregarded for the sake of mathematical simplicity. The two *HAR* models are schematically demonstrated in Fig. 3.4 and will be detailed below.

3.3.2   (i) Model A – Indirect (Two-Step) Hydrogen Absorption Reaction (HAR) Through Adsorbed Phase (State) – (a) Diffusion-Controlled HAR Limit and – (b) Interface-Controlled HAR Limit
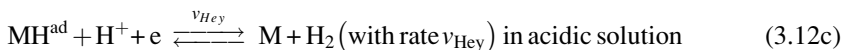
This model developed by Bockris et al. [59] considers the presence of the adsorbed intermediate stage. After its entry, the electrolytic hydrogen passes through the adsorbed state into the metal substrate. The adsorbed state commonly leads to both the *HER* and *HAR*. At the cathodic surface in alkaline/acidic solutions, the first step of the *HER* involves an electrochemical reduction of the water molecules, with the formation of hydrogen adsorbed on the electrode surface (the Volmer adsorption, Eq. 3.12a), followed by either the Tafel chemical desorption Eq. 3.12b or the Heyrovsky electrochemical desorption Eq. 3.12c:

$$H_2O + M + e \underset{k_{-1}}{\overset{k_1}{\rightleftarrows}} MH^{ad} + OH^- (\text{with rate } v_1)$$

in alkaline solution and

$$H^+ + M + e \underset{k_{-1}}{\overset{k_1}{\rightleftarrows}} MH^{ad} (\text{with rate } v_1) \text{ in acidic solution} \tag{3.12a}$$

$$2MH^{ad} \underset{k_{-1}}{\overset{k_1}{\rightleftarrows}} 2M + H_2 (\text{with rate } v_2) \tag{3.12b}$$

$$MH^{ad} + H_2O + e \overset{v_{Hey}}{\rightleftarrows} M + H_2 + OH^- (\text{with rate } v_{Hey})$$

in alkaline solution and

$$MH^{ad} + H^+ + e \overset{v_{Hey}}{\rightleftarrows} M + H_2 (\text{with rate } v_{Hey}) \text{ in acidic solution} \tag{3.12c}$$
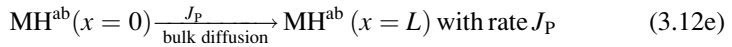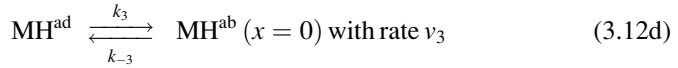
The fast discharge by the Volmer adsorption and the slow Tafel-recombination mechanism proposed by many authors [30, 62, 63] dominate the *HER* on Pd.

Therefore, the electrochemical Heyrovsky-desorption reaction Eq. 3.12c was not considered in this chapter.

The adsorbed hydrogen can pass on into the absorbed state by jumping into the interstitial sites beneath the first atomic layer [59]. From this absorbed state, hydrogen diffuses toward the exit side of the Pd electrode.

$$MH^{ad} \underset{k_{-3}}{\overset{k_3}{\rightleftharpoons}} MH^{ab} (x = 0) \text{ with rate } v_3 \tag{3.12d}$$

$$MH^{ab}(x = 0) \xrightarrow[\text{bulk diffusion}]{J_P} MH^{ab} (x = L) \text{ with rate } J_P \tag{3.12e}$$

where MH^{ab} refers to the absorbed hydrogen just beneath the metal surface. k_3 and k_{-3} with units of [mol cm^{-2} s^{-1}] and [cm s^{-1}] are the rate constants of hydrogen transfer from the surface (2-dimensional [2D] adsorbed state) to the bulk (3-dimensional [3D] absorbed state) and from the bulk (absorbed state) to the surface (adsorbed state), respectively, and J_p is the flux density of hydrogen permeating out through the planar Pd electrode from the entry side. It is assumed that for low hydrogen coverages and for low degrees of saturation of hydrogen at the entry side of the membrane, the rate of the *HAR* [59–61] is given by

$$v_3 = k_3 \cdot \theta - k_{-3} \cdot c_s \tag{3.23}$$

where θ ($=\Gamma/\Gamma_{max}$) is the hydrogen coverage on the entry side of the electrode, Γ the surface concentration [mol cm^{-2}] of adsorbed hydrogen, Γ_{max} the maximum surface concentration [mol cm^{-2}] of adsorbed hydrogen due to sinusoidal oscillations, and c_s is the concentration of hydrogen at $x = 0$.

Considering that the diffusion of absorbed hydrogen through the planar electrode under the permeable *BC*, as expressed by Eq. 3.19, is experimentally accessible, the Faradaic admittance involving the *HER* and *HAR* can be derived in the following way.

The charge and mass balances are given by the reaction scheme of Eq. 3.12 above

$$-\frac{i_F}{F} = v_1 \tag{3.24}$$

and

$$\Gamma_{max} \frac{d\theta}{dt} = v_1 - 2v_2 - J_{x=0}, \tag{3.25}$$

respectively, where i_F [A cm^{-2}] is the Faradaic current density and F is the Faraday constant. The negative sign appearing in Eq. 3.24 is due to the fact that the (−) sign of the cathodic Faradaic current density i_F is the opposite to that of the rate of the Volmer adsorption reaction.

The electrochemical response to the sinusoidal oscillation of the potential can be expressed in terms of a Taylor series expansion. Neglecting the second- and higher order terms of the series expansion, the sinusoidal response is given by

$$v_1 = v_1^{ss} + \left(\frac{\partial v_1}{\partial E}\right)\tilde{E}\exp(j\omega t) + \left(\frac{\partial v_1}{\partial \theta}\right)\tilde{\theta}\exp(j\omega t) + \left(\frac{\partial v_1}{\partial c_s}\right)\tilde{c}_s\exp(j\omega t), \quad (3.26)$$

$$v_2 = v_2^{ss} + \left(\frac{\partial v_2}{\partial E}\right)\tilde{E}\exp(j\omega t) + \left(\frac{\partial v_2}{\partial \theta}\right)\tilde{\theta}\exp(j\omega t) + \left(\frac{\partial v_2}{\partial c_s}\right)\tilde{c}_s\exp(j\omega t), \quad (3.27)$$

and

$$v_3 = v_3^{ss} + \left(\frac{\partial v_3}{\partial E}\right)\tilde{E}\exp(j\omega t) + \left(\frac{\partial v_3}{\partial \theta}\right)\tilde{\theta}\exp(j\omega t) + \left(\frac{\partial v_3}{\partial c_s}\right)\tilde{c}_s\exp(j\omega t) \quad (3.28)$$

where E is the electrode potential and $\tilde{E}$ is the amplitude of the sinusoidal oscillation of the electrode potential ($\tilde{E}\exp(j\omega t)$).

From the characteristics of the Volmer adsorption reaction expressed by Eq. 3.12a and the Tafel desorption reaction expressed by Eq. 3.12b [42], and the *HAR* given by Eq. 3.23, it is apparent that

$$\left(\frac{\partial v_1}{\partial c_s}\right) = 0, \quad \left(\frac{\partial v_2}{\partial E}\right) = 0, \quad \left(\frac{\partial v_2}{\partial c_s}\right) = 0, \quad \text{and} \quad \left(\frac{\partial v_3}{\partial E}\right) = 0, \quad (3.29)$$

which are termed reaction constraints. Substituting Eqs. 3.22, 3.26, and 3.27 into Eqs. 3.24 and 3.25 under the reaction constraints given by Eq. 3.29 and equating the time-dependent terms with each other, one gets

$$-\frac{\tilde{i}_F}{F} = \left(\frac{\partial v_1}{\partial E}\right)\tilde{E} + \left(\frac{\partial v_1}{\partial \theta}\right)\tilde{\theta}, \quad (3.30)$$

and

$$j\omega\,\Gamma_{max}\tilde{\theta} = \left(\frac{\partial v_1}{\partial E}\right)\tilde{E} + \left(\frac{\partial v_1}{\partial \theta}\right)\tilde{\theta} - 2\left(\frac{\partial v_2}{\partial \theta}\right)\tilde{\theta} - \sqrt{j\omega D_H}\coth\left(\sqrt{\frac{j\omega}{D_H}}L\right)\tilde{c}_s, \quad (3.31)$$

respectively, where $\tilde{i}_F$ is the perturbation in the Faradaic current density due to the sinusoidal oscillation and $\tilde{\theta}$ is the perturbation in the coverage of adsorbed hydrogen due to the sinusoidal oscillation.

Considering the mass balance between the rate of the *HAR* into the metal given by Eq. 3.23, the flux of hydrogen diffusing away from the entry surface through the

planar metal electrode given by Eq. 3.22, and the sinusoidal response of v_3 given by Eq. 3.28 under the reaction constraints given by Eq. 3.29, one can obtain

$$\frac{c_s^{ss}}{\theta} = \left[\frac{k_3}{\left(\dfrac{D_H}{L} \right) + k_{-3}} \right] \tag{3.32}$$

from the dc condition (steady-state term) and

$$\frac{\tilde{c}_s}{\tilde{\theta}} = \left[\frac{\left(\dfrac{\partial v_3}{\partial \theta} \right)}{-\left(\dfrac{\partial v_3}{\partial c_s} \right) + \sqrt{j\omega D_H} \coth\left(\sqrt{\dfrac{j\omega}{D_H}} L \right)} \right] \tag{3.33}$$

from the ac condition (oscillating term). It should be noted that Eq. 3.32 coincides well with the steady-state relation determined by Iyer et al. [61].

Substituting $\tilde{c}_s$ into Eq. 3.31 for $\tilde{c}_s$ in Eq. 3.33, one obtains

$$\frac{\tilde{\theta}}{\tilde{E}} = \left\{ \frac{\left(\dfrac{\partial v_1}{\partial E} \right)}{j\omega\, \Gamma_{max} - \left[\left(\dfrac{\partial v_1}{\partial \theta} \right) - 2\left(\dfrac{\partial v_2}{\partial \theta} \right) \right] + \dfrac{\left(\dfrac{\partial v_3}{\partial \theta} \right)}{\left[1 - \dfrac{\left(\dfrac{\partial v_3}{\partial c_s} \right)}{\sqrt{j\omega D_H} \coth\left(\sqrt{\dfrac{j\omega}{D_H}} L \right)} \right]}} \right\} \tag{3.34}$$

Substituting $\tilde{\theta}$ in Eq. 3.34 for $\tilde{\theta}$ in Eq. 3.30, the Faradaic admittance Y_F is finally determined as a rather awkward-looking expression

$$Y_F = \frac{\tilde{i}_F}{\tilde{E}} = -F\left(\frac{\partial v_1}{\partial E}\right) \cdot$$

$$\left\{ 1 + \frac{\frac{1}{\Gamma_{max}}\left(\frac{\partial v_1}{\partial \theta}\right)}{j\omega - \frac{1}{\Gamma_{max}}\left[\left(\frac{\partial v_1}{\partial \theta}\right) - 2\left(\frac{\partial v_2}{\partial \theta}\right)\right] + \frac{\frac{1}{\Gamma_{max}}\left(\frac{\partial v_3}{\partial \theta}\right)}{\left[1 - \frac{\left(\frac{\partial v_3}{\partial c_s}\right)}{\sqrt{j\omega D_H}\coth\left(\sqrt{\frac{j\omega}{D_H}}L\right)}\right]}} \right\},$$
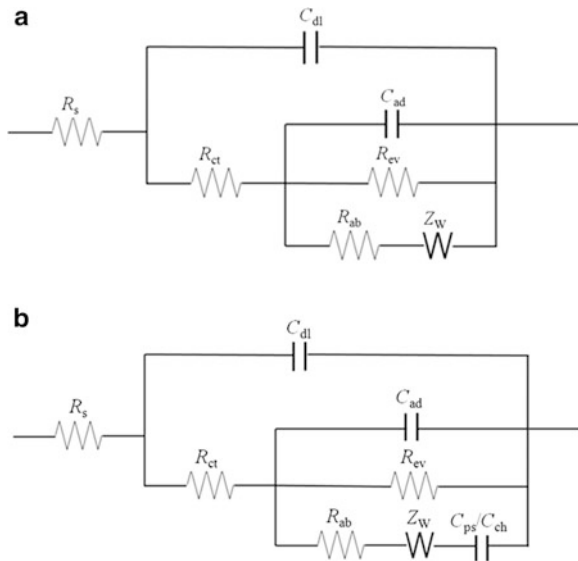
$$(3.35)$$

which is expressed in terms of the kinetic rate coefficients and constants. One sets

$$R_{ct} = -\frac{1}{F\left(\frac{\partial v_1}{\partial E}\right)}, \quad B = -\left(\frac{\partial v_1}{\partial \Gamma}\right), \quad C = 2\left(\frac{\partial v_2}{\partial \Gamma}\right), \quad k_3 = \left(\frac{\partial v_3}{\partial \theta}\right), \text{ and } k_{-3} = -\left(\frac{\partial v_3}{\partial c_s}\right).$$

It is clear from Eq. 3.35 that the parameters B and C have a simpler meaning than the equivalent circuit elements, which are much more complex functions of the kinetic parameters. Equation 3.35 expresses Y_F for the *HAR* of adsorbed hydrogen and subsequent diffusion of absorbed hydrogen at the entry side of the electrode.

On the basis of the electrical equivalent circuit which is given in Fig. 3.6a, Eq. 3.35 representing the Faradaic admittance can be converted into the following impedance equation:

$$Z_F = \frac{\tilde{E}}{\tilde{i}_F} = R_{ct} + \left\{ \frac{1}{j\omega C_{ad} + \left(\frac{1}{R_{ev}}\right) + \frac{1}{\left[R_{ab} + \frac{\sigma \tanh\left(\sqrt{\frac{j\omega}{D_H}}L\right)}{\sqrt{j\omega D_H}}\right]}} \right\}, \quad (3.36)$$

Fig. 3.6 (**a**) Equivalent circuit for hydrogen evolution reaction (*HER*) on/from and hydrogen absorption reaction (*HAR*) into planar metal membrane electrode in transmissive permeable boundary (*PB*) condition, described by the model considering adsorbed phase/state of hydrogen [6, 7], and (**b**) equivalent circuit for hydrogen evolution reaction (*HER*) on/from and hydrogen absorption reaction (*HAR*) into planar metal membrane electrode in reflective impermeable boundary (*IPB*) condition. R_s = Solution resistance; C_{dl} = Double-layer capacitance; R_{ct} = Charge-transfer resistance; C_{ad} = Adsorption capacitance; R_{ev} = Evolution resistance; R_{ab} = Absorption resistance; Z_W = Warburg impedance; C_{ps} = Pseudocapacitance or C_{ch} = Chemical capacitance (Reprinted from Lim and Pyun [6], Copyright ©1993 and Lim and Pyun [7], Copyright ©1994, with permissions from Elsevier Science)

where $C_{ad} = \dfrac{1}{BR_{ct}}$ with a dimension [F cm^{-2}],

$$R_{ev} = \frac{BR_{ct}}{C} \text{ with a dimension } \left[\Omega \text{ cm}^2\right],$$

$$R_{ab} = \frac{B\Gamma_{max}R_{ct}}{k_3} \text{ with a dimension } \left[\Omega \text{ cm}^2\right],$$

$\sigma = \dfrac{k_{-3}}{k_3}\Gamma_{max}BR_{ct}$ with a dimension [Ω cm^{3}s^{-1}]. It is especially noted that the Warburg coefficient $\sigma_W = \dfrac{\sigma}{\sqrt{2D_H}}$ has a dimension [Ω cm^{2}s$^{-1/2}$]. The equivalent circuit given in Fig. 3.6a corresponds to Eq. 3.36. The relation between the parameters B, C and equivalent circuit elements ideally needs discussion regarding their possible signs and physical dimensions, but this is beyond the scope of this chapter. All of the circuit elements such as R_{ct}, R_{ab}, and σ constituting the

Faradaic admittance/impedance are quantitatively expressed as above in terms of the kinetic rate coefficients and constants. Moreover, the comparison of the coefficients, R_{ab} and σ, appearing in Eq. 3.36 with the corresponding coefficients in Eq. 3.35 permits us to estimate R_{ab} and σ that are coupled with each other by means of R_{ct}.

The Faradaic impedance in Eq. 3.36 is generally defined only for a linear, stable, and causal system in another form of Ohm's law. Conversely, this impedance cannot be applied to describe the response of a system that does not conform to these constraints. Ohm's law is only effective under the constraint of electrochemical energy due to an electrochemical potential difference $|zFE| \ll$ thermal energy $|RT|$. Furthermore, the ratio of the voltage vector (voltage oscillation, voltage in complex number) to the current vector (current oscillation, current in complex number) is generally referred to as a transfer function.

The physical significances of the parameters C_{ad} and R_{ev} have been discussed elsewhere [42]. From Fig. 3.6, one readily notices that the absorption and diffusion of hydrogen into and through the metal electrode provides another relaxation path of adsorbed hydrogen, which is in parallel to the relaxation path of adsorbed hydrogen through the Tafel chemical desorption (recombination). This result exactly reflects the physical situation of this model. It should be noted that the resistance R_{ab} and the Warburg impedance coefficient σ_W are not independent, but rather are closely coupled with each other. This strongly indicates that hydrogen insertion into the planar Pd electrode proceeds by absorption into the electrode coupled with subsequent diffusion through the electrode. One should consider the two limiting cases of Eq. 3.35, representing Y_F for the *HAR* and subsequent diffusion at the entry side of the electrode, depending upon the magnitude of the rate constant k_{-3} of hydrogen transfer from the absorbed to adsorbed state and the height of the hydrogen diffusivity-related term as shown below.

3.3.3   (i) – (a) Diffusion-Controlled HAR Limit

If $-\left(\dfrac{\partial v_3}{\partial c_s}\right) = k_{-3} \gg \sqrt{j\omega D_H}\coth\left(\sqrt{\dfrac{j\omega}{D_H}}L\right)$, Eq. 3.33 reduces to

$$\frac{\tilde{c}_s}{\tilde{\theta}} = -\frac{\left(\dfrac{\partial v_3}{\partial \theta}\right)}{\left(\dfrac{\partial v_3}{\partial c_s}\right)} = \frac{k_3}{k_{-3}} \tag{3.37}$$

Substituting $\tilde{c}_s$ in Eq. 3.31 for $\tilde{c}_s$ in Eq. 3.37, one obtains $\dfrac{\tilde{\theta}}{\tilde{E}}$. Substituting the value of $\tilde{\theta}$ so obtained into Eq. 3.30, one readily finds the Faradaic admittance Y_F. The Faradaic admittance in Eq. 3.35 then becomes further simplified as follows:

$$Y_F = \frac{1}{R_{ct}} \cdot \left\{ 1 - \frac{B}{\left[j\omega + B + C + \frac{1}{l_{eq}} \sqrt{j\omega D_H} \coth\left(\sqrt{\frac{j\omega}{D_H}} L \right) \right]} \right\}, \qquad (3.38)$$

where l_{eq} is the equilibrium length, $\dfrac{1}{l_{eq}} = \dfrac{k_3}{\Gamma_{max}k_{-3}}$. Equation 3.38 expresses Y_F for the diffusion-controlled indirect *HAR*.

If $k_{-3} \gg \dfrac{D_H}{L}$, Eq. 3.32 becomes

$$\frac{c_s^{ss}}{\theta} = \frac{k_3}{k_{-3}} \qquad (3.39)$$

Equation 3.39 suggests that the *HAR* given by Eq. 3.12d is in local equilibrium under the applied cathodic potential. The slowest step in hydrogen permeation which includes absorption into and diffusion of hydrogen through the Pd electrode is known as the diffusion process [33, 69]. Under the diffusion-controlled *HAR*, the *HAR* step given by Eq. 3.12d can be considered to be in local equilibrium. The equilibrium absorption constant, K_{eq}, that is, the ratio of the concentration of 3D absorbed hydrogen, c_s [mol cm^{-3}], to the surface concentration of 2D adsorbed hydrogen, Γ [mol cm^{-2}], is defined by Breger and Gileadi [69] as

$$K_{eq} = \frac{c_s}{\Gamma} = \frac{k_3}{\Gamma_{max} k_{-3}} = \frac{1}{l_{eq}} \qquad (3.40)$$

Therefore, l_{eq} is identical to the inverse of the equilibrium absorption constant, K_{eq}, having the physical dimension of length [cm].

The diffusion-controlled *HAR* [28, 70] implies that for hydrogen insertion into the electrode, both the preceding charge-transfer reaction by the Volmer adsorption Eq. 3.12a and *HAR* Eq. 3.12d are practically undisturbed from their equilibrium where the respective forward and backward reactions for Eqs. 3.12a and 3.12d proceed with the same rate but with different signs, respectively. Both equilibria are kinetically symmetric. In a similar way, the equilibrium for Eq. 3.12e is attained if the hydrogen concentration at the entry point $x = 0$ is the same as that at the exit $x = L$, implying that there is no concentration gradient across the membrane. In contrast, the equilibrium for the succeeding diffusion Eq. 3.12e is strongly hindered, assuming that the rate of the backward diffusion reaction of Eq. 3.12e, that is, hydrogen diffusion from $x = L$ toward $x = 0$ can be practically neglected. Any departure from the equilibrium for Eq. 3.12e entails the spontaneous development of a diffusion resistance to Eq. 3.12e and, hence, a corresponding overvoltage/overpotential, which is regarded as a measure of the degree of deviation/impediment from equilibrium for the diffusion pathway.

Such diffusion in the presence of a concentration gradient across the membrane is considered to be kinetically asymmetric with a directional character. This indicates that hydrogen diffusion through the planar bulk can be the *RDS* for hydrogen insertion. In other words, as an extremely limiting case, the value of the interfacial absorption resistance, R_{ab}, is much less than the Warburg coefficient, σ_W (fast absorption and slow diffusion). In this way, the overvoltage, η_{ab}, accompanying the absorption resistance, R_{ab}, also becomes much less than the overvoltage, η_d, accompanying the diffusion resistance, σ_W.

3.3.4   (i) – (b) Interface-Controlled HAR Limit

If $-\left(\dfrac{\partial v_3}{\partial c_s}\right) = k_{-3} << \sqrt{j\omega D_H}\,\coth\left(\sqrt{\dfrac{j\omega}{D_H}}L\right)$, Eq. 3.33 reduces to

$$\frac{\tilde{c}_s}{\tilde{\theta}} = \frac{\left(\dfrac{\partial v_3}{\partial \theta}\right)}{\sqrt{j\omega D_H}\,\coth\left(\sqrt{\dfrac{j\omega}{D_H}}L\right)} \tag{3.41}$$

Substituting $\tilde{c}_s$ in Eq. 3.31 for $\tilde{c}_s$ in Eq. 3.41, one obtains $\dfrac{\tilde{\theta}}{\tilde{E}}$. Substituting the value of $\tilde{\theta}$ so obtained into Eq. 3.30, one readily finds the Faradaic admittance Y_F. In this way, the Faradaic admittance given by Eq. 3.35 is modified to

$$Y_F = \frac{1}{R_{ct}} \cdot \left\{ 1 - \frac{B}{\left[j\omega + B + C + \left(\dfrac{k_3}{\Gamma_{max}}\right) \right]} \right\}, \tag{3.42}$$

which expresses Y_F for the interface-controlled indirect (two-step) *HAR*. It is obvious that Y_F expressed in Eqs. 3.42 and 3.64 for the interface-controlled indirect *HAR* remains invariant, irrespective of whether the transmissive *PB* condition or reflective *IPB* condition applies, because the succeeding diffusion by Eq. 3.12e deviates only slightly from equilibrium, as mentioned later in Sect. 3.3.7.

The result of the simulation of the complex-plane impedance spectra based upon Eq. 3.35 for various values of k_{-3}, provided $k_3' = \left(\dfrac{k_3}{\Gamma_{max}}\right) = 10 \text{ s}^{-1}$ demonstrates that as the value of k_{-3} in Eq. 3.35 decreases, the complex-plane impedance spectra approach these spectra on the basis of the purely interface-controlled absorption, consisting of two semicircles, simulated based upon Eq. 3.42. It is obvious that if k_{-3} decreases to zero as an extremely limiting case, the purely interface-controlled relaxation strongly deviates from the equilibrium for Eq. 3.12d. The two semicircles (arcs) are related to the couples between the two different time
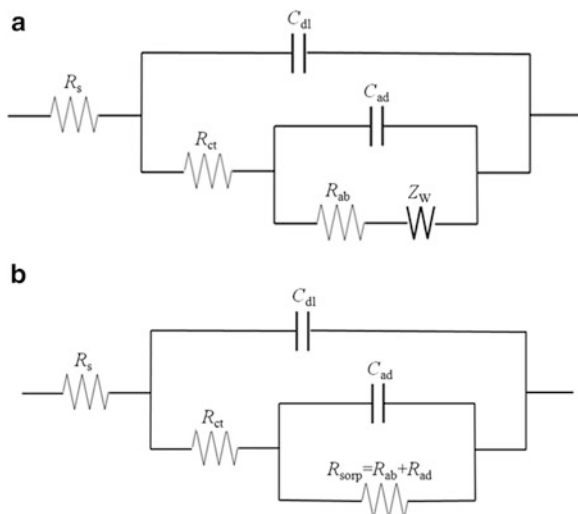
Fig. 3.7 Equivalent circuit for the indirect hydrogen absorption reaction *(HAR)* into planar metal membrane electrode [72]. (**a**) the diffusion-controlled hydrogen absorption reaction*(HAR)*, (**b**) the interfacial reaction-controlled hydrogen absorption reaction *(HAR)*. R_s = Solution resistance; C_{dl} = Double-layer capacitance; R_{ct} = Charge-transfer resistance; C_{ad} = Adsorption capacitance; R_{ab} = Absorption resistance; Z_W = Warburg impedance; R_{ad} = Adsorption resistance; R_{sorp} = Sorption resistance (Reprinted from Lasia [72], Copyright ©2002 with permission from Kluwer Academic/Plenum Publishers)

constants, $R_{ct} - C_{dl}$ and $(R_{ab} + R_{ad}) - C_{ad}$. Similar results were reported elsewhere [71, 72] for experiments performed in the reflective *IPB* condition.

In order for the reader to clearly understand such a physical situation, the appropriate equivalent circuits are presented in Fig. 3.7 for the indirect *HAR* into a Pd electrode. Here, R_{sorp} means the sum of R_{ab} and R_{ad}. The impedance spectrum for the diffusion-controlled *HAR* is composed of two contributions consisting of one semicircle corresponding to the single time constant $R_{ct} - C_{dl}$ couple and the Warburg impedance. The latter is divided into two categories: One is the Warburg impedance expressed in the transmissive *PB* condition and the other involves the Warburg impedance expressed in the reflective *IPB* condition, which is described in detail in Sect. 3.2. By contrast, the impedance spectrum for the interface-controlled *HAR* consists of two arcs related to the couples between the two different time constants, $R_{ct} - C_{dl}$ and $R_{sorp} - C_{ad}$.

In contrast to the diffusion control mentioned above, the interface-controlled *HAR* [28, 70] means that for hydrogen insertion into the electrode, both the preceding charge-transfer reaction by the Volmer adsorption Eq. 3.12a and the succeeding diffusion Eq. 3.12e are practically undisturbed from their equilibrium where the forward and backward reactions for both steps run with the same rate but with different signs. Both equilibria are kinetically symmetric. However, the equilibrium for the *HAR* is strongly impeded, assuming that the transfer kinetics of absorbed hydrogen atoms are so facile that the rate of the backward reaction of

Eq. 3.12d, that is, hydrogen transfer of the 3D absorbed state to 2D adsorbed state, can be practically neglected. This zero reaction rate requires that the value of either k_{-3} or c_s approaches zero because the constraint in Eq. 3.23 is generally valid even for any noticeably disturbed equilibrium.

Such an *HAR* is kinetically asymmetric with a directional character. This means that the hydrogen transfer from the adsorbed state to absorbed state has the potential to be the *RDS* for hydrogen insertion. In other words, as an extremely limiting case, the value of R_{ab} is much greater than the Warburg coefficient σ_W (slow absorption and fast diffusion). In a similar way, the overvoltage η_{ab} accompanying the absorption resistance R_{ab} also becomes much greater than the overvoltage η_d accompanying the diffusion resistance σ_W.

Furthermore, it would be worthwhile to expound on the terminology "kinetically more facile (favored) or more limited (impeded) atomistic relaxation process/macroscopic reaction process" such as the absorption of adsorbed hydrogen and diffusion of absorbed hydrogen. Let us consider now the *HAR* and subsequent diffusion connected in series. The net reaction rate of any partial step is generally given under the applied cathodic/anodic potentials for hydrogen insertion/desertion by the difference in rate between the forward and backward reactions, for instance Eq. 3.23. At equilibrium, both the net rate $v_3 = 0$ and hydrogen permeation flux density $J_p = 0$ for no concentration gradient across the planar electrode with a thickness L and ideally reversible reactions Eqs. 3.12d and 3.12e finally come to a standstill as well, in which case the charge-transfer resistance R_{ct} to Eq. 3.12d and diffusion resistance to Eq. 3.12e would be zero as well.

By contrast, in general, for nonequilibrium cases, the resulting net reaction rate upon the superposition of the forward and backward reactions is not zero, but has a finite value. Assuming, for example, that the backward reactions Eqs. 3.12d and 3.12e can be neglected as well, then both equations strongly or weakly deviate from their equilibrium, depending upon either the level of the resistances, R_{ct} and R_d, to the respective partial relaxation or the height of the corresponding overvoltages, η_{ct} and η_d.

At steady state, the electrochemical equivalent rate (flux density) v^{st} for both partial steps of absorption and diffusion is the same: $\eta_{ab} = v^{st} R_{ab}$; $\eta_d = v^{st}R_d$ (η_{ab} = absorption overvoltage; R_{ab} = absorption resistance; η_d = diffusion overvoltage; R_d = diffusion resistance). R_{ab} and R_d are in general known to be inversely proportional to the "surface- and bulk-sensitive intrinsic properties" of the exchange current density and maximum limiting diffusion current density, respectively. Therefore, for example, a fast relaxation/reaction step is characterized by a smaller diffusion resistance with a higher diffusion current density, while a slow relaxation/reaction step is represented by a higher charge-transfer resistance with a lower exchange current density.
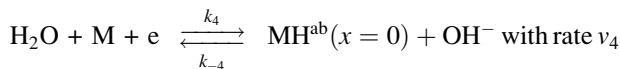
Thus, the steady-state flux density v^{st} is limited by a single relaxation/reaction step with a large value of the resistance R/overvoltage η. Accordingly, when hydrogen absorption is the *RDS* among all of the partial relaxation steps for hydrogen insertion, it refers to the condition where R_{ct} significantly exceeds R_d, leading to $\eta_{ct} \gg \eta_d$, so that v^{st} is exclusively determined by the exchange current

density for the transfer of hydrogen from the adsorbed state to absorbed state. The kinetically more facile/favored relaxation/reaction for hydrogen diffusion is held back from the maximum diffusion current density by the kinetically more sluggish/limited/disturbed hydrogen absorption.
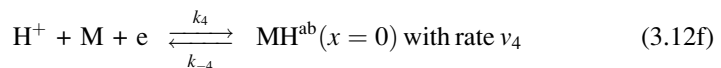
The transfer of hydrogen from the adsorbed state to absorbed state is coupled with the subsequent diffusion in the electrode interior. This is similar to the case where fast moving electrons with a higher component diffusivity are retarded through semiconducting lithium insertion metal oxides under open circuit conditions in the same direction as lithium ions, due to the electrical neutrality constraint caused by slow moving lithium ions for the chemical/ambipolar diffusion of neutral lithium atoms.

3.3.5   (ii) Model B: Direct (One-Step) Hydrogen Absorption Reaction (HAR) Without Adsorbed Phase (State)

Bagotskaya [66] and Frumkin [67] postulated that hydrogen directly enters the metal in the same elementary act as that in which it is discharged, and that the absorbed intermediate state through which hydrogen enters the metal lattice is quite different from that which leads to the *HER*. The reaction sequence at the cathode in alkaline/acidic solutions is presented as follows:

$$H_2O + M + e \underset{k_{-4}}{\overset{k_4}{\rightleftarrows}} MH^{ab}(x=0) + OH^- \text{ with rate } v_4$$

in alkaline solution and

$$H^+ + M + e \underset{k_{-4}}{\overset{k_4}{\rightleftarrows}} MH^{ab}(x=0) \text{ with rate } v_4 \tag{3.12f}$$

in acidic solution

$$MH^{ab}(x=0) \xrightarrow[\text{bulk diffusion}]{J_P} MH^{ab}(x=L) \text{ with rate } J_P \tag{3.12e}$$
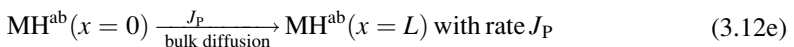
implying that the *HER* does not occur, that is, $C = 2\left(\dfrac{\partial v_2}{\partial \Gamma}\right) = 0$. Therefore, the above reaction is adequately liable to such electrodes which absorb mostly hydrogen, which is infinitesimally evolved, as electrochromic oxides [73] and metal hydride-forming electrodes [74].

Under the permeable *BC*, Eq. 3.19, the charge and mass balances are given by the reaction scheme described by Eqs. 3.12f and 3.12e listed above,

$$-\frac{i_{\mathrm{F}}}{F} = v_4 \tag{3.43}$$

and

$$-\frac{i_{\mathrm{F}}}{F} = J_{x=0}, \tag{3.44}$$

respectively, where v_4 is the rate of the proton (H$^+$) discharge reaction Eq. 3.12f. The cathodic Faradaic current density is bestowed a negative sign by definition and the reaction rate/flux density is usually taken as having a positive sign. Therefore, the $(-)$ sign is purposely given Eqs. 3.43 and 3.44 in order to make the two opposite signs of i_{F} and v_4 or $J_{x=0}$ equal. The sinusoidal response of v_4 can be linearized as

$$v_4 = v_4^{\mathrm{ss}} + \left(\frac{\partial v_4}{\partial E}\right)\tilde{E}\exp(j\omega t) + \left(\frac{\partial v_4}{\partial \theta}\right)\tilde{\theta}\exp(j\omega t) + \left(\frac{\partial v_4}{\partial c_{\mathrm{s}}}\right)\tilde{c}_{\mathrm{s}}\exp(j\omega t) \tag{3.45}$$

Substituting Eq. 3.45 into Eq. 3.43 under the reaction constraint of $\left(\dfrac{\partial v_4}{\partial \theta}\right) = 0$, followed by further inserting Eq. 3.22 into Eq. 3.44 and finally equating the time-dependent terms with each other, one obtains

$$-\frac{\tilde{i}_{\mathrm{F}}}{F} = \left(\frac{\partial v_4}{\partial E}\right)\tilde{E} + \left(\frac{\partial v_4}{\partial c_{\mathrm{s}}}\right)\tilde{c}_{\mathrm{s}} \tag{3.46}$$

and

$$-\frac{\tilde{i}_{\mathrm{F}}}{F} = \sqrt{j\omega D_{\mathrm{H}}}\coth\left(\sqrt{\frac{j\omega}{D_{\mathrm{H}}}}L\right)\tilde{c}_{\mathrm{s}}, \tag{3.47}$$

respectively. Eliminating $\tilde{c}_{\mathrm{s}}$ from Eq. 3.46 by combining Eq. 3.46 with Eq. 3.47, the Faradaic admittance is finally given again by the rather awkward-looking formula:

$$Y_{\mathrm{F}} = -F\left(\frac{\partial v_4}{\partial E}\right) \cdot \left\{1 + \frac{\left(\dfrac{\partial v_4}{\partial c_{\mathrm{s}}}\right)}{\left[-\left(\dfrac{\partial v_4}{\partial c_{\mathrm{s}}}\right) + \sqrt{j\omega D_{\mathrm{H}}}\coth\left(\sqrt{\dfrac{j\omega}{D_{\mathrm{H}}}}L\right)\right]}\right\} \tag{3.48}$$

If one sets

$$R_{\mathrm{ct}} = -\frac{1}{F\left(\dfrac{\partial v_4}{\partial E}\right)} \quad \text{and} \quad B' = -\left(\frac{\partial v_4}{\partial c_{\mathrm{s}}}\right),$$

Equation 3.48 is simplified as

$$Y_F = \frac{1}{R_{ct}} \left\{ 1 - \frac{B'}{\left[B' + \sqrt{j\omega D_H} \coth\left(\sqrt{\frac{j\omega}{D_H}} \right) \right]} \right\}$$
(3.49)

which represents the Faradaic admittance Y_F for the direct (one-step) *HAR* "model B."

Equation 3.38 expressing Y_F for the diffusion-controlled indirect *HAR* can then be rearranged under the constraint of the absence of the *HER*, $C = 2\left(\dfrac{\partial v_2}{\partial \Gamma}\right) = 0$, to a formula in order to make a bird's-eye comparison with Eq. 3.49

$$Y_F = \frac{1}{R_{ct}} \left\{ 1 - \frac{B''}{\left[j\omega l_{eq} + B'' + \sqrt{j\omega D_H} \coth\left(\sqrt{\frac{j\omega}{D_H}} L \right) \right]} \right\}$$
(3.50)

where $B'' = l_{eq} \cdot B$, $B = -\left(\dfrac{\partial v_1}{\partial \Gamma}\right)$. Thus, Eq. 3.50 simply represents Y_F for the diffusion-controlled indirect (two-step) *HAR* "model A" without *HER*.

The Faradaic impedance characterized by Eq. 3.49 simply represents the Randles circuit in the transmissive *PB* condition as follows:

$$Z_F = R_{ct} + \left[\frac{\sigma \tanh\left(\sqrt{\frac{j\omega}{D_H}} L \right)}{\sqrt{j\omega D_H}} \right]$$
(3.51)

where $\sigma = R_{ct}\left[-\left(\dfrac{\partial v_4}{\partial c_s}\right) \right]$ with dimension $[\Omega \text{ cm}^3 \text{ s}^{-1}]$, $\sigma_W = \dfrac{\sigma}{\sqrt{2D_H}}$ with a dimension $[\Omega \text{ cm}^2 \text{s}^{-1/2}]$. Equation 3.51 corresponds to Eqs. 3.4 and 3.8 in the transmissive *PB* condition.

Equation 3.49 expressing Y_F for the diffusion-controlled direct (one-step) *HAR* "model B" differs from Eq. 3.50 for the diffusion-controlled indirect (two-step) *HAR* "model A," in that B$'$ (=surface concentration coefficient of direct absorption rate v_4) appears instead of B$''$ (= surface concentration coefficient of adsorption rate v_1). Also, it should be stressed here that the only difference between these models is that in the former case, "model B," the double-layer capacitance C_{dl} is relatively constant, irrespective of the applied potential, while in the latter case, "model A," the adsorption capacitance C_{ad} varies with the applied potential. A comparison of the simulation and experimental results will be given in Sect. 3.3.6(iii).

The impedance spectra measured on solid electrodes often show deviations from the ideal semicircle. In this case, the double-layer impedance, $Z_{dl} = 1/j\omega C_{dl}$, is represented by the constant phase element (CPE), defined as [52, 75]

$$Z_{CPE} = \frac{1}{Y_o(j\omega)^{\varphi}} \tag{3.52a}$$

where Z_{CPE} has dimensions of $[\Omega\,cm^2]$, Y_o is the CPE constant or parameter having dimensions of $[F\,cm^{-2}\,s^{-(1-\varphi)}]$ or $[\Omega^{-1}\,cm^{-2}\,s^{\varphi}]$, and φ is the CPE exponent or the fractional parameter with a dimension $[-]$ expressing the degree of depression of the semicircle. Y_0 is generally termed CPE if $-1<\varphi<0$ and $0<\varphi<1$. For special cases, R(Ohmic resistance) $= 1/Y_o$ with physical dimensions of $[\Omega\,cm^2]$ if $\varphi = 0$. C (double-layer capacitance) $= Y_o$ with physical dimensions of $[F\,cm^{-2}]$ if $\varphi = 1$. L(inductance) $= 1/Y_o$ with physical dimensions of $[Henry\,cm^2]$ if $\varphi = -1$.

$Z_W = \frac{1}{Y_0\sqrt{2\omega}}(1-j)$ or $|Z_W| = \frac{1}{Y_0\sqrt{\omega}}$ with physical dimensions of $[\Omega\,cm^2]$ if φ $= 1/2$. Of course, one does not refer to Y_0 in these four special cases as CPEs, but simply as admittances/impedances with corresponding respective circuit elements such as resistances, capacitances, inductances, and Warburg impedances with the same absolute value $Z_W = \frac{1}{Y\sqrt{2\omega}}$ of the real and imaginary impedance or $|Z_W| = \frac{1}{Y_W\sqrt{\omega}}$ where $\frac{1}{Y_W\sqrt{2}} = \sigma_W =$ Warburg coefficient with dimensions of $[\Omega\,cm^2\,s^{-1/2}]$. In another expression $Z_W = \frac{\sigma_W}{\sqrt{\omega}}(1-j)$ or $|Z_W| = \frac{\sqrt{2}\sigma_W}{\sqrt{\omega}}$ where $\sigma_W =$ Warburg coefficient with dimensions of $[\Omega\,cm^2\,s^{-1/2}]$. Thus, the total interfacial impedance Z_{total} is

$$Z_{total} = R_s + \frac{1}{B_o(j\omega)^{\varphi} + Y_F} \tag{3.52b}$$

where R_s is the solution resistance, $B_0 = C_{d1}^{\varphi} \cdot (R_s^{-1} + R_{ct}^{-1})^{1-\varphi}$ with dimensions of $[F\,cm^{-2}\,s^{-(1-\varphi)}]$.

The real and imaginary components Z' and Z'' obtained at each applied dc potential are analyzed using the complex nonlinear least squares (CNLS) fitting method first written by Macdonald et al. [76] and modified in our laboratory [77] to determine the parameters involved in the theoretically derived Faradaic admittance equations. The calculations were performed with an IBM 486 personal computer. Modulus weighting (MWT) was selected as the weighting factor for each experimental point. The curve-fitting error representing the goodness of curve-fitting was calculated using:

$$E_{error}(\%) = \sqrt{\frac{1}{n}\sum_{i=1}^{n}\{[(a_i - A_i)^2 + (b_i - B_i)^2]/(a_i^2 + b_i^2)\}} \tag{3.53}$$

where a_i and b_i are the real and imaginary components of the experimental impedance data, respectively, A_i and B_i the real and imaginary components of the curve fitted impedance data at the same frequency as a_i and b_i, respectively, and n is the number of experimental data points. The values of the curve-fitting errors for all of the fitting results obtained from our laboratory were within 5%.

3.3.6 (iii) Comparison of Simulation with Experimental Results

In order to validate the Faradaic admittance described by Eq. 3.38 expressing the diffusion-controlled *HAR*, we simulated the behavior of the combined *HAR* and subsequent diffusion process at the entry side of the membrane represented by Eq. 3.35 in the frequency range of 10^{-6} to 10^5 Hz by combining Eq. 3.35 with Eq. 3.52b, assuming that the Tafel chemical desorption (recombination) step is neglected, that is, $C = 2\left(\dfrac{\partial v_2}{\partial \Gamma}\right)$. Figure 3.8 shows the impedance spectra in the form of the Nyquist plot simulated according to Eq. 3.52b combined with Eq. 3.35 for various values of k_{-3}, assuming that $l_{eq} = 4.33 \times 10^{-4}$ cm. We compared the simulated impedance spectra with those experimentally measured from a 50--μm-thick Pd planar membrane in 0.1 M LiOH solution at room temperature (*RT*) and with an applied anodic potential $E_{app} = 0.13$ V$_{RHE}$ or an overvoltage $\eta = 0.13$ V in the transmissive *PB* condition. As the value of k_{-3} in Eq. 3.35 increases, the complex-plane impedance spectra simulated on the basis of Eq. 3.35 come closer to those simulated according to Eq. 3.38. It is obvious that if k_{-3} increases to infinity as an extremely limiting case, the equilibrium for Eq. 3.12e is then strongly disturbed, so that the relaxation by Eq. 3.12e comes to be under pure diffusion control.

When the steady-state hydrogen permeation is attained under the transmissive *PB* condition achieved usually by using a electrochemical permeation double cell (see Fig. 3.4), the electrode impedance for the *HAR* then starts to be measured on the cathodic side of the membrane with thickness L constituting the double cell and also acting as the hydrogen entry point. The measurement of the ac-impedance spectra is made by superimposing an ac signal with an amplitude of 5 mV on a dc applied anodic potential much lower than 0.94 V$_{RHE}$ over the frequency range from 1 mHz to 10 kHz. Therefore, the hydrogen absorbed into the cathodic side of the planar membrane diffuses toward its anodic side, which is subjected to a constant anodic potential of 0.94 V$_{RHE}$. Here, RHE means a reversible hydrogen electrode which is related to an SHE (standard hydrogen electrode) as [E against RHE $= E$ against SHE $+ 0.0591$ pH] at 298 K.

Severe depressions or tailings of the second semicircle in the Nyquist plot are often found for an *HER* on Pt [78] and amorphous metals [79]. Bai et al. [78] performed a simulation of the impedance spectra in terms of the diffusion of H$_2$ away from the electrode surface, but they failed to explain the origin of the tailing of the second semicircle. In this chapter, we simulated the impedance spectra from the Faradaic admittance described by Eq. 3.38 for pure diffusion control, by adopting the rate constants obtained from activated Pt in 0.5 M NaOH solution
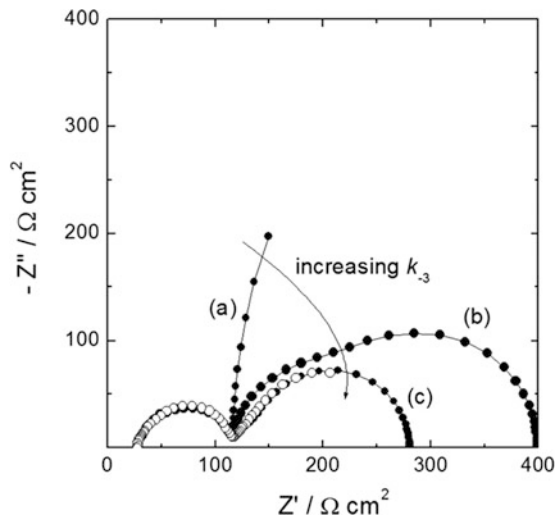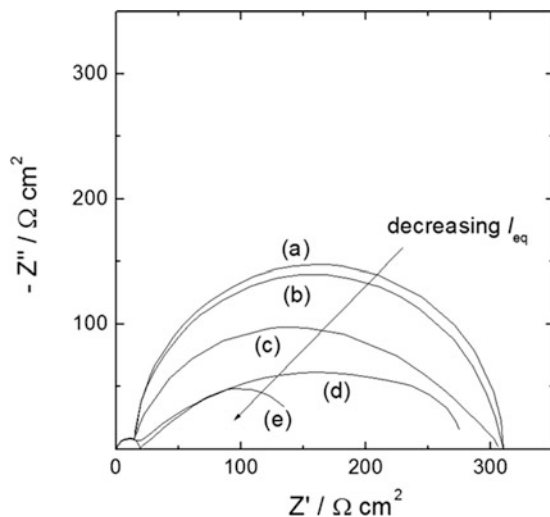
Fig. 3.8 Complex-plane impedance spectra [6] simulated based upon Eq. 3.35 at different values of k_{-3} [cm s^{-1}]: (a) 1×10^{-5}, (b) 1×10^{-4}, (c) 1×10^{-2} with the parameters of $R_s = 28\ \Omega\ \text{cm}^2$, $B_0 = 1.92 \times 10^{-4}\ \text{F cm}^{-2}\ \text{s}^{-(1-\varphi)}$, $\varphi = 0.88$, $R_{ct} = 88.6\ \Omega\ \text{cm}^2$, $B = -\left(\dfrac{\partial v_1}{\partial \Gamma}\right) = 3.1 \times 10^{-2} \text{s}^{-1}$, $l_{eq} = 4.33 \times 10^{-4}\ \text{cm}$, $D_H = 3.72 \times 10^{-7}\ \text{cm}^2\ \text{s}^{-1}$, $L = 5 \times 10^{-3}\ \text{cm}$. Equation 3.35 expresses Y_F for the hydrogen absorption reaction (*HAR*) and subsequent diffusion at the entry side. Circled points($\bigcirc$) represent the experimental data obtained from hydrogen permeation double cell with a 50 μm-thick Pd planar membrane in 0.1 M LiOH solution at $E_{app} = 0.13\ \text{V}_{RHE}$ (Reprinted from Lim and Pyun [6], Copyright ©1993 with permission from Elsevier Science)

[78], for various values of l_{eq}, assuming that the purely diffusion-controlled *HAR* applies and not the Heyrovsky electrochemical desorption (recombination). The steady-state hydrogen coverage was obtained by substituting Eq. 3.22 into Eq. 3.25 and by setting the constraint $\left[\dfrac{d\theta}{dt} = 0\right]$. The kinetic equations describing the rates of the Volmer adsorption and Tafel desorption reactions were taken as those employed by Bai et al. [78].

The result of the simulation is shown in Fig. 3.9 as a Nyquist plot. As the value of l_{eq} decreases, the second semicircle is converted ultimately to a pure Warburg impedance due to its depression and tailing. The results of the depressed Warburg impedance with tailing suggest that the relaxation of the adsorbed hydrogen through absorption into and subsequent diffusion through the metal substrate is kinetically more disturbed than relaxation through the Tafel chemical desorption (recombination) as the equilibrium absorption constant, K_{eq}, increases. Since the relaxation caused by the combined *HAR* and subsequent diffusion connected in series is believed to deviate more or less from the equilibria for both Eqs. 3.12d and 3.12e, it can be referred to as being under mixed *HAR* and diffusion control.

We are not presently able to assign the respective contributions of pure diffusion control and interface control to the overall mixed control. In order to solve this problem, we experimentally determined the ratio of the diffusion current to the
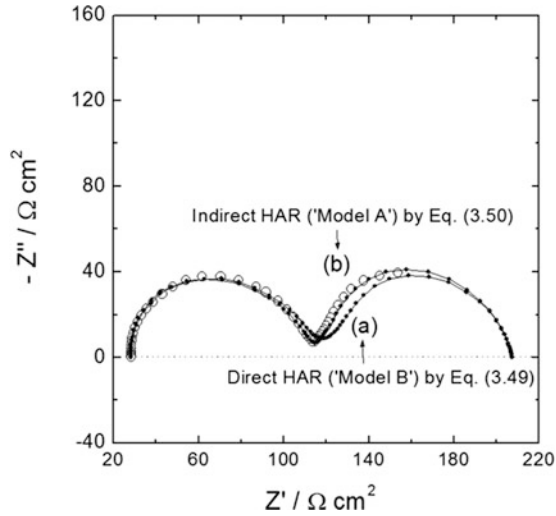
Fig. 3.9 Complex-plane impedance spectra [6] simulated based upon Eq. 3.38 in Nyquist presentation at different values of l_{eq} [cm]: (*a*) 1×10^{-3}, (*b*) 1×10^{-4}, (*c*) 1×10^{-5}, (*d*) 1×10^{-6}, (*e*) 1×10^{-7} using the parameters of $C_{dl} = 2.5 \times 10^{-5}$ F cm^{-2}, $\varphi = 1$, β (symmetry factor/charge transfer coefficient for Tafel desorption) $= 0.5$, $\Gamma_{max} = 7.25 \times 10^{-10}$ mol cm^{-2}, $\eta = -0.03$ V, $k_1 = 1 \times 10^{-8}$, $k_{-1} = 3 \times 10^{-7}$ and $k_2 = 2.8 \times 10^{-8}$ mol cm^{-2} s^{-1} taken from the literature [78]. Additionally $D_H = 1 \times 10^{-7}$ cm^2 s^{-1} and $L = 1 \times 10^{-1}$ cm are taken. Equation 3.38 expresses Y_F for the diffusion-controlled indirect hydrogen absorption reaction (*HAR*) (Reprinted from Lim and Pyun [6], Copyright ©1993 with permission from Elsevier Science)

interfacial reaction current by the Butler-Volmer equation by measuring the potentiostatic current transients as described in the previous reports from our laboratory [80, 81].

In order to test the validity of Eqs. 3.49 and 3.50, we simulated the impedance spectra according to Eq. 3.52b combined with Eqs. 3.49 and 3.50, respectively. Figure 3.10 shows the two different simulated complex-plane impedance spectra in Nyquist representation. One can distinguish the diffusion-controlled direct (one-step) *HAR* "model B" characterized by Eq. 3.49 from the diffusion-controlled indirect (two-step) *HAR* "model A" characterized by Eq. 3.50 by the absence of any adsorption capacitance. It is expected from the fact that $C_{ad} > C_{dl}$ that this latter model "A" characterized by Eq. 3.50 would give rise to a slightly smaller high-frequency semicircle than that former model "B" characterized by Eq. 3.49 and would also keep the transition from the high-frequency arc to the low-frequency Warburg impedance sharper.

Similar results were found in the case where $C_{ad} \gg C_{dl}$ [82]. The experimental data from a Pd membrane in the transmissive *PB* condition in 0.1 M LiOH solution at $E_{app} = 0.1$ V$_{RHE}$ follow the indirect (two-step) *HAR* mechanism almost exactly. From the results of the poison effect on the *HAR* into the Pd membrane, it is suggested that the *HAR* usually proceeds by the direct (one-step) pathway [83] in 0.1 M H$_2$SO$_4$ solution at a relatively low applied anodic potential of 0.12 V$_{RHE}$, but by the indirect (two-step) pathway [71] in 0.1 M NaOH solution at a relatively high applied anodic

Fig. 3.10 Complex-plane impedance spectra [6] simulated by combining Eq. 3.52b and the two different Faradaic admittance equations, Y_F: (*a*) Eq. 3.49 for diffusion-controlled direct hydrogen absorption reaction (*HAR*) without adsorbed phase/state, (*b*) Eq. 3.50 for diffusion-controlled indirect hydrogen absorption reaction (*HAR*) through adsorbed phase/state, respectively, using the parameters of $R_s = 28\ \Omega\ cm^2$, $B_0 = 1.92 \times 10^{-4}\ F\ cm^{-2}\ s^{-(1-\varphi)}$, $\varphi = 0.88$, $R_{ct} = 88.6\ \Omega\ cm^2$, $B' = B'' = 7.26 \times 10^{-5}\ cm\ s^{-1}$, $l_{eq} = 4.88 \times 10^{-4}\ cm$, $D_H = 3.47 \times 10^{-7}\ cm^2\ s^{-1}$ and $L = 5 \times 10^{-3}\ cm$. Circled points($\circ$) represent the experimental data obtained from hydrogen permeation double cell with a 50 μm-thick Pd planar membrane in 0.1 M LiOH solution at $E_{app} = 0.1\ V_{RHE}$. (*a*): Direct *HAR* ('model B') by Eq. 3.49 involving only C_{dl} gives a more diffuse transition of a bit more sized high-frequency arc to low-frequency Warburg impedance. (*b*): Indirect *HAR* ('model A') by Eq. 3.50 involving $C_{ad} > C_{dl}$ gives a sharper transition of a bit less sized high-frequency arc to low-frequency Warburg impedance (Reprinted from Lim and Pyun [6], Copyright ©1993 with permission from Elsevier Science)

potential of 0.15 V_{RHE}. Here, the "applied anodic potential" means the application of a potential more positive than the Nernstian equilibrium potential to achieve the underpotential adsorption/deposition (*UPD*) of hydrogen. Interestingly, the transition [71] in the mechanism of the diffusion-controlled indirect *HAR* occurs sufficiently to interface-controlled indirect (two-step) one at a concentration of thiourea of about $10^{-7.5}$ M used as a catalyst poison, as the concentration increases.

3.3.7 Reflective Impermeable (IPB) Boundary Condition

3.3.7.1 Model A: Indirect (Two-Step) Hydrogen Absorption Reaction (*HAR*) Through Adsorbed Phase(State) – (a) Diffusion-Controlled *HAR* Limit and –(b) Interface-Controlled *HAR* Limit

The reflective *IPB* condition for the *HER* and *HAR* is schematically shown in Fig. 3.5. The initial (*IC*) and boundary (*BC*) impermeable (*IPB*) conditions are given as follows:

$t = 0$ (*IC*): $0 \leqslant x \leqslant L$ (finite diffusion bar with a half - thickness), $c = 0$ (3.54)

$t > 0$ (*BC*): $x = 0$, $c = c_s + \tilde{c}_s \exp(j\omega t)$ (potentiostatic oscillation)

$$x = L, \left(\frac{\partial c}{\partial x}\right)_{x=L} = 0 \text{ (reflective } IPB \text{ condition)}$$

(3.55)

where $c(x)$ is the hydrogen concentration within the planar electrode and $c_s(x = 0)$ denotes the hydrogen concentration at the entry surface.

By using the Laplace transform method, the Fick's second law in Eq. 3.16 can be solved [41, 84] under the oscillating concentration/potential perturbation at the electrode/electrolyte interface and in the reflective *IPB* condition at $x = L$ to the oscillation in concentration within the electrode satisfying the *IC* by Eq. 3.54 and *BC* by Eq. 3.55 above

$$\tilde{c} = \tilde{c}_s \frac{\cosh\sqrt{\frac{j\omega}{D_H}}(x - L)}{\cosh\sqrt{\frac{j\omega}{D_H}}L}$$

$$= \tilde{c}_s\left[\cosh\left(\sqrt{\frac{j\omega}{D_H}}x\right) - \tanh\left(\sqrt{\frac{j\omega}{D_H}}L\right)\sinh\left(\sqrt{\frac{j\omega}{D_H}}x\right)\right],$$

(3.56)

which is quite different from Eq. 3.21. According to the Fick's first law, the oscillating flux of hydrogen at the entry side of the electrode, $J_{x=0}$, is then given by

$$J_{x=0} = -D_H\left(\frac{\partial\tilde{c}}{\partial x}\right)_{x=0} = \sqrt{j\omega D_H}\tanh\left(\sqrt{\frac{j\omega}{D_H}}L\right)\tilde{c}_s\exp(j\omega t),$$

(3.57)

which differs from Eq. 3.22 only in that the hyperbolic tangent appears instead of the hyperbolic cotangent and a steady-state concentration gradient does not exist by nature of the *IPB*. The hyperbolic tangent and hyperbolic cotangent functions are characteristic of Y_F as well as $J_{x=0}$ in the reflective *IPB* and transmissive *PB* conditions, respectively.

The theoretical derivation of the Faradaic admittance for the *HAR* with the help of the kinetic equation in the reflective *IPB* condition, which is very similar to that in the transmissive *PB* condition, is as follows. At a low coverage of hydrogen, θ, and low surface concentration, c_s, the rate of the *HAR*, which is expressed by Eq. 3.23 in terms of a linear combination of θ and c_s, is effective for the *IPB* condition as well as the *PB* condition.

If the mechanism of the *HER* follows the Volmer-Heyrovsky reaction mechanism as described by the reaction scheme in Eq. 3.12 above, the charge-transfer reaction rate and the adsorption rate are given by $r_0 = v_1 + v_{Hey}$ and $r_1 = v_1 - v_{Hey}$, respectively. However, the Heyrovsky electrochemical desorption reaction was not considered in this chapter, since the *HER* mechanism on Pd was reported to follow the fast discharge by the Volmer adsorption and slow Tafel-recombination mechanisms [30, 62, 63]. Provided that the *HER* proceeds by the Volmer-Tafel reaction

mechanism, the reaction rates are expressed as $r_0 = v_1$ and $r_1 = v_1 - 2v_2$, respectively. Therefore, Eqs. 3.24 and 3.25 which result from the charge balance and mass balance, respectively, are valid for the *IPB* condition as well as the *PB* condition.

Neglecting the second- and higher order terms of the Taylor series expansion, the rates of the Volmer adsorption, the Tafel desorption, and the *HAR*, v_i (as general designation), are expressed by Eqs. 3.26, 3.27, and 3.28, respectively, in terms of a linear combination of the first derivatives of the rate, v_i, with respect to the electrode potential, $\left(\dfrac{\partial v_i}{\partial E}\right)$, coverage, $\left(\dfrac{\partial v_i}{\partial \theta}\right)$, and surface concentration, $\left(\dfrac{\partial v_i}{\partial c_s}\right)$. The above three equations are the same as those in the transmissive *PB* condition.

The four kinds of reaction constraints (the first derivatives of the rate = 0) expressed by Eq. 3.29 are also effective for the *IPB* condition as well as the *PB* condition:

$$\left(\frac{\partial v_1}{\partial c_s}\right) = 0, \ \left(\frac{\partial v_2}{\partial E}\right) = 0, \ \left(\frac{\partial v_2}{\partial c_s}\right) = 0, \ \text{and} \ \left(\frac{\partial v_3}{\partial E}\right) = 0 \qquad (3.29)$$

Substituting Eqs. 3.26, 3.27, and 3.57 into Eqs. 3.24 and 3.25 under the reaction constraints given by Eq. 3.29 and equating the time-dependent terms with each other, one obtains the following equations from the charge and mass balances:

$$-\frac{\tilde{i}_F}{F} = \left(\frac{\partial r_0}{\partial E}\right)\tilde{E} + \left(\frac{\partial r_0}{\partial \theta}\right)\tilde{\theta} = \left(\frac{\partial v_1}{\partial E}\right)\tilde{E} + \left(\frac{\partial v_1}{\partial \theta}\right)\tilde{\theta}, \qquad (3.30)$$

and

$$j\omega\,\Gamma_{\max}\tilde{\theta} = \left(\frac{\partial v_1}{\partial E}\right)\tilde{E} + \left(\frac{\partial v_1}{\partial \theta}\right)\tilde{\theta} - 2\left(\frac{\partial v_2}{\partial \theta}\right)\tilde{\theta} - \sqrt{j\omega D_H}\ \tanh\!\left(\sqrt{\frac{j\omega}{D_H}}L\right)\tilde{c}_s, \quad (3.58)$$

respectively. Equation 3.30 is valid in common for both the *PB* and *IPB* conditions. Equation 3.58 differs from Eq. 3.31 only in that the hyperbolic tangent function appears instead of the hyperbolic cotangent function. This is responsible for the difference in the Faradaic admittance Y_F in the transmissive *PB* and reflective *IPB* conditions.

Combining the mass balance equation given by Eq. 3.23 and the sinusoidal response of v_3 given by Eq. 3.28 along with the flux of hydrogen diffusion given by Eq. 3.57 under the reaction constraints given by Eq. 3.29, one can obtain from the ac condition (oscillating term)

$$\frac{\tilde{c}_s}{\tilde{\theta}} = \left[\frac{\left(\dfrac{\partial v_3}{\partial \theta}\right)}{-\left(\dfrac{\partial v_3}{\partial c_s}\right) + \sqrt{j\omega D_H}\tanh\!\left(\sqrt{\dfrac{j\omega}{D_H}}L\right)}\right] \qquad (3.59)$$

Substituting $\tilde{c}_s$ in Eq. 3.58 for $\tilde{c}_s$ in Eq. 3.59 and eliminating $\tilde{c}_s$, one obtains

$$\frac{\tilde{\theta}}{\tilde{E}} = \left\{ \frac{\left(\dfrac{\partial v_1}{\partial E}\right)}{j\omega\,\Gamma_{\max} - \left[\left(\dfrac{\partial v_1}{\partial\theta}\right) - 2\left(\dfrac{\partial v_2}{\partial\theta}\right)\right] + \dfrac{\left(\dfrac{\partial v_3}{\partial\theta}\right)}{\left[1 - \dfrac{\left(\dfrac{\partial v_3}{\partial c_s}\right)}{\sqrt{j\omega D_{\mathrm{H}}}\,\tanh\left(\sqrt{\dfrac{j\omega}{D_{\mathrm{H}}}}L\right)}\right]}} \right\}$$

$$(3.60)$$

Substituting $\tilde{\theta}$ in Eq. 3.60 for $\tilde{\theta}$ in Eq. 3.30 and eliminating $\tilde{\theta}$, the Faradaic admittance Y_{F} is finally determined as the following rather awkward-looking expression:

$$Y_{\mathrm{F}} = \frac{\tilde{i}_{\mathrm{F}}}{\tilde{E}} = -F\left(\frac{\partial v_1}{\partial E}\right) \cdot$$

$$\left\{ 1 + \frac{\dfrac{1}{\Gamma_{\max}}\left(\dfrac{\partial v_1}{\partial\theta}\right)}{j\omega - \dfrac{1}{\Gamma_{\max}}\left[\left(\dfrac{\partial v_1}{\partial\theta}\right) - 2\left(\dfrac{\partial v_2}{\partial\theta}\right)\right] + \dfrac{\dfrac{1}{\Gamma_{\max}}\left(\dfrac{\partial v_3}{\partial\theta}\right)}{\left[1 - \dfrac{\left(\dfrac{\partial v_3}{\partial c_s}\right)}{\sqrt{j\omega D_{\mathrm{H}}}\,\tanh\left(\sqrt{\dfrac{j\omega}{D_{\mathrm{H}}}}L\right)}\right]}} \right\},$$

$$(3.61)$$

which is also expressed in terms of the kinetic rate coefficients and constants, as in the case of the transmissive *PB* condition, but differs from Eq. 3.35 in that the hyperbolic tangent function appears instead of the hyperbolic cotangent function. For the sake of comparison with the *PB* condition, one may set

$$R_{ct} = -\frac{1}{F\left(\frac{\partial r_0}{\partial E}\right)} = -\frac{1}{F\left(\frac{\partial v_1}{\partial E}\right)}, B = -\left(\frac{\partial v_1}{\partial \Gamma}\right), C = 2\left(\frac{\partial v_2}{\partial \Gamma}\right), k_3 = \left(\frac{\partial v_3}{\partial \theta}\right), \text{ and } k_{-3} = -\left(\frac{\partial v_3}{\partial c_s}\right),$$

which are exactly the same relations as those in the *PB* condition.

On the basis of the electrical equivalent circuit given in Fig. 3.6b, the Faradaic admittance can be converted into the following impedance equation,

$$Z_F = \frac{\tilde{E}}{\tilde{i}_F} = R_{ct} + \left\{ \frac{1}{j\omega\ C_{ad} + \left(\frac{1}{R_{ev}}\right) + \dfrac{1}{\left[R_{ab} + \dfrac{\sigma \coth\left(\sqrt{\dfrac{j\omega}{D_H}}L\right)}{\sqrt{j\omega D_H}}\right]}} \right\}, \quad (3.62)$$

where $C_{ad} = \dfrac{1}{BR_{ct}}$ with a dimension [F cm^{-2}],

$$R_{ev} = \frac{BR_{ct}}{C} \text{ with a dimension } \left[\Omega \text{ cm}^2\right],$$

$$R_{ab} = \frac{B\Gamma_{max}R_{ct}}{k_3} \text{ with a dimension } \left[\Omega \text{ cm}^2\right],$$

$$\sigma = \frac{k_{-3}}{k_3}\Gamma_{max}BR_{ct} \text{ with a dimension } \left[\Omega \text{ cm}^3\text{s}^{-1}\right],$$

$\sigma_W = \dfrac{\sigma}{\sqrt{2D_H}}$ with a dimension [Ω cm^{2}s$^{-1/2}$] , which are exactly the same relations among the circuit element, kinetic rate coefficient, and rate constant as those in the *PB* condition. Equation 3.62 corresponds to the equivalent circuit given in Fig. 3.6b. The chemical capacitance (C_{ch})/pseudocapacitance (C_{ps}) in Fig. 3.6b acts simply as an *IPB* blocking the diffusants.

Considering the two extremely limiting cases of the diffusion- and interface-controlled *HAR*, Eq. 3.61 can be simplified as follows.

3.3.7.2 - (a) Diffusion-Controlled *HAR* Limit

If $k_{-3} \gg \sqrt{j\omega D_H}\tanh\left(\sqrt{j\omega/D_H}L\right)$, the Faradaic admittance described by Eq. 3.61 is simplified as follows:

$$Y_F = \frac{1}{R_{ct}} \cdot \left\{ 1 - \frac{B}{\left[j\omega + B + C + \frac{1}{l_{eq}} \sqrt{j\omega D_H} \tanh \left(\sqrt{\frac{j\omega}{D_H}} L \right) \right]} \right\}, \qquad (3.63)$$

where l_{eq} means the equilibrium length [cm], $\dfrac{1}{l_{eq}} = \dfrac{k_3}{\Gamma_{max} k_{-3}} = K_{eq}$. Equation 3.63 expresses Y_F for the diffusion-controlled indirect *HAR* in the reflective *IPB* condition. Provided that, for the diffusion-controlled *HAR*, the *HAR* partial step described by Eq. 3.12d is considered to be in local equilibrium, the equilibrium absorption constant, K_{eq}, can be uniquely defined.

3.3.7.3 - (b) Interface-Controlled *HAR* Limit

If $k_{-3} << \sqrt{j\omega D_H} \tanh \left(\sqrt{j\omega/D_H} L \right)$, the Faradaic admittance described by Eq. 3.61 is readily reduced to

$$Y_F = \frac{1}{R_{ct}} \cdot \left\{ 1 - \frac{B}{\left[j\omega + B + C + \left(\frac{k_3}{\Gamma_{max}} \right) \right]} \right\}, \qquad (3.64)$$

which expresses Y_F for the interface-controlled indirect (two-step) *HAR* in the reflective *IPB* condition. It should be emphasized here that Y_F theoretically derived and expressed in Eq. 3.64 shares the same physical significance as Y_F obtained from the transmissive *PB* and expressed in Eq. 3.42 for the interface-controlled indirect *HAR*, since the succeeding diffusion by Eq. 3.12e is almost in equilibrium, as mentioned in Sect. 3.3.4(i) - (b). In contrast to the diffusion-controlled *HAR*, it can be recognized that the partial step described by Eq. 3.12d departs the furthest from equilibrium, thus causing K_{eq} either to go to infinity or to approach to zero, regardless of whether the *PB* or *IPB* condition applies. The characteristic feature of the strong departure from equilibrium is not fixed at the specific electrode/electrolyte system by itself, but it is simultaneously determined even at any electrode/electrolyte system by the applied potential and the nature of the electrode surface roughness [85].

The Faradaic admittance in Eq. 3.64 is similar to that in Eq. 3.65 for the pure *HER* derived by Harrington and Conway [42].

$$Y_F = \frac{1}{R_{ct}} + \frac{B'}{j\omega + C'} \qquad (3.65)$$

where $B' = -F \left(\dfrac{\partial r_0}{\partial \Gamma} \right) \left(\dfrac{\partial r_1}{\partial E} \right) = \left(\dfrac{1}{R_{ct}} \right) \left(\dfrac{\partial v_1}{\partial \Gamma} \right)$ with $[\Omega^{-1} \text{ cm}^{-2} \text{ s}^{-1}]$, $C' = - \left(\dfrac{\partial r_1}{\partial \Gamma} \right)$ $= \left(\dfrac{\partial v_1}{\partial \Gamma} \right) - 2 \left(\dfrac{\partial v_2}{\partial \Gamma} \right)$ with $[\text{ s}^{-1}]$, r_0 is the net charge-transfer reaction rate and r_1 is the net adsorption rate.

3.3.8 Evidence for Direct (One-Step) Hydrogen Absorption Reaction (HAR) and the Indirect to Direct Transition in HAR Mechanism

A clue to the diffusion-controlled direct (one-step) *HAR* into a metal without any adsorbed intermediate state (phase) or purely interface-controlled indirect (two-step) *HAR* with decreasing applied anodic potential was found in the studies of Pyun and coworkers [6, 7, 9–11, 39, 40]. They reported that as the applied potential decreases, the equilibrium absorption constant, K_{eq} is abruptly increased below a certain potential range, irrespective of the *PB* and *IPB* geometries of the Pd planar membrane, indicating that the transition of the diffusion-controlled two-step mechanism to the diffusion-controlled one-step mechanism or purely interface-controlled *HAR* occurs at a characteristic/critical applied potential (range). This may provide evidence for the occurrence of the one-step *HAR* mixed with subsequent diffusion or purely interface-controlled two-step *HAR* in the relatively low applied anodic or even cathodic potential ranges.

Figure 3.11 shows the impedance spectra for the *HAR* in the case of a 50-μm-thick Pd planar membrane in the transmissive *PB* condition measured in 0.1 M LiOH solution at E_{app} values of 0.18, 0.16, 0.13 V_{RHE}. As E_{app} is lowered in value, the Warburg impedance increasingly appears in the Nyquist plot. The Warburg impedance in the Nyquist plot represents ideal diffusion control like the Cottrell equation in the current transient expresses ideal diffusion control. It should be stressed here that the oscillation around the steady-state hydrogen permeation current was clearly observed at the exit side during the impedance measurement. The kinetic and equivalent circuit parameters best fitted to Eq. 3.52b combined with Eq. 3.38 expressing the diffusion-controlled two-step *HAR* are determined by using the *CNLS* fitting method assuming the absence of the *HER*, $C'' = l_{eq}C = 2l_{eq}$ $\left(\dfrac{\partial v_2}{\partial \Gamma}\right) = 0$ which is reasonable. The values of the best-fit parameters are summarized in Table 3.1. From the optimum-fit parameters, one obtains "the theoretically calculated Nyquist plots" denoted by the solid lines in Fig. 3.11. The measured impedance spectra are found to satisfactorily follow the solid lines, indicating the occurrence of the diffusion-controlled two-step *HAR* in the given applied potential range.

From Table 3.1, one notices that the constant for the local equilibrium between the adsorbed and absorbed hydrogen, K_{eq}, abruptly increases to infinity at 0.08 V_{RHE} with decreasing applied anodic potential, E_{app}, indicating that β-PdH is formed due to the increased hydrogen concentration just beneath the electrode surface at 0.08 V_{RHE} and that the *RDS* of the *HAR* is changed from the indirect *HAR* via an adsorbed state to the direct *HAR*, which is predominant below 0.08 V_{RHE} (see Table 3.2). This result is in good agreement with that measured in the reflective *IPB* condition (see Fig. 3.14). The threshold potential for the formation of β-PdH, 0.08 V_{RHE}, measured in this work coincides satisfactorily with the value of 0.05 V_{RHE} at *RT*, thermodynamically calculated by Pourbaix [86]. The present detailed investigation showed us that α-PdH is stable above 0.05 V_{RHE} and that
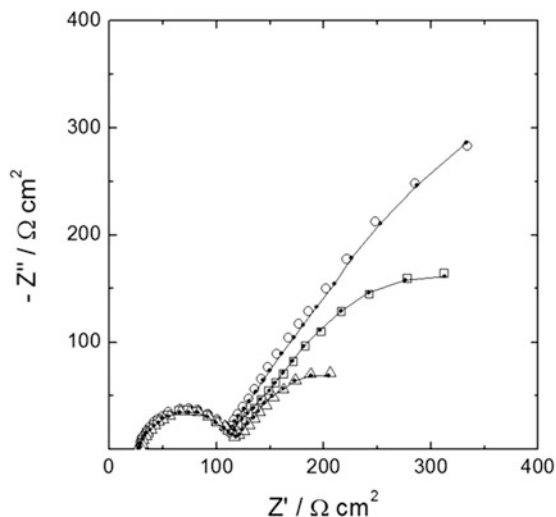
Fig. 3.11 Impedance spectra in Nyquist presentation for *HAR* into a 50 μm-thick Pd planar membrane in transmissive *PB* condition being achieved through electrochemical hydrogen permeation double cell in 0.1 M LiOH solution at various applied anodic potentials and *RT*: ○, $E_{app} = 0.18$ V_{RHE}; □, $E_{app} = 0.16$ V_{RHE}; △, $E_{app} = 0.13$ V_{RHE}. *Solid lines* represent the curves calculated using optimum best fit-parameters based upon Eq. 3.52b combined with Eq. 3.38 for diffusion-controlled indirect (two-step) *HAR* [7] (Reprinted from Lim and Pyun [7], Copyright ©1994 with permission from Elsevier Science)

Table 3.1 Optimum kinetic and circuit parameters best fitted to Eq. 3.52b combined with Eq. 3.38 representing diffusion-controlled indirect (two-step) *HAR*, for impedance spectra experimentally obtained during the *HAR* into Pd planar membrane in transmissive *PB* condition in 0.1 M LiOH solution at various applied anodic potentials and *RT* [7]

E_{app} [V_{RHE}]	$B_o \times 10^4$ [$Fcm^{-2} s^{-(1-\varphi)}$]	$\varphi \times 10^1$ [−]	R_{ct} [Ω cm^2]	$B'' = (l_{eq}$ $B) \times 10^5$ [cm s^{-1}]	$l_{eq} \times 10^4$ [cm]	$D_H \times 10^7$ [cm^2 s^{-1}]	E_{error} (%) [−]
0.28	3.72	8.04	317.5	601.46	38.99	5.37	3.16
0.23	3.06	8.18	152.7	183.13	14.00	2.86	2.12
0.18	2.06	8.88	86.6	56.01	5.58	3.08	1.47
0.16	2.01	8.84	87.1	30.43	4.25	3.61	0.95
0.13	1.92	8.86	88.5	13.53	4.32	3.71	1.17
0.10	1.95	8.86	87.7	7.26	4.88	3.47	1.24
0.08	1.95	9.34	66.9	0.54	2×10^{-9}	3.15	1.40
0.03	1.95	9.21	60.6	0.34	1×10^{-17}	3.09	1.00

β-PdH is stable below 0.05 V_{RHE}. The deposition of a monolayer of hydrogen on the surface of Pd is frequently found to take place at a potential positive to the Nernstian equilibrium potential, which is termed the *UPD*. The formation of *UPD* hydrogen is attributed to the fact that the chemical potential of a "monolayer of hydrogen" in Pd is less than the standard chemical potential of "the bulk hydrogen" in Pd, in contrast to overpotential deposition/adsorption (*OPD*).

Table 3.2 Optimum kinetic and circuit parameters best fitted to Eq. 3.52b combined with Eq. 3.49 representing diffusion-controlled direct (one-step) *HAR*, for impedance spectra experimentally obtained during the *HAR* into Pd planar membrane in transmissive *PB* condition in 0.1 M LiOH solution at various applied anodic potentials and *RT* [7]

E_{app} [V$_{RHE}$]	$B_o \times 10^4$ [F cm^{-2} s$^{-(1-\varphi)}$]	$\varphi \times 10^1$ [−]	R_{ct} [Ω cm^2]	$B' \times 10^5$ [cm s^{-1}]	$D_H \times 10^7$ [cm^2 s^{-1}]	E_{error} (%) [−]
0.08	1.96	9.34	66.9	0.54	3.15	1.40
0.03	1.95	9.21	60.6	0.35	3.09	1.00
0.00	2.02	9.20	58.0	0.34	3.81	0.90
−0.02	2.13	9.12	56.5	0.35	5.63	0.79
−0.04	2.28	9.13	48.3	0.53	23.36	0.75
−0.07	2.13	9.32	32.5	0.29	9.64	0.93

The value of K_{eq} was found to be 7.1×10^2 cm^{-1} at an E_{app} of 0.23 V$_{RHE}$ and 1.8 to 2.4×10^3 cm^{-1} at 0.18 to 0.13 V$_{RHE}$ for the *HAR* in a Pd planar membrane, which are similar in terms of their order of magnitude to the data (7.9×10^2 to 3.0×10^3 cm^{-1}) measured in the applied potential range of 0.25 to 0.10 V$_{RHE}$ under the reflective *IPB* condition (see Fig. 3.14), but are one order of magnitude smaller than that (6×10^3 cm^{-1}) determined at 0.23 V$_{RHE}$ and that (2 to 5×10^4 cm^{-1}) measured at 0.18 to 0.08 V$_{RHE}$ by Breger and Gileadi [69] in 0.3 M NaOH solution from a Pd membrane. It is still not clear whether the discrepancies in the equilibrium constant for the *HAR* arise from the method used or the chemical pretreatment and heat treatment of the specimen. Here, it is emphasized that the value of K_{eq} was determined by using a small-amplitude perturbation analysis, that is, the ac-impedance method excluding the ambiguity arising from double-layer charging.

Figure 3.12 demonstrates the impedance spectra for the *HAR* in a 50-μm -thick Pd planar membrane in the transmissive *PB* condition measured in 0.1 M LiOH solution at E_{app} values of 0.1, 0.08, 0.03, −0.07 V$_{RHE}$. Since below 0.08 V$_{RHE}$, K_{eq} is found to be infinite (the inverse of $K_{eq} = l_{eq} \approx$ zero) from Eq. 3.38, as given in Table 3.1, implying that the equilibrium for the partial step given by Eq. 3.12d is noticeably disturbed, the diffusion-controlled two-step *HAR* loses its physical significance as the *RDS* and, hence, Eq. 3.38 does not hold any more in the given potential ranges. Two possibilities of conceiving a new *RDS* can be substituted for Eq. 3.38. The first one is the most strongly hindered equilibrium for Eq. 3.12a and 3.12d combined in series which one might call the purely interface-controlled two-step *HAR*. The second one is where the two-step *HAR* and subsequent diffusion in series represented by the combined Eqs. 3.12a, 3.12d, and 3.12e is first replaced with the one-step *HAR* given by the combined Eqs. 3.12f and 3.12e. Finally, the latter partial step then strongly departs from equilibrium. Such a strong deviation is forced to additionally generate both the absorption and diffusion resistances, *R*, and hence the corresponding overvoltage/overpotential, η, to establish a new equilibrium. Thus, the kinetic and equivalent circuit parameters best fitted to Eq. 3.52b combined with Eq. 3.49 expressing the diffusion-controlled one-step *HAR* are determined by using the *CNLS* fitting method at E_{app} values below 0.08 V$_{RHE}$. The optimum-fit parameters are summarized in Table 3.2.
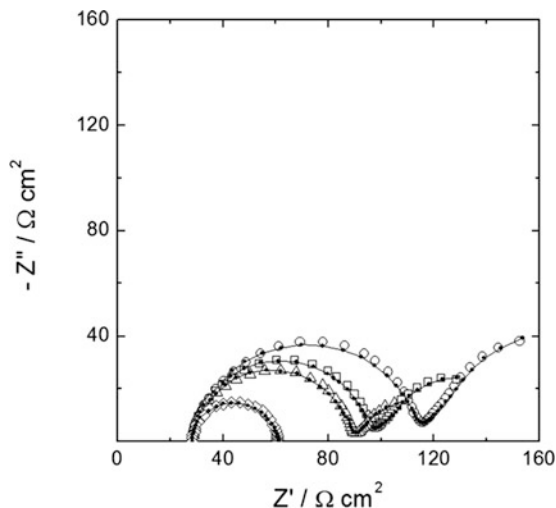
Fig. 3.12 Impedance spectra in Nyquist presentation for *HAR* into a 50 μm-thick Pd planar membrane in transmissive *PB* condition being achieved through electrochemical hydrogen permeation double cell in 0.1 M LiOH solution at various applied anodic potentials and *RT*: ○, $E_{app} = 0.1$ V_{RHE}; □, $E_{app} = 0.08$ V_{RHE}; Δ, $E_{app} = 0.03$ V_{RHE}; ◇, $E_{app} = -0.07$ V_{RHE}. *Solid lines* represent the curves calculated by using optimum best fit-parameters based upon Eq. 3.52b combined with Eq. 3.38 for diffusion-controlled indirect (two-step) *HAR* and *dotted lines* represent those parameters based upon Eq. 3.52b combined with Eq. 3.49 for diffusion-controlled direct (one-step) *HAR* [7] (Reprinted from Lim and Pyun [7], Copyright ©1994 with permission from Elsevier Science)

The fit parameters determined at 0.08 and 0.03 V_{RHE} in Table 3.1 are essentially the same as those in Table 3.2. Consequently, it is suggested that below 0.08 V_{RHE} the expression of Y_F for the *HAR* in a Pd planar membrane changes from that represented by Eq. 3.38 to that represented by Eq. 3.49 in view of the *RDS*, that is, hydrogen directly enters into the interior of the Pd membrane without passing through the adsorbed phase at relatively low applied potentials. The transitions in the *RDS* and mechanism have frequently been observed as functions of the applied potential and the nature of the electrode surface roughness in metal hydride [85] and carbon-hydrogen systems [80, 81] in our laboratory. Figure 3.12 shows that as E_{app} is lowered, the Warburg impedance deviates more negatively from the ideal straight line with a slope of -1. Such a deviation from the ideal Warburg/Cottrell behavior is referred to as anomalous hydrogen diffusion.

In other words, the *RDS* is shifted from pure diffusion control to mixed absorption and diffusion control. Finally, the Warburg impedance submerges at potentials below -0.02 V_{RHE}, indicating that the transition in the *RDS* of the *HAR* occurs from the mixed absorption and diffusion control to the purely interface-controlled *HAR*. Tables 3.1 and 3.2 show that the hydrogen diffusivity D_H in α-PdH determined from the impedance spectra in the applied potential range of 0 to 0.28 V_{RHE} is 3.49 (± 0.69) $\times 10^{-7}$ cm^2 s^{-1} (a tendency for D_H to slightly increase with rising E_{app}),

Fig. 3.13 Impedance spectra in Nyquist presentation for *HAR* into a 60 μm-thick Pd planar membrane in reflective *IPB* condition being achieved by simply immersing the planar membrane into 0.1 M NaOH solution at various applied anodic potentials (**a**) 0.16, 0.12 and 0.10 V_{RHE}, (**b**) 0.08, 0.06 and 0.02 V_{RHE} and *RT*. *Solid lines* represent the curves calculated using optimum best fitted-parameters based upon Eq. 3.52b combined with Eq. 3.63 for diffusion-controlled indirect (two-step) *HAR* [9] (Reprinted from Yang and Pyun [9], Copyright ©1996 with permission from Elsevier Science)
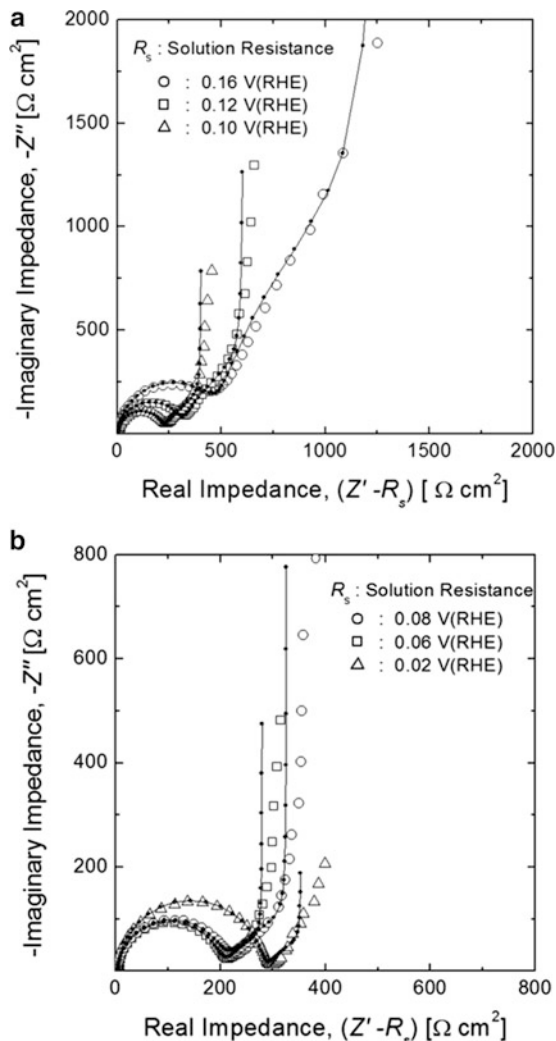
which is comparable to the value of $3.07(\pm 0.07) \times 10^{-7}$ cm^2 s^{-1} reported by Bucur [87], but is slightly lower than the value of $5.57(\pm 1.21) \times 10^{-7}$ cm^2 s^{-1} obtained in the potential range of 0.02 to 0.22 V_{RHE} in the reflective *IPB* condition [9].

When the equilibrium state, meaning a constant hydrogen concentration, is attained at the input surface under the reflective *IPB* condition which is usually achieved by simply immersing the planar electrode with a thickness of 2 *L* into the electrolyte (see Fig. 3.5), the electrode impedance for the *HAR* starts to be measured at the input surface of the electrode in the same manner as in the case of the *PB* condition.

Figure 3.13a, b show the Nyquist plots of the impedance spectra for the *HAR* in a 60-μm-thick Pd planar membrane (*L* = 30 μm) in the reflective *IPB* condition in

Fig. 3.14 Dependence of equilibrium absorption constant K_{eq} on applied anodic potential E_{app}, obtained from the impedance spectra given in Fig. 3.13 for the *HAR* into Pd planar membrane in reflective *IPB* condition in 0.1 M NaOH solution and *RT* [9] (Reprinted from Yang and Pyun [9], Copyright ©1996 with permission from Elsevier Science)
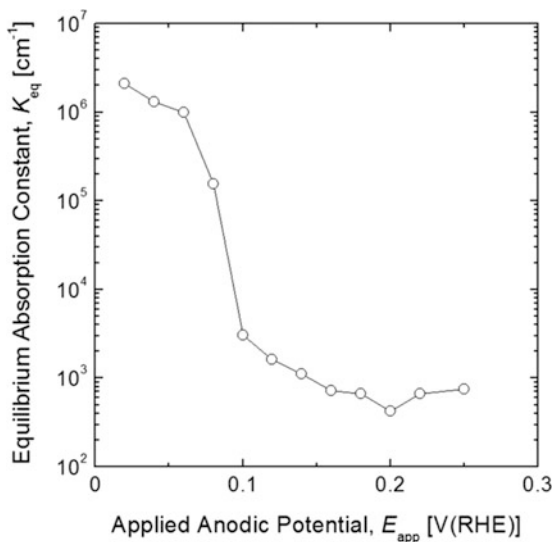
0.1 M NaOH solution at *RT* in the applied potential range of 0.02 to 0.16 V_{RHE}. The impedance spectra involve the charge transfer, adsorption and absorption reactions and, finally, diffusion in the electrode in sequence as the frequency decreases. The semicircle in the high-frequency range corresponds to the charge-transfer reaction. In the potential range of 0.04 to 0.16 V_{RHE}, the Warburg impedance appears in the low-frequency range, representing the finite length diffusion process of hydrogen under the reflective *IPB* condition. With decreasing potential, the Warburg impedance deviates more negatively from the ideal straight line with a slope of 45°, expressing the finite length diffusion process, as in the transmissive *PB* condition. The anomalous hydrogen diffusion can be traced back to many origins [28], including the transition of pure diffusion control to mixed control with charge transfer or hydrogen absorption/desorption, in the presence of hydrogen traps, stresses, fractals and the coexistence of two phases. This anomalous behavior of hydrogen atoms will be discussed in detail in Chaps. 5, 6, and 7. Finally the Warburg impedance disappears at potentials below −0.02 V_{RHE}, indicating that the *HAR* mechanism is shifted from mixed absorption and diffusion control to the purely interface-controlled *HAR*.

Figure 3.14 presents the equilibrium absorption constant K_{eq} determined from Fig. 3.13 and Eq. 3.63 for the diffusion-controlled *HAR* in a Pd electrode in 0.1 M NaOH solution as a function of the applied anodic potential E_{app}. The value of K_{eq} slowly increases from 7.9×10^2 to 3.0×10^3 cm^{-1} with decreasing applied potential from 0.25 to 0.10 V_{RHE}, and then abruptly increases to 1.6×10^5 cm^{-1} at 0.08 V_{RHE}, which is very similar to the value of 2×10^3 cm^{-1} measured in the potential range of 0.18 to 0.13 V_{RHE} in the transmissive *PB* condition (see Table 3.1). It should be noted that a drastic increase in the value of K_{eq} is observed at 0.08 V_{RHE}, which is indicative of the formation of β-PdH and the occurrence of a transition in the *RDS* of the two-step *HAR* to the one-step *HAR*.

Finally, it seems worthwhile to briefly mention that Lasia [72, 82] recently proposed the mechanism and kinetics of the *HAR* in metals to discuss its problems and limitations : The indirect (two-step) *HAR* is composed of three pathways, one corresponding to hydrogen adsorption by *OPD*, the *HAR* followed by the *HER,* and the second one to hydrogen adsorption by *UPD*. In parallel, there is a third pathway in which the *UPD* hydrogen further undergoes the *HAR* to form the *HAR* in series with the Warburg impedance. The direct (one-step) *HAR* is made up of two pathways consisting of the charge-transfer resistance in series with the Warburg impedance and of hydrogen adsorption by *UPD*, followed by the *HER*. Therefore, the model of the *HAR* has been extended by differentiating between the *OPD* and *UPD* adsorption of hydrogen and even by taking the *HER* step into account.

3.4   Summary and Concluding Remarks

The *HAR* can be categorized into two groups, namely, the indirect (two-step) *HAR* and direct (one-step) *HAR*. The first one is divided into substeps, namely, the interfacial charge (electron) transfer, hydrogen transfer from the 2D adsorbed state to the 3D absorbed state and subsequent hydrogen diffusion through the electrode. The second one is split into substeps, namely, the direct interfacial charge (electron) transfer to the absorbed state without an adsorbed intermediate state and subsequent hydrogen diffusion through the electrode. The reaction kinetic and equivalent circuit models of cathodic hydrogen reduction are satisfactorily employed to derive the Faradaic admittance expressions for Y_F. The resistance R to diffusion as well as to *HAR* and the corresponding overpotential/overvoltage η are also introduced as a measure of the degree of deviation from equilibrium, and it plays a crucial role in determining the *RDS,* which is regarded as the most strongly impeded/disturbed "slowest" step.

The *HAR* coupled with diffusion is a complex reaction. Many problems, for instance the distribution of the weighting factor of pure diffusion control and interface control over the whole hydrogen absorption mixed with subsequent diffusion, the quantitative determination of the *RDS* during the overall hydrogen insertion reaction, still need to be solved. One way to solve these problems is the potentiostatic current method, and ac-impedance spectroscopy should be used in parallel and complementarily, for example, as in the previous works performed in our laboratory [80, 81].

References

1. Lee SJ, Pyun SI, Yoon YG (2011) Pathways of diffusion mixed with subsequent reactions with examples of hydrogen extraction from hydride-forming electrode and oxygen reduction at gas diffusion electrode. J Solid State Electrochem 15:2437–2445
2. Bolzan AE (1995) Phenomenological aspects related to the electrochemical behaviour of smooth palladium electrodes in alkaline solutions. J Electroanal Chem 380:127–138

3. Deng B, Li Y, Wang R, Fang S (1999) Two reduction processes for hydrogen adsorption and absorption at MmNi$_5$-type alloy electrodes (Mm: "Mischmetall"). Electrochim Acta 44:2853–2857

4. Han JN, Lee JW, Seo M, Pyun SI (2001) Analysis of stresses generated during hydrogen transport through a Pd foil electrode under potential sweep conditions. J Electroanal Chem 506:1–10

5. Gamboa SA, Sebastian PJ, Feng F, Geng M, Northwood DO (2002) Cyclic voltametry investigation of a metal hydride electrode for nickel metal hydride batteries. J Electrochem Soc 149:A137–A139

6. Lim C, Pyun SI (1993) Theoretical approach to Faradaic admittance of hydrogen absorption reaction on metal membrane electrode. Electrochim Acta 38:2645–2652

7. Lim C, Pyun SI (1994) Impedance analysis of hydrogen absorption reaction on Pd membrane electrode in 0.1 M LiOH solution under permeable boundary conditions. Electrochim Acta 39:363–373

8. Zhang W, Sridhar Kumar MP, Srinivasan S, Ploehn HJ (1995) Ac impedance studies on metal hydride electrodes. J Electrochem Soc 142:2935–2943

9. Yang TH, Pyun SI (1996) Hydrogen absorption into and diffusion in palladium: ac-impedance analysis under impermeable boundary conditions. Electrochim Acta 41:843–848

10. Yang TH, Pyun SI (1996) An investigation of the hydrogen absorption reaction into and the hydrogen evolution reaction from a Pd foil electrode. J Electroanal Chem 414:127–133

11. Yang TH, Pyun SI (1996) A study of the hydrogen absorption reaction into α- and β-LaNi$_5$H$_x$ porous electrodes by using electrochemical impedance spectroscopy. J Power Sources 62:175–178

12. Wang C (1998) Kinetic behavior of metal hydride electrode by means of ac impedance. J Electrochem Soc 145:1801–1812

13. Montella C (1999) Review and theoretical analysis of ac–av methods for the investigation of hydrogen insertion I. Diffusion formalism. J Electroanal Chem 462:73–87

14. Montella C (2000) Review and theoretical analysis of ac–av methods for the investigation of hydrogen insertion: Part II. Entry side impedance, transfer function and transfer impedance formalism. J Electroanal Chem 480:150–165

15. Montella C (2000) Review and theoretical analysis of ac–av methods for the investigation of hydrogen insertion: Part III. Comparison of entry side impedance, transfer function and transfer impedance methods. J Electroanal Chem 480:166–185

16. Yuan X, Xu N (2002) Electrochemical and hydrogen transport kinetic performance of M$_I$Ni$_{3.75}$Co$_{0.65}$Mn$_{0.4}$Al$_{0.2}$ (Ml denotes La-rich mischmetal being composed of La 61.11 wt %, Ce 27.16 wt %, Pr 3.09 wt %, and Nd 8.64 wt %) metal hydride electrodes at various temperatures. J Electrochem Soc 149:A407–A413

17. Georén P, Hjelm AK, Lindbergh G, Lundqvist A (2003) An electrochemical impedance spectroscopy method applied to porous LiMn$_2$O$_4$ and metal hydride battery electrodes. J Electrochem Soc 150:A234–A241

18. Haran BS, Popov BN, White RE (1998) Theoretical analysis of metal hydride electrodes-studies on equilibrium potential and exchange current density. J Electrochem Soc 145:4082–4090

19. Feng F, Ping X, Zhou Z, Geng M, Han J, Northwood DO (1998) The relationship between equilibrium potential during discharge and hydrogen concentration in a metal hydride electrode. Int J Hydrogen Energy 23:599–602

20. Conway BE, Wojtowicz J (1992) Time-scales of electrochemical desorption and sorption of H in relation to dimensions and geometries of host metal hydride electrodes. J Electroanal Chem 326:277–297

21. Ura H, Nishina T, Uchida I (1995) Electrochemical measurements of single particles of Pd and LaNi$_5$ with a microelectrode technique. J Electroanal Chem 396:169–173

22. Nishina T, Ura H, Uchida I (1997) Determination of chemical diffusion coefficients in metal hydride particles with a microelectrode technique. J Electrochem Soc 144:1273–1277

23. Kim HS, Nishizawa M, Uchida I (1999) Single particle electrochemistry for hydrogen storage alloys, MmNi$_{3.55}$Co$_{0.75}$Mn$_{0.4}$A$_{l0.3}$ (Mm: "Mischmetall"). Electrochim Acta 45:483–488
24. Feng F, Han J, Geng M, Northwood DO (2000) Study of hydrogen transport in metal hydride electrodes using a novel electrochemical method. J Electroanal Chem 487:111–119
25. Yuan X, Xu N (2001) Comparative study on electrochemical techniques for determination of hydrogen diffusion coefficients in metal hydride electrodes. J Appl Electrochem 31:1033–1039
26. Kim HS, Itoh T, Nishizawa M, Mohamedi M, Umeda M, Uchida I (2002) Microvoltammetric study of electrochemical properties of a single spherical nickel hydroxide particle. Int J Hydrogen Energy 27:295–300
27. Lee JW, Pyun SI (2005) Anomalous behaviour in diffusion impedance of intercalation electrodes. Z Metallkd 96:117–123
28. Lee JW, Pyun SI (2005) Anomalous behaviour of hydrogen extraction from hydride-forming metals and alloys under impermeable boundary conditions. Electrochim Acta 50:1777–1805
29. Boes N, Züchner H (1976) Electrochemical methods for studying diffusion, permeation and solubility of hydrogen in metals. J Less-Common Met 49:223–240
30. Subramanyan PK (1981) Electrochemical aspects of hydrogen in metals. In: Bockris JO'M, Conway BE, Yeager E, White RE (eds) Comprehensive treatise of electrochemistry, vol 4. Electrochemical materials science. Plenum, New York, p 411
31. Fullenwider MA (1983) Hydrogen entry and action in metals. Pergamon, New York, p 4
32. Pound BG (1993) Chapter 2 Electrochemical techniques to study hydrogen ingress in metals. In: Bockris JO'M, Conway BE, Yeager E, White RE (eds) Modern aspects of electrochemistry, vol 25. Plenum, New York, p 63
33. Devanathan MAV, Stachurski Z (1962) The absorption and diffusion of electrolytic hydrogen in palladium. Proc R Soc Lond A 270:90–102
34. McBreen J, Nanis L, Beck W (1966) A method for determination of the permeation rate of hydrogen through metal membranes. J Electrochem Soc 113:1218–1222
35. Nanis L, Govindan Namboodhiri TK (1972) Mathematics of the electrochemical extraction of hydrogen from iron. J Electrochem Soc 119:691–694
36. Early JG (1978) Hydrogen diffusion in palladium by galvanostatic charging. Acta Metall 26:1215–1223
37. Bockris JO'M, Genshaw MA, Fullenwider M (1970) The electro-permeation of hydrogen into metals. Electrochim Acta 15:47–60
38. Kirchheim R, McLellan RB (1980) Electrochemical methods for measuring diffusivities of hydrogen in palladium and palladium alloys. J Electrochem Soc 127:2419–2425
39. Pyun SI, Lee WJ, Yang TH (1997) Hydrogen diffusion through palladium-gold alloy coatings electrodeposited on palladium substrate under permeable boundary condition. Thin Solid Films 311:183–189
40. Lee W, Pyun SI, Yang TH, Kim JD, Baek YH, Kim HG (1997) Hydrogen transport through Pd-Ni alloy electrodeposited on Pd substrate. J Solid State Electrochem 1:120–125
41. Pyun SI (2007) Outlines of electrochemistry at materials. Chung-Moon-Gak Book Publishing, Seoul, pp 293, 330, 359, 610, 830, 835; Kim JS, Pyun SI (2011) Comparison of transmissive permeable and reflective impermeable interfaces between electrode and electrolyte. J Solid State Electrochem 15:2447–2452
42. Harrington DA, Conway BE (1987) Ac impedance of Faradaic reactions involving electrosorbed intermediates – I. Kinetic theory. Electrochim Acta 32:1703–1712
43. Raistrick ID (1990) Impedance studies of porous electrodes. Electrochim Acta 35:1579–1586
44. Bisquert J, Garcia-Belmonte G, Bueno P, Longo E, Bulhoes LOS (1998) Impedance of constant phase element (CPE)-blocked diffusion in film electrodes. J Electroanal Chem 452:229–234
45. Bisquert J (2000) Influence of the boundaries in the impedance of porous film electrodes. Phys Chem Chem Phys 2:4185–4192
46. Bisquert J, Compte A (2001) Theory of the electrochemical impedance of anomalous diffusion. J Electroanal Chem 499:112–120

47. Jamnik J, Maier J (2001) Generalised equivalent circuits for mass and charge transport: chemical capacitance and its implications. Phys Chem Chem Phys 3:1668–1678
48. Bisquert J (2002) Analysis of the kinetics of ion intercalation: ion trapping approach to solid-state relaxation processes. Electrochim Acta 47:2435–2449
49. Bisquert J, Vikhrenko VS (2002) Analysis of the kinetics of ion intercalation. Two state model describing the coupling of solid state ion diffusion and ion binding processes. Electrochim Acta 47:3977–3988
50. Bisquert J, Garcia-Belmonte G, Pitarch A (2003) An explanation of anomalous diffusion patterns observed in electroactive materials by impedance methods. A European J ChemPhysChem 4:287–292
51. Boukamp BA (2004) Electrochemical impedance spectroscopy in solid state ionics: recent advances. Solid State Ionics 169:65–73
52. Barsoukov E, Macdonald JR (2005) Impedance spectroscopy. Wiley, New York, pp 16, 54
53. Crank J (1975) The mathematics of diffusion. Clarendon, Oxford, p 11
54. Kim JS, Pyun SI (2008) Theoretical and experimental approaches to oxygen reduction at porous composite electrodes for fuel cells by analyses of ac-impedance spectra and potentiostatic current transients. Isr J Chem 48:277–286
55. Ho C, Raistrick ID, Huggins RA (1980) Application of a-c techniques to the study of lithium diffusion in tungsten trioxide thin films. J Electrochem Soc 127:343–350
56. Jacobsen T, West K (1995) Diffusion impedance in planar, cylindrical and spherical symmetry. Electrochim Acta 40:255–262
57. Ding S, Petuskey WT (1998) Solutions to Fick's second law of diffusion with a sinusoidal excitation. Solid State Ionics 109:101–110
58. Pitarch A, Garcia-Belmonte G, Mora-Sero I, Bisquert J (2004) Electrochemical impedance spectra for the complete equivalent circuit of diffusion and reaction under steady-state recombination current. Phys Chem Chem Phys 6:2983–2988
59. Bockris JO'M, McBreen J, Nanis L (1965) The hydrogen evolution kinetics and hydrogen entry into α-iron. J Electrochem Soc 112:1025–1031
60. Kim CD, Wilde BE (1971) The kinetics of hydrogen absorption into iron during cathodic hydrogen evolution. J Electrochem Soc 118:202–206
61. Iyer RN, Pickering HW, Zamanzadeh M (1989) Analysis of hydrogen evolution and entry into metals for the discharge-recombination process. J Electrochem Soc 136:2463–2470
62. Bockris JO'M (1954) Chapter 4 Electrode kinetics. In: Bockris JO'M (ed) Modern aspects of electrochemistry, vol 1. Butterworths Scientific Publications, London, p 180
63. Enyo M, Maoka T (1980) The overpotential components on the palladium hydrogen electrode. J Electroanal Chem 108:277–292
64. Cabanel R, Barral G, Diard JP, Le Gorrec B, Montella C (1993) Determination of the diffusion-coefficient of an inserted species by impedance spectroscopy- application to the $H/H_xNb_2O_5$ system. J Appl Electrochem 23:93–97
65. Armstrong RD, Henderson M (1972) Impedance plane display of a reaction with an adsorbed intermediate. J Electroanal Chem 39:81–90
66. Bagotskaya IA (1962) Effect of the solution composition on the diffusion rate of electrolytic hydrogen through metallic diaphragms. I. Diffusion of hydrogen through iron diaphragms. Zhur Fiz Khim 36:2667–2673
67. Frumkin AN (1963) Chapter 5 Hydrogen overvoltage and adsorption phenomena part II. In: Delahay P (ed) Advances in electrochemistry and electrochemical engineering, vol 3. Interscience, New York, p 375
68. Franceschetti DR, Macdonald JR, Buck RP (1991) Interpretation of finite-length-Warburg-type impedances in supported and unsupported electrochemical cells with kinetically reversible electrodes. J Electrochem Soc 138:1368–1371
69. Breger V, Gileadi E (1971) Adsorption and absorption of hydrogen in palladium. Electrochim Acta 16:177–190

70. Lee JW, Pyun SI, Filipeck S (2003) The kinetics of hydrogen transport through amorphous $Pd_{82-y}Ni_ySi_{18}$alloys (y = 0 − 32) by analysis of anodic current transient. Electrochim Acta 48:1603–1611
71. Han JN, Pyun SI, Yang TH (1997) Roles of thiourea as an inhibitor in hydrogen absorption into palladium electrode. J Electrochem Soc 144:4266–4272
72. Lasia A (2002) Chapter 1 Application of electrochemical impedance spectroscopy to hydrogen adsorption, evolution and absorption into metals. In: Conway BE, White RE (eds) Modern aspects of electrochemistry, vol 35. Kluwer/Plenum, New York, p 1
73. Reichman B, Bard AJ, Laser D (1980) A digital simulation model for electrochromic processes at WO_3 electrodes. J Electrochem Soc 127:647–654
74. Yayama H, Kuroki K, Hirakawa K, Tomokiyo A (1984) Electrode resistance of metal hydride in alkaline aqueous solution. Jpn J Appl Phys 23:1619–1623
75. Brug GJ, van der Eeden ALG, Sluyters-Rehbach M, Sluyters JH (1984) The analysis of electrode impedances complicated by the presence of a constant phase element. J Electroanal Chem 176:275–295
76. Macdonald JR, Schoonman J, Lehner AP (1982) Applicability and power of complex nonlinear least squares for the analysis of impedance and admittance data. J Electroanal Chem 131:77–95
77. Bae JS, Pyun SI (1994) An ac impedance study of $LiI–Al_2O_3$ composite solid electrolyte. J Mater Sci Lett 13:573–576
78. Bai L, Harrington DA, Conway BE (1987) Behavior of overpotential-deposited species in Faradaic reactions – II. ac Impedance measurements on H_2 evolution kinetics at activated and unactivated Pt cathodes. Electrochim Acta 32:1713–1731
79. Ekdunge P, Jüttner K, Kreysa G, Kessler T, Ebert M, Lorenz WJ (1991) Electrochemical impedance study on the kinetics of hydrogen evolution at amorphous metals in alkaline solution. J Electrochem Soc 138:2660–2668
80. Lee SK, Pyun SI, Lee SJ, Jung KN (2007) Mechanism transition of mixed diffusion and charge transfer-controlled to diffusion-controlled oxygen reduction at Pt-dispersed carbon electrode by Pt-loading, nafion content and temperature. Electrochim Acta, 53: 740–751.
81. Lee SJ, Pyun SI (2010) Kinetics of mixed-controlled oxygen reduction at nafion-impregnated Pt-alloy-dispersed carbon electrode by analysis of cathodic current transients. J Solid State Electrochem 14:775–786.
82. Lasia A (2006) On the mechanism of the hydrogen absorption reaction. J Electroanal Chem 593:159–166.
83. Birry L, Lasia A (2006) Effect of crystal violet on the kinetics of H sorption into Pd. Electrochim Acta 51: 3356–3364.
84. Pyun SI (2007) The fundamentals of corrosion of metals and their application into practice. Chung-Moon-Gak Book Publishing, Seoul, p 566
85. Lee SJ, Pyun SI, Lee JW (2005) Investigation of hydrogen transport through Mm $(Ni_{3.6}Co_{0.7}Mn_{0.4}Al_{0.3})_{1.12}$ (Mm denotes a "Mischmetall") and $Zr_{0.65}Ti_{0.35}Ni_{1.2}V_{0.4}Mn_{0.4}$ hydride electrodes by analysis of anodic current transient. Electrochim Acta 50:1121–1130
86. Pourbaix M (1974) Chapter 4 Establishment and interpretation of potential-pH equilibrium diagrams on Pd. In: Franklin JA (translated from the French) Atlas of electrochemical equilibria in aqueous solutions, 2nd edn. National Association of Corrosion Engineers, Houston, p 358
87. Bucur RV (1985) The influence of experimental conditions upon the measurements of hydrogen diffusion in palladium by electrochemical methods. Z Phys Chem NF 146:217–229

Chapter 4
Hydrogen Transport Under Impermeable Boundary Conditions

4.1 Redox Reactions of Hydrogen Injection and Extraction

The hydrogen injection reaction into metals and oxides involves hydrogen absorption, followed by hydrogen diffusion through the bulk electrode. There are two models that describe hydrogen absorption in an alkaline solution: (1) the one-step (direct) mechanism and (2) the two-step mechanisms [1–3].

1. One-step absorption mechanism: hydrogen is directly absorbed into the electrode as follows

$$M + H_2O + e^- \leftrightarrow MH_{abs} + OH^- \qquad (4.1)$$
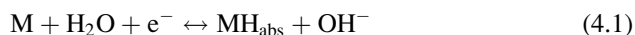
   where MH_{abs} denotes a hydrogen atom absorbed at the electrode subsurface just beneath the topmost surface layer of the metal M.
2. Two-step mechanism: hydrogen is first adsorbed on the electrode surface (Volmer adsorption) and then transferred from the adsorbed state (MH_{ads}) on the electrode surface to the absorbed state (MH_{abs}) at the electrode subsurface,

$$M + H_2O + e^- \leftrightarrow MH_{ads} + OH^- \qquad (4.2)$$

$$MH_{ads} \leftrightarrow MH_{abs} \qquad (4.3)$$
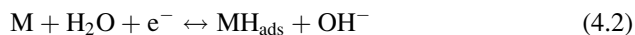
Then, the absorbed hydrogen atom diffuses toward the interior of the electrode.

The hydrogen evolution reaction occurs simultaneously with the cathodic hydrogen injection. Hydrogen evolution proceeds by the chemical desorption (Tafel reaction) or electrochemical desorption (Heyrovsky reaction) of the adsorbed hydrogen atoms [4–6]. Therefore, the hydrogen evolution reaction provides an alternative reaction path parallel to hydrogen injection. The adsorbed hydrogen
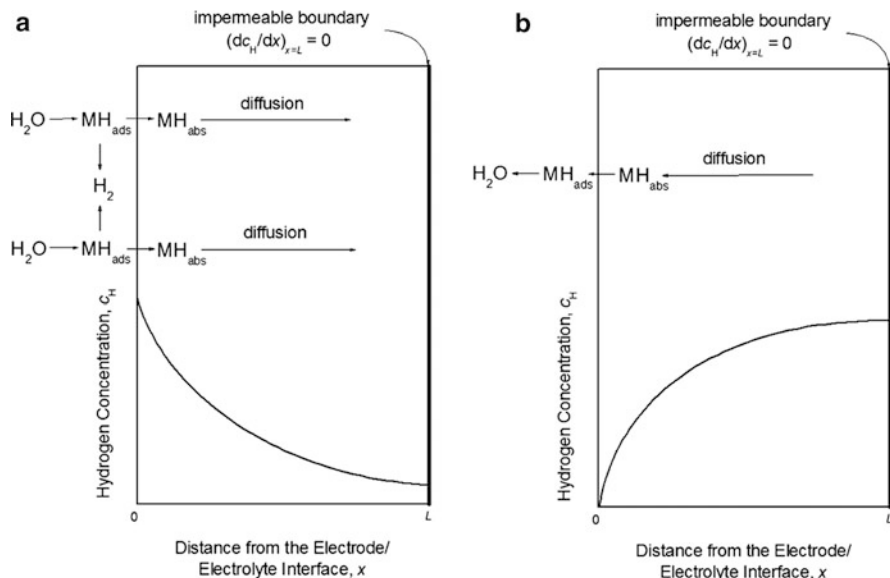
Fig. 4.1 Schematic diagrams of the (**a**) hydrogen injection and (**b**) extraction reactions

state for hydrogen evolution is identical to that for hydrogen injection, and, thus hydrogen injection is closely associated with the hydrogen evolution reaction. It is difficult to uniquely determine the contribution of hydrogen injection to the measured cathodic current because part of the electric charge is consumed by hydrogen evolution. In order to study the mechanism of hydrogen transport, therefore, it is more useful to analyze the anodic currents measured during hydrogen extraction from the electrode than the cathodic currents. The hydrogen injection and extraction reactions are schematically shown in Fig. 4.1a, b, respectively, along with the corresponding profiles of the hydrogen concentration c_H across the electrode under the impermeable boundary condition. As shown in Fig. 4.1b, the hydrogen extraction reaction proceeds through the following reactions:

1. Hydrogen diffusion within the bulk electrode
2. Hydrogen transfer of MH_{abs} at the electrode subsurface to MH_{ads} on the electrode surface
3. Electrochemical oxidation of the adsorbed hydrogen atom on the electrode surface involving the charge transfer reaction

The hydrogen extraction reaction has been studied using a wide range of electrochemical techniques, for example, cyclic voltammetry [7–10], ac-impedance spectroscopy [11–21], the galvanostatic potential transient technique (chronopotentiometry) [22, 23], and potentiostatic current transient technique (chronoamperometry) [24–29]. Among these, the potentiostatic current transient technique is a valuable method of examining hydrogen transport, due to the simple mathematics involved in the theoretical treatment. It is sometimes possible to obtain an analytical solution to the appropriate diffusion equation for any set of boundary conditions.

In this chapter, the analysis of the anodic current transients through mathematical calculations will be demonstrated to show the key features of the current transients. For this purpose, we introduce the "virtual" electrode potential curve for the redox reactions of hydrogen injection and extraction, even though real electrode potential curves may deviate from the virtual one depending on the electrode system. From the well-known Nernst equation, one can formulate the expression of the electrode potential E for any solid-state redox system,

$$E = E_o - \frac{RT}{F} \ln\left(\frac{\delta}{1-\delta}\right) \tag{4.4}$$

where δ is the dimensionless atomic content, which is defined as the molar ratio of the intercalated atoms to the host electrode, for example, H/M or MH_δ, E_o is the standard electrode potential given at $\delta = 0.5$, and F is the Faraday constant. The notations R and T are usually used symbols. Equation 4.4 indicates that the value of E decreases monotonously with increasing δ. This means that a single phase is maintained over the whole composition range.

Equation 4.4 is modified to Eq. 4.5 which represents the electrode potential curve involving both single-phase and two-phase reactions, when the interaction between the atoms is considered,

$$E = E_o - \frac{z\phi}{F}(1 - 2\delta) - \frac{RT}{F} \ln\left(\frac{\delta}{1-\delta}\right) \tag{4.5}$$

where z is the number of neighboring sites and ϕ designates the interaction energy between atoms (positive values of ϕ correspond to attractive interactions, whereas negative values refer to repulsive ones). Equation 4.5 was used to describe the thermodynamic behavior of nonideal, ionic solid solutions where the protons are dissociated in the host lattice of $Ni(OH)_2/NiOOH$. Aurbach and his coworkers [30, 31] showed that the isotherm derived based on Eq. 4.5 could fit satisfactorily into the electrode potential curves measured on Pd, as well as transition metal oxide electrodes. This indicates that Eq. 4.5 can be successfully used to describe the electrode potential curve for hydrogen injection into and extraction from a hydride-forming electrode.

Figure 4.2 presents the E versus δ curve calculated with $E_o = 0$ V, $z\phi = 0.059$ eV, and $T = 298$ K [32]. The electrode potential curve shows a potential plateau at 0 V between $\delta^{\alpha\beta} = 0.205$ and $\delta^{\beta\alpha} = 0.795$. This indicates the coexistence of two hydride phases, α-MH_δ and β-MH_δ. $\delta^{\alpha\beta}$ and $\delta^{\beta\alpha}$ denote the maximum solubility limit of hydrogen in the α phase and the minimum solubility limit of hydrogen in the β phase, respectively. For $z\phi > 0.052$ eV, the electrode potential curve exhibits a local minimum below E_o and a local maximum above E_o, that is, the curve shows an upward concave shape and then a downward concave shape. This suggests that all of the compositions are unstable in the range between $\delta^{\alpha\beta}$ and $\delta^{\beta\alpha}$, which is called the "forbidden composition range"; a disproportionation reaction

Fig. 4.2 E versus δ curve calculated using Eq. 4.5 with $E_o = 0$ V, $z\phi = 0.059$ eV and $T = 298$ K (Reprinted from Lee and Pyun [32], Copyright ©2005 with permission from Elsevier Science)
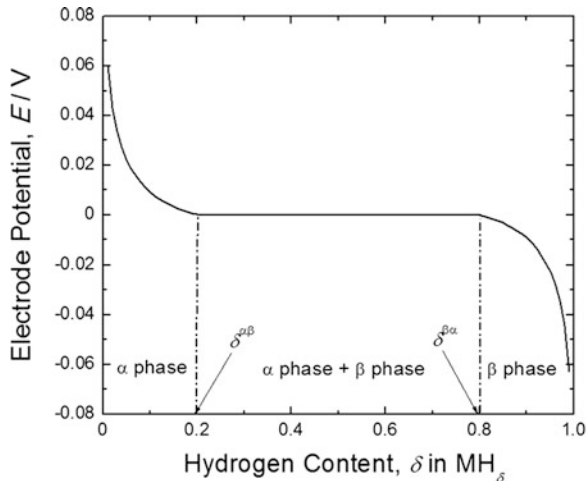
takes place in this "forbidden composition range" into a dilute α phase and a concentrated β phase. Consequently, the electrode potential curve shows a perfectly flat potential plateau at E_o due to the equilibrium of the two phases.

4.2 Concept of Diffusion-Controlled Hydrogen Transport

In most theoretical and experimental investigations, it has been assumed that the rate-determining step of hydrogen transport through hydride-forming electrodes is hydrogen diffusion. The hydrogen extraction reaction can be represented by a series of resistances (or impedances) associated with various reaction steps: the charge transfer resistance R_{ct}, the hydrogen transfer resistance R_{ht}, and the diffusion resistance R_d, as schematically illustrated in Fig. 4.3. A fast reaction step is represented by a small resistance, while a slow reaction step is represented by a high resistance. Let us assume that the linear relationship between the current I and overpotential η is valid for each reaction step. Under a steady-state condition, the rates of all of the reaction steps in a series should be the same, and the overpotential η for each reaction step is expressed by

$$\eta_{ct} = I^{st} R_{ct} \tag{4.6}$$

$$\eta_{ht} = I^{st} R_{ht} \tag{4.7}$$

$$\eta_d = I^{st} R_d \tag{4.8}$$
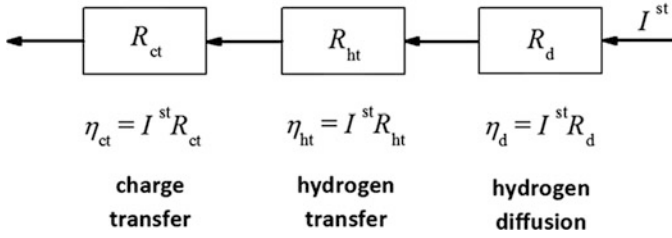
Fig. 4.3 Schematic view of the hydrogen extraction process represented as a series of resistances

where I^{st} is the steady-state current. Summing Eqs. 4.6, 4.7, and 4.8, one obtains

$$I^{st} = \frac{\eta_{ct} + \eta_{ht} + \eta_{d}}{R_{ct} + R_{ht} + R_{d}} \tag{4.9}$$

I^{st} is determined by one or more reaction steps with large values of R. So, the diffusion-controlled hydrogen extraction refers to the condition where R_d is much larger than R_{ct} and R_{ht}, leading to $\eta_d >> \eta_{ct}$ and η_{ht}, so that I^{st} is exclusively determined by the rate of hydrogen diffusion. This also means that the more facile reactions of charge transfer and hydrogen transfer are held back from their maximum rates by the slow hydrogen diffusion. Given that η for a reaction step is a measure of how far the reaction step is hindered from its equilibrium state, the diffusion-control concept implies that the charge transfer and hydrogen transfer reactions are practically undisturbed from the respective equilibria, but hydrogen diffusion is noticeably disturbed from its equilibrium state.

4.3 Diffusion-Controlled Hydrogen Transport in the Presence of Single Phase

4.3.1 Flat Electrode Surface

First, we present mathematical expressions for the current transients describing hydrogen transport in a planar electrode with a flat surface. The following is assumed:

1. The geometry is a planar electrode with a flat surface.
2. The electrode is homogeneous in structure, for example, the electrode does not have any trap sites for hydrogen and comprises only a single phase.
3. The concentration gradient of hydrogen across the electrode is the unique factor that drives hydrogen transport.
4. The chemical diffusivity of hydrogen $\tilde{D}_H$ remains constant during hydrogen extraction.
5. The double-layer charging current is neglected.

Then the governing equation is Fick's diffusion equation,

$$\frac{\partial c_H}{\partial t} = \tilde{D}_H \frac{\partial^2 c_H}{\partial x^2} \tag{4.10}$$

where x is the distance from the electrode/electrolyte interface and t is the hydrogen extraction time.

Chemical diffusion is a process in which the transport of all species within the electrode is involved. The chemical diffusivity of hydrogen $\tilde{D}_H$ is related to the component diffusivity D_K which is a measure of the random motion of hydrogen ions in the electrode as follows [33]:

$$\tilde{D}_H = D_K W_{th} \tag{4.11}$$

Here, W_{th} denotes the thermodynamic enhancement factor. In the case of a metal-hydrogen system in which one ionic species (hydrogen ion) and one electronic species are considered in the electrode, W_{th} is defined as

$$W_{th} = t_e \left(\frac{\partial \ln a_H}{\partial \ln c_H} \right) \tag{4.12}$$

The metal electrode is predominantly an electronic conductor, that is, $t_e \approx 1$, and hence W_{th} simply becomes

$$W_{th} = \frac{\partial \ln a_H}{\partial \ln c_H} = 1 + \frac{\partial \ln \gamma_H}{\partial \ln c_H} \tag{4.13}$$

where γ_H is the activity coefficient, that is, $\gamma_H = a_H/c_H$. Since a metal-hydrogen system is generally considered to be an ideal dilute solution, the thermodynamic enhancement factor W_{th} of hydrogen should be unity, so that the chemical diffusivity of hydrogen $\tilde{D}_H$, the component diffusivity D_K, the random diffusivity D_{rand}, and the self-diffusivity D_{self} are all equal to each other.

The initial condition (IC) and boundary conditions (BCs) are written as follows:

$$IC: c_H = c_H^o \qquad \text{for } 0 \leq x \leq L \text{ at } t = 0 \tag{4.14}$$

$$BC: c_H = c_H^s \qquad (\text{diffusion} - \text{control } BC) \tag{4.15}$$

$$\text{for } x = 0 \text{ at } t \geq 0$$

$$\left(\frac{\partial c_H}{\partial x} \right) = 0 \qquad (\text{impermeable } BC) \tag{4.16}$$

$$\text{for } x = L \text{ at } t \geq 0$$

where L is the electrode thickness and c_H^o and c_H^s denote the initial equilibrium concentration of hydrogen and the surface concentration of hydrogen which correspond to E_{ini} and E_{ext}, respectively.

The solution of Eq. 4.10 under the above IC and BCs has one of two standard forms of c_H. It is in the form of either a series of error functions as given in Eq. 4.17 or a trigonometrical series as given in Eq. 4.18 [34, 35]:

$$c_H(x,t) = c_H^o - (c_H^o - c_H^s)$$
$$\times \sum_{n=0}^{\infty} (-1)^n \left[\text{erfc}\left(\frac{2L(n+1) - x}{2\sqrt{\tilde{D}_H t}} \right) + \text{erfc}\left(\frac{2Ln + x}{2\sqrt{\tilde{D}_H t}} \right) \right] \quad (4.17)$$

$$c_H(x,t) = c_H^s + \frac{4(c_H^o - c_H^s)}{\pi}$$
$$\times \sum_{n=0}^{\infty} \frac{1}{(2n+1)} \sin\left(\frac{(2n+1)\pi x}{2L} \right) \exp\left(-\frac{(2n+1)^2 \pi^2 \tilde{D}_H t}{4L^2} \right) \quad (4.18)$$

Equations 4.17 and 4.18 are used to derive the current-time relation at short times and long times, respectively. The time-dependent current during hydrogen extraction is related to the concentration gradient of hydrogen at the electrode surface by Fick's first law,

$$I(t) = FA_{ea} \tilde{D}_H \left(\frac{\partial c_H}{\partial x} \right) \qquad \text{for } x = 0 \text{ at } t \geq 0 \quad (4.19)$$

where A_{ea} is the electrochemical active area. Note that the anodic current is taken to be positive in accordance with the IUPAC convention. Neglecting the higher order terms in Eqs. 4.17 and 4.18, the current-time relation for hydrogen extraction can be obtained from Eq. 4.19 as Eq. 4.20 for the early stage of hydrogen extraction and as Eq. 4.21 for the later stage,

$$I(t) = FA_{ea}(c_H^o - c_H^s)\left(\frac{\tilde{D}_H}{\pi t} \right)^{1/2} \text{ for } t \ll \frac{L^2}{\tilde{D}_H} \quad (4.20)$$

$$I(t) = \frac{2FA_{ea}(c_H^o - c_H^s)\tilde{D}_H}{L} \exp\left(-\frac{\pi^2 \tilde{D}_H}{4L^2} t \right) \text{ for } t \gg \frac{L^2}{\tilde{D}_H} \quad (4.21)$$

Equation 4.20 is referred to as the Cottrell equation.

Figure 4.4a illustrates the log I versus log t curve calculated by jumping $E_{ini} = 0.01$ V to $E_{ext} = 0.08$ V [32]. The anodic current transient was calculated by assuming $L = 1$ cm, $A_{ea} = 1$ cm^2, and $F\tilde{D}_H = 1$ A cm^{2}mol^{-1}. Here, c_H was taken to be δ mol cm^{-3} for the molar volume of the electrode $V_m = 1$ cm^3 mol^{-1}. The current

Fig. 4.4 (**a**) log I versus log t curve, (**b**) $It^{1/2}$ versus log t plot, and (**c**) the hydrogen concentration profile transients calculated by jumping $E_{ini} = 0.01$ V to $E_{ext} = 0.08$ V (Reprinted from Lee and Pyun [32], Copyright ©2005 with permission from Elsevier Science)
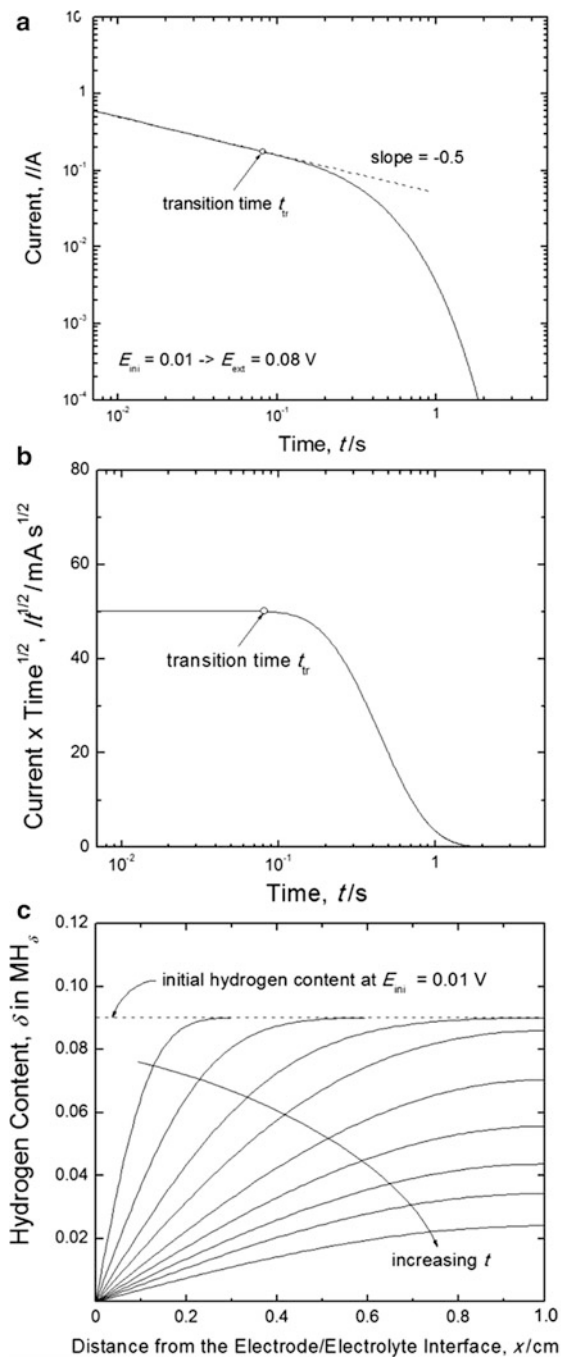
transient exhibits a linear relationship between $\log I$ and $\log t$ with an absolute slope of 0.5 (i.e., Cottrell behavior), followed by an exponential decay of current with time, as predicted from Eqs. 4.20 and 4.21. Moreover, the simulation showed that all of the anodic current transients determined at various values of E_{ext} in the range of 0.08 to 0.16 V exactly coincide with each other in shape as well as in value. This is because the values of E_{ext} correspond to c_H of zero as well and, hence, $(c_H^o - c_H^s)$ keeps a constant value regardless of E_{ext}. According to Eq. 4.20, the Cottrell region is characterized in the plot of $It^{1/2}$ versus $\log t$ by a plateau with a constant value of $It^{1/2}$, as demonstrated in Fig. 4.4b. The transition time, t_{tr}, which is designated as an open circle in Fig. 4.4a, b, is determined as the time at which the current transient shows a transition from semi-infinite diffusion behavior (Cottrell behavior) to finite-length diffusion behavior (exponential decay of current with time). Defining the time constant for linear diffusion as $\tau_d = L^2/\widetilde{D}_H$, such a transition appears in a narrow time range near $t = 0.2\tau_d$ [35]. Figure 4.4c demonstrates the hydrogen concentration profile transients at ΔE_{jump} of 0.01 to 0.08 V, simultaneously calculated with the anodic current transients. Note that under the diffusion-control BC, the hydrogen concentration c_H at the electrode surface is fixed at zero, corresponding to E_{ext} over the whole hydrogen extraction time.

Equations 4.20 and 4.21 have been used for the estimation of the hydrogen diffusivity from the current transient experiments. For example, Ura et al. [25] used the current transient method to determine the diffusion coefficient of an $LaNi_5$ electrode. Figure 4.5a shows the typical anodic current-time response of an $LaNi_5$ alloy particle measured after the potential was jumped from -1.0 V for hydrogen injection to -0.1 V for hydrogen extraction. The current responses are divided into two time domains:

1. The short-time region ($t = 8$ to 60 s): I is proportional to $t^{-1/2}$ (Fig. 4.5b).
2. The long-time region: $\log I$ is proportional to t (Fig. 4.5c).

The diffusion coefficient was determined by applying Eq. 4.21 to the current response for the long-time region. The value of $\widetilde{D}_H$ obtained for the $LaNi_5$ alloy is 3.6×10^{-8} cm^2 s^{-1}, which is consistent with the values obtained by *NMR* measurements [36].

4.3.2 Rough Electrode Surface

Real electrode surfaces are not strictly flat, but are rather irregular and rough and, thus, hydrogen transport may be affected by the surface roughness. In fact, the classical theories for the diffusion kinetics at the flat electrode surface place a limitation on describing hydrogen diffusion toward a real electrode surface that is either rough or porous. By using fractal geometry, the current transient at a rough surface can be analyzed in terms of the generalized Cottrell equation under the diffusion-control BC [37–40]. More information on fractal geometry can be found in Chapter 9. According to the literature on the diffusion process toward fractal

Fig. 4.5 (**a**) Anodic current transient of an LaNi$_5$ alloy particle measured by jumping the potential from -1.0 V to -0.1 V. (**b**) I versus $t^{-1/2}$ plot in the short-time region and (**c**) log I versus t plot in the long-time region (Reprinted from Ura et al. [25], Copyright ©1995 with permission from Elsevier Science)
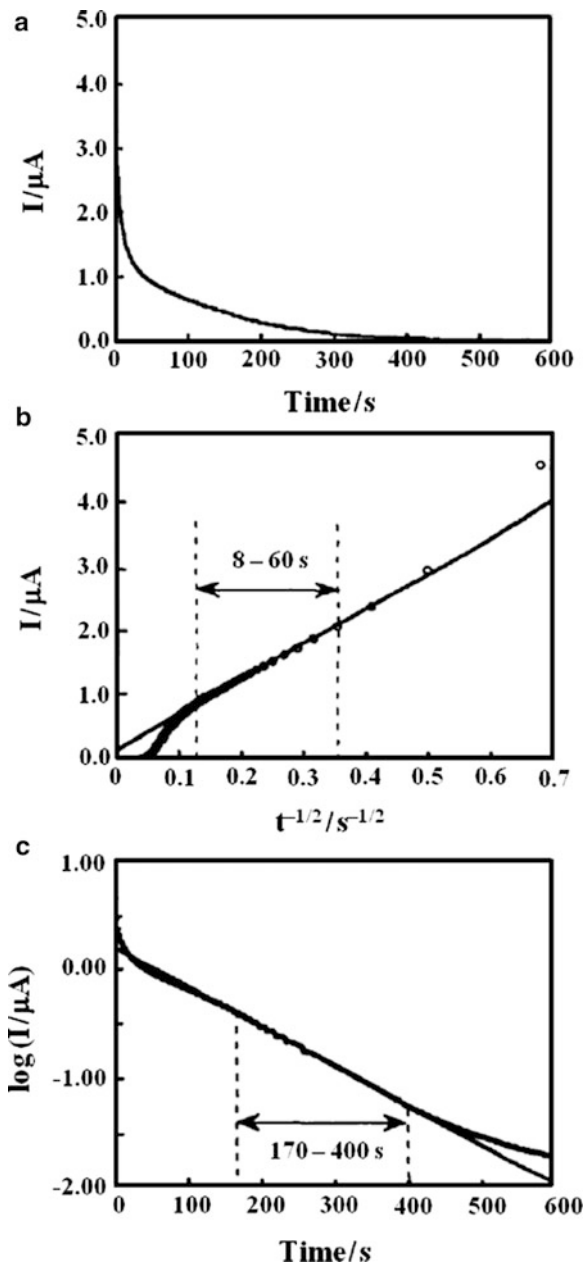
surfaces [37–40], the generalized Cottrell equation is valid for hydrogen transport through the fractal electrode:

$$I(t) \propto t^{-\alpha} \qquad \text{(generalized Cottrell equation)} \qquad (4.22)$$

with the exponent α that is solely determined by the fractal dimension of the surface $d_{F,ss}$,

$$\alpha = \frac{d_{F,ss} - d_E + 2}{2} \qquad (4.23)$$

where d_E is the dimension of the Euclidean space where the electrode is embedded ($d_E = 2$). It should be pointed out that Eq. 4.22 holds in a limited range of t between the temporal inner cutoff τ_i (crossover time required for the flat to fractal transition) and the temporal outer cutoff τ_o (crossover time needed for the fractal to flat transition) [38]. For diffusion-controlled hydrogen transport, τ_i and τ_o are exclusively determined by the spatial cutoffs and the hydrogen diffusivity.

The Weierstrass function $f_{WS}(y)$ has been widely used to model a rough surface and to generate a self-affine fractal profile with a desired fractal dimension [41]:

$$f_{WS}(y) = \sum_{k=1}^{N} b^{(d_{F,sa}-2)k} \cos(b^k y) \qquad (4.24)$$

where $d_{F,sa}$ denotes the self-affine fractal dimension of the function. Figure 4.6 shows the self-affine fractal profiles with $d_{F,sa} = 1.3$ and 1.5 modeled using $b = 1.5$ and $N = 50$ [42]. The fractal curve with $d_{F,sa} = 1.5$ appears to be more irregular and rougher than that curve with $d_{F,sa} = 1.3$. According to the theoretical and experimental works on a self-affine fractal surface by Pyun and coworkers [41, 43], atomic/ionic diffusion toward a self-affine fractal surface should be described in terms of the apparent self-similar fractal dimension rather than the self-affine fractal dimension. The self-similar fractal dimensions $d_{F,ss}$ of the self-affine fractal profiles of Fig. 4.6 were estimated to be 1.32 for $d_{F,sa} = 1.3$ and 1.47 for $d_{F,sa} = 1.5$ by using a triangulation method [43]. The spatial inner and outer cutoffs, λ_i and λ_o, for the fractal surface of Fig. 4.6 were evaluated to be ca. 0 and ca. 16, respectively.

The potentiostatic current transients for hydrogen transport through rough electrodes can be simulated using the kinetic Monte Carlo (MC) algorithm [42]. The MC method has been well established in many research works dealing with lithium transport through flat electrodes consisting of transition metal oxides [44, 45]. Full details of the simulation are described in a previous publication [42]. On the basis of the electrode potential curve in Fig. 4.2, the current transients were theoretically calculated under the diffusion-control BC by jumping $E_{ini} = 0.024$ V to $E_{ext} = 0.08$ V. Figure 4.7 illustrates the log I versus log t curves calculated from the flat electrode with $d_{F,ss} = 1.0$ and the fractal electrodes with $d_{F,ss} = 1.32$ and 1.47 [42]. The Monte Carlo step (MCS) on the x-axis was used as the unit of t. The current transients from the fractal electrodes show

Fig. 4.6 Self-affine fractal profiles generated by Weierstrass function (Reprinted from Lee and Pyun [42], Copyright ©2005 with permission from Elsevier Science)
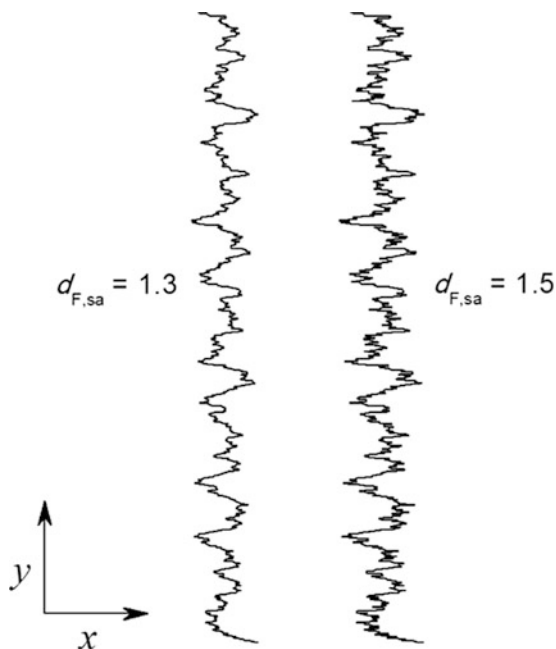
Fig. 4.7 log I versus log t curves calculated from the flat electrode with $d_{F,ss} = 1.0$ and the fractal electrodes with $d_{F,ss} = 1.32$ and 1.47. Note that the values of I for $d_{F,ss} = 1.32$ and 1.47 were multiplied by the factors 2.0 and 4.0, respectively (Reprinted from Lee and Pyun [42], Copyright ©2005 with permission from Elsevier Science)
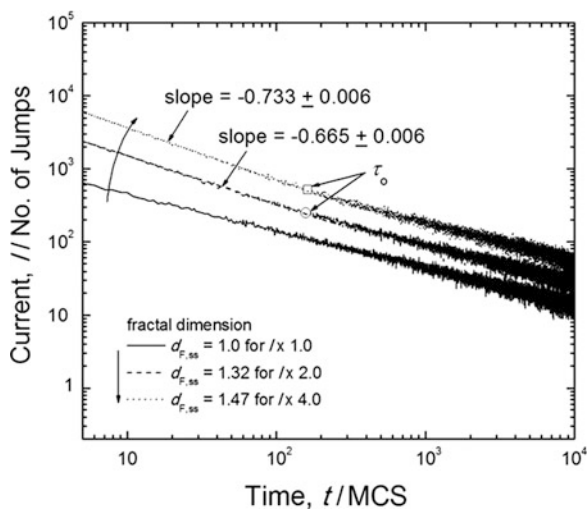
generalized Cottrell behavior at $t < \tau_o$ and conventional Cottrell behavior at $t > \tau_o$. The values of τ_o were determined to be approximately 160 MCS as well for both of the fractal electrodes, as shown in Fig. 4.7.

4.3.3   Effect of Diffusion Length Distribution

The composite electrode consists of particles with different sizes, and such particles have a size distribution. Even for a composite electrode with a narrow distribution of particle sizes, the cracking of the hydride particles during charge–discharge cycling may broaden the size distribution. According to Eq. 4.21, the diffusion length (particle size) L is one of the key parameters that determine the current transient. For simplicity, let us assume that all of the particles have the same electrochemical active area and that the diffusion length L takes a log-normal distribution $f(r)$ given by [46]

$$f(r) = \frac{1}{\sigma\sqrt{2\pi}} \exp\left[-\frac{(r-\mu)^2}{2\sigma^2}\right]$$ (4.25)

$$r = \ln\left(\frac{L}{L_o}\right)$$ (4.26)

where r denotes the natural logarithm of L divided by an arbitrary unit length L_o to obtain a dimensionless quantity and μ and σ represent the mean value and standard deviation of r, respectively.

If N particles are located in parallel and the current passing through each particle I is expressed by Eq. 4.27, then the total current I_{total} can be written as [46]

$$I_{total}(t) = N\int_{-\infty}^{\infty} f(r)I(t)\,\mathrm{d}r$$ (4.27)

where $Nf(r)\mathrm{d}r$ means the number of particles between r and $r + \mathrm{d}r$. Substituting $y = (r - \mu)/\sigma$ into Eqs. 4.25 and 4.27, one obtains

$$I_{total}(t) = \int_{-\infty}^{\infty} Nf(y)I(t)\mathrm{d}y = \int_{-\infty}^{\infty} I(t)\frac{N}{\sqrt{2\pi}}\exp\left(-\frac{y^2}{2}\right)\mathrm{d}y$$ (4.28)

Figure 4.8 demonstrates the log I versus log t curves theoretically calculated from Eq. 4.28 for various values of σ. The current transient computed with $\sigma = 0$ exhibits the ideal behavior predicted from Eqs. 4.20 and 4.21 in the short-time and long-time regions, respectively. However, the current transients calculated considering the diffusion length distribution deviate from such ideal behavior: As the value of σ increases, the absolute slope becomes larger than 0.5 in the short-time region, and the current decays more slowly in the long-time region. Remembering that the transition time t_{tr} for the semi-infinite diffusion behavior to the finite-length diffusion behavior is proportional to the square of the diffusion length L, it follows that the deviation of the current transient from the ideal behavior is attributable to the dispersion of t_{tr} that is caused by the diffusion length distribution.

Fig. 4.8 log I versus log
t curves calculated considering
the log-normal distribution of
particle sizes with various
values of standard deviation σ
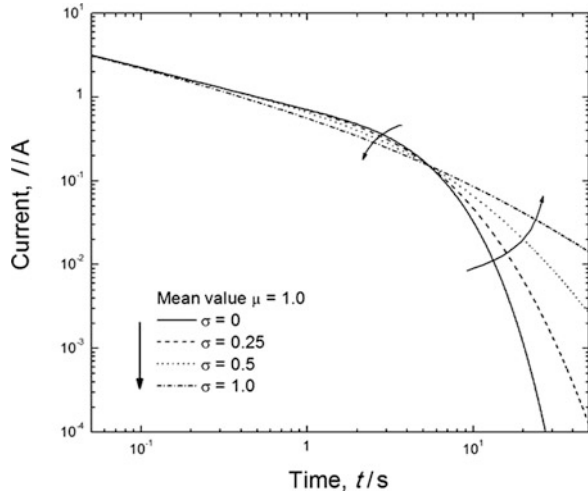
4.4   Diffusion-Controlled Hydrogen Transport in the Case Where Two Phases Coexist

During the hydrogen injection and extraction reactions, the hydride-forming electrode undergoes a phase transformation of the α-MH$_\delta$ phase to β-MH$_\delta$ phase and vice versa, respectively. When these two hydride phases coexist in the electrode, two regions with different concentrations of hydrogen are separated by a phase boundary and, thus, hydrogen transport involves the movement of the phase boundary, as schematically presented in Fig. 4.9 [47].

4.4.1   Diffusion-Controlled Phase Boundary Movement in the Case Where Two Phases Coexist

Wagner and Jost [48] provided useful mathematical approaches to the phase boundary movement in the case where two phases coexist, and then their model was implemented by Millet et al. [49] who studied hydrogen transport through a Pd electrode consisting of α-PdH$_\delta$ and β-PdH$_\delta$. Millet et al. [49] provided the exact, closed-form solutions to the problem of hydrogen transport under the diffusion-control BC at the electrode surface. When dealing with two-phase problems, one should have the two differential equations for the diffusion processes in the α-PdH$_\delta$ and β-PdH$_\delta$ phases,

$$\frac{\partial c_{H}^{\alpha}}{\partial t} = \tilde{D}_{H}^{\alpha} \frac{\partial^2 c_{H}^{\alpha}}{\partial x^2} \qquad \text{(in the } \alpha \text{ phase)} \qquad (4.29)$$

Fig. 4.9 Schematic diagram of hydrogen transport (charging and discharging) in the case where two phases co-exist (Reprinted from Cui et al. [47], Copyright ©2001 with permission from Elsevier Science)
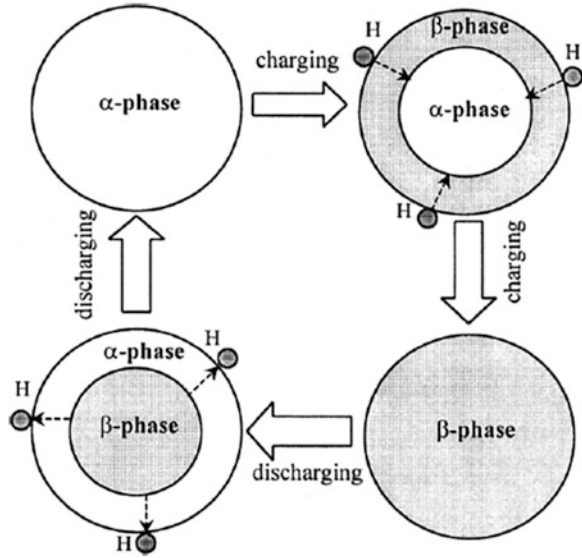
$$\frac{\partial c_H^\beta}{\partial t} = \tilde{D}_H^\beta \frac{\partial^2 c_H^\beta}{\partial x^2} \qquad \text{(in the } \beta \text{ phase)} \qquad (4.30)$$

where $\tilde{D}_H^\alpha$ and $\tilde{D}_H^\beta$ represent the hydrogen diffusivities in the α and β phases, respectively. The *IC* and *BC* are given as follows:

$$IC: c_H = c_H^o \qquad \text{for } 0 \leq x \leq L \text{ at } t = 0 \qquad (4.31)$$

$$BC: c_H = c_H^s \qquad \text{(diffusion} - \text{control } BC) \qquad (4.32)$$

$$\text{for } x = 0 \text{ at } t \geq 0$$

Let us assume that the interfacial reaction at the α/β phase boundary is very fast, so that the phase boundary movement is controlled by diffusion. In this case, the α phase with $c_H^{\alpha\beta}$ is in a quasi-equilibrium with the β phase with $c_H^{\beta\alpha}$ and hence the following *BC* is valid at the α/β phase boundary, $x = \xi$, during hydrogen extraction:

$$BC: c_H = c_H^{\alpha\beta} \qquad \text{for } x = \xi^- \text{ at } t \geq 0 \qquad (4.33)$$

$$c_H = c_H^{\beta\alpha} \qquad \text{for } x = \xi^+ \text{ at } t \geq 0 \qquad (4.34)$$

In the case where the α phase completely covers the surface of the β phase matrix, the location of the α/β phase boundary is represented by

$$\xi = 2\gamma\sqrt{\tilde{D}_H^\alpha t} \qquad (4.35)$$

where γ is a dimensionless parameter which is called the growth factor.

The Laplace transform of Eqs. 4.29 and 4.30 under the semi-infinite diffusion condition yields Eqs. 4.36 and 4.37 for the hydrogen concentrations c_H^α and c_H^β in the α and β phases, respectively:

$$c_H^\alpha(x, t) = c_H^s + \frac{c_H^{\alpha\beta} - c_H^s}{\operatorname{erf}(\gamma)} \operatorname{erf}\left(\frac{x}{2\sqrt{\widetilde{D}_H^\alpha t}}\right) \tag{4.36}$$

$$c_H^\beta(x, t) = c_H^o - \frac{c_H^o - c_H^{\beta\alpha}}{\operatorname{erfc}(\gamma\varphi^{-1/2})} \operatorname{erfc}\left(\frac{x}{2\sqrt{\widetilde{D}_H^\beta t}}\right) \tag{4.37}$$

where $\varphi = \widetilde{D}_H^\beta / \widetilde{D}_H^\alpha$. The flux balance for hydrogen at the α/β phase boundary is written as

$$(c_H^{\beta\alpha} - c_H^{\alpha\beta})\frac{\partial \xi}{\partial t} = \widetilde{D}_H^\alpha \left(\frac{\partial c_H^\alpha}{\partial x}\right)_{x=\xi^-} - \widetilde{D}_H^\beta \left(\frac{\partial c_H^\beta}{\partial x}\right)_{x=\xi^+} \tag{4.38}$$

The following equation is obtained by substituting Eqs. 4.36 and 4.37 into Eq. 4.38,

$$c_H^{\beta\alpha} - c_H^{\alpha\beta} = \frac{c_H^{\alpha\beta} - c_H^s}{\gamma\sqrt{\pi}\operatorname{erf}(\gamma)}\exp(-\gamma^2) - \frac{(c_H^o - c_H^{\beta\alpha})\varphi^{1/2}\exp(-\gamma^2/\varphi)}{\gamma\sqrt{\pi}\operatorname{erfc}(\gamma\varphi^{-1/2})} \tag{4.39}$$

Equation 4.39 allows us to determine the value of γ.

Figure 4.10 gives the typical hydrogen concentration profile transient under the semi-infinite diffusion condition calculated by jumping $E_{ini} = -0.01$ to $E_{ext} = 0.08$ V [32]. The parameters used are: $c_H = \delta$, $\widetilde{D}_H^\alpha = 1.2 \times 10^{-7}$ cm^2 s^{-1}, $\widetilde{D}_H^\beta = 1.2 \times 10^{-7}$ cm^2 s^{-1}, and $\gamma = 0.470$. According to Fick's first law, the current can be obtained as a function of time as follows:

$$I(t) = FA_{ea}\frac{c_H^{\alpha\beta} - c_H^s}{\operatorname{erf}(\gamma)}\left(\frac{\widetilde{D}_H^\alpha}{\pi t}\right)^{1/2} \tag{4.40}$$

Equation 4.40 indicates that the log I versus log t curve shows an absolute slope of 0.5, which is similar to the case of hydrogen transport through the electrode in the presence of a single phase. Such a relationship between I and $\sqrt{t}$ can be understood as follows: The velocity of the phase boundary movement $d\xi/dt$ decreases with the reciprocal of $\sqrt{t}$, as inferred from Eq. 4.35.

Fig. 4.10 Hydrogen concentration profile transients calculated based on Eq. 4.39 by jumping $E_{ini} = -0.01$ V to $E_{ext} = 0.08$ V (Reprinted from Lee and Pyun [32], Copyright ©2005 with permission from Elsevier Science)
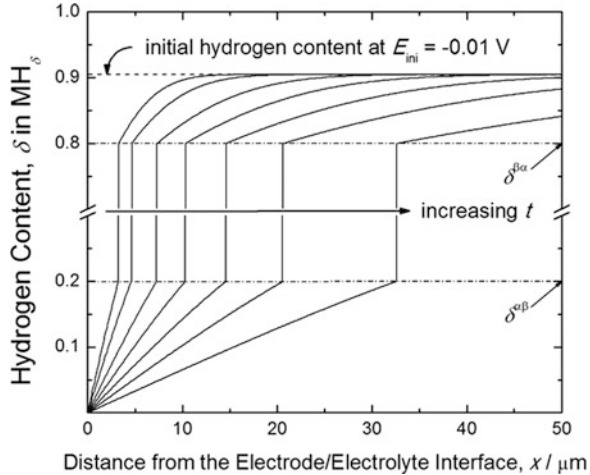
The model explained above has two critical limitations:

1. The α/β phase boundary moves toward $x = L$ with the velocity determined by Eq. 4.35 during hydrogen extraction. This implies that the flux leaving the phase boundary should always be much larger than that entering the phase boundary. Thus, the assumption of Eq. 4.35 is only valid for $\tilde{D}_H^\alpha >> \tilde{D}_H^\beta$, but it is unlikely to be realistic for most hydride electrodes. The values of $\tilde{D}_H^\alpha$ in hydride-forming metals, for example, a Pd electrode, are known to be about one-order of magnitude smaller than the values of $\tilde{D}_H^\beta$.
2. The decomposition process of the β phase that may occur at the beginning of hydrogen extraction is not completely discussed in the above model. For this reason, Eq. 4.40 has a limitation on describing the measured current transients, particularly in the short-time region.

4.4.2 Diffusion-Controlled Phase Boundary Movement Coupled with Boundary Pining

A modified model of hydrogen transport in a hydride-forming electrode in the case where two phases coexist is developed from the theoretical work by Shin and Pyun [50, 51]. A numerical method suggested by Murray and Landis [48] was used to solve the diffusion equation inside each phase on expanding grids in the growing α phase and contracting grids in the shrinking β phase. The following expressions are given for the change of the hydrogen concentration gradients across the α phase

$$\frac{\partial c_H^\alpha(n)}{\partial t} = \tilde{D}_H^\alpha \frac{\partial^2 c_H^\alpha(n)}{\partial x(n)^2} + \frac{\partial c_H^\alpha(n)}{\partial x(n)} \frac{x(n)}{\xi} \frac{d\xi}{dt} \tag{4.41}$$

$$\text{for } 0 < x(n) < \xi, n = 2, 3, \ldots, r-1$$

and across the β phase

$$\frac{\partial c_H^\beta(n)}{\partial t} = \tilde{D}_H^\beta \frac{\partial^2 c_H^\beta(n)}{\partial x(n)^2} + \frac{\partial c_H^\beta(n)}{\partial x(n)} \frac{L - x(n)}{L - \xi} \frac{d\xi}{dt} \tag{4.42}$$

$$\text{for } \xi < x(n) < L, n = r+1, r+2, \ldots, N$$

where $c_H(n)$ is the hydrogen concentration at the n-th grid point and $x(n)$ is the position of the n-th grid point. In order to describe in more detail the decomposition process of the β phase at the beginning of hydrogen extraction, the concept of "pinning" of the α/β phase boundary is introduced. This assumes that the α/β phase boundary is pinned at the location $x = L_{pin}$ close to the electrode/electrolyte interface, between the α phase completely covering the whole β matrix surface and the matrix β phase until the flux leaving the α/β phase boundary exceeds that entering the α/β phase boundary. Then, the IC is modified to reflect the pinning limitation as follows:

$$IC: c_H = c_H^s + c_H^{\alpha\beta} \frac{x}{L_{pin}} \qquad \text{for } 0 \le x \le L_{pin} \text{ at } t = 0 \tag{4.43}$$

$$c_H = c_H^o \qquad \text{for } L_{pin} \le x \le L \text{ at } t = 0 \tag{4.44}$$

The BCs at $x = 0$, ξ^- and ξ^+ are given by Eqs. 4.32, 4.33, and 4.34, respectively. The phase boundary begins to move at the time when the value of c_H^β at $x = \xi^+$ reaches the maximum solubility limit of hydrogen $c_H^{\beta\alpha}$ in the β phase. From this time on, the flux leaving the phase boundary always exceeds that entering the phase boundary and hence the α/β phase boundary continues to move toward $x = L$. When the α/β phase boundary reaches $x = L$, it disappears and, then, hydrogen extraction proceeds by hydrogen diffusion in the single α phase.

Figure 4.11a demonstrates the log I versus log t curve calculated by jumping $E_{ini} = -0.01$ V to $E_{ext} = 0.08$ V [32]. The anodic current transient was simulated with $L_{pin} = 0.05$ cm. The hydrogen concentration profile transient simultaneously calculated with the anodic current transient is also presented in Fig. 4.11b. The simulated current transient exhibits three-stage behavior:

1. A current plateau in the time interval between $t = 0$ and $t = t_{tr(1)}$
2. An upward concave shape to $t = t_{tr(2)}$
3. A rapid decay of current with time

During the first, second, and third stages of the simulated current transient, the corresponding concentration profile runs can be divided into three stages:
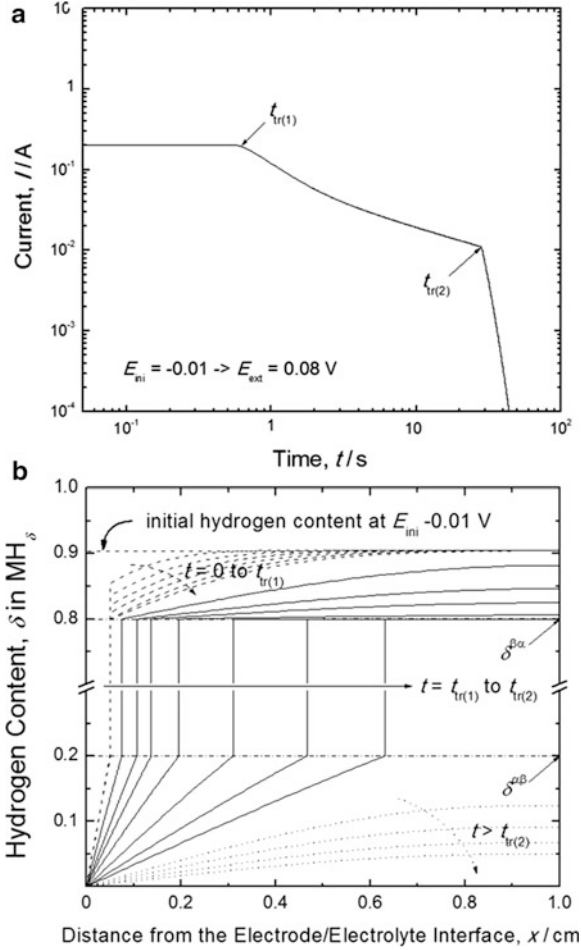
1. The pinning of the α/β phase boundary
2. The α/β phase boundary movement
3. Hydrogen extraction from the single α phase.

   Figure 4.12 displays the anodic current transients experimentally obtained from the LaNi$_5$ electrode in 6 M KOH solution [52]. The log I versus log t curve is composed of a current plateau and then an upward concave curve, followed by a sudden fall of current with time. Furthermore, the duration of the current plateau in the first stage was found to be extended with increasing hydrogen preinjection time. The theoretically calculated anodic current transient shown in Fig. 4.11a is in good agreement with the experimentally measured one shown in Fig. 4.12. This means that hydrogen extraction proceeds by a mechanism involving the α/β phase boundary pinning and the diffusion-controlled phase boundary movement. Considering that the higher the initial hydrogen concentration c_H^o in the β phase, the longer the

Fig. 4.12 Anodic current transients experimentally measured on the LaNi$_5$ electrode in 6 M KOH solution (Reprinted from Pyun et al. [52], Copyright ©1997 with permission from Elsevier Science)
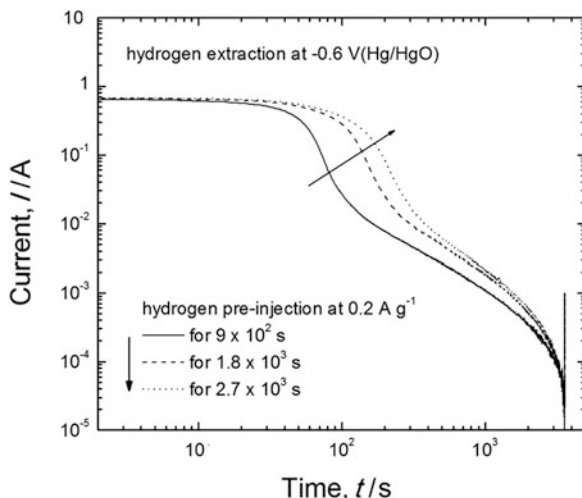
time necessary until the value of c_H^β reaches $c_H^{\beta\alpha}$, the increase in the duration of the current plateau with increasing hydrogen preinjection time in the measured current transient of Fig. 4.12 can be accounted for in terms of the increased value of c_H^o. The slight discrepancy between the simulated and measured current transients observed around $t = t_{tr(1)}$ and $t = t_{tr(2)}$ can be attributed to the nonuniform size distribution of LaNi$_5$ particles in the composite electrode [53].

References

1. Yang TH, Pyun SI (1996) An investigation of the hydrogen absorption reaction into, and the hydrogen evolution reaction from, a Pd foil electrode. J Electroanal Chem 414:127–133
2. Montella C (1999) Discussion on permeation transients in terms of insertion reaction mechanism and kinetics. J Electroanal Chem 465:37–50
3. Conway BE, Jerkiewicz G (1993) Thermodynamic and electrode kinetic factors in cathodic hydrogen sorption into metals and its relationship to hydrogen adsorption and poisoning. J Electroanal Chem 357:47–66
4. Bockris JOM, McBreen J, Nanis L (1965) The hydrogen evolution kinetics and hydrogen entry into α-iron. J Electrochem Soc 112:1025–1031
5. Kim CD, Wilde BE (1971) The kinetics of hydrogen absorption into iron during cathodic hydrogen evolution. J Electrochem Soc 118:202–206
6. Hitz C, Lasia A (2002) Determination of the kinetics of the hydrogen evolution reaction by the galvanostatic step technique. J Electroanal Chem 532:133–140
7. Bolzán AE (1995) Phenomenological aspects related to the electrochemical behaviour of smooth palladium electrodes in alkaline solutions. J Electroanal Chem 380:127–138
8. Deng B, Li Y, Wang R, Fang S (1999) Two reduction processes for hydrogen adsorption and absorption at MmNi$_5$-type alloy electrodes. Electrochim Acta 44:2853–2857
9. Han JN, Lee JW, Seo M, Pyun SI (2001) Analysis of stresses generated during hydrogen transport through a Pd foil electrode under potential sweep conditions. J Electroanal Chem 506:1–10

10. Gamboa SA, Sebastian PJ, Feng F, Geng M, Northwood DO (2002) Cyclic voltammetry investigation of a metal hydride electrode for nickel metal hydride batteries. J Electrochem Soc 149:A137–A139

11. Lim C, Pyun SI (1993) Theoretical approach to faradaic admittance of hydrogen absorption reaction on metal membrane electrode. Electrochim Acta 38:2645–2652

12. Lim C, Pyun SI (1994) Impedance analysis of hydrogen absorption reaction on Pd membrane electrode in 0.1 M LiOH solution under permeable boundary conditions. Electrochim Acta 39:363–373

13. Zhang W, Sridhar Kumar MP, Srinivasan S (1995) Ac impedance studies on metal hydride electrodes. J Electrochem Soc 142:2935–2943

14. Yang TH, Pyun SI (1996) Hydrogen absorption and diffusion into and in palladium: ac-impedance analysis under impermeable boundary conditions. Electrochim Acta 41:843–848

15. Yang TH, Pyun SI (1996) A study of hydrogen absorption reaction into α- and β-LaNi$_5$H$_x$ porous electrodes by using electrochemical impedance spectroscopy. J Power Sources 62:175–178

16. Wang C (1998) Kinetic behavior of metal hydride electrode by means of ac impedance. J Electrochem Soc 145:1801–1812

17. Montella C (1999) Review and theoretical analysis of ac–av methods for the investigation of hydrogen insertion I. Diffusion formalism. J Electroanal Chem 462:73–87

18. Montella C (2000) Review and theoretical analysis of ac–av methods for the investigation of hydrogen insertion: part II. Entry side impedance, transfer function and transfer impedance formalism. J Electroanal Chem 480:150–165

19. Montella C (2000) Review and theoretical analysis of ac–av methods for the investigation of hydrogen insertion: part III. Comparison of entry side impedance, transfer function and transfer impedance methods. J Electroanal Chem 480:166–185

20. Yuan X, Xu N (2002) Electrochemical and hydrogen transport kinetic performance of MlNi$_{3.75}$Co$_{0.65}$Mn$_{0.4}$Al$_{0.2}$ metal hydride electrodes at various temperatures. J Electrochem Soc 149:A407–A413

21. Georén P, Hjelm AK, Lindbergh G, Lundqvist A (2003) An electrochemical impedance spectroscopy method applied to porous LiMn$_2$O$_4$ and metal hydride battery electrodes. J Electrochem Soc 150:A234–A241

22. Haran BS, Popov BN, White RE (1998) Theoretical analysis of metal hydride electrodes: studies on equilibrium potential and exchange current density. J Electrochem Soc 145:4082–4090

23. Feng F, Ping X, Zhou Z, Geng M, Han J, Northwood DO (1998) The relationship between equilibrium potential during discharge and hydrogen concentration in a metal hydride electrode. Int J Hydrog Energy 23:599–602

24. Conway BE, Wojtowicz J (1992) Time-scales of electrochemical desorption and sorption of H in relation to dimensions and geometries of host metal hydride electrodes. J Electroanal Chem 326:277–297

25. Ura H, Nishina T, Uchida I (1995) Electrochemical measurements of single particles of Pd and LaNi$_5$ with a microelectrode technique. J Electroanal Chem 396:169–173

26. Nishina T, Ura H, Uchida I (1997) Determination of chemical diffusion coefficients in metal hydride particles with a microelectrode technique. J Electrochem Soc 144:1273–1277

27. Kim HS, Nishizawa M, Uchida I (1999) Single particle electrochemistry for hydrogen storage alloys, MmNi$_{3.55}$Co$_{0.75}$Mn$_{0.4}$Al$_{0.3}$. Electrochim Acta 45:483–488

28. Feng F, Han J, Geng M, Northwood DO (2000) Study of hydrogen transport in metal hydride electrodes using a novel electrochemical method. J Electroanal Chem 487:111–119

29. Kim HS, Itoh T, Nishizawa M, Mohamedi M, Umeda M, Uchida I (2002) Microvoltammetric study of electrochemical properties of a single spherical nickel hydroxide particle. Int J Hydrog Energy 27:295–300

30. Levi MD, Aurbach D (1999) Frumkin intercalation isotherm – a tool for the description of lithium insertion into host materials: a review. Electrochim Acta 45:167–185

31. Tsirlina GA, Levi MD, Petrii OA, Aurbach D (2001) Comparison of equilibrium electrochemical behavior of PdH_x and $Li_xMn_2O_4$ intercalation electrodes in terms of sorption isotherms. Electrochim Acta 46:4141–4149
32. Lee JW, Pyun SI (2005) Anomalous behaviour of hydrogen extraction from hydride-forming metals and alloys under impermeable boundary conditions. Electrochim Acta 50:1777–1850
33. Weppner W, Huggins RA (1977) Determination of the kinetic parameters of mixed-conducting electrodes and application to the system Li_3Sb. J Electrochem Soc 124:1569–1578
34. Wen CJ, Boukamp BA, Huggins RA (1976) Thermodynamic and mass transport properties of "LiAl". J Electrochem Soc 126:2258–2266
35. Montella C (2002) Discussion of the potential step method for the determination of the diffusion coefficients of guest species in host materials: part I, Influence of charge transfer kinetics and ohmic potential drop. J Electroanal Chem 518:61–83
36. Sakai T, Oguro K, Miymura H, Kuriyama N, Kato A, Ishikawa H, Iwakura C (1990) Some factors affecting the cycle lives of $LaNi_5$-based alloy electrodes of hydrogen batteries. J Less Common Met 161:193–202
37. Nyikos L, Pajkossy T (1986) Diffusion to fractal surfaces. Electrochim Acta 31:1347–1350
38. Pajkossy T (1991) Electrochemistry at fractal surfaces. J Electroanal Chem 300:1–11
39. Pajkossy T, Borosy AP, Imre A, Martemyanov SA, Nagy G, Schiller R, Nyikos L (1994) Diffusion kinetics at fractal electrodes. J Electroanal Chem 366:69–73
40. Dassas Y, Duby P (1995) Diffusion toward fractal interfaces: potentiostatic, galvanostatic, and linear sweep voltammetric techniques. J Electrochem Soc 142:4175–4180
41. Shin HC, Pyun SI, Go JY (2002) A study on the simulated diffusion-limited current transient of a self-affine fractal electrode based upon the scaling property. J Electroanal Chem 531:101–109
42. Lee JW, Pyun SI (2005) A study on the potentiostatic current transient and linear sweep voltammogram simulated from fractal intercalation electrode: diffusion coupled with interfacial charge transfer. Electrochim Acta 50:1947–1955
43. Go JY, Pyun SI, Hahn YD (2003) A study on ionic diffusion towards self-affine fractal electrode by cyclic voltammetry and atomic force microscopy. J Electroanal Chem 549:49–59
44. Kim SW, Pyun SI (2002) Lithium transport through a sol–gel derived $LiMn_2O_4$ film electrode: analyses of potentiostatic current transient and linear sweep voltammogram by Monte Carlo simulation. Electrochim Acta 47:2843–2855
45. Jung KN, Pyun SI, Kim SW (2003) Thermodynamic and kinetic approaches to lithium intercalation into $Li[Ti_{5/3}Li_{1/3}]O_4$ film electrode. J Power Sources 119–121:637–643
46. Diard JP, Gorrec L, Montella C (2001) Influence of particle size distribution on insertion processes in composite electrodes. Potential step and EIS theory: part I. Linear diffusion. J Electroanal Chem 499:67–77
47. Cui N, Luo JL, Chuang KT (2001) Study of hydrogen Diffusion in α- and β-phase hydrides of Mg_2Ni alloy by microelectrode technique. J Electroanal Chem 503:92–98
48. Jost W (1960) Diffusion in solids, liquids, gases. Academic, New York
49. Millet P, Srour M, Faure R, Durand R (2001) A study of the hydrogen absorption and desorption reactions in palladium electrodes using the potential step method. Electrochem Commun 3:478–482
50. Shin HC, Pyun SI (1999) An investigation of the electrochemical intercalation of lithium into a $Li_{1-\delta}CoO_2$ electrode based upon numerical analysis of potentiostatic current transients. Electrochim Acta 44:2235–2244
51. Shin HC, Pyun SI (1999) The kinetics of lithium transport through $Li_{1-\delta}CoO_2$ by theoretical analysis of current transient. Electrochim Acta 45:489–501
52. Pyun SI, Han JN, Yang TH (1997) Performance evaluation of $LaNi_{4.7}Al_{0.3}$ and $LaNi_5$ electrodes used as anodes in nickel/metal hydride secondary batteries by analysis of current transients. J Power Sources 65:9–13
53. Lundqvist A, Lindbergh G (1999) Kinetic study of a porous metal hydride electrode. Electrochim Acta 44:2523–2542

Chapter 5
Hydrogen Trapping Inside Metals and Metal Oxides

The anomalous behavior of hydrogen in terms of its solubility and diffusivity in metals and oxides has been the subject of repeated investigations [1–6]. The diffusion coefficients of hydrogen in metals reported in the literature have usually been determined under the assumption that the hydrogen concentration is governed by Fick's law. Figure 5.1 summarizes some of the experimental data on the diffusivity of hydrogen reported in the literature [1]. It should be noted that small values of the diffusion coefficient were obtained for work-hardened samples (designated as curves 6). Figure 5.1 indicates that the diffusion coefficient is a function of other variables besides the temperature and that these neglected variables are in some way related to the work hardening experienced by the specimen. There are, therefore, some doubts about the validity of Fick's law and the simple physical model of random motion through the electrode.

Real metals are known to contain structural defects, e.g., dislocations, grain boundaries, microcracks, and internal interfaces, which can act as trap sites for hydrogen atoms. These trap sites deepen the potential well, and thus, a trapped hydrogen atom must acquire an activation energy larger than the energy for normal lattice diffusion to escape a trap site. The mean residence time of a diffusing hydrogen atom is significantly longer in a trap site than in a normal lattice site, resulting in the substantial decrease of the apparent diffusivity [7]. Darken and Smith [8] first suggested that hydrogen diffusion is impeded by lattice imperfections in cold-worked steel. They treated the diffusion process of hydrogen with trapping in a way analogous to the problem of oxygen diffusion into copper containing small amounts of silicon with which it could be trapped in the form of SiO_2. McNabb and Foster [1] developed a more general modelistic formulation for the phenomenon of hydrogen diffusion with accompanying trapping at one kind of trap. Oriani [9] later reformulated the work of McNabb and Foster using the assumption of a local equilibrium between the hydrogen atoms in the normal lattice sites and trap sites. He applied this concept to obtain the trap density in steels from hydrogen charging or

Fig. 5.1 Literature data for the diffusion coefficient of hydrogen in iron and steels (Reprinted from McNabb and Foster [1], Copyright ©1963 with permission from AIME)
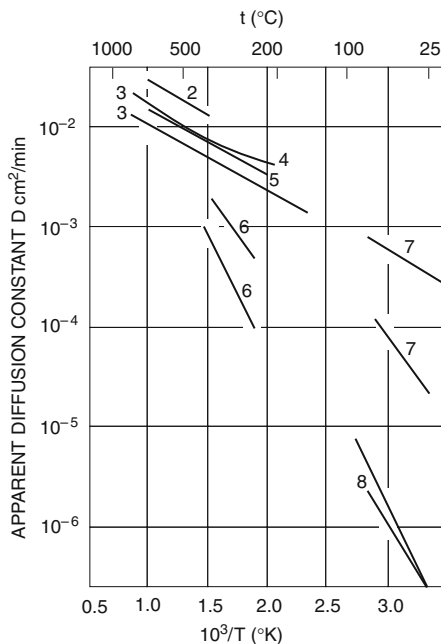
permeation measurements. Iino [10, 11] considered irreversible trapping when analyzing the hydrogen permeation data, and then, Leblond and Dubois [12, 13] studied the combined effects of reversible and irreversible trappings on hydrogen transport.

5.1   Hydrogen Trapping in Insertion Electrodes: Modified Diffusion Equation

The physical model introduced in this chapter assumes the following:

1. The hydrogen atoms wander in a random manner through the metal.
2. Trap sites are regarded as potential wells of significantly greater depth than those encountered in normal lattice sites (no assumptions are made concerning their nature or origin).
3. There are two types of traps: reversible and irreversible trap sites.
4. The trap sites are uniformly distributed throughout the metal.
5. Hydrogen atoms tend to get trapped or delayed at trap sites.
6. The trap sites do not form an extended network.
7. Hydrogen transport between trap sites occurs by normal lattice diffusion.

A model for the reversible and irreversible trap sites is schematically presented in Fig. 5.2.
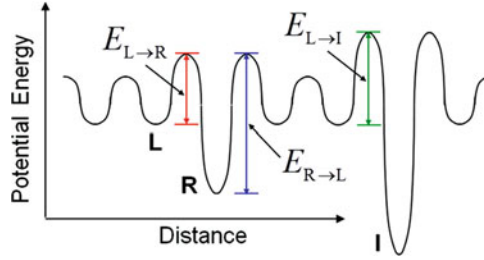
Fig. 5.2 Schematic diagram of reversible and irreversible trap sites for hydrogen in a metal. *L, R* and *I* represent a normal lattice site, a reversible trap site and an irreversible trap site, respectively

Hydrogen transport through the electrode in the presence of trap sites can be described by the modified Fick's diffusion equation [1, 14]:

$$\tilde{D}_H \frac{\partial^2 c_H}{\partial x^2} = \frac{\partial c_H}{\partial t} + N_r \frac{\partial f_r}{\partial t} + N_i \frac{\partial f_i}{\partial t} \tag{5.1}$$

$$\frac{\partial f_r}{\partial t} = k_r c_H (1 - f_r) - p_r f_r \tag{5.2}$$

$$\frac{\partial f_i}{\partial t} = k_i c_H (1 - f_i) \tag{5.3}$$

where c_H is the hydrogen concentration, $\tilde{D}_H$ the chemical diffusivity of hydrogen (see Chap. 4), x the distance from the electrode/electrolyte interface, t the hydrogen diffusion time, N the total trap concentration, f the fraction of trap sites that are occupied, and the subscripts r and i refer to the reversible and irreversible trap sites, respectively. k_r and p_r are the capture rate and release rate for a reversible trap site, respectively, and k_i means the irreversible trap strength. It is assumed that the electrode contains a very low fraction of trap sites occupied, i.e., f_r and $f_i \ll 1$. Then, Eqs. 5.2 and 5.3 reduce to Eqs. 5.4 and 5.5, respectively:

$$\frac{\partial f_r}{\partial t} = k_r c_H - p_r f_r \tag{5.4}$$

$$\frac{\partial f_i}{\partial t} = k_i c_H \tag{5.5}$$

When treating complicated mathematical problems, it is convenient to use dimensionless variables as follows:

$$C = c_H / c_H^o \tag{5.6}$$

$$X = x / L \tag{5.7}$$

$$T = \tilde{D}_\mathrm{H} t / L^2 \tag{5.8}$$

$$V = N_\mathrm{t} f_\mathrm{r} / c_\mathrm{H}^\mathrm{o} \tag{5.9}$$

$$W = N_\mathrm{i} f_\mathrm{i} / c_\mathrm{H}^\mathrm{o} \tag{5.10}$$

$$\lambda = k_\mathrm{r} N_\mathrm{r} L^2 / \tilde{D}_\mathrm{H} \tag{5.11}$$

$$\mu = p_\mathrm{r} L^2 / \tilde{D}_\mathrm{H} \tag{5.12}$$

$$\kappa = k_\mathrm{i} N_\mathrm{i} L^2 / \tilde{D}_\mathrm{H} \tag{5.13}$$

Now Eqs. 5.1, 5.4, and 5.5 are written as

$$\frac{\partial^2 C}{\partial X^2} = \frac{\partial C}{\partial T} + \frac{\partial V}{\partial T} + \frac{\partial W}{\partial T} \tag{5.14}$$

$$\frac{\partial V}{\partial T} = \lambda C - \mu V \tag{5.15}$$

$$\frac{\partial W}{\partial T} = \kappa C \tag{5.16}$$

5.2 Hydrogen Trapping Determined by Current Transient Technique

We now consider the current transient behavior of hydrogen transport in the presence of traps based on the modified diffusion equation, Eqs. 5.14, 5.15, and 5.16. We assume that the diffusion-control boundary condition (BC) is effective at the electrode surface (see Chap. 4). The initial condition (IC) and BCs for hydrogen extraction from the electrode are given by

$$IC: C = 1, \ V = V^\mathrm{o}, \ W = W^\mathrm{o} \quad \text{for } 0 \leqslant X \leqslant 1 \text{ at } T = 0 \tag{5.17}$$

$$BC: C = C^\mathrm{S} (\text{diffusion} - \text{control } BC) \text{ for } X = 0 \text{ at } T \geqslant 0 \tag{5.18}$$

$$\left(\frac{\partial C}{\partial X} \right) = 0 (\text{impermeable } BC) \text{ for } X = 1 \text{ at } T \geqslant 0 \tag{5.19}$$

where $C^\mathrm{S} = c_\mathrm{H}^\mathrm{s} / c_\mathrm{H}^\mathrm{o}$, $V^\mathrm{o} = N_\mathrm{t} f_\mathrm{r}^\mathrm{o} / c_\mathrm{H}^\mathrm{o}$ and $W^\mathrm{o} = N_\mathrm{i} f_\mathrm{i}^\mathrm{o} / c_\mathrm{H}^\mathrm{o}$. Here, f^o denotes the initial fraction of trap sites that are occupied in the electrode.

Applying the Laplace transformation to Eqs. 5.14, 5.15, 5.16, 5.17, 5.18, and 5.19 followed by the inverse Laplace transformation, the solution of Eq. 5.14 is given by

$$
C = \sum_{n=0}^{\infty} (-1)^n \frac{s_n^+ + 2\mu}{s_n^+ - \mu} \frac{2\cos\left[\left(n+\frac{1}{2}\right)\pi X\right]}{\left[1 + \dfrac{\lambda\mu}{\left(s_n^+ - \mu\right)^2}\right]} e^{-s_n^+ T}
$$

$$
+ \sum_{n=0}^{\infty} (-1)^n \frac{s_n^- + 2\mu}{s_n^- - \mu} \frac{2\cos\left[\left(n+\frac{1}{2}\right)\pi X\right]}{\left(n+\frac{1}{2}\right)\pi\left[1 + \dfrac{\lambda\mu}{\left(s_n^- - \mu\right)^2}\right]} e^{-s_n^- T} \tag{5.20}
$$

$$
s_n^{\pm} = \frac{1}{2}\left\{\left[\lambda + \mu + \kappa + \left(n+\frac{1}{2}\right)^2 \pi^2\right]\right.
$$

$$
\left. \pm \sqrt{\left[\lambda + \mu + \kappa + \left(n+\frac{1}{2}\right)^2 \pi^2\right]^2 - 4\mu\left[\kappa + \left(n+\frac{1}{2}\right)^2 \pi^2\right]}\right\} \tag{5.21}
$$

By differentiating C with respect to X and letting $X = 1$, we obtain a reduced hydrogen flux as follows:

$$
j(T) = -\sum_{n=0}^{\infty} \frac{s_n^+ + 2\mu}{s_n^+ - \mu} \frac{2}{\left[1 + \dfrac{\lambda\mu}{\left(s_n^+ - \mu\right)^2}\right]} e^{-s_n^+ T}
$$

$$
- \sum_{n=0}^{\infty} \frac{s_n^- + 2\mu}{s_n^- - \mu} \frac{2}{L\left[1 + \dfrac{\lambda\mu}{\left(s_n^- - \mu\right)^2}\right]} e^{-s_n^- T} \tag{5.22}
$$

Equation 5.22 is the general flux-time relation for hydrogen transport through an electrode with a low hydrogen concentration having reversible and irreversible traps of one kind.

The anodic current transients were calculated from the modified diffusion equations using the virtual electrode potential curve described in Chap. 4 (Fig. 4.2). Figure. 5.3a–c illustrates the log (current I) versus log (time t) curves simulated in the presence of only reversible trap sites as functions of the capture rate λ, the release rate μ, and the relative trap concentration V° initially occupied in the electrode, respectively [15]. The current transients were calculated by jumping $E_{ini} = 0.01$ V to $E_{ext} = 0.08$ V. For comparison, the anodic current transient for hydrogen transport in the absence of any trap sites is plotted, and it shows simple

Fig. 5.3 log I versus log t curves simulated in the presence of reversible trap sites as functions of (**a**) the capture rate λ, (**b**) the release rate μ and (**c**) the relative trap concentration V^o initially occupied in the electrode (Reprinted from Lee and Pyun [15], Copyright ©2005 with permission from Elsevier Science)
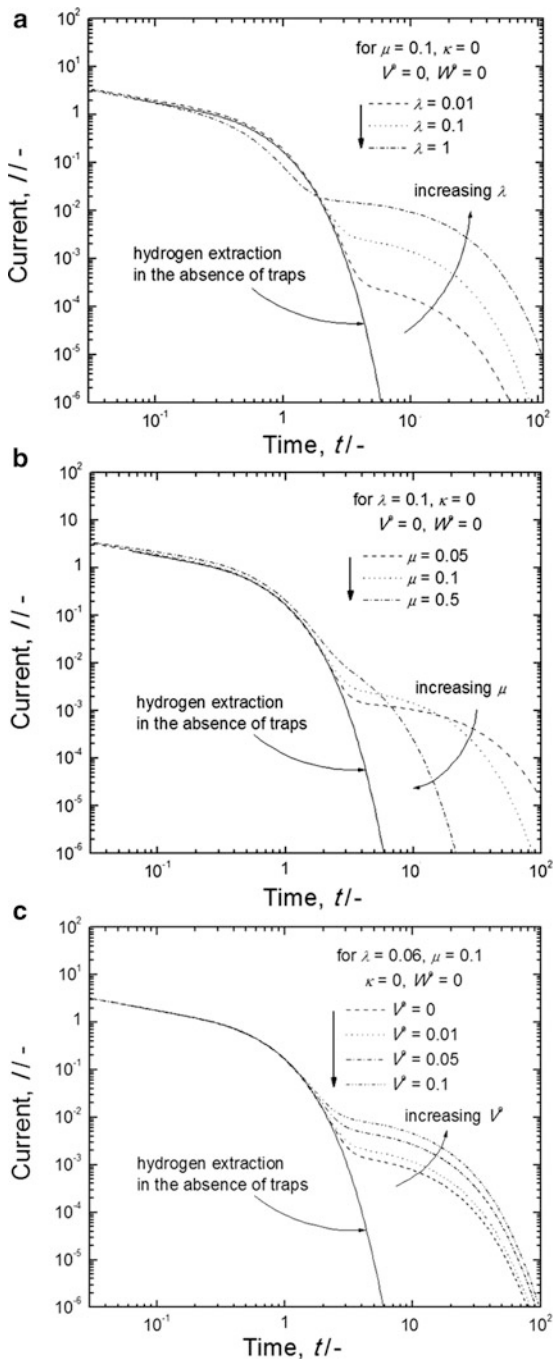
two-stage behavior, which is typical of the diffusion-control model (see Chap. 4). The current transients for hydrogen transport in the presence of reversible trap sites show an additional downward concave curve in the long-time region, i.e., three-stage shape. The results may be summarized as follows:

1. The first and second stages remain unchanged regardless of the values of λ, μ, and V^o.
2. The duration of the third stage is prolonged with increasing λ at a constant value of μ (Fig. 5.3a).
3. The duration of the third stage is prolonged with decreasing μ at a constant value of λ (Fig. 5.3b).
4. As the value of V^o increases, the current level of the third stage increases and the duration of the third stage is prolonged (Fig. 5.3c).

The mean residence time of a diffusing hydrogen atom is considerably longer in a trap site than in a normal lattice site, and thus, the hydrogen atoms residing in normal lattice sites should be extracted first, followed by those in trap sites. Therefore, the first and second stages of the anodic current transient results mostly from hydrogen extraction from normal lattice sites, and the third stage reflects the extraction of hydrogen from reversible trap sites. The relative trap concentration profiles at various reduced times T are presented in Fig. 5.4 [14]. During hydrogen extraction, the hydrogen concentration across the electrode should decrease monotonically with time, regardless of the absence or presence of trap sites. However, Fig. 5.4 shows that the trap concentration across the electrode increases with increasing T up to $T = 2$ and then decreases. This indicates that the hydrogen atoms are extracted from the interstitial sites and trap sites and/or the hydrogen atoms are trapped and re-trapped in the initial stage. Note that the reduced time below $T = 2$ in Fig. 5.4 corresponds to the first and second stages of the current transient in Fig. 5.3, indicating that the current transient is affected very little by reversible trapping, due to the combined actions of trapping and re-trapping. By contrast, the reduced time above $T = 3$ in Fig. 5.4 corresponds to the third stage, which confirms the release of the trapped and re-trapped hydrogen atoms.

Figure 5.5 demonstrates the combined effect of reversible and irreversible traps on the hydrogen transport [15]. The anodic current transients were numerically calculated by jumping $E_{ini} = 0.01$ V to $E_{ext} = 0.08$ V for various values of the irreversible trap strength, κ. Here, we assume that all of the irreversible trap sites are initially empty, i.e., $W^o = 0$, as in the study of irreversible hydrogen trapping under permeable boundary conditions by Iino [10, 11]. If all of the irreversible trap sites are initially occupied, the irreversible hydrogen trapping does not affect the anodic current transient at all. This is because the irreversible trap sites are not capable of releasing hydrogen over the whole time period. In the presence of irreversible trap sites, the total number of diffusing hydrogen atoms does not remain constant. As κ increases from 0.1 to 10, therefore, the slope of the first stage of the anodic current transient deviates negatively from -0.5, and the current levels in all of the stages are reduced.

Figure 5.6 gives the exemplary log I versus log t curves that show the effect of hydrogen trapping on the hydrogen transport [16]. The anodic current transients

Fig. 5.4 Relative trap
concentration profiles across
the electrode at various
reduced times T (Reprinted
from Pyun and Yang [14],
Copyright ©1998 with
permission from Elsevier
Science)
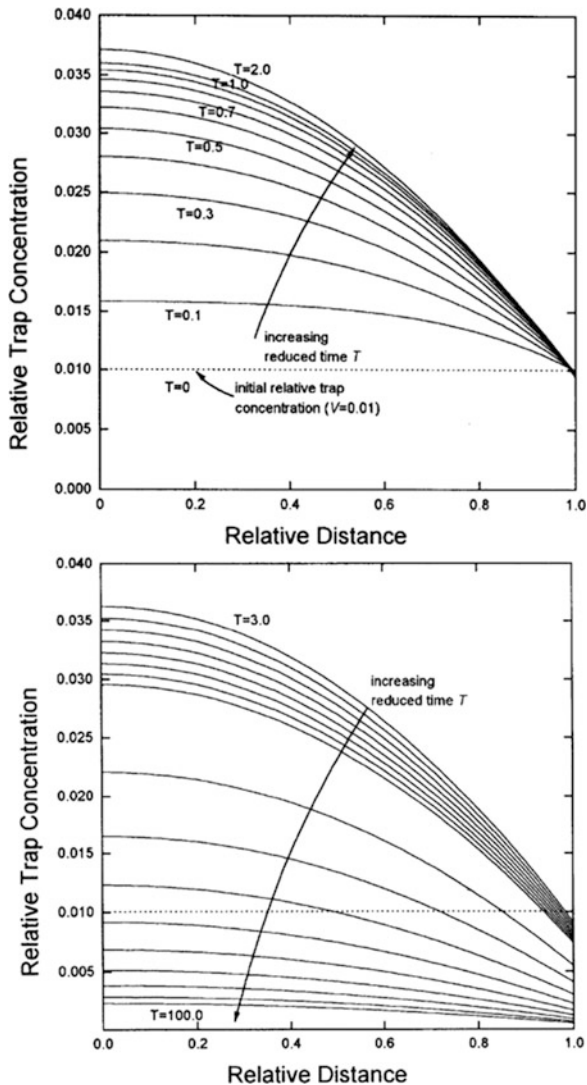
(plotted in terms of the reduced current) were experimentally measured on a Pd
electrode in 0.1 M NaOH solution. The reduced current was defined as the
measured anodic current I divided by the total anodic charge Q_{total} transferred
during hydrogen extraction. Hydrogen was previously injected into the electrode
at $E_{ini} = 0.02$–0.1 V(RHE), and then E_{ini} was jumped to $E_{ext} = 0.9$ V(RHE).
The anodic current transient from the electrode precharged with hydrogen at $E_{ini} = 0.1$
V(RHE) exhibits a simple two-stage shape with Cottrell character, but the transition
from a two-stage current transient to a three-stage current transient is observed at
$E_{ini} = 0.08$ V(RHE). This indicates that hydrogen trapping tends to occur below
$E_{ini} = 0.08$ V(RHE). The absence of any significant deviation of the absolute slope

Fig. 5.5 log I versus log t curves calculated in the case where reversible and irreversible trap sites coexist (Reprinted from Lee and Pyun [15], Copyright ©2005 with permission from Elsevier Science)
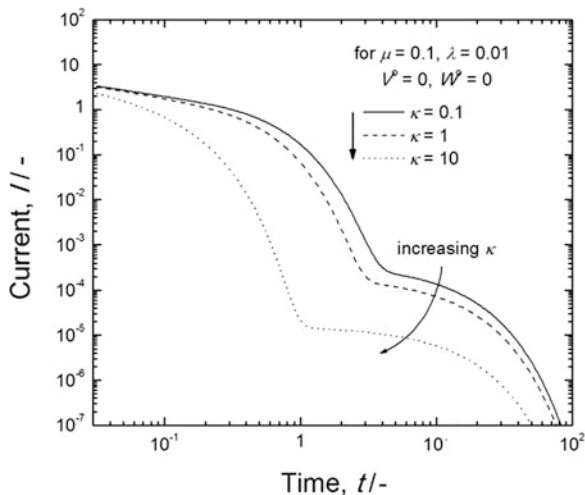
Fig. 5.6 log (I/Q_{total}) versus log t curves measured on a Pd electrode in 0.1 M NaOH solution (Reprinted from Yang et al. [16], Copyright ©1997 with permission from Elsevier Science)
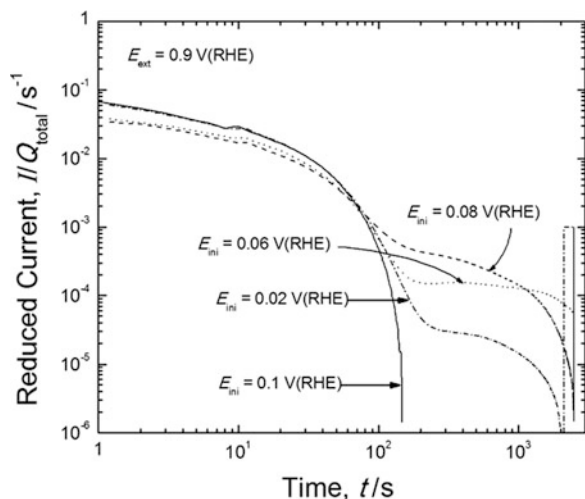
of the logarithmic current transient from 0.5 in the first stage implies that hydrogen trapping is not noticeable in the irreversible trap sites. The good agreement between the shapes of the measured and simulated current transients in the third stage further suggests that the release rate of hydrogen from the reversible trap sites increases with decreasing E_{ini}.

Another example of hydrogen trapping can be found in the current transient on electro-synthesized Ni(OH)$_2$ (*ESN*) electrodes [17]. *ESN* has a fine-grained structure with water and hydroxyl groups at the grain boundaries. The hydrogen transport behavior strongly depends on the constituents at the grain boundaries. Foreign species such as water, electrolyte species and additives (e.g., cobalt hydroxide), and their neighboring sites are considered to act as trap sites, depending on their nature.

Fig. 5.7 log (I/Q_m) versus
log t curves measured the
ESN films containing various
fractions of Co(OH)$_2$ by
jumping the applied potential
of 0.22–0.40 V(SCE): ○,
0 mol.%; □ 10 mol.%; △,
20 mol.%; ●, 30 mol.%; ■,
50 mol.% (Reprinted from
Yoon and Pyun [17],
Copyright ©1997 with
permission from Elsevier
Science)
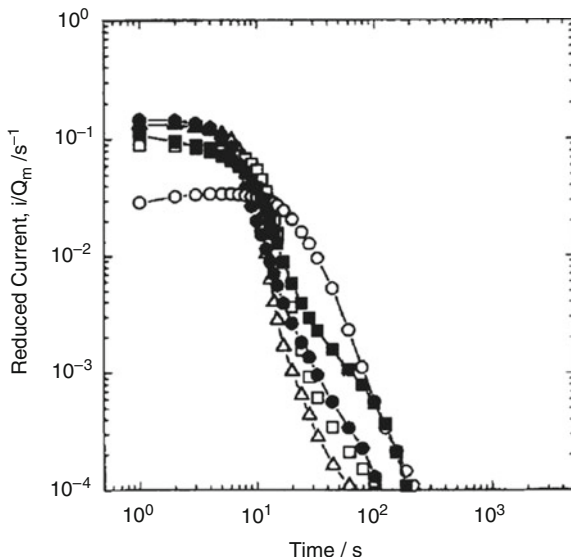
Figure 5.7 presents the typical anodic current transients for *ESN* films containing various fractions of Co(OH)$_2$ just after jumping the applied potential of 0.22–0.40 V (SCE). The current transients of the 0–20 mol.% Co(OH)$_2$-incorporated films show a two-staged shape. In contrast, those of the 30 and 50 mol.% Co(OH)$_2$-incorporated films exhibit a three-staged shape, indicating that hydrogen extraction occurs in the presence of traps (introduced by Co(OH)$_2$ species).

5.3 Hydrogen Trapping Determined by Ac-Impedance Technique

Ac-impedance spectroscopy has been established over many years as a powerful technique for the electrochemical characterization of hydride-forming metals and oxides, as described in Chap. 3 [17–28]. It allows us to study separately the dynamics of transport processes with different relaxation times. It is well known that the ac-impedance spectrum for diffusion in a planar electrode under the impermeable boundary condition should show two characteristic features depending on the frequency range [29, 30]:

1. Warburg behavior with an absolute phase angle |θ| of 45° in the high-frequency range
2. Capacitive behavior with |θ| of 90° in the low-frequency range

Hydrogen diffusion can be described by a transmission line that is composed of distributed resistive and capacitive elements, because the basic differential equation involved in a transmission line network has some formal mathematical similarity to
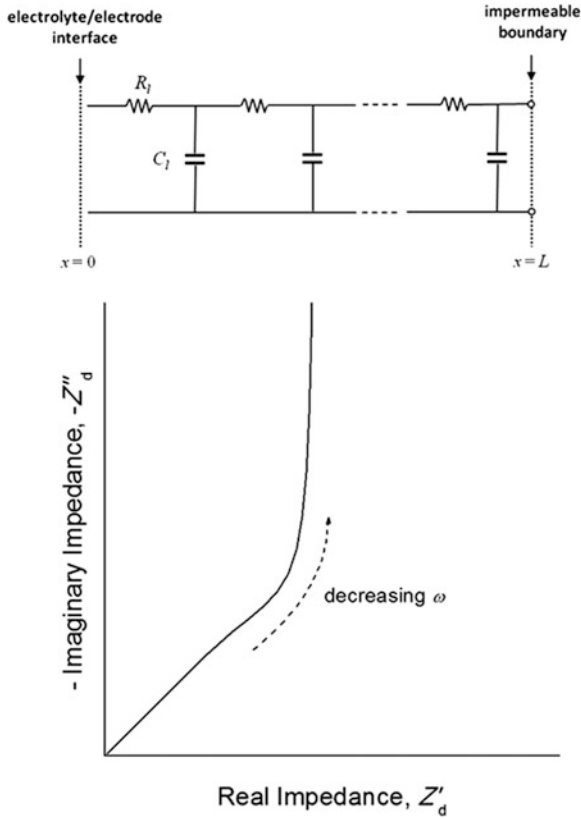
Fig. 5.8 Schematic diagrams of the equivalent circuit and the impedance diagram for the ideal diffusion process

that for the diffusion process [31–37]. The equivalent circuit and impedance diagram for the ideal diffusion process are schematically displayed in Fig. 5.8. See Chap. 3 for detailed information on the ac-impedance behavior of hydrogen diffusion.

For hydrogen transport in the presence of reversible trap sites, the transmission line network can be modified as shown in Fig. 5.9. R_l and C_l represent the resistance and intercalation capacitance associated with hydrogen diffusion through the normal lattice sites, respectively. R_r and C_r mean the resistance and intercalation capacitance for the trap sites, respectively. It should be noted that the intercalation capacitance for reversible trap sites is a function of the frequency, ω. The frequency-dependent capacitance for reversible trap sites, denoted as $C_r^*(\omega)$, can be derived from the modified diffusion equation on the basis of the McNabb-Foster's trapping concept. From Eq. 5.2, the steady-state fraction of trap sites that are occupied $\bar{f_r}$ is given by

$$\bar{f_r} = \frac{k_r \bar{c}_H}{k_r \bar{c}_H + p_r} \tag{5.23}$$
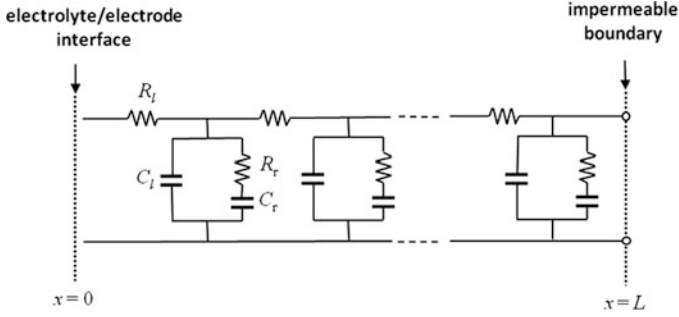
Fig. 5.9 Modified equivalent circuit for hydrogen diffusion involving the reversible trapping process

where $\bar{c}_H$ refers to the steady-state concentration of hydrogen in the normal lattice sites that is achieved during the ac-impedance measurement. The steady-state trap capacitance C_r can be obtained from Eq. 5.23 as follows:

$$C_r = \left(\frac{N_r d\bar{f}_r}{d\bar{c}_H}\right)C_1 = \left(\frac{N_r k_r(1-\bar{f}_r)}{k_r\bar{c}_H + p_r}\right)C_1 \tag{5.24}$$

Under an oscillating potential perturbation, f_r and c_H are expressed as

$$f_r = \bar{f}_r + \Delta f_r \exp(j\omega t) \tag{5.25}$$

$$c_H = \bar{c}_H + \Delta c_H \exp(j\omega t) \tag{5.26}$$

where j stands for the complex number, i.e., $\sqrt{-1}$, and Δf_r and Δc_H represent the ac-amplitudes of f_r and c_H, respectively. Substituting Eqs. 5.25 and 5.26 into Eq. 5.2, we obtain

$$\Delta f_r = \left(\frac{k_r(1-\bar{f}_r)}{k_r\bar{c}_H + p_r + j\omega}\right)\Delta c_H \tag{5.27}$$

Finally, the frequency-dependent trap capacitance $C_r^*(\omega)$ is obtained as

$$C_r^*(\omega) = \left(\frac{N_r k_r(1-\bar{f}_r)}{k_r\bar{c}_H + p_r + j\omega}\right)C_1 = \left(1+\frac{j\omega}{\omega_r}\right)^{-1}C_r \tag{5.28}$$

with the characteristic angular frequency ω_r for reversible trapping expressed as

$$\omega_r = k_r\bar{c}_H + p_r \tag{5.29}$$

The diffusion impedance Z_d in the presence of trap sites under the impermeable *BC* is given by

$$Z_d(\omega) = R_1 \frac{\coth[L(j\omega R_1 C^*(\omega))^{1/2}]}{(j\omega R_1 C^*(\omega))^{1/2}} \tag{5.30}$$

The diffusion impedance $Z_d(\omega)$ of Eq. 5.30 has two characteristic frequencies, ω_o and ω_r characterizing the diffusion and trapping kinetics, respectively:

$$\omega_o = \frac{1}{R_1 C_1 L^2} \tag{5.31}$$

$$\omega_r = \frac{1}{R_r C_r L^2} \tag{5.32}$$

Figure 5.10a, b present the typical Nyquist plot of the ac-impedance spectrum and the variation of the phase angle θ with log ω, respectively, calculated from Eq. 5.30 for the first case $\omega_r < \omega_o$. The simulation parameters used are $R_1 = 0.1$ kΩ cm^{-1}, $C_1 = 1$ mF cm^{-1}, $R_r = 1$ kΩ cm^{-1}, $C_r = 10$ mF cm^{-1}, and $L = 1$ cm. The results may be summarized as follows:

1. At $\omega > \omega_o$, the ac-impedance spectrum exhibits the ideal Warburg behavior, since at these frequencies the slow trapping reaction has no influence on the transport process.
2. At $\omega_r < \omega < \omega_o$, an arc appears in the impedance spectrum, which corresponds to the characteristic feature of trap relaxation. This arc arises from the parallel combination of R_r and C_1.
3. At $\omega < \omega_r$, the ac-impedance spectrum shows a capacitive line in the low-frequency range, due to the accumulation of hydrogen in both the normal lattice sites and trap sites at the impermeable boundary.

The typical Nyquist plot of the ac-impedance spectrum and the variation of θ with log ω for the second case $\omega_r > \omega_o$ are illustrated in Fig. 5.11a, b, respectively. The ac-impedance spectrum was calculated by assuming $R_1 = 10$ kΩ cm^{-1}, $C_1 = 1$ mF cm^{-1}, $R_r = 10$ Ω cm^{-1}, and $C_r = 10$ mF cm^{-1}. In this case, the trap sites would not slow down the diffusion kinetics in the electrode, but would act as homogeneous reaction sites. For example, it has been reported that the transport process in a WO_3 electrode proceeds under the condition in which diffusion is coupled with a relatively fast immobilization reaction at the W^{6+} sites, leading to the reduction of W^{6+} to W^{5+} [38–40]. The ac-impedance spectrum in Fig. 5.11 shows three distinctive features:

1. At $\omega > \omega_r$, the ac-impedance spectrum exhibits the ideal Warburg behavior, followed by a small arc.
2. At $\omega_o < \omega < \omega_r$, the Warburg behavior of the diffusion impedance appears again.
3. At $\omega < \omega_o$, the ac-impedance spectrum shows the ideal capacitive line.

Fig. 5.10 (**a**) Nyquist plot of the ac-impedance spectrum and (**b**) the variation of phase angle θ with log ω for $\omega_r < \omega_o$
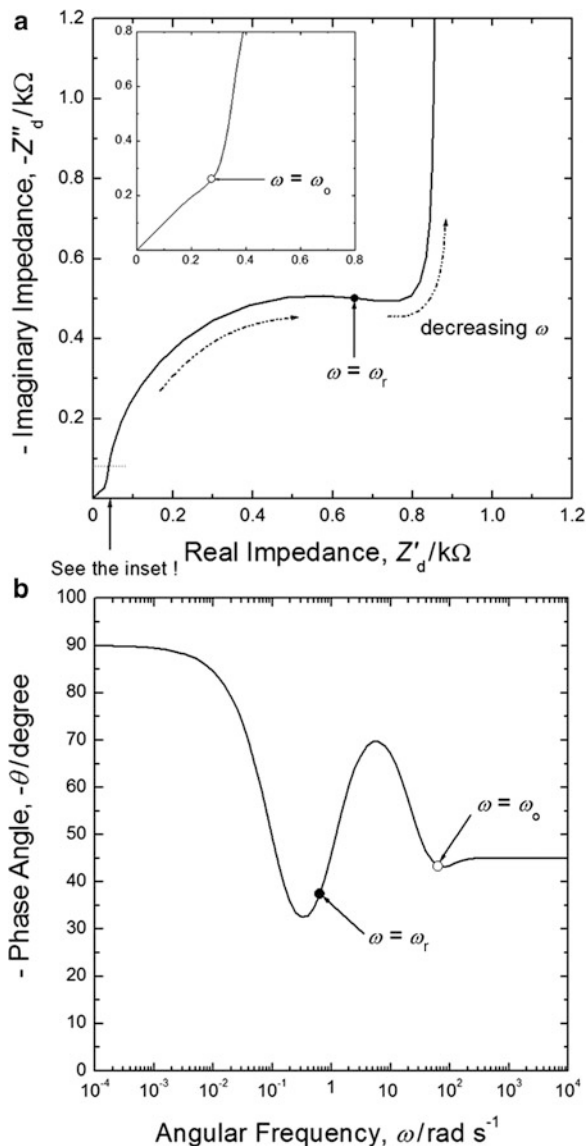
It should be pointed out that various kinds of trap sites with different capture rates k and release rates p may coexist in real hydride-forming electrodes. In this case, the characteristic angular frequencies ω_r for the trapping reactions are widely distributed over the whole frequency range, and hence, the ac-impedance spectrum may exhibit a straight line with $|\theta|$ larger or smaller than $45°$, which can be approximated to the constant phase element (CPE).

Fig. 5.11 (a) Nyquist plot of the ac-impedance spectrum and (b) the variation of phase angle θ with log ω for $\omega_r > \omega_o$
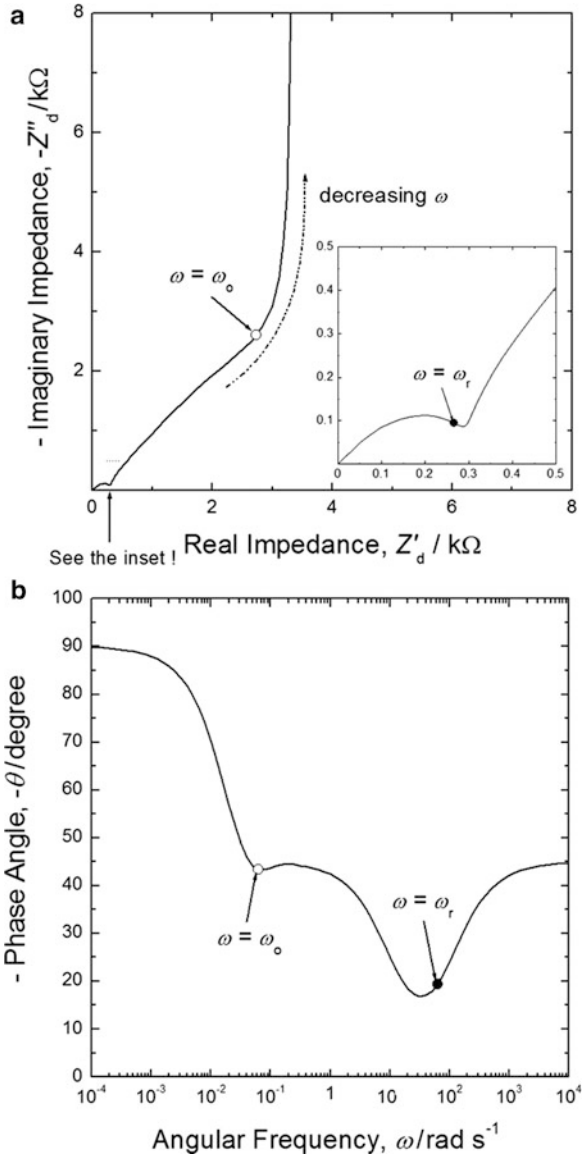
References

1. McNabb A, Foster PK (1963) A new analysis of the diffusion of hydrogen in iron and ferritic steels. Trans Metall Soc AIME 227:618–627
2. Bockris JOM, Subramanyan PK (1971) Hydrogen embrittlement and hydrogen traps. J Electrochem Soc 118:1114–1119
3. Kumnick AJ, Johnson HH (1980) Deep trapping states for hydrogen in deformed iron. Acta Metall 28:33–39

4. Riecke E, Bohnenkamp K (1984) On the influence of lattice imperfections in iron on hydrogen diffusion. Z Metallkd 75:76–81

5. McKibben R, Sharp RM, Harrington DA, Pound BG, Wright GA (1987) A potentiostatic double-step method for measuring hydrogen atom diffusion and trapping in metal electrodes – I. Theory. Acta Metall 35:253–262

6. Turnbull A, Carroll MW, Ferriss DH (1989) Analysis of hydrogen diffusion and trapping in a 13 % chromium martensitic stainless steel. Acta Metall 37:2039–2046

7. Krom AHM, Bakker AD (2000) Hydrogen trapping models in steel. Metall Mater Trans B 31B:1475–1482

8. Darken LS, Smith RP (1949) Behavior of hydrogen in steel during and after immersion in acid. Corrosion 5:1–7

9. Oriani RA (1970) The diffusion and trapping of hydrogen in steel. Acta Metall 18:147–157

10. Iino M (1982) A more generalised analysis of hydrogen trapping. Acta Metall 30:367–375

11. Iino M (1982) Analysis of irreversible hydrogen trapping. Acta Metall 30:377–383

12. Leblond JB, Dubois D (1983) A general mathematical description of hydrogen diffusion in steels – I. Derivation of diffusion equations from boltzmann-type transport equations. Acta Metall 31:1459–1469

13. Leblond JB, Dubois D (1983) A general mathematical description of hydrogen diffusion in steels – II. Numerical study of permeation and determination of trapping parameters. Acta Metall 31:1471–1478

14. Pyun SI, Yang TH (1998) Theoretical analysis of hydrogen transport through an electrode at the coexistence of two hydrogen-poor and –rich phases based upon the concept of hydrogen trapping. J Electroanal Chem 441:183–189

15. Lee JW, Pyun SI (2005) Anomalous behaviour of hydrogen extraction from hydride-forming metals and alloys under impermeable boundary conditions. Electrochim Acta 50:1777–1850

16. Yang TH, Pyun SI, Yoon YG (1997) Hydrogen transport through Pd electrode: current transient analysis. Electrochim Acta 42:1701–1708

17. Yoon YG, Pyun SI (1997) Hydrogen transport through nickel hydroxide film: current transient analysis. Electrochim Acta 42:2465–2474

18. Lim C, Pyun SI (1993) Theoretical approach to faradaic admittance of hydrogen absorption reaction on metal membrane electrode. Electrochim Acta 38:2645–2652

19. Lim C, Pyun SI (1994) Impedance analysis of hydrogen absorption reaction on Pd membrane electrode in 0.1 M LiOH solution under permeable boundary conditions. Electrochim Acta 39:363–373

20. Zhang W, Sridhar Kumar MP, Srinivasan S (1995) Ac impedance studies on metal hydride electrodes. J Electrochem Soc 142:2935–2943

21. Yang TH, Pyun SI (1996) Hydrogen absorption and diffusion into and in palladium: ac-impedance analysis under impermeable boundary conditions. Electrochim Acta 41:843–848

22. Yang TH, Pyun SI (1996) A study of hydrogen absorption reaction into α- and β-LaNi$_5$H$_x$ porous electrodes by using electrochemical impedance spectroscopy. J Power Sources 62:175–178

23. Wang C (1998) Kinetic behavior of metal hydride electrode by means of ac impedance. J Electrochem Soc 145:1801–1812

24. Montella C (1999) Review and theoretical analysis of ac–av methods for the investigation of hydrogen insertion I. Diffusion formalism. J Electroanal Chem 462:73–87

25. Montella C (2000) Review and theoretical analysis of ac–av methods for the investigation of hydrogen insertion: part II. Entry side impedance, transfer function and transfer impedance formalism. J Electroanal Chem 480:150–165

26. Montella C (2000) Review and theoretical analysis of ac–av methods for the investigation of hydrogen insertion: part III. Comparison of entry side impedance, transfer function and transfer impedance methods. J Electroanal Chem 480:166–185

27. Yuan X, Xu N (2002) Electrochemical and hydrogen transport kinetic performance of MlNi$_{3.75}$Co$_{0.65}$Mn$_{0.4}$Al$_{0.2}$ metal hydride electrodes at various temperatures. J Electrochem Soc 149:A407–A413

28. Georén P, Hjelm AK, Lindbergh G, Lundqvist A (2003) An electrochemical impedance spectroscopy method applied to porous $LiMn_2O_4$ and metal hydride battery electrodes. J Electrochem Soc 150:A234–A241
29. Ho C, Raistrick ID, Huggins RA (1980) Application of a-c technique to the study of lithium diffusion in tungsten trioxide thin films. J Electrochem Soc 127:343–350
30. Cabanel R, Barral G, Diard JP, Gorrec B, Montella C (1993) Determination of the diffusion coefficient of an inserted species by impedance spectroscopy: application to the $H/H_xNb_2O_5$ system. J Appl Electrochem 23:93–97
31. Macdonald JR (1987) Impedance spectroscopy. Wiley, New York
32. Bisquert J, Garcia-Belmonte G, Bueno P, Longo E, Bulhoes LOS (1998) Impedance of constant phase element (CPE)-blocked diffusion in film electrodes. J Electroanal Chem 452:229–234
33. Bisquert J, Compte A (2001) Theory of the electrochemical impedance of anomalous diffusion. J Electroanal Chem 499:112–120
34. Bisquert J (2002) Analysis of the kinetics of ion intercalation: ion trapping approach to solid-state relaxation processes. Electrochim Acta 47:2435–2449
35. Bisquert J, Vikhrenko VS (2002) Analysis of the kinetics of ion intercalation: two state model describing the coupling of solid state ion diffusion and ion binding processes. Electrochim Acta 47:3977–3988
36. Bisquert J, Garcia-Belmonte G, Pitarch A (2003) An explanation of anomalous diffusion patterns observed in electroactive materials by impedance methods. Chemphyschem 3:287–292
37. Lee JW, Pyun SI (2005) Anomalous behaviour in diffusion impedance of intercalation electrodes. Z Metallkd 96:117–123
38. Fabregat-Santiago F, Garcia-Belmonte G, Bisquert J, Ferriols NS, Bueno PR, Longo E, Anton JS, Castro-Garcia S (2001) Dynamic processes in the coloration of WO_3 by lithium insertion. J Electrochem Soc 148:E302–E309
39. Bohnke O, Rezrazi M, Vuillemin B, Bohnke C, Gillet PA, Rousselot C (1992) "In situ" optical and electrochemical characterization of electrochromic phenomena into tungsten trioxide thin films. Solar Energy Mat Solar Cells 25:361–374
40. Vuillemin B, Bohnke O (1994) Kinetics study and modelling of the electrochromic phenomenon in amorphous tungsten trioxide thin films in acid and lithium electrolytes. Solid State Ion 68:257–267

Chapter 6
Generation of Internal Stress During Hydrogen and Lithium Transport
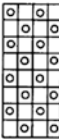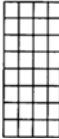
6.1 Relationship Between Diffusion and Macroscopic Deformation

Atomic diffusion in insertion electrodes such as hydride-forming metals and transition metal oxides may induce structural deformation due to a volume change, modifying the physical properties of the electrode. Also, the strain or stress field induced by an external force, for example, elastic bending, may influence the diffusion process in the electrode, because of the resulting inhomogeneous distribution of the atoms. The relationship between the diffusion and macroscopic deformation of the electrode can be classified into the elasto-diffusive and diffusion-elastic phenomena as schematically illustrated in Table 6.1 [1].

6.1.1 Elasto-Diffusive Phenomenon

The elasto-diffusive phenomenon is presented in Fig. 6.1, which shows the variation of the hydrogen pressure within a $Pd_{81}Pt_{19}$ tubular membrane with time from the initial, virtual value, p_o [1]. The hydrogen pressure was initially kept constant within the tubular membrane and the hydrogen gas was in equilibrium with the hydrogen distributed over the tubular membrane. A subsequent increase of hydrogen concentration at the outer surface caused by the increase of the outer hydrogen pressure results in an initial decrease of the hydrogen pressure within the tube (B in Fig. 6.1a). This phenomenon is known to occur by the outward bending of the tubular membrane, as illustrated in Fig. 6.1b. The outward bending of the tubular membrane causes hydrogen to diffuse from the inner surface toward the outer surface, which is referred to as the elasto-diffusive phenomenon or "Gorsky effect."

Table 6.1 Elasto-diffusive and diffusion-elastic phenomena (Reprinted from Han and Pyun [1], Copyright ©2001 with permission from Korean Electrochemical Society)

Phenomenon	Original state	Primary cause	Consequence	Direction of flux (final state)
Elasto-diffusive		Elastic bending	Inhomogeneous hydrogen distribution	
Diffusion-elastic		Diffusion flux	Inhomogeneous elastic deformation	
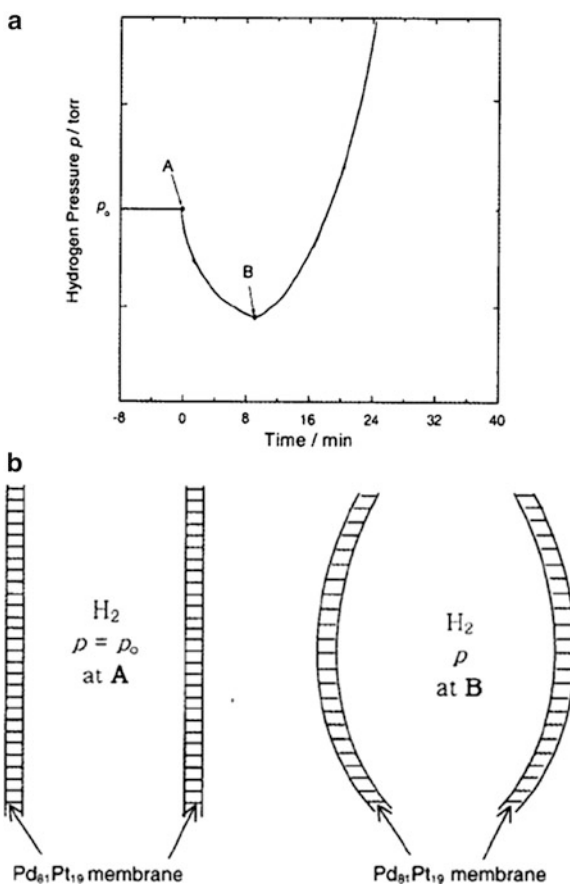
Fig. 6.1 (a) Variation of the hydrogen pressure within a Pd$_{81}$Pt$_{19}$ tubular membrane, and (b) the shapes of the tubular membrane at A and B (Reprinted from Han and Pyun [1], Copyright ©2001 with permission from Korean Electrochemical Society)

It is known that the relative magnitude of this phenomenon is related to the initial hydrogen concentration. The stress field developed in tubular membranes of Pd and Pd alloys during the Gorsky effect was determined by several researchers using hydrogen permeation techniques [2, 3].

6.1.2   Diffusion-Elastic Phenomenon

The diffusion-elastic phenomenon refers to the situation where stress or strain fields are generated by diffusion. The inhomogeneous distribution of atoms during the diffusion process causes an inhomogeneous volume change of the electrode, leading to bending distortions. The bending distortions generated during the diffusion process may also induce the Gorsky effect. However, previous studies [4–7] indicated that the contribution of the Gorsky effect is too small to affect the overall bending distortion. In this chapter, we restrict our discussion to the diffusion-elastic phenomena that are observed during hydrogen or lithium transport.

6.2   Theory of Stress Change Measurements

6.2.1   Laser Beam Deflection (LBD) Method

The laser beam deflection (*LBD*) technique is a powerful tool for monitoring in situ the stresses developed during the diffusion process. Pyun et al. [8–14] used the *LBD* method combined with electrochemical measurements in order to follow the stress generated during hydrogen or lithium diffusion. Before going into the details of the experimental procedures, we first present the mathematical expressions for the deflections induced by the diffusion process in a planar electrode. As an example, we consider the deflection measurements during potentiostatic hydrogen extraction from a hydride-forming electrode. For the analysis of the stresses generated during hydrogen transport through the electrode, it is essential to know the change in the hydrogen concentration profile with time across the electrode.

The governing equation is Fick's diffusion equation,

$$\frac{\partial c_{\mathrm{H}}}{\partial t} = \tilde{D}_{\mathrm{H}} \frac{\partial^2 c_{\mathrm{H}}}{\partial x^2} \tag{6.1}$$

where c_{H} is the hydrogen concentration, $\tilde{D}_{\mathrm{H}}$ the chemical diffusivity of hydrogen (see Chap. 4), x the distance from the electrode/electrolyte interface, and t the hydrogen extraction time. In the case of current transient measurements under the impermeable boundary condition, the initial condition (*IC*) and boundary conditions (*BC*s) are written as follows:

$$IC: c_H = \overset{\circ}{c}_H \qquad \text{for } 0 \leq x \leq L \text{ at } t = 0 \qquad (6.2)$$

$$BC: c_H = 0 \qquad (\text{diffusion} - \text{control } BC) \qquad (6.3)$$

$$\text{for } x = 0 \text{ at } t \geq 0$$

$$\left(\frac{\partial c_H}{\partial x}\right) = 0 \qquad (\text{impermeable } BC) \qquad (6.4)$$

$$\text{for } x = L \text{ at } t \geq 0$$

where $\overset{\circ}{c}_H$ is the initial equilibrium concentration of hydrogen corresponding to the applied potential.

The dissolved hydrogen expands the crystal lattice of the host metal. According to Vegard's second law, the relative volume change $\Delta V/V$ is proportional to c_H:

$$\Delta V/V = k_3 c_H \qquad (6.5)$$

where k_3 is the proportionality coefficient of Vegard's second law. For $\Delta V/V \ll 1$, the relative change of the linear dimension $\Delta l/l$ in the y direction obeys the same Vegard's law with a different coefficient, k_1:

$$\Delta l/l \equiv \varepsilon = k_1 c_H \qquad (6.6)$$

where ε represents the linear strain, that is, the relative linear deformation. Here, the y-axis is taken to be parallel to the longitudinal axis of the electrode specimen and perpendicular to the diffusion flux.

Now the stress distribution originating from the hydrogen distribution across the electrode can be calculated by solving the equation for Hooke's law as follows [1]:

$$\sigma_y(x,t) = E\varepsilon(x,t) = k_1 E c_H(x,t) = k c_H(x,t) \qquad (6.7)$$

where k is the proportionality constant. The bending moment of the electrode specimen $M_b(t)$ is given as

$$M_b(t) = \int_0^L \sigma_y(x,t) \times \left(x - \frac{1}{2}\right) dx = \int_0^L k c_H(x,t) \times \left(x - \frac{1}{2}\right) dx \qquad (6.8)$$

Under the assumption that the deflection is proportional to $M_b(t)$, one can calculate the deflection transients from the hydrogen concentration profiles. Equation 6.8 indicates that the hydrogen located in the region $0 < x < L/2$ contributes to the compressive deflection, whereas the hydrogen in the region $L/2 < x < L$ induces the tensile deflection.

The deflection transients were theoretically calculated using the virtual electrode potential curve described in Chap. 4 (Fig. 4.2) and the results are presented in Fig. 6.2a [1]. The transients were simulated by jumping various initial potentials
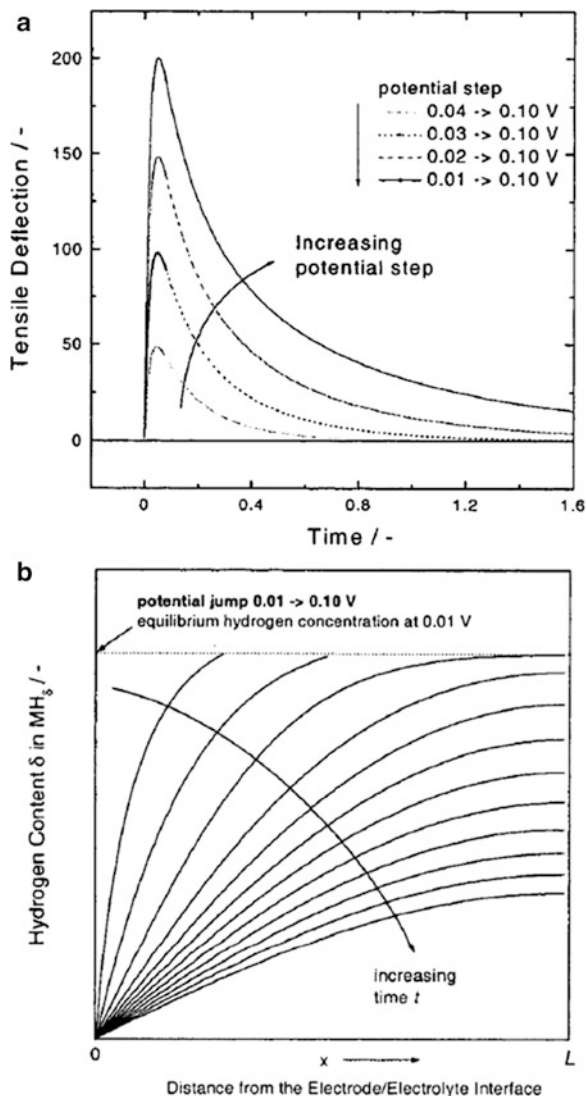
$E_{ini} = 0.01 - 0.04$ V to the extraction potential $E_{ext} = 0.10$ V. Figure 6.2b presents the changes in the hydrogen concentration profile across the electrode with time, which were simultaneously calculated at the potential jump of 0.01–0.10 V. During hydrogen extraction, the tensile deflections drastically increase to a maximum value and then are completely annihilated. The tensile stresses indicate that the extracted hydrogen contracts the lattice. It is seen that the maximum value of the tensile deflection increases with decreasing hydrogen injection potential, that is, with increasing initial hydrogen concentration. On the other hand, the time to maximum deflection t_{max} has the same value, regardless of the hydrogen injection potential. Figure 6.3 displays the effect of the hydrogen diffusivity on the deflection transient.

Fig. 6.3 Deflection transients calculated with various hydrogen diffusivities (Reprinted from Han and Pyun [1], Copyright ©2001 with permission from Korean Electrochemical Society)
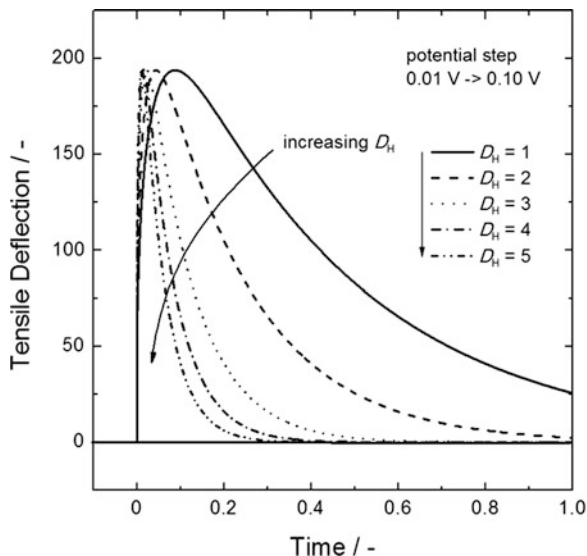
The deflection transients were calculated at the potential jump of 0.01–0.10 V using the various $\tilde{D}_H$ values indicated in Fig. 6.3. As the value of $\tilde{D}_H$ increases, t_{max} is shortened, whereas the maximum value of the tensile deflection remains constant. Under the diffusion-control BC, the following relationship between t_{max} and $\tilde{D}_H$ is established [15]:

$$\frac{\tilde{D}_H t_{max}}{L^2} = 0.05 \tag{6.9}$$

Equation 6.9 allows us to determine $\tilde{D}_H$ from the measured values of t_{max} and the given value of L.

6.2.2 Double Quartz Crystal Resonator (DQCR) Method

When an alternating voltage is applied to electrodes coated on both sides of a quartz plate, a piezoelectric mechanical vibration is induced within the plate. Since quartz crystal is anisotropic, its vibration mode is critically dependent on the cutting type or the crystal orientation of the quartz plate [16]. The cutting orientations and corresponding vibration modes of the quartz are presented in Fig. 6.4.

Particularly for a quartz crystal vibrating in thickness shear mode (i.e., AT and BT-cut quartz plates), the change in its resonant frequency, Δf, has a linear relationship with the mass loading, ΔM, on it [17, 18].

$$\Delta f = -\left(\frac{\Delta M}{A}\right)\left(\frac{f_Q^2}{\rho_Q N_Q}\right) \tag{6.10}$$

Fig. 6.4 (**a**) Various cut angular orientations of quartz crystal and (**b**) the thickness-shear-mode oscillation of *AT*- and *BT*-cut quartz crystal
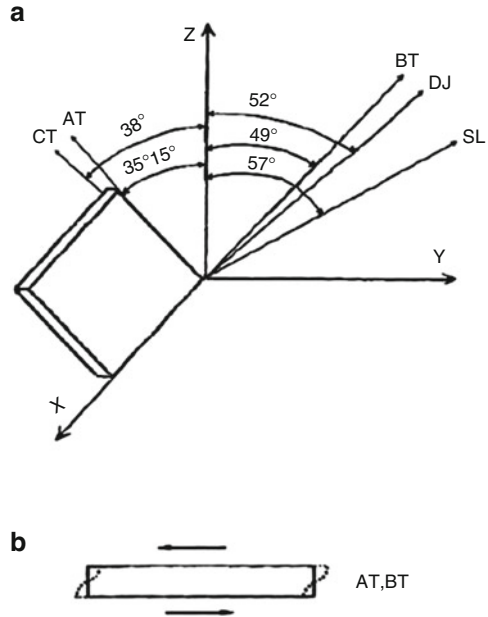
where A is the piezoelectrically vibrating area; f_Q, the natural frequency of the quartz; ρ_Q, the density of the quartz; and N_Q, the frequency constant of the quartz (for *AT*-cut quartz crystal $N_Q^{AT} = 1,666$ Hz m and for *BT*-cut quartz crystal $N_Q^{BT} = 2,536$ Hz m).

Shown in Fig. 6.5 is the side and top view of a typical quartz crystal resonator sample. In general, a gold or platinum thin layer (several hundreds of microns thick) is coated on both sides of the quartz plate in a keyhole pattern. A titanium underlayer is predeposited on the quartz to afford good adhesion of the gold or platinum film.

The measurement of the internal stress generated in a thin film by using two quartz crystals with different cutting types (i.e., *AT* and *BT* cuts) was first introduced by EerNisse [19, 20], which is frequently called the double quartz crystal resonator (*DQCR*) technique. The *AT* and *BT*-cut quartz crystals respond to the applied stress in a completely different way: A tensile stress leads to a decrease in the resonant frequency of the *AT*-cut quartz crystal, whereas it causes a frequency increase of the *BT*-cut quartz crystal. Accordingly, the contribution of the internal stress induced in the thin layer coated on the quartz to its resonant frequency can be separated from the mass contribution given in Eq. 6.10 when the thin layers are coated on the *AT* and *BT*-cut quartz crystals and the two samples are tested under the same experimental conditions. When we assume that the stress is uniformly distributed in the film, and the contribution of the film surface roughness and the electrolyte viscosity to the resonant frequency of the quartz can be neglected, the total frequency change is just the superposition of the effects of the
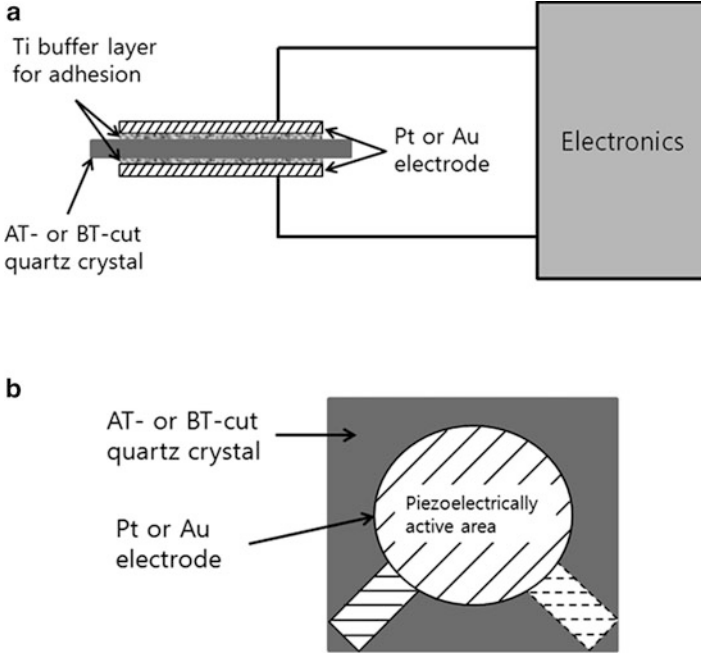
Fig. 6.5 (**a**) Cross-sectional and (**b**) surface views of typical quartz crystal resonator sample

mass change, ΔM, and the stress change integrated through the film thickness, ΔS, as follows [21]:

$$\Delta f = -\left(\frac{\Delta M}{A}\right)\left(\frac{f_Q^2}{\rho_Q N_Q}\right) + K\Delta S\left(\frac{f_Q^2}{N_Q}\right) \tag{6.11}$$

Here, K is the stress coefficient ($K^{AT} = 2.75 \times 10^{-11} \text{m}^2\text{N}^{-1}$ and $K^{BT} = -2.65 \times 10^{-11}\text{m}^2\text{N}^{-1}$ for the AT and BT-cut quartz crystals, respectively).

Under the assumption that ΔM and ΔS for the AT-cut quartz crystal are identical to the corresponding values for the BT-cut quartz crystal, the mass and stress changes can be estimated from Eq. 6.11 with the following equations [19–21].

$$\Delta M = \frac{\rho_Q K^{AT} K^{BT}}{K^{AT} - K^{BT}}\left(\frac{\Delta f^{AT} d^{AT}}{K^{AT} f_Q^{AT}} + \frac{\Delta f^{BT} d^{BT}}{K^{BT} f_Q^{BT}}\right) \tag{6.12}$$

$$\Delta S = \frac{1}{K^{AT} - K^{BT}}\left(\frac{\Delta f^{AT} d^{AT}}{f_Q^{AT}} - \frac{\Delta f^{BT} d^{BT}}{f_Q^{BT}}\right) \tag{6.13}$$

Here, d^{AT} and d^{BT} are the thicknesses of the AT and BT-cut quartz crystals, respectively.

Fig. 6.6 Typical *LBD* apparatus for deflection measurements

1. specimen (working electrode)
2. laser source
3. window
4. position-sensitive detector
5. stainless steel rod
6. Micrometer
7. reference electrode
8. counter electrode
9. electrolyte
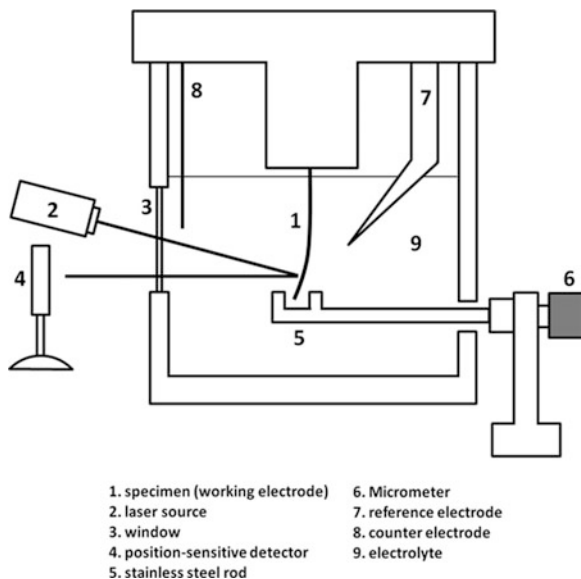
6.3 Setups for the Stress Change Measurements

6.3.1 LBD Method

A typical *LBD* apparatus for deflection measurements is schematically illustrated in Fig. 6.6. A commonly used laser source is a He-Ne beam with a spot size of 590 μm and a maximum output of 5 mW at 632.8 nm. To monitor the deflection during the electrochemical experiments, the laser beam is directed through a flat window in the side of the cell to the mirror near the end of the strip. The reflected beam from the mirror is detected by a position-sensitive detector (*PSD*). As the beam moves across the *PSD*, the position of the beam spot is converted to the output voltage in the range of −10 V to l0 V.

In general, there are two types of electrode specimens used for *LBD* measurements as shown in Fig. 6.7, depending on the thickness of the active electrode:

1. Thin film electrode (specimen *A*): The active electrode is much thinner than the substrate thickness. This type of the specimen is suitable for the investigation of the stresses generated during the anodic oxidation of metals, electrodeposition, or hydrogen/lithium insertion into thin films. In the case of the anodic oxidation of W, for example, the thicknesses of the active material (WO_3) and substrate (W) are 1–10 nm and several tens of micrometers, respectively [8]. In this case, the plane stress condition is satisfied and, thus, the measured deflection can be quantitatively converted to the stress value by using the Stoney equation [22, 23].

Fig. 6.7 Electrode specimens used for *LBD* measurements
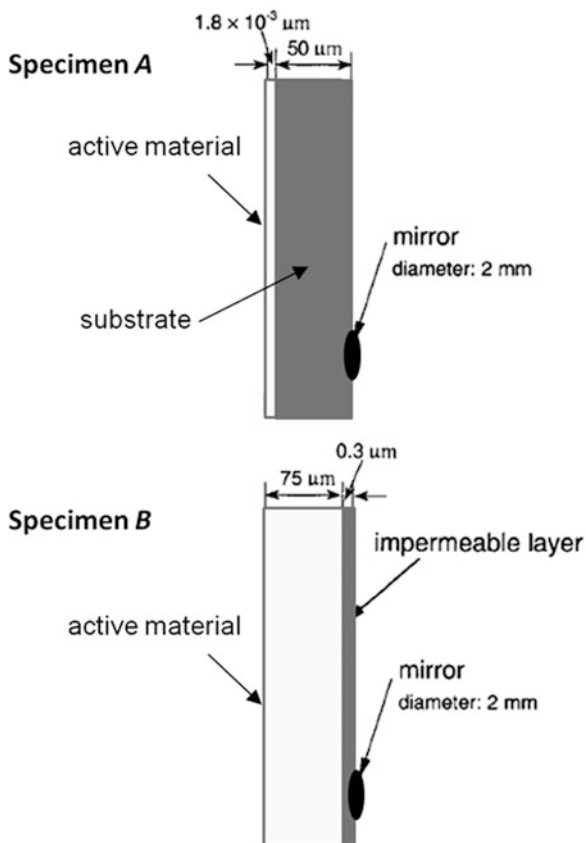
2. Thick foil electrode (specimen *B*): The thickness of the active material (e.g., 50–100 μm for Pd foil) is much larger than that of the impermeable layer (e.g., 0.1–0.5 μm for Au layer) [9, 10]. This specimen can be effectively used to study the stresses developed during hydrogen or lithium diffusion. The measured deflection is proportional to the stress value, but it cannot be quantitatively translated into the stress value, because the plane strain condition is no longer valid. As shown in Fig. 6.8, the injection process of hydrogen or lithium into the active material causes compressive stresses in the whole electrode specimen, whereas the extraction process induces tensile stresses.

6.3.2   DQCR Method

The thin layers to be tested are deposited on one side of the platinum (or gold)-coated *AT* and *BT*-cut quartz plates, as shown in Fig. 6.5. The thin layers can be formed through typical wet- or dry processes, such as physical/chemical vapor

Fig. 6.8 Stress generation during hydrogen injection into and extraction from a foil electrode (Reprinted from Han and Pyun [1], Copyright ©2001 with permission from Korean Electrochemical Society)

Hydrogen injection into the electrode
→ **compressive deflection** (stress)

Pd
Impermeable boundary

hydrogen ⟹

Hydrogen extraction from the electrode
→ **tensile deflection** (stress)

Pd
Impermeable boundary

hydrogen ⟸
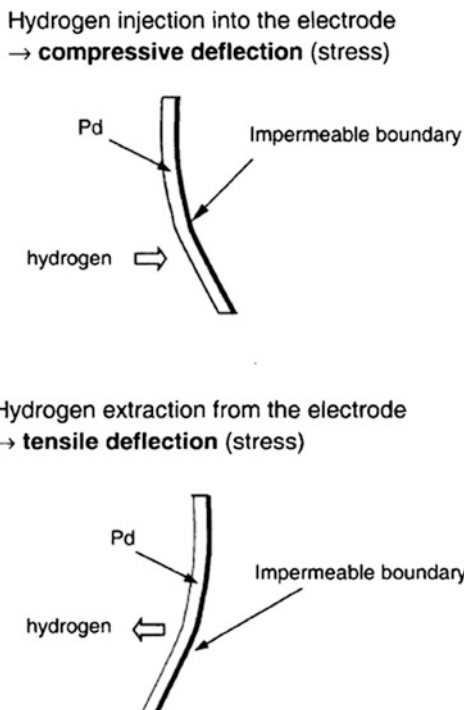
Fig. 6.9 Schematic representation of the experimental setup for the electrochemical measurement combined with a double quartz crystal resonator test (Reprinted from Go and Pyun [25], Copyright ©2003 with permission from The Electrochemical Society)

QCM main unit
(EG & G QCA 917)

IBM compatible computer

IEEE 488 bus

Oscillator circuit unit

Potentiostat
(EG & G M263A)

Glass tube

Teflon holder

R. E. (Lithium)

C. E.
(Lithium)

LiCoO₂ coated quartz crystal

1M LiClO₄ - PC solution
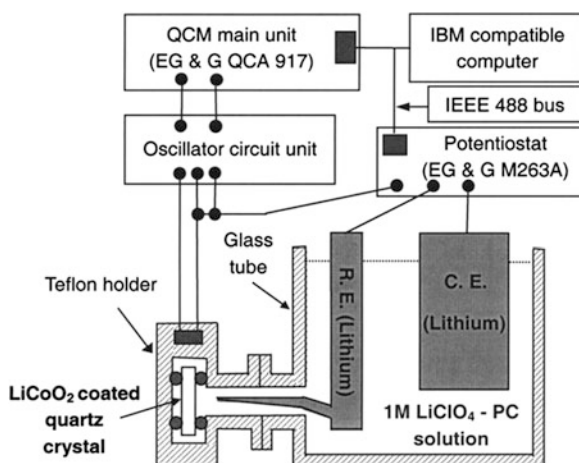
deposition, electroless/electrolytic coating, etc. If the layers need to be heat treated to improve their crystallinity, the temperature for heat treatment should be kept below 573°C to avoid thermal damage to the quartz by phase transformation [24].

Shown in Fig. 6.9 is the usual setup for the *DQCR* test [25]. Together with the mass change detection, the electrochemical response is recorded by a three-electrode

electrochemical cell configuration. Here, the thin layer coated *AT* or *BT*-cut quartz crystal, which is frequently mounted in a Teflon cell and kept in position with two O-rings, acts as a working electrode. For example, in a battery field, the thin layer coated on the quartz or the working electrode might be lithium cobalt dioxide ($LiCoO_2$) and the reference or counter electrode might be lithium metal. The electrochemical data, such as the charge/discharge curve, current transient, and cyclic or linear sweep voltammogram, are obtained concurrently with the resonant frequency or mass change plots. For the combined measurement of the electrochemical and mass change signal, potentiostat/galvanostat is basically used in conjunction with a quartz crystal microbalance (*QCM*) unit under the remote control of a personal computer, as shown in Fig. 6.9.

6.4   Interpretation of Insertion-Induced Internal Stress

6.4.1   Analysis of LBD Results

By using the *LBD* technique, Pyun and his coworkers [9, 10, 12] conducted extensive investigations into the diffusion-induced internal stresses in a Pd foil electrode with an impermeable boundary. They adopted a Pd metal as a model for the metal–hydrogen system, because of its experimental advantages over other hydride materials, such as its high resistance to irreversible deformation and high hydrogen solubility [26, 27]. Some of the experimental results on the deflection measurements during hydrogen transport under potentiostatic and potential sweep conditions will be discussed below.

Shown in Fig. 6.10a are the deflection versus time plots measured during hydrogen injection into the Pd foil electrode in a 0.1 M NaOH solution [9]. Hydrogen was potentiostatically injected by dropping the open-circuit potential to various injection potentials in the range of 0.06–0.12 V(RHE). Figure 6.10a shows that, during hydrogen injection, the compressive deflection increases to a maximum value and then it is relaxed. The time to the maximum compressive deflection t_{max} is prolonged with decreasing overpotential. It appears that the lower the injection potential, that is, the larger the amount of hydrogen injected into the electrode, the higher the maximum value of the compressive deflection. The deflection behavior in Fig. 6.10a may be explained in detail by the concentration profiles of hydrogen across the electrode shown in Fig. 6.10b. The concentration profiles *A*, *B*, and *C* corresponding to the compressive deflections are also indicated in Fig. 6.10a. Due to the difference between the molar volume of Pd at the electrolyte/electrode interface and that at the Au layer/electrode interface, the local volume change across the specimen increases to a maximum value as the hydrogen injection progresses. Then, the local volume change begins to decrease as hydrogen is accumulated at the Au layer/electrode interface. Consequently, the compressive stresses developed at the Au layer/electrode interface and distributed across the

whole electrode attain their maximum value when the injected hydrogen firstly
reaches the Au layer/electrode interface and then begin to be relaxed as hydrogen is
accumulated at this interface.

The deflection versus time curves obtained for hydrogen extraction are presented
in Fig. 6.11a [9]. The deflection was measured by jumping various injection
potentials to an extraction potential of 0.3 V(RHE). During hydrogen extraction,
the tensile deflection increases to a maximum value and then is completely
annihilated. Figure 6.11b shows the hydrogen concentration profiles across the
electrode during hydrogen extraction. Similar to the case of hydrogen injection,
the difference between the molar volume of Pd at the electrolyte/electrode interface
and that at the Au layer/electrode interface increases to a maximum value as
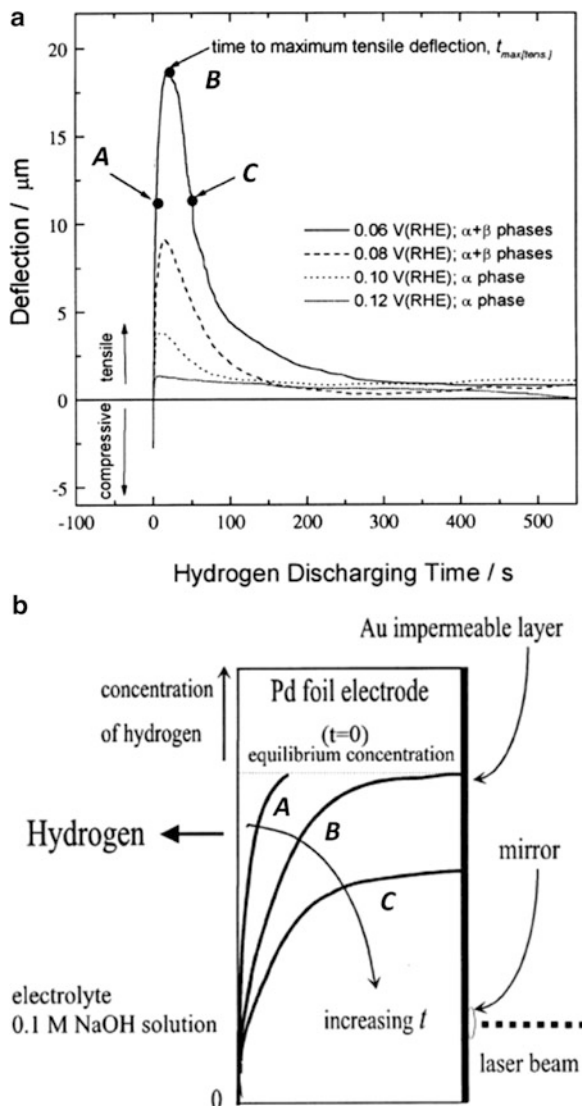
hydrogen is extracted. After that, it begins to decrease as the concentration of hydrogen at the impermeable boundary drops below the equilibrium concentration. Corresponding to the local change in the molar volume across the electrode, the tensile stresses generated at the Au layer/electrode interface and distributed across the whole electrode attain their maximum value and then are entirely annihilated. By using Eq. 6.9, the authors determined the value of $\tilde{D}_H$ from the measured values of t_{max}: The value of $\tilde{D}_H$ estimated during hydrogen extraction was found to vary between 1×10^{-7} and 5×10^{-7} cm^2 s^{-1}, depending on the hydrogen injection potential. These values of $\tilde{D}_H$ are in good agreement with the other previously reported values [28, 29].

Figure 6.12 shows the plots of the deflection versus applied potential (or reduced time) measured simultaneously with the cyclic voltammograms, that is, under potential sweep conditions [12]. Note that the time is presented in scales of reduced time defined as

$$\xi = \frac{t}{2(E_{ini} - E_{rev}) \times 1000} v \tag{6.14}$$

where t means the instantaneous time of any applied potential E_{app} during potential scanning, v is the scan rate, and E_{ini} and E_{rev} represent the initial and reverse potentials, respectively. So, ξ means the time interval needed for the execution of one cycle at a given scan rate. Three remarks should be made in respect to Fig. 6.12:

1. At $v = 1$–12 mV s^{-1}, the deflection exhibits a maximum compressive deflection, a transition from compressive to tensile deflection, a maximum tensile deflection, and finally the complete decay of the tensile deflection in sequence.
2. At $v = 12$–25 mV s^{-1}, the compressive deflection first increases to a maximum value and then is completely annihilated with time.
3. As the scan rate decreases, the values of the maximum compressive and tensile deflections are increased and also move toward the reverse potential E_{rev} as well. Similar to the case of hydrogen diffusion under potentiostatic conditions, this is attributed to the larger amount of hydrogen in the electrode with decreasing v.

The deflection transients were also simulated under potential sweep conditions and the results are presented in Fig. 6.13. It is found that the calculated deflection

Fig. 6.13 Plots of deflection versus applied potential (or reduced time) simulated under potential sweep conditions (Reprinted from Han et al. [12], Copyright ©2001 with permission from Elsevier Science)
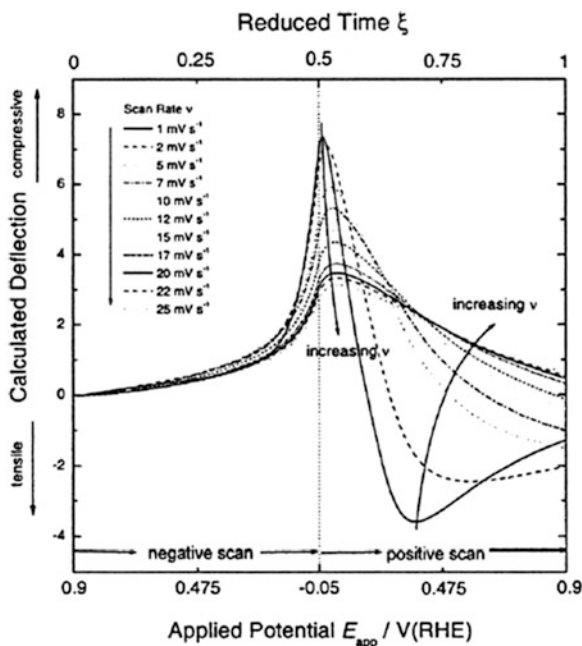
transients coincide well with the measured ones. The hydrogen concentration profiles across the electrode were calculated at various times during potential scanning. The characteristic hydrogen concentration profiles at $v = 1$ and 25 mV s^{-1} are demonstrated in Fig. 6.14a, b, respectively. As a consequence, the movement of the deflection in the compressive and tensile directions can be explained in terms of the difference between the molar volume near the electrode surface and that near the impermeable layer, which is developed during hydrogen diffusion.

The *LBD* technique can be successfully applied to electrochemical systems operated in a nonaqueous electrolyte [30–33]. Shown in Fig. 6.15 is the stress change, $\Delta\sigma$, versus the lithium stoichiometry, $(1 - \delta)$ plot, obtained simultaneously with the cyclic voltammogram for an $Li_{1-\delta}CoO_2$ film sputter deposited on a Pt/Ti/ thin glass plate in a 1 M solution of $LiClO_4$ in propylene carbonate [33]. The cyclic voltammogram features three sets of current peaks, namely, (3.95, 3.86), (4.08, 4.05), (4.17, 4.15). The first set of current peaks is caused by the phase transition between two hexagonal phases (Li-dilute phase α and Li-rich phase β), while the second and third sets are due to the order/disorder phase transition and lattice distortion from hexagonal to monoclinic symmetry, respectively [34]. The stress change measured by *LBD* shows that in the region of the first set of current peaks, the negative compressive stress is generated during the anodic scan when lithium is extracted from the oxide layer and the positive tensile stress is produced during the cathodic scan when lithium is inserted into the layer (the second stage in Fig. 6.15). On the other hand, in the region of the second/third sets of current peaks, the stress change plot features an upward concave shape (the third stage). The variation of the

Fig. 6.14 Hydrogen concentration profiles at $v = 1$ and 25 mV s^{-1} (Reprinted from Han et al. [12], Copyright ©2001 with permission from Elsevier Science)
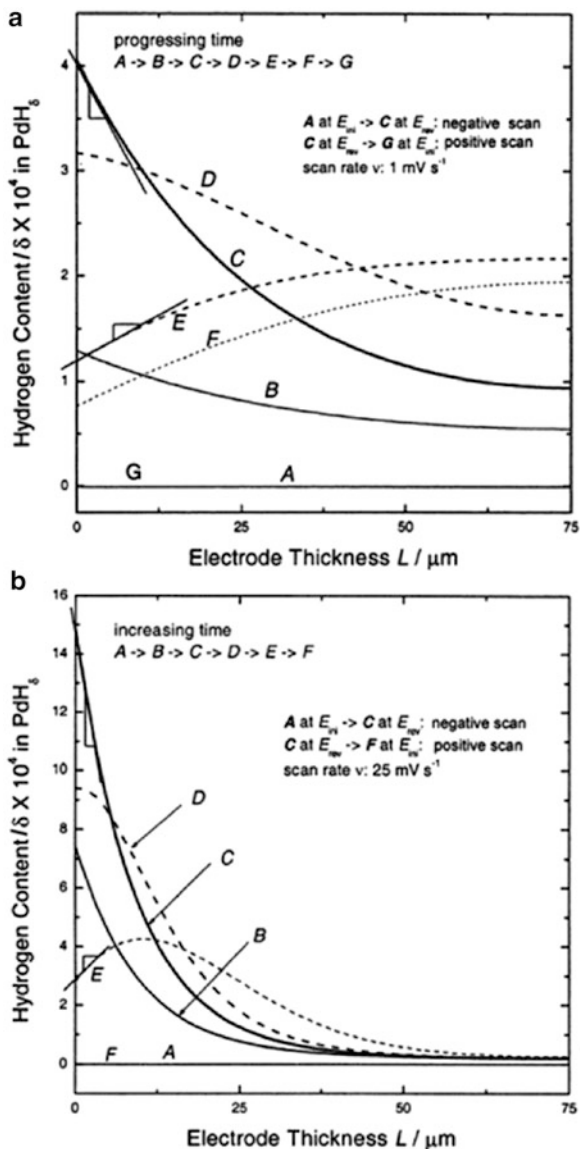
stress with the potential is relatively small below ca. 3.8 V versus Li/Li$^+$ (the first stage).

The dependence of the stress change induced in the oxide layer on the lithium stoichiometry can be more exactly estimated during the galvanostatic intermittent discharging experiment where the value of stress change is determined in the equilibrium state (Fig. 6.16). The open circuit potential (or electrode potential) curve obtained from the intermittent experiment exhibits a three-stage behavior:

Fig. 6.15 Stress change versus lithium stoichiometry plot together with the concomitantly recorded cyclic voltammogram, obtained from the $Li_{1-\delta}CoO_2$ coated on the Pt/Ti/thin glass plate in a 1 M $LiClO_4$–PC solution (Reprinted from Pyun et al. [13], Copyright ©2004 with permission from Elsevier Science)
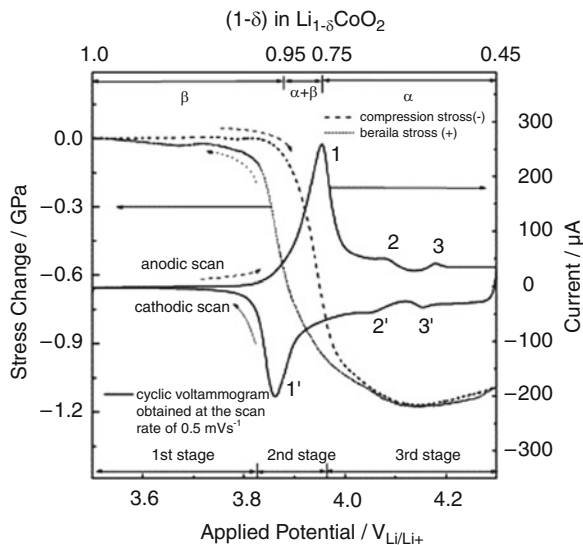
Fig. 6.16 Stress change versus lithium stoichiometry plot together with the concomitantly recorded electrode potential plot during galvanostatic intermittent discharging, obtained from the $Li_{1-\delta}CoO_2$ coated on the Pt/Ti/thin glass plate in a 1 M $LiClO_4$–PC solution (Reprinted from Pyun et al. [13], Copyright ©2004 with permission from Elsevier Science)
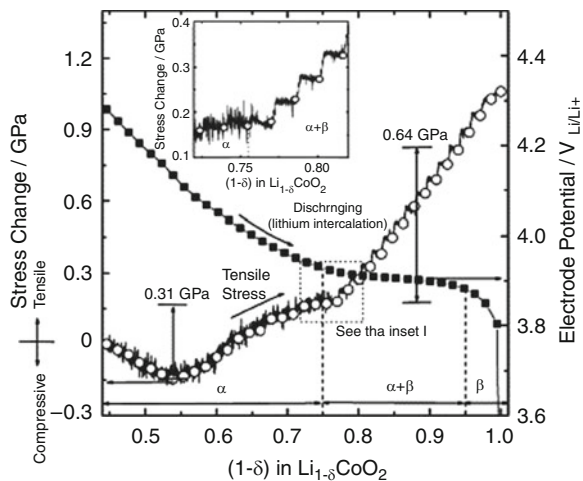
a monotonic decrease in potential (single α phase region), potential plateau (two-phase coexistence region), and rapid decrease in potential (single β phase region). These three stages correspond to the third, second, and first regions in the cyclic voltammogram, respectively. As regards the stress change, the compressive and the subsequent tensile stress is generated in the single α phase region, as the lithium content increases, leading to a stress change plot with an upward concave shape, and then the tensile stress rapidly increases in the two-phase coexistence region, similar to the corresponding plot obtained during the voltammetric experiment (Fig. 6.15). The stress change in the single β phase region is similar to that in the

Fig. 6.17 Anodic current transients and the corresponding stress change transients, obtained from the $Li_{1-\delta}CoO_2$ electrode in a 1 M $LiClO_4$–PC solution (Reprinted from Pyun et al. [13], Copyright ©2004 with permission from Elsevier Science)
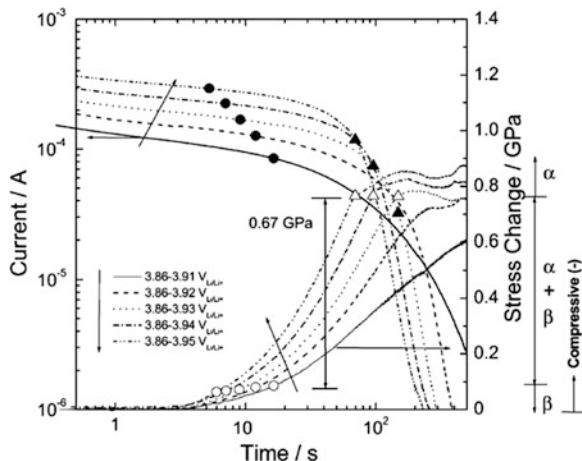
two-phase region. Considering that the potential decreases extremely rapidly with increasing lithium content, this result is actually consistent with the relatively mild change in the first stage of the stress transient curve of Fig. 6.15.

The stress change transient measured simultaneously with the current transient gives useful quantitative information on the stress change generated during the lithium transport. When the initial potential is above (or below) the plateau potential and the final potential is below (or above) it, the stress change and current transients reflect the effect of the phase transition of α to β (or β to α). As an example, Fig. 6.17 presents the anodic current transients when the potential jumps from 3.86 V versus Li/Li^+ to the potentials above the plateau potential 3.90 V versus Li/Li^+, along with the concurrently obtained stress change transients.

All of the anodic current transients feature the slow decay of the logarithmic current, followed by its steep decrease. The closed circles and triangles on the current transients correspond to the onset and end times of the β to α phase transformation, respectively, calculated on the basis of the cumulative charge passed during the lithium extraction (the open circles and triangles on the stress change transients have the same meaning). In the case of the final potentials of 3.91 and 3.92 V versus Li/Li^+, the phase transition is not completed during the experiment and, therefore, there are no closed triangles on their transients, since the driving force for the phase transition is quite small. It is noted that the stress changes developed from $t = 0$ to the onset times of the phase transition (i.e., open circles) are almost equal to each other (0.1 GPa). This time span corresponds to the potential interval between 3.86 and 3.88 V versus Li/Li^+ in Fig. 6.16. Similarly, for the stress change transients of the final potentials above 3.92 V versus Li/Li^+, the stress changes developed from the onset to end times of the phase transition are identical to each other, regardless of the final potentials. In addition, the stress change generated in this time duration (0.67 GPa) matches well with that between 3.88 and 3.93 V versus Li/Li^+ in the galvanostatic intermittent discharge curve (Fig. 6.16). This also proves that the stress change measured concurrently

with the cathodic current during the potential drops (i.e., lithium insertion) shows quantitative agreement with that estimated in Fig. 6.16 (please see the reference for details) [33].

Taking the insertion-/extraction-induced strain into consideration, the stress change can be theoretically calculated. When lithium is inserted into or extracted from the single α phase, the stress is determined from the molar volume change or the volume strain, ε_{vol}. Under the assumptions that the $Li_{1-\delta}CoO_2$ oxide layer is single crystal and has isotropic elasticity, ε_{vol} of the oxide is expressed as [35]

$$\sigma = Y\frac{\varepsilon_{vol}}{3} = -Y\frac{\varepsilon_x + \varepsilon_y + \varepsilon_z}{3} = -Y\varepsilon_{mean} \qquad (6.15)$$

where Y is the elastic modulus of the oxide, ε_{mean} is the mean strain, and ε_x, ε_y, and ε_z represent the strains in the x, y, and z directions of hexagonal symmetry, respectively. In the literature on the lattice parameters of $Li_{1-\delta}CoO_2$, it has been reported that ε_{vol} in the single α phase region shows an upward concave shape and has a maximum value in the $(1-\delta)$ range of 0.55–0.75. If we take the maximum ε_{vol} $\approx -9.0 \times 10^{-3}$, the maximum stress change in the single α phase region is estimated to be 0.21 GPa from Eq. 6.15.

In the case where the two phases coexist, the stress mainly originates from the mismatch of the lattice parameters of the two phases. Under the assumptions that the plate-shaped second phase is formed in the matrix and only the principal misfit strains, that is, $\varepsilon_{x\ misfit}$, $\varepsilon_{y\ misfit}$, and $\varepsilon_{z\ misfit}$, contribute to the total misfit strain, the stress per unit volume of the coherent second phase is given as [36]

$$\sigma = -\frac{2f(1+v)}{(1-2v)}G\varepsilon_{mean\ misfit} = -\frac{2f(1+v)}{(1-2v)}G\frac{\varepsilon_{x\ misfit} + \varepsilon_{y\ misfit} + \varepsilon_{z\ misfit}}{3} \quad (6.16)$$

where f is the ratio of the elastic moduli of the two phases; v, the Poisson's ratio; G, the shear modulus of the second phase; $\varepsilon_{mean\ misfit}$, the mean misfit strain. From the literature, the values of $\varepsilon_{mean\ misfit}$ at $(1-\delta) = 0.75$ and 0.95 were estimated to be ca. -36×10^{-3} and -2.1×10^{-3}, respectively [34], v is about 0.16 (the strain of the lattice parameter a divided by that of the lattice parameter c) [36], and G is 80 GPa [37]. If the elastic moduli of the two phases are virtually equal ($f = 1$), the stress change in the two-phase region can be theoretically calculated to be 0.57–1.0 GPa from Eq. 6.16.

The calculated stress changes in the single α phase region (0.21 GPa) and two-phase coexistence region (0.57–1.0 GPa) coincide well with the measured values (about 0.31 and 0.64 GPa, respectively. See Fig. 6.16). From the above comparative analysis of the dependences of the stress change and crystal structure (or its lattice parameter) on the lithium content, it is proved that the stress change in the α phase and two-phase coexistence regions are attributed to the molar volume change of the α phase and the mismatch of the lattice parameters between the two phases (α and β phases) with the lithium content, respectively.

6.4.2 Analysis of DQCR Results

Shown in Fig. 6.18a, b are the galvanostatic charge curves obtained from the $Li_{1-\delta}CoO_2$ films sputter-deposited on the *AT* and *BT*-cut quartz crystals and the corresponding normalized resonant frequency change (Δf) curves, respectively. For the normalization, it is assumed that there is no side reaction in the course of the lithium extraction process and that the mass changes of the films on the two quartz crystals equal each other during the experiment. The two charge curves of
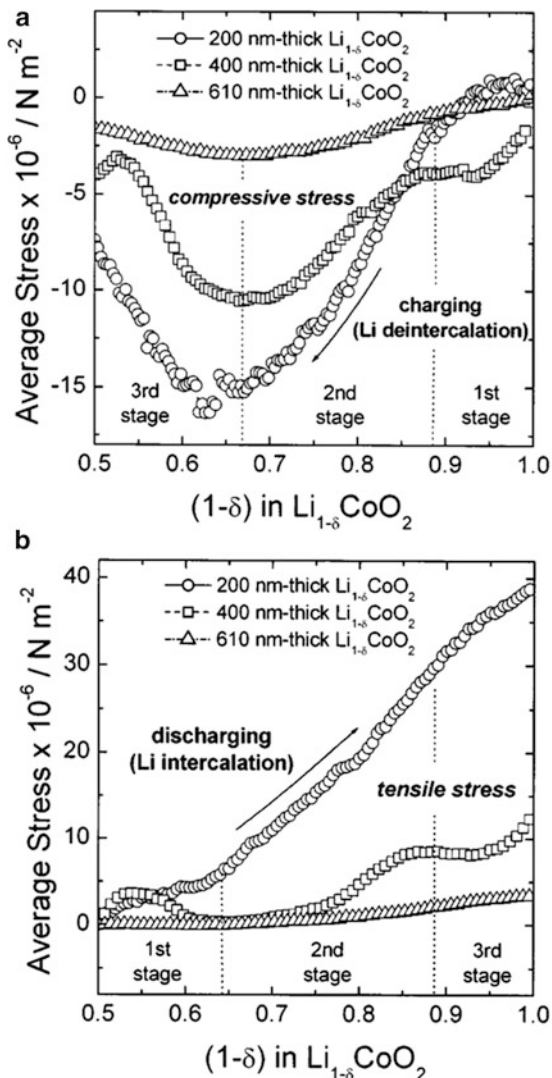
the films on the *AT* and *BT*-cut quartz crystals are nearly identical, whereas the changes in the normalized resonant frequency with lithium content look quite different: The frequency change curve of the *AT*-cut crystal shows an upward deviation from linearity, whereas that of the *BT*-cut crystal exhibits a downward one.

If the mass reduction of the films were the only source for Δf during the galvanostatic (or constant mass loss) situation, Δf would show a linear relationship with the lithium content [17, 18]. This deviation from linearity is known to arise mainly from the surface roughness of the film [38–40], the lateral stress in the film [19, 20], and the electrolyte viscosity [41]. Since the viscosity and roughness effects

can be considered to be trivial [25], the nonlinearity is most likely ascribed to the lateral stress. The Δf versus lithium content curves feature three different rates of frequency change, as indicated in Fig. 6.18b, which is possibly bound up with the phase transition during the lithium extraction based on the comparison of the stages in Fig. 6.18a, b. The Δf curves during the discharging process (i.e., lithium insertion into the films) proved to be quite consistent with the trend of the Δf curves during the charging process, in view of their upward/downward deviation from linearity and three different rates of change.

The lateral stresses that are produced in the films and then are exerted on the quartz crystals below them can be calculated from Eqs. 6.2, 6.3, and 6.4 on the basis of the resonant frequency changes of the AT-cut (Δf^{AT}) and BT-cut (Δf^{BT}) quartz crystals. Shown in Fig. 6.19a, b are the curves of the average stress change ($=$ stress integrated with respect to the film thickness ΔS divided by the film thickness) during the galvanostatic charging (lithium extraction) and discharging (lithium insertion) processes, respectively.

Compressive $(-)$ and tensile $(+)$ stresses are generated in the films during the charging (lithium extraction) and discharging (lithium insertion), respectively, and their magnitudes decrease as the film becomes thicker. The stress changes in the second stage (i.e., the phase transition region) are particularly large, regardless of the film thickness. The volume contraction and expansion of the film is the most plausible reason for the lateral stress, because the other possible effects, such as the electrostrictive force, formation of a surface layer, and surface tension due to the adsorption of some species from the electrolyte, can be considered to be extremely small [25].

References

1. Han JN, Pyun SI (2001) Application of laser beam deflection technique to analysis of stresses generated during hydrogen diffusion through Pd foil electrode. J Korean Electrochem Soc 4:70–76
2. Lewis FA, Kandasamy K, Baranowski B (1988) The "uphill" diffusion of hydrogen. Platinum Met Rev 32:22–26
3. Baranowski B (1989) Stress-induced diffusion in hydrogen permeation through $Pd_{81}Pt_{19}$ membranes. J Less-Common Met 154:329–353
4. Cermak J, Kufudakis A (1976) Diffusion-elastic phenomenon and diffusivity of hydrogen in nickel. J Less-Common Met 49:309–322
5. Kandasamy K (1995) Influences of self-induced stress on permeation flux and space-time variation of concentration during diffusion of hydrogen in a palladium alloy. Int J Hydrogen Energy 20:455–463
6. Sakamoto Y, Tanaka H, Lewis FA, Tong XQ, Kandasamy K (1996) "Uphill" hydrogen diffusion effects of hydrogen interstitial strain gradients in palladium and palladium alloys. Int J Hydrogen Energy 21:1025–1032
7. Cermak J, Kufudakis A, Lewis FA (1993) A comparison of measurements of diffusivity of hydrogen in Pd for three different diffusion-elastic processes. Z Phys Chem 181:233–238
8. Kim DJ, Pyun SI (1999) Stress generation and annihilation during hydrogen injection into and extraction from anodic WO_3 films. Electrochim Acta 44:1723–1732

9. Han JN, Pyun SI, Kim DJ (1999) Analysis of the compressive and tensile stresses generation/relaxation during hydrogen ingress into and egress from Pd foil electrode. Electrochim Acta 44:1797–1804
10. Han JN, Pyun SI (2000) Analysis of open-circuit potential transient and laser beam deflection transient simultaneously measured from Pd foil electrode pre-charged with hydrogen. Electrochim Acta 45:2781–2790
11. Pyun SI, Kim KH, Han JN (2000) Analysis of stresses generated during hydrogen extraction from and injection into Ni(OH)$_2$/NiOOH film electrode. J Power Sources 91:92–98
12. Han JN, Lee JW, Seo M, Pyun SI (2001) Analysis of stresses generated during hydrogen transport through a Pd foil electrode under potential sweep conditions. J Electroanal Chem 506:1–10
13. Pyun SI, Go JY, Jan TS (2004) An investigation of intercalation-induced stresses generated during lithium transport through Li$_{1-\delta}$CoO$_2$ film electrode using a laser beam deflection method. Electrochim Acta 49:4477–4486
14. Kim YH, Pyun SI, Go JY (2005) An investigation of intercalation-induced stresses generated during lithium transport through sol–gel derived Li$_x$Mn$_2$O$_4$ film electrode using a laser beam deflection method. Electrochim Acta 51:441–449
15. Crank J (1975) The mathematics of diffusion. Clarendon, Oxford/New York
16. Lu C, Czanderna AW (1984) Application of piezoelectric quartz crystal microbalances. Elsevier, New York
17. Sauerbrey G (1959) Verwendung von Schwingquarzen zur Wägung dünner Schichten und zur Mikrowägung. Z Phys A Hadron Nuclei 155:206–222
18. Lostis P (1959) The study, production and control of thin films giving a chosen path difference between perpendicularly polarized components. Rev Opt Theor Instr 38:1–5
19. EerNisse EP (1972) Simultaneous thin-film stress and mass-change measurements using quartz resonators. J Appl Phys 43:1330–1337
20. EerNisse EP (1973) Extension of the double resonator technique. J Appl Phys 44:4482–4485
21. Smyrl WH, Lien M (1992) New trends and approaches in electrochemical technology. Kodansha, Tokyo
22. Nelson JC, Oriani RA (1992) Stresses produced by the anodic oxidation of nickel. Electrochim Acta 37:2051–2057
23. Kim DJ, Pyun SI, Oriani RA (1996) Effects of chloride ion and applied current density on the stress generation during anodic oxidation of tungsten in 0.1 M H$_2$SO$_4$ solution. Electrochim Acta 41:57–62
24. West AR (1984) Solid state chemistry and its applications. Wiley, New York
25. Go JY, Pyun SI (2003) Investigation of stresses generated during lithium transport through the RF sputter-deposited Li$_{1-\delta}$CoO$_2$ film by a DQCR technique. J Electrochem Soc 150:A1037–A1043
26. Yang TH, Pyun SI (1996) Hydrogen absorption and diffusion into and in palladium: ac-impedance analysis under impermeable boundary conditions. Electrochim Acta 41:843–848
27. Yang TH, Pyun SI, Yoon YG (1997) Hydrogen transport through Pd electrode: current transient analysis. Electrochim Acta 42:1701–1708
28. Lim C, Pyun SI (1993) Theoretical approach to faradaic admittance of hydrogen absorption reaction on metal membrane electrode. Electrochim Acta 38:2645–2652
29. Ura H, Nishina T, Uchida I (1995) Electrochemical measurements of single particles of Pd and LaNi$_5$ with a microelectrode technique. J Electroanal Chem 396:169–173
30. Scarminio J, Talledo A, Andersson AA, Passerini DF (1993) Stress and electrochromism induced by Li insertion in crystalline and amorphous V$_2$O$_5$ thin film electrodes. Electrochim Acta 38:1637–1642
31. Lee SJ, Lee JK, Chung SH, Lee HY, Lee SM, Baik HK (2001) Stress effect on cycle properties of the silicon thin-film anode. J Power Sources 97–98:191–193
32. Chung KY, Kim KB (2002) Investigation of structural fatigue in spinel electrodes using in situ laser probe beam deflection technique. J Electrochem Soc 149:A79–A85

33. Pyun SI, Go JY, Jang TS (2004) An investigation of intercalation-induced stresses generated during lithium transport through $Li_{1-\delta}CoO_2$ film electrode using a laser beam deflection method. Electrochim Acta 49:4477–4486
34. Reimers JN, Dahn JR (1992) Electrochemical and in situ X-ray diffraction studies of lithium intercalation in Li_xCoO_2. J Electrochem Soc 139:2091–2097
35. Dieter GE (1988) Mechanical metallurgy. McGraw-Hill, Singapore
36. Kato M, Fujii T, Onaka S (1996) Elastic strain energies of sphere, plate and needle inclusions. Mater Sci Eng A 211:95–103
37. Bauccio M (1994) ASM engineered materials reference book, 2nd edn. ASM International, Materials Park
38. Schumacher R, Gordon JG, Melroy O (1987) Observation of morphological relaxation of copper and silver electrodes in solution using a quartz microbalance. J Electroanal Chem Interfacial Electrochem 216:127–135
39. Yang M, Thompson M (1993) Surface morphology and the response of the thickness-shear mode acoustic wave sensor in liquids. Langmuir 9:1990–1994
40. Martin SJ, Frye GC, Ricco AJ, Senturia SD (1993) Effect of surface roughness on the response of thickness-shear mode resonators in liquids. Anal Chem 65:2910–2922
41. Reed CE, Kanazawa KK, Kaufman JH (1990) Physical description of a viscoelastically loaded AT-cut quartz resonator. J Appl Phys 68:1993–2001

Chapter 7
Abnormal Behaviors in Hydrogen Transport: Importance of Interfacial Reactions

7.1 Interfacial Reactions Involved in Hydrogen Transport

As described in Sect. 3.1, the redox reactions of hydrogen absorption into and desorption from hydride-forming metals and oxides proceed via one of the following two mechanisms: (1) the one-step (direct) and (2) two-step mechanisms [1–3]. In both mechanisms, the (faradaic) charge-transfer reaction on the electrode surface is the essential step for hydrogen absorption and desorption, leading to reduced and oxidized species, respectively. Many of the ac-impedance results obtained on hydride-forming metals and oxides indicated slow charge-transfer kinetics, i.e., a large resistance for the charge-transfer reaction at the electrode/electrolyte interface [4–9]. In addition, physicochemical and electrochemical studies on Pt, Pd, and Ni single crystals demonstrated that an absorbed state for hydrogen exists at the electrode subsurface, which represents hydrogen atom residing just beneath the topmost surface layer [10–13]. This means that hydrogen transport in hydride-forming metals and oxides may involve the hydrogen transfer reaction between the adsorbed state (MH_{ads}) on the electrode surface and the absorbed state (MH_{abs}) at the electrode subsurface. As a result, one cannot rule out the possibility that in addition to hydrogen diffusion, interfacial charge transfer, hydrogen transfer, or both may determine the overall rate of hydrogen transport. In fact, abnormal behaviors in hydrogen transport have been revealed by current transient analysis, which showed a strong deviation from the diffusion-control model. The key feature is that the log (current I) versus log (time t) curve exhibits a simple two-stage shape, but the absolute value of its slope is lower than 0.5 in the early stage, and no plateau region appears in the plot of $It^{1/2}$ versus log t [14–18].

7.2 Hydrogen Diffusion Coupled with the Charge Transfer Reaction

The diffusion-control model assumes that the charge-transfer reaction on the electrode surface is too facile to affect hydrogen transport. From the thermodynamic viewpoint, this means that the interfacial charge-transfer reaction is practically undisturbed from the equilibrium (see Sect. 4.2). However, there is much experimental evidence which indicates that the charge-transfer rate is not sufficiently fast and that the kinetic limitation due to the charge-transfer reaction cannot be neglected. In this case, hydrogen diffusion and interfacial charge transfer may be disturbed from the equilibria, namely, hydrogen diffusion and interfacial charge transfer simultaneously determine the rate of hydrogen transport, i.e., a mixed control model by hydrogen diffusion and interfacial charge transfer.

7.2.1 Flat Electrode Surface

Chen et al. [15] formulated kinetic theories of hydrogen transport under the kinetic limitations due to interfacial charge transfer. They assumed that the insertion reaction can be represented by the charge-transfer resistance R_{ct} and the diffusion impedance Z_d in series, as discussed in Sect 4.2, and derived a theoretical expression for the current transient. The Laplace transform of the current response $\overline{I(s)}$ to a small potential step ΔE is related to the electrode impedance $Z(s)$ by

$$\overline{I(s)} = \frac{\Delta E}{sZ(s)} \tag{7.1}$$

where s is the Laplace complex variable. In the mixed control model by hydrogen diffusion and charge transfer, the electrode impedance is represented by the charge-transfer resistance R_{ct} and the diffusion impedance $Z_d(s)$ in series as follows:

$$Z(s) = R_{ct} + Z_d(s) \tag{7.2}$$

$Z_d(s)$ for an electrode with an impermeable boundary is expressed as

$$Z_d(s) = R_d \frac{\coth\left(sL^2/\tilde{D}_H\right)^{1/2}}{\left(sL^2/\tilde{D}_H\right)^{1/2}} \tag{7.3}$$

$$R_d = \frac{L}{FA_{ea}\tilde{D}_H}\left(\frac{dE}{dc_H}\right) \tag{7.4}$$

where R_d is the diffusion resistance, $\tilde{D}_H$ the chemical diffusivity of hydrogen, and L the electrode thickness.

If one defines $\Lambda = R_d/R_{ct}$, the Laplace transform of the current is then written as

$$\overline{I(s)} = \frac{(\Delta E/R_{ct})}{s\left[1 + \Lambda \coth\left(sL^2/\tilde{D}_H\right)^{1/2} \Big/ \left(sL^2/\tilde{D}_H\right)^{1/2}\right]} \tag{7.5}$$

Finally, the inverse Laplace transform of Eq. 7.5 yields the current-time relation:

$$I(t) = \frac{2\Delta E}{R_{ct}} \sum_{n=1}^{\infty} \frac{\Lambda}{\Lambda^2 + \Lambda + b_n^2} \exp\left(-\frac{b_n^2 \tilde{D}_H}{L^2}t\right) \tag{7.6}$$

where b_n is the n-th positive root of $(b \tan b - \Lambda = 0)$. For a small potential step ΔE (for hydrogen extraction), the relationship between the potential E and the hydrogen concentration c_H is given by

$$\Delta E = (E_{ext} - E_{ini}) = \left(\frac{dE}{dc_H}\right)(c_H^s - c_H^o) \tag{7.7}$$

where c_H^o and c_H^s denote the initial equilibrium and surface concentrations of hydrogen corresponding to E_{ini} and E_{ext}, respectively. The following theoretical expression for the current transient is obtained for the mixed control model by hydrogen diffusion and interfacial charge transfer:

$$I(t) = \frac{2FA_{ea}(c_H^o - c_H^s)\tilde{D}_H}{L} \sum_{n=1}^{\infty} \frac{\Lambda^2}{\Lambda^2 + \Lambda + b_n^2} \exp\left(-\frac{b_n^2 \tilde{D}_H}{L^2}t\right) \tag{7.8}$$

where A_{ea} is the electrochemical active area.

Equation 7.8 holds only when the potential step is so small that the relationship between the current I and the overpotential η can be linearized [19]. In simulation studies [17, 20], Pyun and coworkers considered the case where the charge-transfer reaction is represented by the Butler-Volmer kinetics. They assumed that the hydrogen flux at the electrode surface is determined by the rate of interfacial charge transfer represented by the Butler-Volmer equation. The boundary condition (BC) at the electrode surface is then written as

$$BC : I(t) = FA_{ea}\tilde{D}_H\left(\frac{\partial c_H}{\partial x}\right)$$

$$= I_o\left[\exp\left(\frac{(1-\alpha)F}{RT}(E_{ext} - E(t))\right) - \exp\left(-\frac{\alpha F}{RT}(E_{ext} - E(t))\right)\right]$$

(mixed control BC by hydrogen diffusion and interfacial charge transfer)
for $x = 0$ at $t \geq 0$ $\hspace{2cm}$ (7.9)

where I_o is the exchange current, α the transfer coefficient for hydrogen reduction, $(1 - \alpha)$ the transfer coefficient for hydrogen oxidation, and F the Faraday constant. The notations R and T are the symbols that are usually used. The equilibrium potential E in the Butler-Volmer equation is determined by the hydrogen concentration c_H at the electrode surface. Since c_H changes with time during hydrogen transport, E is a function of time. When simulating the anodic current transient, we used the functional relation between E and δ of Eq. 4.5 in Sect 4.1.

Figure 7.1a presents the log I versus log t curve calculated by jumping $E_{ini} = 0.01$ V to $E_{ext} = 0.08 - 0.16$ V [20]. The anodic current transient was calculated by assuming $L = 1$ cm, $A_{ea} = 1$ cm^2, and $F\tilde{D}_H = 1$ A cm^2 mol^{-1}. c_H was taken to be δ mol cm^{-3} for the molar volume of the electrode $V_m = 1$ cm^3 mol^{-1}. None of the current transients show Cottrell behavior. The absolute slope of the log I versus log t curve is smaller than 0.5. No plateau region (Cottrell region) is observed in the plots of $It^{1/2}$ against log t in Fig. 7.1b. The $It^{1/2}$ versus log t plot shows an upward convex shape and the time to its local maximum is shortened with increasing E_{ext}. As shown in Fig. 7.1a, the shape and value of the current transient strongly depend on the value of E_{ext}. At the moment of the potential jump ($t = 0$), the electrode potential $E(0)$ is equal to the initial electrode potential E_{ini}. When a relatively large potential jump $\Delta E = (E_{ext} - E_{ini})$ is applied across the electrode, the contribution of the cathodic current to the total current becomes negligibly small, so that the initial current I_{ini} at $t = 0$ is simply given by

$$I_{ini} = I(0) = I_o \exp\left(\frac{(1 - \alpha)F}{RT}\Delta E\right) \tag{7.10}$$

Equation 7.10 indicates that I_{ini} increases exponentially with increasing ΔE. The linear relationship between log I_{ini} and ΔE is a decisive piece of experimental evidence that hydrogen transport proceeds via the mixed control mechanism involving hydrogen diffusion and charge transfer. Figure 7.1c shows the hydrogen concentration profile transients simultaneously calculated with the anodic current transients in Fig. 7.1a. c_H at the electrode surface is not maintained to zero corresponding to E_{ext}, due to the kinetic limitations induced by charge transfer, but gradually goes to zero with time. Figure 7.2a shows the typical log I versus log t curves measured on a Pd electrode in 0.1 M NaOH solution [17]. The current transients were measured by jumping $E_{ini} = -0.02$ V (RHE) to $E_{ini} = 0.2 - 0.6$ V (RHE). The dependence of log I_{ini} on ΔE observed at 0.5 s is also illustrated in Fig. 7.2b. The absolute slope increases with increasing E_{ext}, and log I_{ini} is linearly proportional to ΔE. As shown in Fig. 7.2b, the measured I_{ini} can be fitted to I_{ini} calculated from the Butler-Volmer equation with $I_o = 3.4 \times 10^{-5}$ A and $\alpha = 0.64$. The fitted values of I_o and α are comparable to those determined by Enyo and Biswas [21].

Another example of the mixed control model is found in an Mm (Ni$_{3.6}$Co$_{0.7}$Mn$_{0.4}$Al$_{0.3}$)$_{1.12}$ electrode. Figure 7.3a presents the log i versus log t curves measured from the Mm(Ni$_{3.6}$Co$_{0.7}$Mn$_{0.4}$Al$_{0.3}$)$_{1.12}$ electrode in 6 M KOH

Fig. 7.1 (**a**) log I versus log t curve, (**b**) $It^{1/2}$ versus log t plot, and (**c**) the hydrogen concentration profile transients calculated by jumping $E_{ini} = 0.01$ V to $E_{ext} = 0.08$–0.16 V (Reprinted from Lee and Pyun [20], Copyright ©2005 with permission from Elsevier Science)
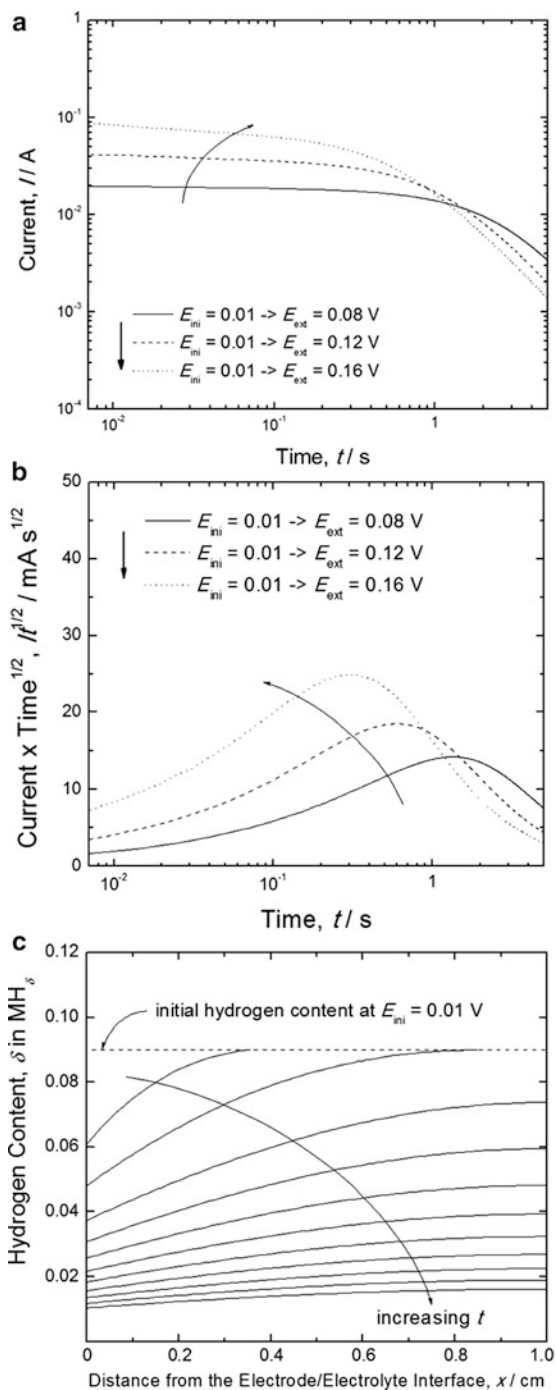
Fig. 7.2 (**a**) log I versus log t curves and (**b**) the dependence of log I_{ini} on ΔE measured on a Pd electrode in 0.1 M NaOH solution (Reprinted from Han et al. [17], Copyright ©2001 with permission from Elsevier Science)
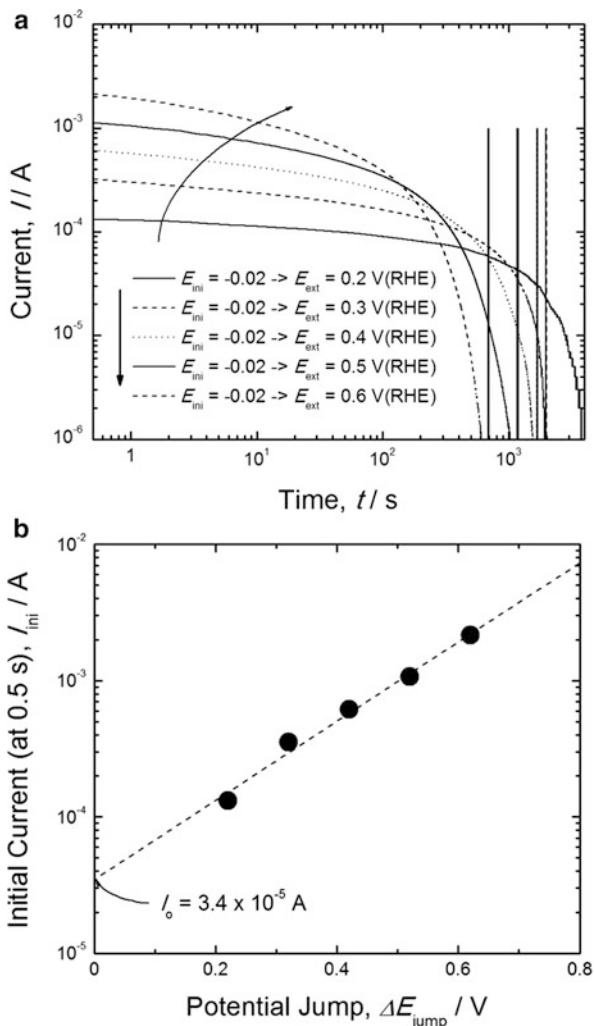
solution by jumping $E_{ini} = -1.0$ V(Hg/HgO) to $E_{ext} = -0.85$ to -0.65 V(Hg/HgO) [22]. The anodic current transient shows a linear relationship between log i and log t with an absolute slope of between 0 and 0.5, followed by the exponential decay of the current density with time. The initial current density i_{ini} observed at 1 s is plotted in Fig. 7.3b as a function of E_{ext}. In order to more clearly specify the boundary condition at the electrode surface during hydrogen extraction, the values of i_{ini} at 1 s were theoretically determined from Eq. 7.10, and then quantitatively compared with the value of i_{ini} measured experimentally. It can be seen from Fig. 7.3b that the measured value of i_{ini} is consistent with that calculated from Eq. 7.10, implying that the mixed control BC of Eq. 7.9 is satisfied at the electrode surface.

Fig. 7.3 (**a**) log i versus log t curves and (**b**) the dependence of log i_{ini} on E_{ext} measured from the Mm $(Ni_{3.6}Co_{0.7}Mn_{0.4}Al_{0.3})_{1.12}$ electrode in 6 M KOH solution (Reprinted from Lee et al. [22], Copyright ©2005 with permission from Elsevier Science)
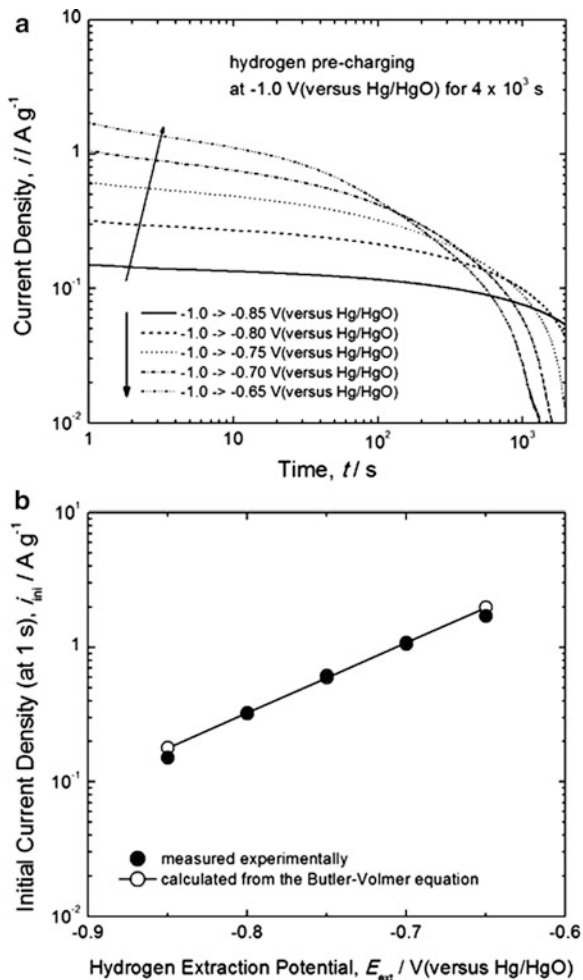
Han et al. [23] later found that the mixed control BC of Eq. 7.9 is not restricted to hydrogen transport during the current transient experiment, but it is also appropriate for hydrogen transport during cyclic voltammetric measurements, depending on the scan rate. The linear sweep voltammograms measured on a Pd electrode in 0.1 M NaOH solution are displayed for various scan rates in Fig. 7.4a [23]. In the case where c_H at the electrode surface is determined by the applied potential E_{app}, the relation between the peak current density i_p and the scan rate v is theoretically well established under the impermeable boundary condition as follows [24–26]:

$$i_p = 0.046F\left(\frac{c_H^o \tilde{D}_H}{L}\right)w^{1/2} \tanh(0.56w^{1/2} + 0.05w) \qquad (7.11)$$

Fig. 7.4 (a) Linear sweep voltammograms and (b) the dependence of the peak current density on the scan rate measured on a Pd electrode in 0.1 M NaOH solution (Reprinted from Han et al. [23], Copyright ©2001 with permission from Elsevier Science)
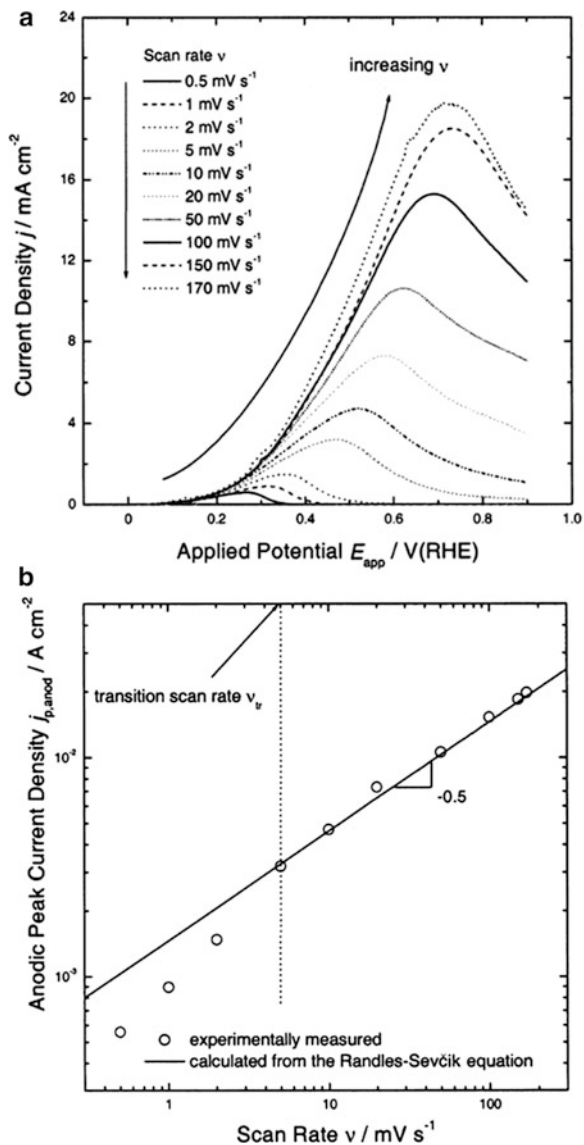
$$w = \left(\frac{F}{RT}\right)\frac{vL^2}{\tilde{D}_H} \tag{7.12}$$

Equation 7.11 is called the Randles-Sevčik equation. The experimental log i_p versus log v curve is plotted in Fig. 7.4b. The anodic peak current density i_p was calculated as a function of v, and the result is presented in the form of a solid line in Fig. 7.4b. The experimental data follow the Randles-Sevčik relation above 5 mV s^{-1}; however, it deviates from the Randles-Sevčik relation below

$5 \, \text{mV s}^{-1}$. This means that above $5 \, \text{mV s}^{-1}$ c_H at the electrode surface is determined by E_{app} whereas, below $5 \, \text{mV s}^{-1}$, it is no longer determined by E_{app}. Taking into account that, in the low scan rate range, the hydrogen flux induced by the charge-transfer reaction at the electrode surface is smaller than that induced by diffusion inside the electrode, it is reasonable to suppose that the change in c_H at the electrode surface with time is given by the Butler-Volmer equation under the potential sweep condition.

7.2.2   Rough Electrode Surface

On the basis of fractal geometry, Lee and Pyun [27] examined hydrogen transport from the bulk electrode matrix toward the rough electrode surface under mixed control *BC* by hydrogen diffusion and interfacial charge transfer. They used a kinetic Monte Carlo (*MC*) simulation based upon the random walk approach [28, 29]. The current transients were theoretically calculated using the fractal surface generated by the Weierstrass function (see Sect. 4.3.2) [30]. More information on fractal geometry can be found in Chap. 9. Under the mixed control *BC*, the current *I* is limited by the rate of interfacial charge transfer represented by the Butler-Volmer equation. In the *MC* simulation, the jump probability of hydrogen W_{tr} across the electrode/electrolyte interface should take the same form as the Butler-Volmer equation of Eq. 7.13,

$$W_{tr} = f \left[\exp\left(\frac{(1-\alpha)F}{RT} (E_{ext} - E(t)) \right) - \exp\left(-\frac{\alpha F}{RT} (E_{ext} - E(t)) \right) \right] \quad (7.13)$$

where f designates a dimensionless conversion factor, which represents the exchange current I_o or the rate constant of charge transfer k^o in I_o. f was arbitrarily taken as a value below unity, so W_{tr} in Eq. 7.13 is a dimensionless parameter with a value below unity ($0 \le W_{tr} < 1$).

   Figure 7.5 presents the log I versus log t curves calculated from the flat electrode with $d_{F,ss} = 1.0$ and the fractal electrodes with $d_{F,ss} = 1.32$ and 1.47 by jumping $E_{ini} = 0.024 \, \text{V}$ to $E_{ext} = 0.08 \, \text{V}$ [27]. The simulation was performed with $f = 2 \times 10^{-3}$. The logarithmic current transient computed from the flat electrode with $d_{F,ss} = 1.0$ shows an absolute slope of log I with log t flatter than 0.5, followed by a monotonic increase with time, which is a typical feature of the current transient under the mixed control *BC*. On the other hand, an inflection point appears at $t = \text{ca. } 1{,}200$ Monte Carlo steps (*MCS*) in both current transients simulated from the fractal electrodes with $d_{F,ss} = 1.32$ and 1.47. Figure 7.6a, b shows the concentration profiles of hydrogen in the fractal electrode with $d_{F,ss} = 1.47$ computed at $t = 150 \, MCS$ before the occurrence of the inflection point and at $t = 1{,}250 \, MCS$ just after the appearance of the inflection point, respectively [27]. The local concentrations of hydrogen in the electrode were marked in different contrast levels from white for $\delta = 0$–0.02 to black for $\delta = 0.08$–0.1.

Fig. 7.5 log I versus log t curves calculated from the flat electrode with $d_{F,ss} = 1.0$ and the fractal electrodes with $d_{F,ss} = 1.32$ and 1.47. Note that the values of I for $d_{F,ss} = 1.32$ and 1.47 were multiplied by the factors 2.0 and 4.0, respectively (Reprinted from Lee and Pyun [27], Copyright ©2005 with permission from Elsevier Science)
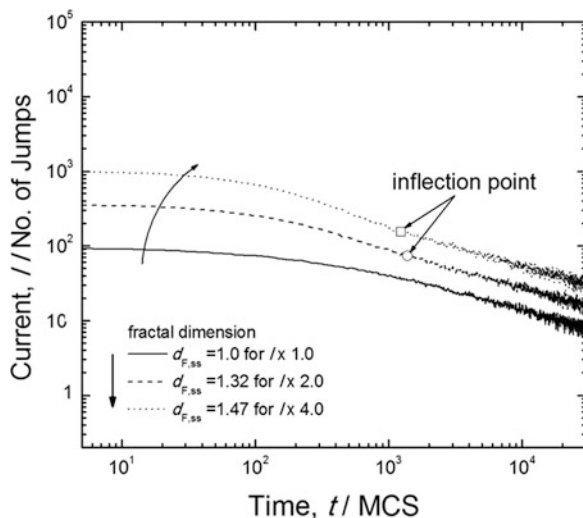
At $t = 150$ MCS, only those hydrogen atoms residing in the vicinity of the electrode surface are extracted from the electrode and, hence, the equiconcentration lines in the diffusion layer tend to follow the fractal topography of the electrode surface. At $t = 1,250$ MCS, on the other hand, the shape of the equiconcentration lines in the diffusion layer is no longer similar to that of the fractal topography of the electrode surface, but is nearly flat. As a result, the simulation analysis demonstrates that the inflection point is caused by the fractal to flat transition of the current transient; namely, the current transient under the mixed control BC exhibits an inflection point at a time that corresponds to the temporal outer cutoff τ_o of fractality. The results in Figs. 7.5 and 7.6 are summarized as follows:

1. At $t < \tau_o$, the diffusing hydrogen senses the fractal electrode surface with the microscopic area.
2. As the time goes on, the diffusion layer grows from the electrode surface and, thus, the equiconcentration lines in the diffusion layer resemble less and less the fractal topography of the electrode surface.
3. At $t > \tau_o$, the equiconcentration lines in the diffusion layer become straight, and the thickness of the diffusion layer exceeds the spatial outer cutoff λ_o of fractality, so that the diffusing hydrogen senses the flat electrode surface with the geometric area.

Figure 7.7a, b illustrates the effects of f and ΔE on the current transients calculated for hydrogen transport through the fractal electrode with $d_{F,ss} = 1.47$, respectively [27]. As the values of the simulation parameters, f and ΔE, increase, the current decays more rapidly with time until τ_o is encountered and, at the same time, τ_o is gradually shortened. The values of k^o and ΔE increase the rate of interfacial charge transfer (see Eq. 7.13) and, thus, τ_o decreases with increasing f and ΔE.

Fig. 7.6 Concentration profiles of hydrogen in the fractal electrode with $d_{F,ss} = 1.47$ computed (**a**) at $t = 150$ MCS and (**b**) at $t = 1250$ MCS (Reprinted from Lee and Pyun [27], Copyright ©2005 with permission from Elsevier Science)
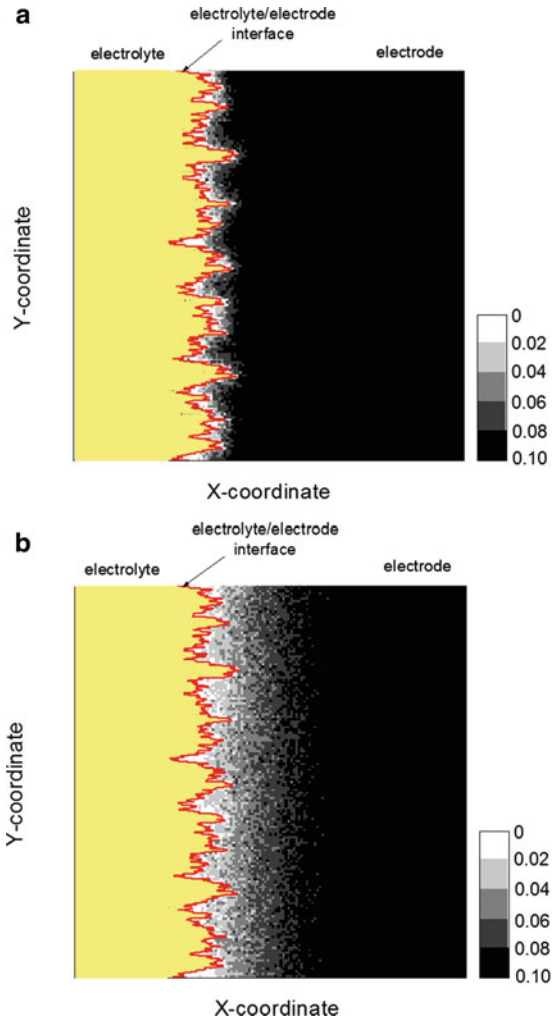
7.3   Hydrogen Diffusion Coupled with the Hydrogen Transfer Reaction

Yang et al. [31, 32] first performed galvanostatic potential transient experiments to systematically study hydrogen transport under the influence of the hydrogen transfer reaction. In their works, theoretical formulations were made for the galvanostatic discharge process including hydrogen diffusion followed by the hydrogen transfer reaction, and the experimental data obtained from Zr-based amorphous alloys were found to be successfully explained by the theoretical model. The current transient behaviors for the mixed control by hydrogen diffusion and hydrogen transfer were examined for spherical particles of metal hydrides and

Fig. 7.7 Effects of (**a**) f and (**b**) ΔE on the current transients calculated for hydrogen transport through the fractal electrode with $d_{F,ss} = 1.47$ (Reprinted from Lee and Pyun [27], Copyright ©2005 with permission from Elsevier Science)
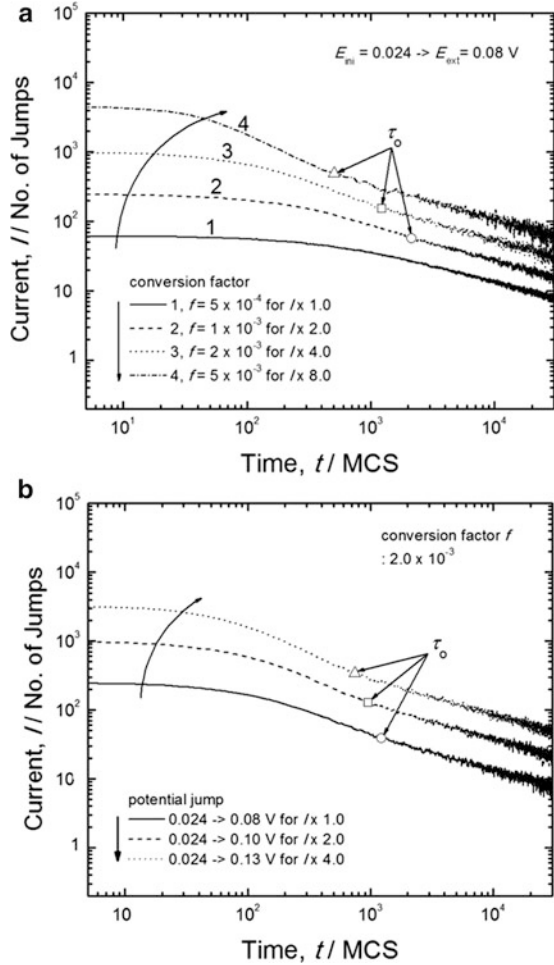
for amorphous $Pd_{82-y}Ni_ySi_{18}$ ($y = 0$–32) alloy foils [16, 18, 33]. When the equilibria for both hydrogen diffusion and hydrogen transfer are noticeably disturbed, while the interfacial charge transfer is practically undisturbed, the following BC is established at the electrode surface during the anodic current transient experiment [18]:

$$BC : I(t) = FA_{ea}\tilde{D}_H\left(\frac{\partial c_H}{\partial x}\right) = FA_{ea}\left[k_f\left(\frac{c_H}{c_H^{max}}\right)(1-\theta_H) - k_b\,\theta_H\left(1 - \left(\frac{c_H}{c_H^{max}}\right)\right)\right]$$

(mixed control BC by hydrogen diffusion and hydrogen transfer)

$$\text{for } x = 0 \text{ at } t \geq 0 \tag{7.14}$$

where k_f is the forward rate constant of hydrogen transfer from MH_{abs} to MH_{ads}; k_b, the backward rate constant of hydrogen transfer from MH_{ads} to MH_{abs}; θ_H, the surface coverage of adsorbed hydrogen; and c_H^{max}, the maximum available concentration of hydrogen which is equal to the total number of interstitial sites available for hydrogen.

It is assumed that the charge-transfer kinetics is so facile that the hydrogen adsorbed on the electrode surface resulting from the preceding hydrogen transfer reaction can be immediately oxidized. This means that the value of θ_H approaches zero at the moment of the potential jump. The backward transfer reaction, i.e., hydrogen transfer of MH_{ads} to MH_{abs}, can be then neglected and Eq. 7.14 can be simplified as:

$$BC: I(t) = FA_{ea}\tilde{D}_H\left(\frac{\partial c_H}{\partial x}\right) = FA_{ea}k_f\left(\frac{c_H}{c_H^{max}}\right)$$
$$\text{for } x = 0 \text{ at } t \geq 0 \qquad (7.15)$$

The parameter (c_H/c_H^{max}) means the fraction of absorbed states occupied at the electrode subsurface. Equation 7.15 is equivalent to the BC involved in the diffusion process coupled with the surface evaporation reaction for which the mathematical treatment can be readily made under semi-infinite and finite diffusion conditions [34].

The analytical solution to the diffusion equation under the BC of Eq. 7.15 can be derived as follows: From the Laplace transform of diffusion equation under the semi-infinite diffusion condition, one can obtain the Laplace transform of c_H:

$$\overline{c_H(x,s)} = \frac{c_H^o}{s} - \frac{c_H^o H}{s(H + s^{1/2})}\exp\left(-\frac{s^{1/2}x}{\tilde{D}_H^{1/2}}\right) \qquad (7.16)$$

$$H = \frac{k_f}{\tilde{D}_H^{1/2} c_H^{max}} \qquad (7.17)$$

Now one obtains the current expression:

$$\overline{I(s)} = FA_{ea}\tilde{D}_H\left(\frac{\partial \overline{c_H}}{\partial x}\right) = \frac{FA_{ea}\tilde{D}_H^{1/2}c_H^o H}{s^{1/2}(H + s^{1/2})} \quad \text{for } x = 0 \text{ at } t \geq 0 \qquad (7.18)$$

Finally, the inverse Laplace transform of Eq. 7.18 gives the following current-time relation:

$$I(t) = FA_{ea}\tilde{D}_H^{1/2} c_H^o H \exp(H^2 t)\,\text{erfc}(Ht^{1/2})$$
$$= FA_{ea}\left(\frac{k_f}{c_H^{max}}\right)c_H^o \exp\left[\left(\frac{k_f}{c_H^{max}}\right)^2 \frac{t}{\tilde{D}_H}\right]\text{erfc}\left[\left(\frac{k_f}{c_H^{max}}\right)\left(\frac{t}{\tilde{D}_H}\right)^{1/2}\right] \qquad (7.19)$$

At very short times, the factor $\exp(H^2 t)\,\mathrm{erfc}(Ht^{1/2})$ can be linearized and, thus, Eq. 7.19 can be written as

$$I(t) = FA_{ea}\left(\frac{k_f}{c_H^{max}}\right)c_H^o\left[1 - \frac{2}{\pi^{1/2}}\left(\frac{k_f}{c_H^{max}}\right)\left(\frac{t}{\tilde{D}_H}\right)^{1/2}\right] \tag{7.20}$$

The theoretical expressions for the current transient of Eqs. 7.19 and 7.20 can be used to estimate the kinetic parameters of the rate constant of hydrogen transfer and the hydrogen diffusivity.

Figure 7.8a illustrates the log I versus log t curves calculated by jumping $E_{ini} = 0.01\,\mathrm{V}$ to $E_{ext} = 0.08$ V under the impermeable BC [20]. The simulated current transient exhibits a linear relationship between log I and log t with an absolute slope lower than 0.5, followed by a rapid fall of the current with time. As the value of k_f increases from 2×10^{-6} to 2×10^{-5} mol cm^{-2} s^{-1}, the current level in the early stage increases and, at the same time, the absolute slope of the logarithmic current transient rises. In addition, the plot of $It^{1/2}$ vs. log t in Fig. 7.8b shows no plateau region with Cottrell character, but exhibits an upward convex shape with a local maximum. It should be noted that the value of I_{ini} under the mixed control BC by hydrogen diffusion and hydrogen transfer is linearly proportional to k_f. However, I_{ini} should remain constant, irrespective of the value of ΔE, because k_f is essentially independent of ΔE. Similar to the case of the mixed control by hydrogen diffusion and charge transfer, Fig. 7.8c shows that c_H at the electrode surface gradually decreases with time, because of the kinetic limitations induced by hydrogen transfer.

Figure 7.9a displays the log I versus log t curve measured on the amorphous $Pd_{82}Si_{18}$ electrode in 0.1 M NaOH solution by jumping $E_{ini} = -0.1$ V(RHE) to $E_{ext} = 0.9$ V(RHE) [18]. The value of I_{ini} determined at 0.2 s from the anodic current transient is also plotted in Fig. 7.9b as a function of ΔE. Three remarks should be made concerning the experimental current transients:

1. The Cottrell relationship between log I and log t is not observed in the anodic current transient.
2. The value of log I_{ini} remains almost constant, irrespective of ΔE.
3. The measured anodic current transient can be fitted quite well to that theoretically calculated from Eq. 7.20, as shown in the inset of Fig. 7.9a. $\tilde{D}_H$ and $k_f(c_{max})^{-1}$ in Eq. 7.20 were used as variable parameters. $\tilde{D}_H = 1.6 \times 10^{-8}\mathrm{cm}^2\mathrm{s}^{-1}$ and $k_f(c_{max})^{-1} = 2.3 \times 10^{-4}$ cm s^{-1} gave the best fit to the experimental data.

The results in Fig. 7.9 indicate that hydrogen transport through the amorphous $Pd_{82}Si_{18}$ electrode proceeds via the mixed control mechanism involving hydrogen diffusion and hydrogen transfer.

The rate constant of hydrogen transfer k_f, which determines the shape and value of the current transient, may depend on the nature of the electrode surface [18]. As an example, Fig. 7.10 displays the value of $k_f(c_{max})^{-1}$ as a function of the Ni content y in $Pd_{82-y}Ni_ySi_{18}$. The value of $k_f(c_{max})^{-1}$ is $(2.4 \pm 0.4) \times 10^{-4}$ cm s^{-1},

Fig. 7.8 (**a**) log I versus log t curve, (**b**) $It^{1/2}$ versus log t plot, and (**c**) the hydrogen concentration profile transients calculated by jumping $E_{ini} = 0.01$ V to $E_{ext} = 0.08$ V (Reprinted from Lee and Pyun [20], Copyright ©2005 with permission from Elsevier Science)

irrespective of the Ni content [18]. It is difficult to determine quantitatively the rate constant of hydrogen transfer k_f from the value of $k_f(c_{max})^{-1}$ because c_{max} is not known. Considering the significant decrease of c^o with the Ni content due to the lower solubility of hydrogen in Ni, it can be assumed that c_{max} decreases with increasing Ni content. It is thus inferred that k_f decreases with increasing Ni content. The cyclic voltammograms on the Ni-free Pd$_{82}$Si$_{18}$ and Ni-containing Pd$_{50}$Ni$_{32}$Si$_{18}$ electrodes given in Fig. 7.11 indicate that an Ni(OH)$_2$ layer is formed partly on the surface of the Ni-containing electrode [18]. From the fact that the value of k_f decreases with increasing Ni content (or with increasing surface coverage by Ni (OH)$_2$ phase), it seems that the Ni(OH)$_2$ layer on the electrode surface may act as an effective barrier to hydrogen extraction from the electrode by reducing the rate constant of hydrogen transfer k_f [35, 36].

Fig. 7.10 Plot of $k_f(c_{max})^{-1}$ versus Ni content y in $Pd_{82-y}Ni_ySi_{18}$ (Reprinted from Lee et al. [18], Copyright ©2003 with permission from Elsevier Science)
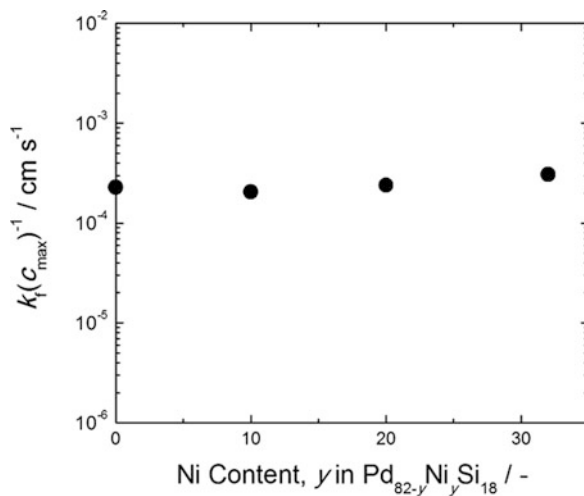
Fig. 7.11 Cyclic voltammograms measured on Ni-free $Pd_{82}Si_{18}$ and Ni-containing $Pd_{50}Ni_{32}Si_{18}$ electrodes (Reprinted from Lee et al. [18], Copyright ©2003 with permission from Elsevier Science)
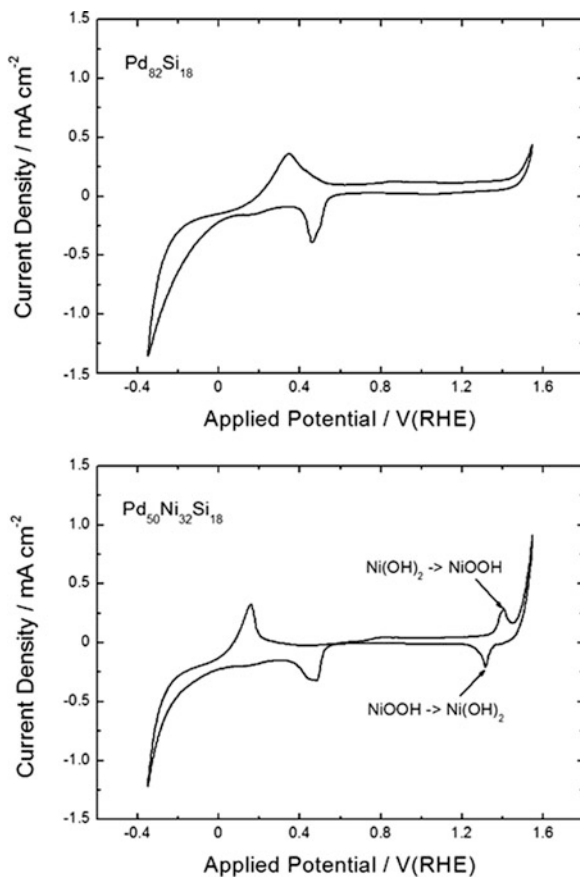
Fig. 7.12 log I versus log
t curves measured on a Pd
electrode in 0.1 M NaOH
solution by jumping
$E_{ini} = -0.02$ V(RHE) to
$E_{ext} = 0.9$ V(RHE). Different
distances d between the
working and reference
electrodes were used in an
electrochemical cell
(Reprinted from Han et al.
[17], Copyright ©2001 with
permission from Elsevier
Science)
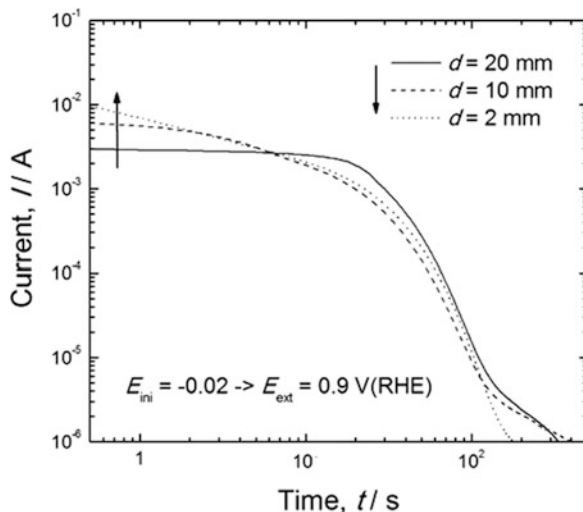
7.4 Change in Boundary Condition with Driving Force for Hydrogen Transport

The boundary condition at the electrode surface for hydrogen transport is not fixed at the specific electrode/electrolyte system by itself, but it is determined at any electrode/electrolyte system by the applied potential step, the overpotential induced by the electrolyte resistance and/or the nature of the electrode surface.

7.4.1 Effect of Ohmic Potential Drop

An ohmic potential drop due to the uncompensated solution resistance R_S, i.e., the overpotential induced by IR_S, must be minimized in the current transient experiment. However, it is very difficult to totally eliminate the overpotential induced by IR_S, even when a Luggin probe and IR_S compensation device are used. The overpotential induced by IR_S affects the effective potential step $\Delta E(\text{eff}) = \{E_{ext} - E(t) - IR_S\}$ applied across the electrode and, hence, the BC at the electrode surface for hydrogen transport. Figure 7.12 shows the log I versus log t curves measured on the Pd electrode in 0.1 M NaOH solution by jumping $E_{ini} = -0.02$ V (RHE) to $E_{ext} = 0.9$ V(RHE) [17]. Different distances d between the working and reference electrodes were used. As d decreases from 20 to 2 mm, the absolute slope of the log I versus log t curve increases from ca. 0 to 0.5. The overpotential induced by IR_S is linearly proportional to the value of d in an electrochemical cell with a planar configuration. Taking into account that the larger the value of IR_S, the smaller the magnitude of the effective potential jump, $\Delta E(\text{eff})$, applied across the electrode, it seems that the mixed control BC by hydrogen diffusion and charge

Fig. 7.13 Plot of log I_{ini} versus E_{ext} measured on a Pd foil electrode in 0.1 M NaOH solution (Reprinted from Han et al. [17], Copyright ©2001 with permission from Elsevier Science)
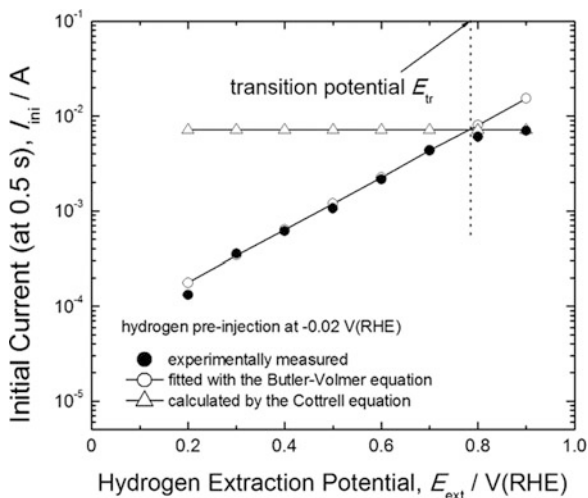
transfer is valid for a large overpotential induced by IR_S, while the diffusion-control BC is satisfied for a small overpotential induced by IR_S.

7.4.2   Effect of Potential Step

Figure 7.13 presents the plot of log I_{ini} versus E_{ext}, obtained from the Pd foil electrode in 0.1 M NaOH solution [22]. The value of log I_{ini} increases linearly with increasing E_{ext} up to ca. 0.8 V(RHE) and then remains nearly constant regardless of E_{ext}:

1. At $E_{ext} < 0.8$ V(RHE), the measured I_{ini} can be fitted well with the value calculated from the Butler-Volmer equation. This means that the mixed control BC by hydrogen diffusion and charge transfer is effective at the electrode surface during hydrogen transport.
2. At $E_{ext} > 0.8$ V(RHE), the measured value of I_{ini} is almost identical to that theoretically calculated from the Cottrell equation. This clearly indicates that the diffusion-control BC is valid at the electrode surface.

In Fig. 7.13, the transition potential E_{tr} is defined as E_{ext} at which the plot of log I_{ini} against E_{ext} determined from the Butler-Volmer equation intersects that plot of log I_{ini} versus E_{ext} calculated from the Cottrell equation. Similar to the case of the Pd electrode, Fig. 7.14 shows that a transition of the boundary condition occurs at the $Mm(Ni_{3.6}Co_{0.7}Mn_{0.4}Al_{0.3})_{1.12}$ electrode surface from mixed control to diffusion control when the potential step exceeds a certain value [22].
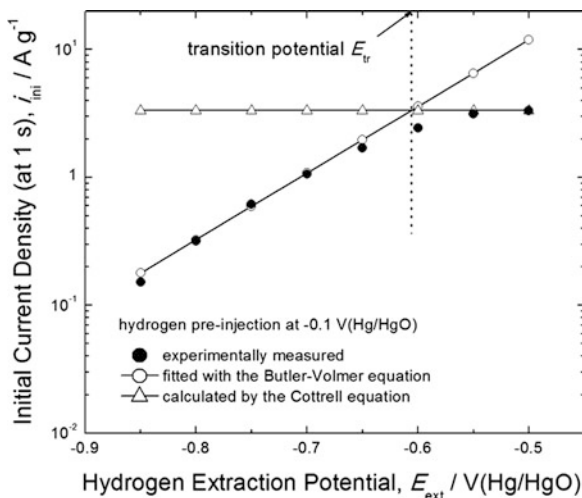
Fig. 7.14 Plot of log i_{ini} versus E_{ext} measured on an $Mm(Ni_{3.6}Co_{0.7}Mn_{0.4}Al_{0.3})_{1.12}$ electrode in 6 M KOH solution (Reprinted from Lee et al. [22], Copyright ©2005 with permission from Elsevier Science)

7.4.3   Effect of Surface Properties

Figure 7.15a compares the anodic current transients obtained from the as-annealed and as-surface-treated $Zr_{0.65}Ti_{0.35}Ni_{1.2}V_{0.4}Mn_{0.4}$ hydride electrodes in 6 M KOH solution [22]. The $Zr_{0.65}Ti_{0.35}Ni_{1.2}V_{0.4}Mn_{0.4}$ alloy is very susceptible to oxidation during the alloy preparation process involving arc-melting and annealing treatment and, hence, its surface is usually covered with dense and passive oxide scales such as ZrO_2 and V_2O_5 [36–40]. The as-annealed $Zr_{0.65}Ti_{0.35}Ni_{1.2}V_{0.4}Mn_{0.4}$ electrode was immersed in boiling 6 M KOH solution to remove the surface oxide scales. Figure 7.16a, b presents the results of energy dispersive spectroscopy (*EDS*) determined from the as-annealed and as-surface-treated $Zr_{0.65}Ti_{0.35}Ni_{1.2}V_{0.4}Mn_{0.4}$ electrodes, respectively [22]. The Zr L_a, Ti K_a, V K_a, and Mn K_a peaks shown in the *EDS* spectra of the as-annealed electrode disappear completely in the *EDS* spectra of the as-surface-treated electrode. The intensities of the Ni peaks of L_a and K_a in Fig. 7.16b were found to be much larger than those in Fig. 7.16a. These results indicate that the oxide scales on the surface of the as-annealed electrode were removed by the surface treatment, and at the same time the metallic Ni was enriched on the surface of the as-surface-treated electrode [41].

As shown in Fig. 7.15a, the log I_{ini} versus E_{ext} curve obtained from the as-annealed electrode exhibits an absolute slope flatter than 0.5. The fact that the theoretically calculated anodic current transient is consistent with the experimentally measured one as shown in Fig. 7.15b confirms that the mixed control *BC* by hydrogen diffusion and hydrogen transfer is effective at the electrode surface for hydrogen extraction. On the other hand, the current transient obtained from the
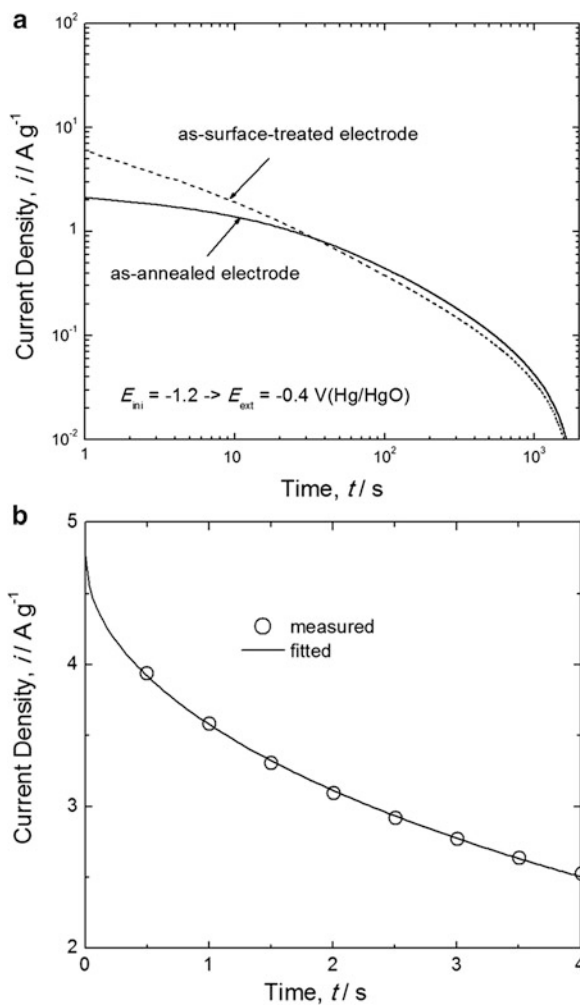
Fig. 7.15 log *I* versus log *t* curves obtained from as-annealed and as-surface-treated $Zr_{0.65}Ti_{0.35}Ni_{1.2}V_{0.4}Mn_{0.4}$ hydride electrodes in 6 M KOH solution (Reprinted from Lee et al. [22], Copyright ©2005 with permission from Elsevier Science)
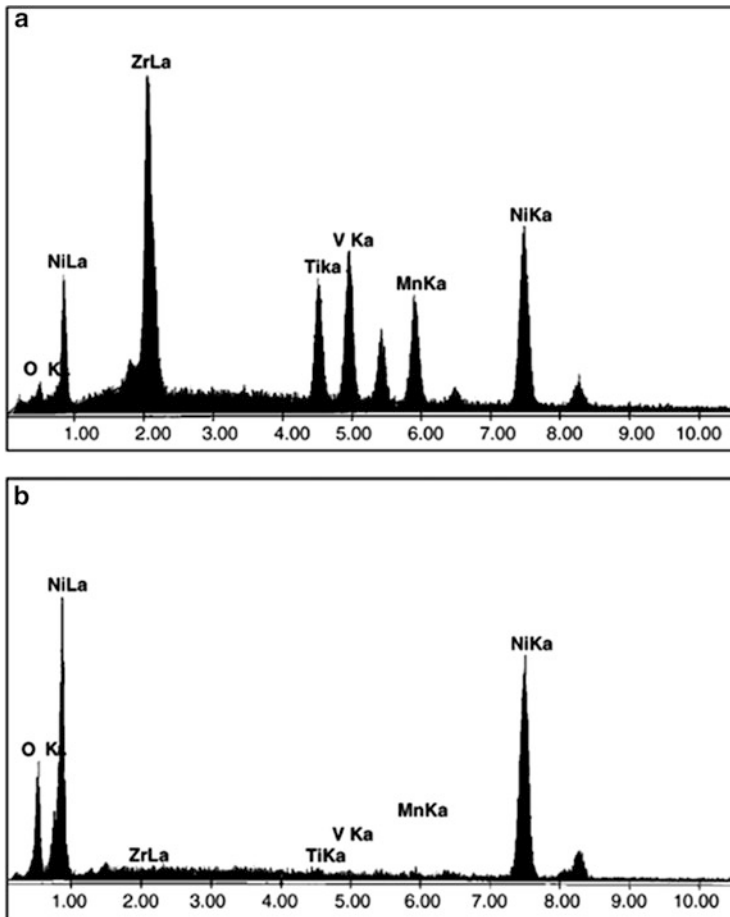
Fig. 7.16 *EDS* spectra determined from (**a**) as-annealed and (**b**) as-surface-treated $Zr_{0.65}Ti_{0.35}Ni_{1.2}V_{0.4}Mn_{0.4}$ electrodes (Reprinted from Lee et al. [22], Copyright ©2005 with permission from Elsevier Science)

as-surface-treated electrode in Fig. 7.15a shows Cottrell behavior, which suggests that the diffusion-control *BC* is valid for hydrogen extraction.

References

1. Yang TH, Pyun SI (1996) An investigation of the hydrogen absorption reaction into, and the hydrogen evolution reaction from, a Pd foil electrode. J Electroanal Chem 414:127–133
2. Montella C (1999) Discussion on permeation transients in terms of insertion reaction mechanism and kinetics. J Electroanal Chem 465:37–50

3. Conway BE, Jerkiewicz G (1993) Thermodynamic and electrode kinetic factors in cathodic hydrogen sorption into metals and its relationship to hydrogen adsorption and poisoning. J Electroanal Chem 357:47–66

4. Yang TH, Pyun SI (1996) Hydrogen absorption and diffusion into and in palladium: ac-impedance analysis under impermeable boundary conditions. Electrochim Acta 41:843–848

5. Yang TH, Pyun SI (1996) A study of hydrogen absorption reaction into α- and β-LaNi$_5$H$_x$ porous electrodes by using electrochemical impedance spectroscopy. J Power Sources 62:175–178

6. Wang C (1998) Kinetic behavior of metal hydride electrode by means of ac impedance. J Electrochem Soc 145:1801–1812

7. Yuan X, Xu N (2002) Electrochemical and hydrogen transport kinetic performance of MlNi$_{3.75}$Co$_{0.65}$Mn$_{0.4}$Al$_{0.2}$ metal hydride electrodes at various temperatures. J Electrochem Soc 149:A407–A413

8. Georén P, Hjelm AK, Lindbergh G, Lundqvist A (2003) An electrochemical impedance spectroscopy method applied to porous LiMn$_2$O$_4$ and metal hydride battery electrodes. J Electrochem Soc 150:A234–A241

9. Yuan X, Xu N (2001) Comparative study on electrochemical techniques for determination of hydrogen diffusion coefficients in metal hydride electrodes. J Appl Electrochem 31:1033–1039

10. Eberhardt W, Greuter F, Plummer EW (1981) Bonding of H to Ni, Pd, and Pt surfaces. Phys Rev Lett 46:1085–1088

11. Chan CT, Louie SG (1983) Electronic structure of subsurface and surface chemisorption for hydrogen on the Pd(111) surface. Solid State Commun 48:417–420

12. Felter TE, Foiles SM, Daw MS, Stulen RH (1986) Order–disorder transitions and subsurface occupation for hydrogen on Pd(111). Surf Sci 171:L379–L386

13. Kristen E, Parschau G, Stocker S, Rieder KH (1990) Successive population of subsurface and surface sites upon hydrogen chemisorption on 1 × 2-reconstructed Pt(110). Surf Sci 231: L183–L188

14. Feng F, Han J, Geng M, Northwood DO (2000) Study of hydrogen transport in metal hydride electrodes using a novel electrochemical method. J Electroanal Chem 487:111–119

15. Chen JS, Diard JP, Durand R, Montella C (1996) Hydrogen insertion reaction with restricted diffusion. Part 1. Potential step-EIS theory and review for the direct insertion mechanism. J Electroanal Chem 406:1–13

16. Lundqvist A, Lindbergh G (1998) Determination of the diffusion coefficient and phase-transfer rate parameters in LaNi$_5$ and MnNi$_{3.6}$Co$_{0.8}$Mn$_{0.4}$Al$_{0.3}$ using microelectrodes. J Electrochem Soc 145:3740–3746

17. Han JN, Seo M, Pyun SI (2001) Analysis of anodic current transient and beam deflection transient simultaneously measured from Pd foil electrode pre-charged with hydrogen. J Electroanal Chem 499:152–160

18. Lee JW, Pyun SI, Filipek S (2003) The kinetics of hydrogen transport through amorphous Pd$_{82-y}$Ni$_y$Si$_{18}$ alloys (y = 0–32) by analysis of anodic current transient. Electrochim Acta 48:1603–1611

19. Montella C (2002) Discussion of the potential step method for the determination of the diffusion coefficients of guest species in host materials: Part I. Influence of charge transfer kinetics and ohmic potential drop. J Electroanal Chem 518:61–83

20. Lee JW, Pyun SI (2005) Anomalous behaviour of hydrogen extraction from hydride-forming metals and alloys under impermeable boundary conditions. Electrochim Acta 50:1777–1850

21. Enyo M, Biswas P (1992) Hydrogen absorption in palladium electrodes in alkaline solutions. J Electroanal Chem 335:309–319

22. Lee SJ, Pyun Sl, Lee JW (2005) Investigation of hydrogen transport through Mm (Ni$_{3.6}$Co$_{0.7}$Mn$_{0.4}$Al$_{0.3}$)$_{1.12}$ and Zr$_{0.65}$Ti$_{0.35}$Ni$_{1.2}$V$_{0.4}$Mn$_{0.4}$ hydride electrodes by analysis of anodic current transient. Electrochim Acta 50:1121–1130

23. Han JN, Lee JW, Seo M, Pyun SI (2001) Analysis of stresses generated during hydrogen transport through a Pd foil electrode under potential sweep conditions. J Electroanal Chem 506:1–10
24. Aoki K, Tokuda K, Matsuda H (1983) Theory of linear sweep voltammetry with finite diffusion space. J Electroanal Chem 146:417–424
25. West K, Jacobson T, Zachau-Christiansen B, Atlung S (1983) Determination of the differential capacity of intercalation electrode materials by slow potential scans. Electrochim Acta 28:97–107
26. Armand M, Dalard F, Deroo D, Mouliom C (1985) Modelling the voltammetric study of intercalation in a host structure: application to lithium intercalation in RuO_2. Solid State Ion 15:205–210
27. Lee JW, Pyun SI (2005) A study on the potentiostatic current transient and linear sweep voltammogram simulated from fractal intercalation electrode: diffusion coupled with interfacial charge transfer. Electrochim Acta 50:1947–1955
28. Kim SW, Pyun SI (2002) Lithium transport through a sol–gel derived $LiMn_2O_4$ film electrode: analyses of potentiostatic current transient and linear sweep voltammogram by Monte Carlo simulation. Electrochim Acta 47:2843–2855
29. Jung KN, Pyun SI, Kim SW (2003) Thermodynamic and kinetic approaches to lithium intercalation into $Li[Ti_{5/3}Li_{1/3}]O_4$ film electrode. J Power Sources 119–121:637–643
30. Shin HC, Pyun SI, Go JY (2002) A study on the simulated diffusion-limited current transient of a self-affine fractal electrode based upon the scaling property. J Electroanal Chem 531:101–109
31. Yang QM, Ciureanu M, Ryan DH, Stroem-Olsen JO (1994) Hydrogen surface concentration and overpotential for galvanostatic discharge of hydride electrodes: I. Development of the model. J Electrochem Soc 141:2108–2112
32. Yang QM, Ciureanu M, Ryan DH, Stroem-Olsen JO (1994) Hydrogen surface concentration and overpotential for the galvanostatic discharge of hydride electrodes: II. Quantitative numerical calculations. J Electrochem Soc 141:2113–2117
33. Johnsen SE, Lindbergh G, Lundqvist A, Tunold R (2003) A single particle investigation on the kinetics of metal hydride materials. J Electrochem Soc 150:A629–A637
34. Jost W (1960) Diffusion in solids, gases, liquids. Academic, New York
35. Yoon YG, Pyun SI (1996) Hydrogen permeation through palladium-nickel-hydroxide film bilayer. J Alloys Compd 243:45–50
36. Motupally S, Streinz CC, Weidner JW (1995) Proton diffusion in nickel hydroxide films: measurement of the diffusion coefficient as a function of state of charge. J Electrochem Soc 142:1401–1408
37. Choi WK, Yamataka K, Inoue H, Iwakura C (1999) Kinetic study on the surface treatment of a $Zr_{0.9}Ti_{0.7}Ni_{1.1}Co_{0.1}Mn_{0.6}V_{0.2}$ electrode with a boiling alkaline solution. J Alloys Compd 290:110–113
38. Luo JL, Cui N (1998) Effects of microencapsulation on the electrode behavior of Mg_2Ni-based hydrogen storage alloy in alkaline solution. J Alloys Compd 264:299–305
39. Chen J, Bradhurst DH, Dou SX, Liu HK (1998) Surface and electrode properties of Zr $(V_{0.25}Ni_{0.75})_2$ alloy treated with ultrasound-solution. J Alloys Compd 265:281–285
40. Jiansheng C, Xueping G, Dongfeng L, Xingdi X, Huatang Y, Deying S, Panwen S (2001) Activation behavior of the Zr-based Laves phase alloy electrode. J Power Sources 93:141–144
41. Gao X, Song D, Zhang Y, Zhou Z, Zhang W, Wang M, Shen P (1995) Electrochemical and surface properties of the $Zr(V_{0.2}Mn_{0.2}Ni_{0.6})_{2.4}$ alloy electrode. J Alloys Compd 229:268–273

Chapter 8
Effect of Cell Impedance on Lithium Transport

Lithium transport through intercalation compounds, including transition metal oxides and carbonaceous materials, has been known for a long time to be limited by solid-state lithium diffusion and most studies on the cell reaction kinetics have been accordingly focused on lithium transport through the active materials [1–10]. However, a number of anomalous transport behaviors, which have never been explained on the basis of the "diffusion-controlled" concept, have been reported for various materials, demanding a new model to explain the lithium transport behavior [11–23]. The understanding of these anomalous phenomena entered a new phase when the real mechanism of lithium transport was revealed to be a "cell-impedance-controlled" process, not a "diffusion-controlled" one [24–35]. This chapter deals with the typical anomalous lithium transport behaviors and explains the importance of the cell impedance as the main factor affecting lithium transport.

8.1 Anomalous Features of Lithium Transport

8.1.1 Non-Cottrell Behavior at the Initial Stage of Lithium Transport

In chronoamperometry, it is expected that the current transient would show a linear relation between the logarithmic current and the logarithmic time with a slope of -0.5 in the initial stage of the diffusion process (Cottrell behavior, see Chap. 2 for the details), insofar as the solid-state lithium diffusion governs the whole insertion process. However, this is not the case for most lithium insertion materials. Shown in Fig. 8.1 are the logarithmic current transients, obtained from $Li_{1-\delta}NiO_2$ and graphite.
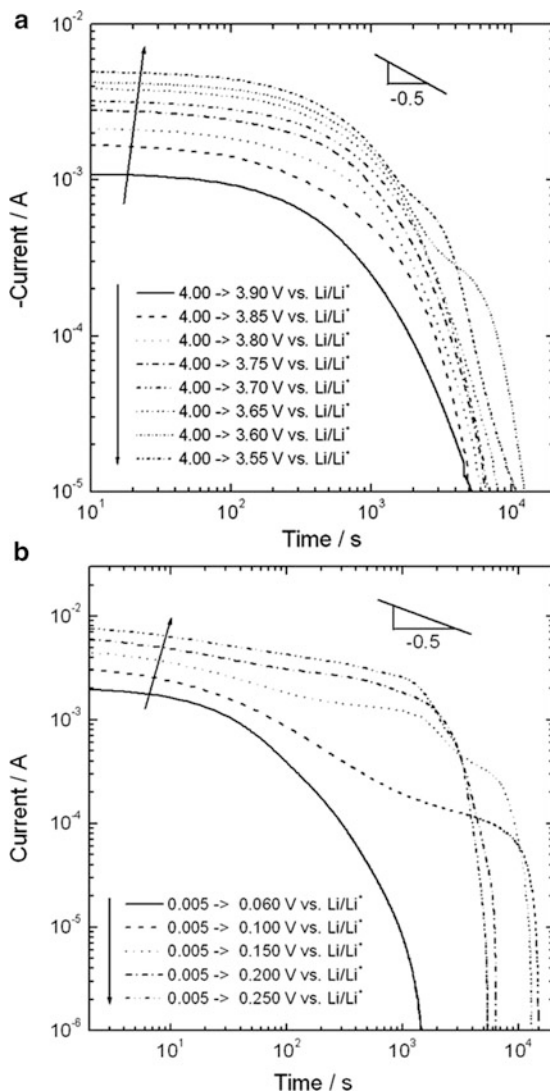
Whether the lithium ion diffusion into them follows the Cottrell behavior or not can be more effectively judged by the $I(t) \cdot t^{1/2}$ versus $\ln t$ plot: In the Cottrell region, the value of $I(t) \cdot t^{1/2}$ remains constant, irrespective of the diffusion time. Shown in Fig. 8.2 is the $I(t) t^{1/2}$ versus $\ln t$ plot reproduced from Fig. 8.1.

There is a local maximum in the plots and no region with the Cottrell character is found. Some researchers claimed that the local maximum corresponded to the semi-infinite planar diffusion region, representing the Cottrell behavior [36–39]. However, it is quite unlikely that this is the Cottrell region, in that it has no time length. That is,

Fig. 8.2 $I(t) \cdot t^{1/2}$ versus ln t plot reproduced from (**a**) Fig. 8.1a and (**b**) Fig. 8.1b (Reprinted from Shin and Pyun [32], Copyright ©2003 with permission from Kluwer Academic/Plenum Publishers)
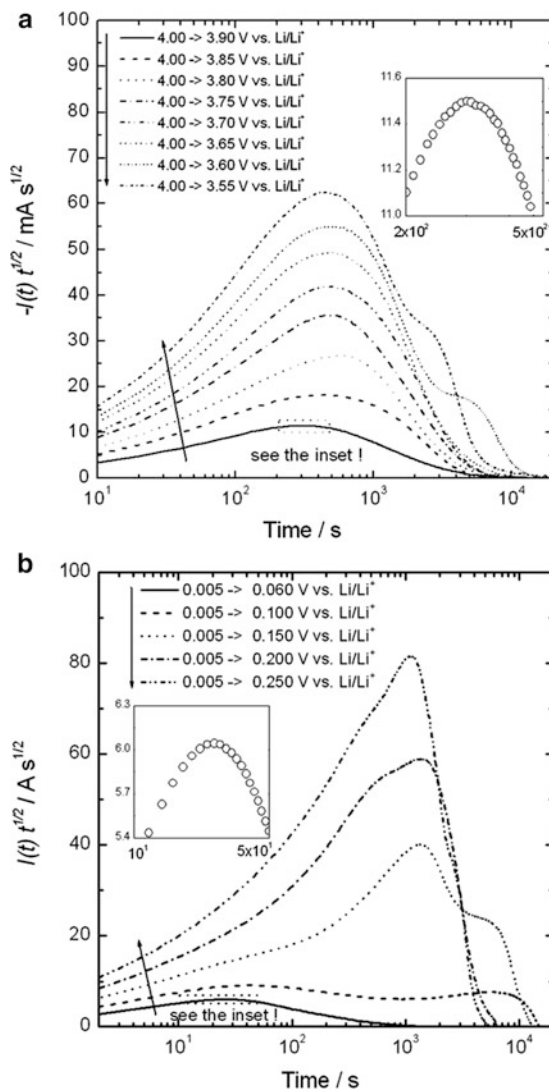
the physical meaning of the pseudo-plateau observed in the $I(t) \cdot t^{1/2}$ versus ln t plots of lithium insertion materials has been quite possibly overestimated.

8.1.2 Discrepancy Between Anodic and Cathodic Behaviors

Assuming that the lithium diffusion into the materials governs the whole lithium insertion process, i.e., the diffusion-controlled process, and the chemical diffusion coefficient of lithium remains constant in the course of lithium insertion (this is

quite true when the applied potential step is small and no phase transition takes place during lithium insertion), the absolute value of the cathodic current transient should be exactly equal to that of the corresponding anodic transient.

Figure 8.3 shows the cathodic and corresponding anodic current transients determined in a single-phase region at the potential drop and jump, respectively. It is noted that the cathodic curves intersect the anodic curves. Considering that the chemical diffusion coefficient is almost invariant in the potential region where the experiment was carried out, the intersection of the two curves might provide clear evidence that the main factor controlling the lithium insertion process is not the lithium diffusion inside the electrodes.

The following point is also noteworthy: The current values of all of the anodic curves exceed those of the corresponding cathodic curves in the initial stage of diffusion (i.e., before the intersection of the two curves), while the former become smaller than the latter in the later stage of diffusion (i.e., after their intersection). It is interesting that such a regular variation in the relative current level seems to reflect the shape of the electrode potential curve. That is, the initial faster and the subsequent slower current drop in the cathodic chronoamperometric curves (as compared to the anodic curves) during the potential drop appears to follow the variation of the electrode potential when it decreases. Also, the electrode potential rises slowly and then quickly when we record the anodic current transients that feature an initial slower and succeeding faster current drop. This indicates that the degree of change of the electrode potential (with the lithium content) in the negative and positive directions is in qualitative agreement with the rate of cathodic and anodic current change (with time), respectively. The above argument is schematically presented in Fig. 8.4.

8.1.3 Quasi-constant Current During Phase Transition

In fact, it is not a surprise that the current transient significantly deviates from the typical Cottrell behavior in the course of the insertion-induced phase transition, because the diffusion process in the presence of two phases would be quite different from that in the presence of a single phase. However, a noteworthy point is the great discrepancy in the shape of the curve from the solutions of the moving phase boundary problem: The current transients, either obtained by numerically solving the modified diffusion equation or predicted on the basis of Wagner's approach [17, 40, 41], are characterized by a monotonic decrease of current with time during the phase transition. This is not the case, however, in the case of the current transients when the potential stepping passes through the plateau potential where two phases coexist. Shown in Fig. 8.5a are the logarithmic current transients of the $Li_{1+\delta}[Ti_{5/3}Li_{1/3}]O_4$ electrode obtained by lowering the potential from 1.7 V versus Li/Li^+ (single-phase potential region) to the region below the plateau potential.

The experimental current transients showed a three-stage shape consisting of a slow drop, quasi-constant value, and steep decay of the current in sequence. In

Fig. 8.3 Experimental cathodic and anodic current transients obtained from (**a**) lithium cobalt dioxide ($Li_{1-\delta}CoO_2$) and (**b**) lithium titanium oxide ($Li_{1+\delta}[Ti_{5/3}Li_{1/3}]O_4$) (Reprinted from Shin and Pyun [24], Copyright ©1999 and Shin et al. [27], Copyright ©2001, with permissions from Elsevier Science)
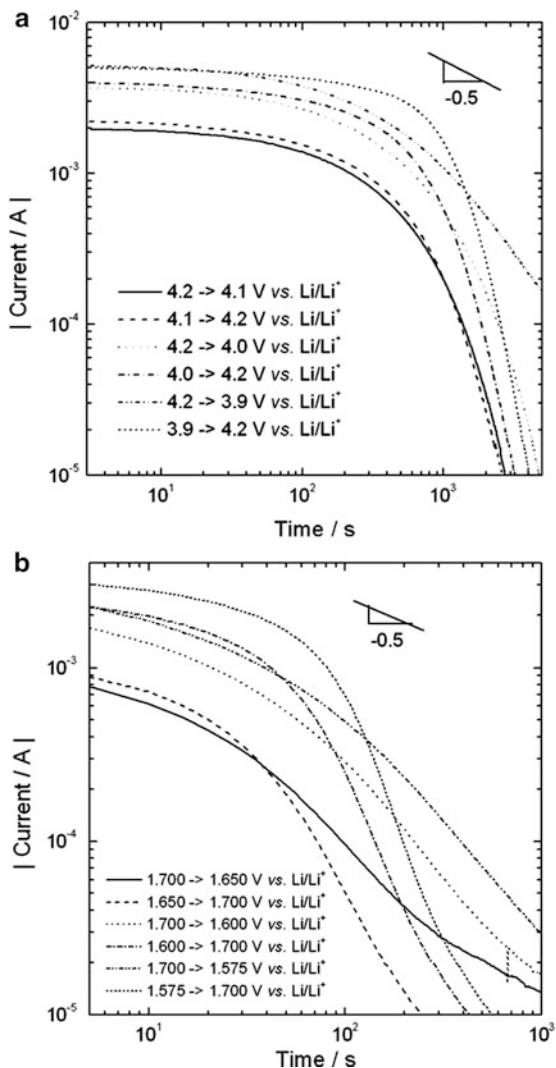
particular, the second stage of the quasi-current plateau is characteristic of the insertion-induced phase transition, which has never been explained in the literature on the basis of the "diffusion-controlled" concept: Based on the experimental finding that the amounts of charge transferred up to the onset and end times of the current plateau are almost equal to the maximum lithium solubility limit of the Li-dilute phase and the minimum solubility limit of the Li-rich phase (Fig. 8.5b), respectively, the quasi-current plateau in Fig. 8.5 is undoubtedly caused by the phase transition of the Li-dilute phase to the Li-rich phase. Accordingly, it is quite improbable that the phase transition is governed by the "diffusion-controlled" process, because the "diffusion-controlled" phase transition would lead to a

Fig. 8.4 Schematic illustrations showing that the downward convex shape of the electrode potential curve possibly causes the intersection of the cathodic and anodic current transients. Rapid drops in current (a^* and B^* in (**b**)) reflect the shape of *upper* part of the electrode potential curve (a and B in (**a**)) while mild drops in current (A^* and b^*) reflect the shape of the *lower* part of the curve (A and b)
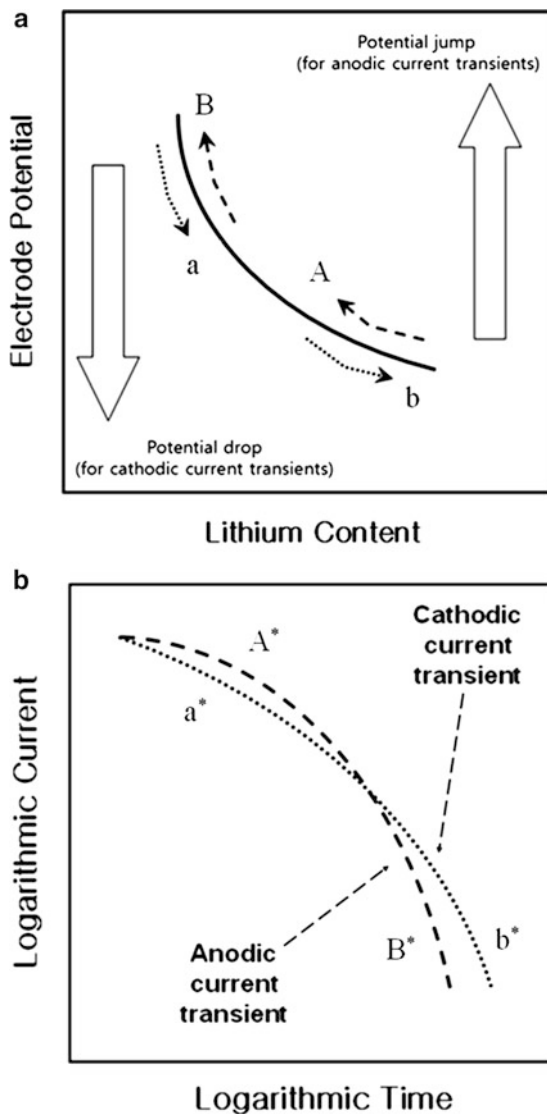
decrease in the rate of phase boundary movement with time and, therefore, a notable drop of the current.

A quasi-current plateau in the current transient is frequently observed in other compounds that undergo a phase transition during the lithium insertion process, although the degrees of the current flatness are different from each other. These include $Li_{1-\delta}CoO_2$ [24], $Li_{1-\delta}NiO_2$ [28], $Li_\delta V_2O_5$ [26], $Li_{1-\delta}Mn_2O_4$ [30], and graphite [32]. An exemplary current transient and a cumulative charge transient of $Li_\delta V_2O_5$ are presented in Fig. 8.6. In the case where the onset and end time points

Fig. 8.5 (**a**) Experimental cathodic current transients obtained from $Li_{1+\delta}[Ti_{5/3}Li_{1/3}]O_4$ and (**b**) cumulative charge versus time plots, reproduced from (**a**), together with the electrode potential curve (Reprinted from Shin et al. [27], Copyright ©2001 with permission from Elsevier Science; Shin and Pyun [32], Copyright ©2003 with permission from Kluwer Academic/Plenum Publishers)
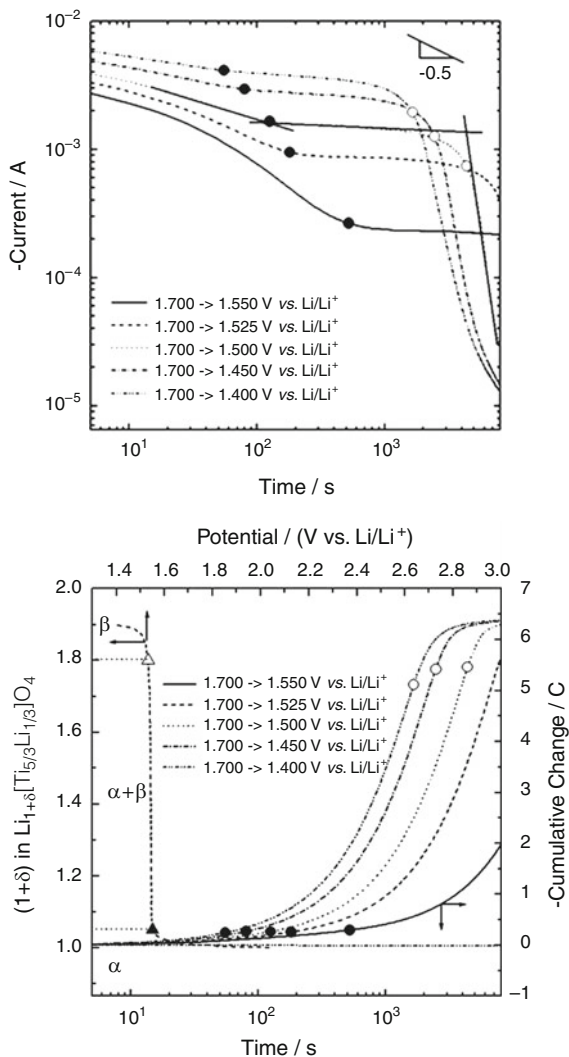
are unclear, the inflexion points can be used to judge whether the quasi-current plateaus are due to the phase transition or not, as indicated in Fig. 8.6b.

8.1.4   Lower Initial Current Level at Larger Potential Step

In the "diffusion-controlled" process, the initial current level of the current transients should increase as the potential step increases, because an increase in the potential level corresponds to an increase in the concentration difference of the

electrode surface from the bulk. However, this is not true for every current transient. Relevant examples can be found in the anodic current transients of $Li_{1-\delta}NiO_2$ (Fig. 8.7). When the applied potential jump was about 0.3 V, the initial current level started deviating from the typical linearity with the degree of potential jump, showing a parabolic relationship between initial current level and applied potential jump. The suppression of the initial current level strongly indicates that the lithium extraction process is seriously retarded.

Another notable point is the increase in current with time: It is natural that, in chronoamperometry, the current continuously drops with time, since the driving force gets smaller during the diffusion process. However, as can be seen in the curves where the initial potentials were 3.60 and 3.55 V versus Li/Li^+, the current increased until several tens to hundreds of seconds had passed. It is quite likely that

Fig. 8.7 (**a**) Experimental anodic current transients obtained from $Li_{1-\delta}NiO_2$ and (**b**) the potential jump dependence of their initial current levels measured at 10 s (Reprinted from Lee et al. [28], Copyright ©2001 with permission from Elsevier Science)
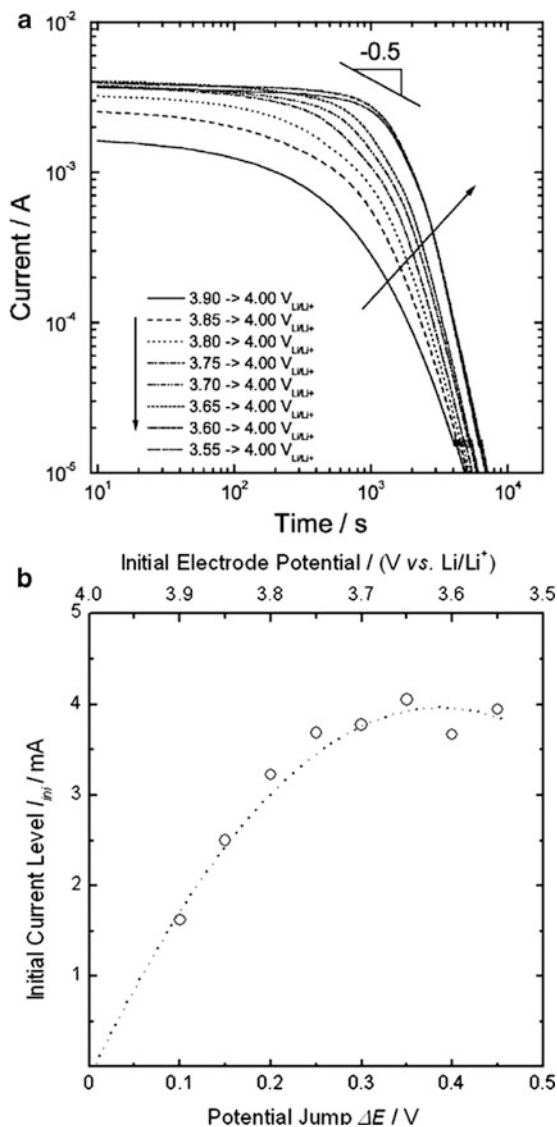
the influence of some of the factors retarding the lithium extraction process is reduced with time.

8.2 Revisiting the Governing Mechanism of Lithium Transport

8.2.1 Ohmic Relationship at the Initial Stage of Lithium Transport

The linear relation between the initial current and the applied potential step is observed in almost all current transients of lithium insertion compounds. Since the initial current level is determined, at least in this book, at an insertion time where all of the capacitive elements in the cell are virtually fully charged or discharged (typically at a time of several to 10 s) [32], the measured initial current is regarded as the value when the current is related solely to the resistive elements of the cell, including the solution, solid electrolyte interface film, and charge transfer resistances. Such linearity implies that the difference between the initial potential and the applied (or final) potential is the driving force of the lithium insertion or extraction process, not the concentration gradient between the materials interface and the bulk. This linearity is particularly valid, with little standard deviation, when the initial potential is set to be invariant (Fig. 8.8). In this case, the reciprocal of the proportionality constant of the linear relation is most likely the cell resistance, which is defined at the initial potential or the lithium content at that potential.

As a matter of fact, the current is expected to increase linearly with the applied potential step even in the "diffusion-controlled" process, insofar as the electrode potential versus lithium content plot is considered to be linear, because the difference in the lithium content between the materials interface and the bulk would be proportional to the applied potential step. However, a linear relation between the initial current and the applied potential step is consistently observed in the experimental current transients, irrespective of whether the electrode potential curves are linear or not. As an exemplary result, please see the initial current versus applied potential step plot reproduced from the current transients of $Li_{1+\delta}[Ti_{5/3}Li_{1/3}]O_4$, whose electrode potential strongly deviates from linearity as the lithium content increases (Fig. 8.8a-1 and a-2).

The above results strongly indicate that the lithium insertion process is not governed by diffusion into the materials. Rather, it is more probable that the cell resistance critically affects the rate of lithium insertion. This condition is called "cell-impedance-controlled" lithium transport. Then, the next question is whether or not the "cell-impedance-controlled" constraint is valid throughout the whole lithium insertion/extraction process.

8.2.2 Validity of Ohmic Relationship throughout the Lithium Transport Process

In order to verify the current-potential Ohmic relation in the course of the lithium insertion/extraction process, the current-potential relation at various amounts of charge transferred during the process needs to be analyzed. For this purpose, the
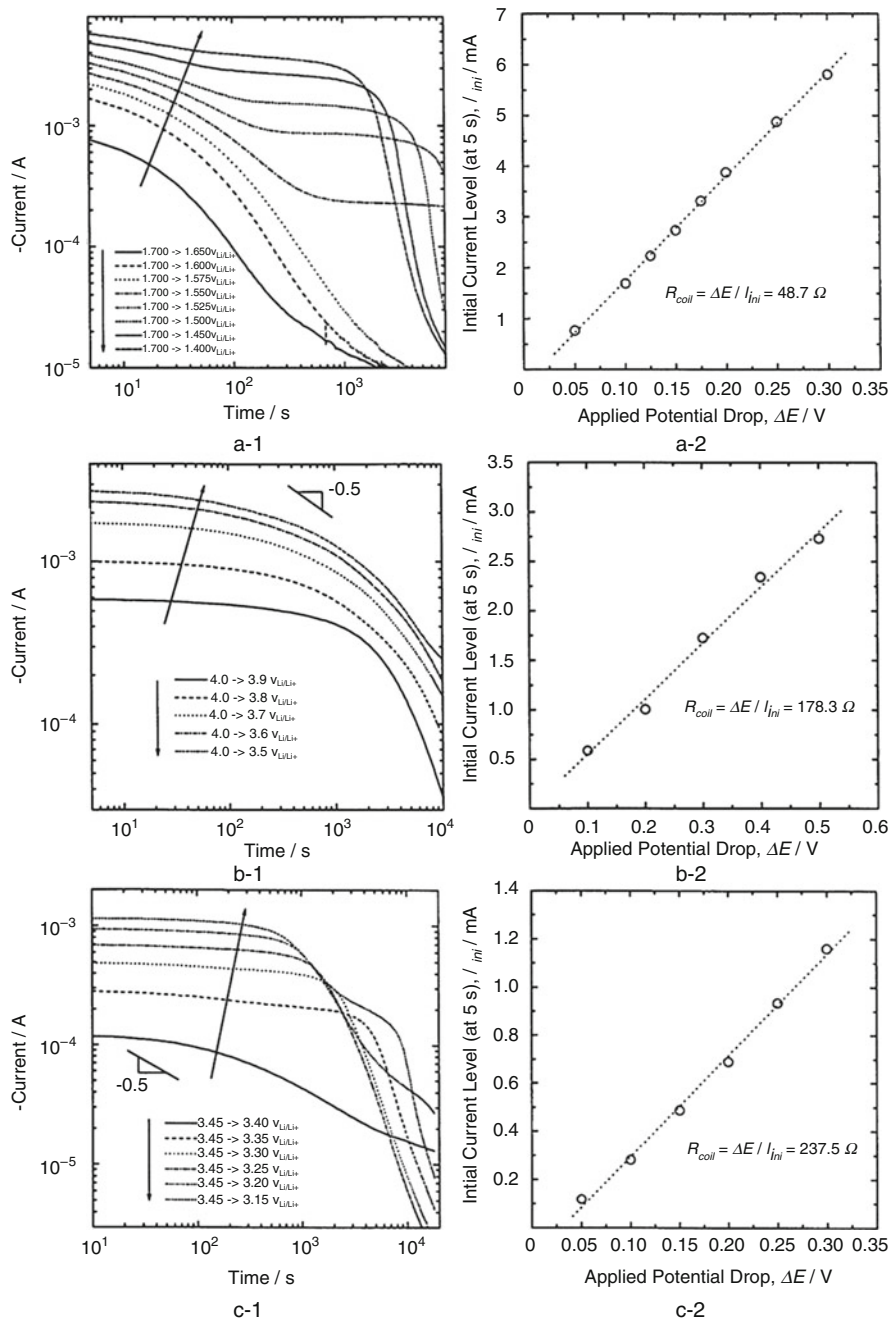
Fig. 8.8 Experimental cathodic current transients (*left*) and the potential drop dependence of their initial current levels (*right*), obtained from $Li_{1+\delta}[Ti_{5/3}Li_{1/3}]O_4$ (**a-1**, **a-2**), $Li_{1-\delta}NiO_2$ (**b-1**, **b-2**) and $Li_\delta V_2 O_5$ (**c-1**, **c-2**) (Reprinted from Shin et al. [27], Copyright ©2001 with permission from Elsevier Science)

Fig. 8.9 Potential drop dependence of instantaneous current at different amounts of cumulative charge, reproduced from (**a**) Fig. 8.1a for $Li_{1-\delta}NiO_2$ and (**b**) Fig. 8.3a for $Li_{1-\delta}CoO_2$ (Reprinted from Shin and Pyun [32], Copyright ©2003 with permission from Kluwer Academic/Plenum Publishers)
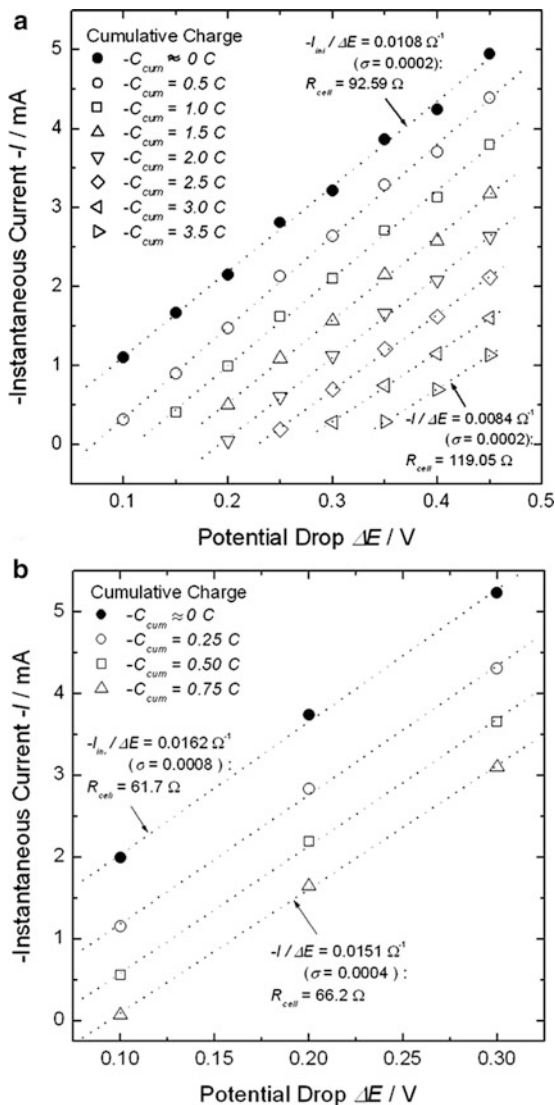
current transients are first obtained by changing from one initial potential to different final potentials. Then, the current values that have the same cumulative charge amounts are read on all of the current transients. Since all of the curves have the same initial potential, when the cumulative charge amounts are identical, the electrode potentials or lithium contents are virtually identical. Finally, the estimated current values are plotted as a function of the applied potential step. The resulting current versus applied potential step plot provides us with the *I-V* relation at a variety of cumulative charges (or electrode potentials, lithium contents) in the course of lithium insertion/extraction. Shown in Fig. 8.9 are the cathodic current

variations with the applied potential step at different cumulative charge transfers, obtained from $Li_{1-\delta}NiO_2$ and $Li_{1-\delta}CoO_2$ in the single-phase potential region where there is no remarkable phase transition during the lithium insertion process.

Linear relations between the current and potential are clearly observed, regardless of the cumulative charge amount. This strongly indicates that the "cell-impedance-controlled" constraint is valid throughout the whole lithium insertion process and, thus, the driving force of the current flow is the difference between the applied potential and the instantaneous electrode potential. This linear relationship is valid even when the cumulative charge amount is in the lithium content range of two-phase coexistence (Fig. 8.10), i.e., the phase transition runs under the "cell-impedance-controlled" constraint, in the same manner as the single-phase insertion reaction.

8.2.3   Origin for Quasi-Constant Current and Suppressed Initial Current

When the lithium transport is limited by the internal cell resistance and is driven by the difference between the applied (final) potential and the instantaneous electrode potential, the reason for the quasi-constant current observed in the current transients when the potential step passes through the plateau potential is quite clear: The electrode potential is basically unchanged during the phase transition and, thus, the potential difference (between the final and electrode potentials) remains constant until the phase transition is finished. This means that the current, which is defined as the potential difference divided by the internal cell resistance, does not change notably as long as the variation of the cell resistance is trivial.

The suppression of the initial current level observed in the anodic current transients of $Li_{1-\delta}NiO_2$ (Fig. 8.7) needs to be dealt with in a slightly different manner, because the initial potential is different in every experiment, while the applied potential remains unchanged. In this case, all of the initial current levels reflect the information of the electrode at different electrode potentials or lithium contents, unlike the case of an invariable initial potential where the initial currents obtained are the result of the electrode properties at a specific initial potential. The experimental results, which indicate that the initial current level showed a strong negative deviation from linearity and even decreased in spite of the increased applied potential step, imply that the internal cell resistance might abruptly increase with decreasing initial electrode potential. This suggestion will be quantitatively confirmed in Sect. 8.4.1.

Fig. 8.10 Potential step
dependence of instantaneous
current at different amounts
of cumulative charge,
reproduced from (**a**) Fig. 8.6a
for Li$_\delta$V$_2$O$_5$ and (**b**) Fig. 8.5a
for Li$_{1+\delta}$[Ti$_{5/3}$Li$_{1/3}$]O$_4$
(Reprinted from Shin and
Pyun [32], Copyright ©2003
with permission from Kluwer
Academic/Plenum
Publishers)
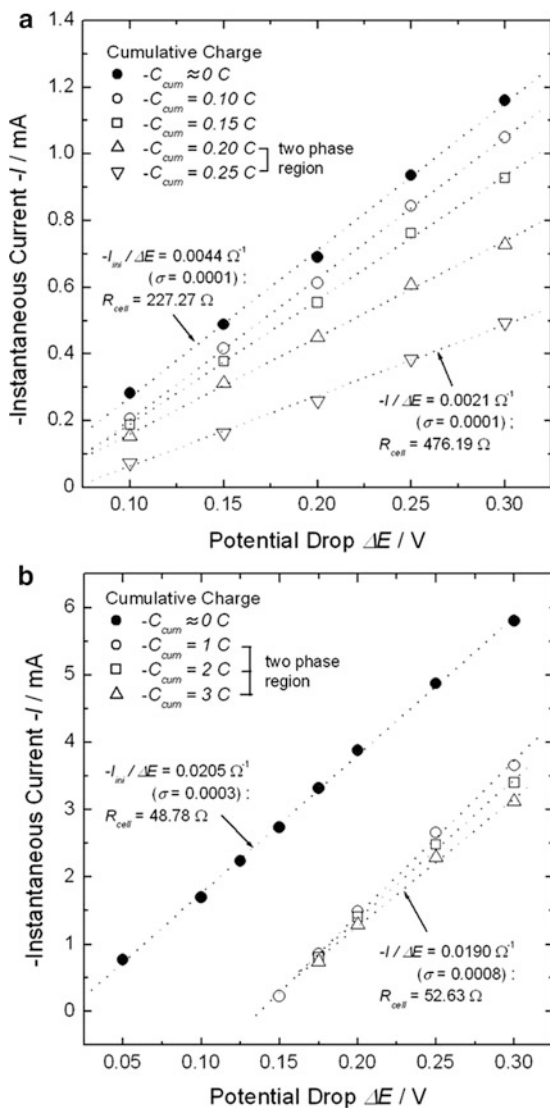
8.2.4   Validation of Internal Cell Resistance Obtained from Chronoamperometry

The findings in Sects. 8.2.1, 8.2.2, and 8.2.3 consistently tell us that the lithium transport proceeds under the "cell-impedance-controlled" constraint during the chronoamperometry experiments. In order to confirm the conclusion drawn from the observations, it would be quite useful to compare the internal cell resistances estimated from the current-potential linear relation with those determined by other techniques.

Fig. 8.11 Variation of internal cell resistance of $Li_{1-\delta}NiO_2$ with its electrode potential, determined from current transients (o: initial current vs. potential drop plot, Δ: instantaneous current vs. potential drop plot of Fig. 8.9a) and electrochemical impedance spectroscopy (•) (Reprinted from Lee et al. [28], Copyright ©2001 with permission from Elsevier Science)
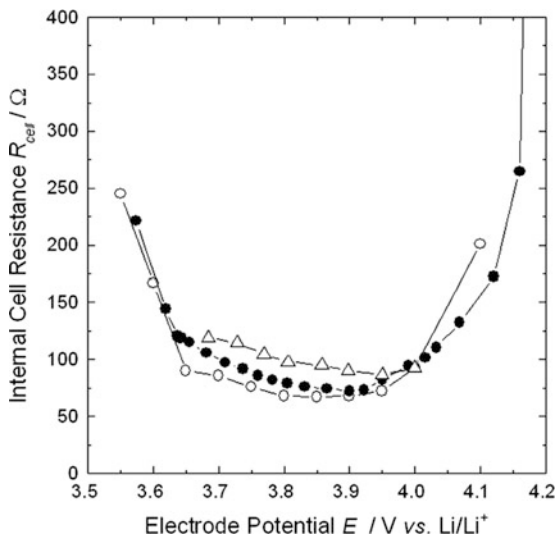
Shown in Fig. 8.11 are the variations of the internal cell resistance with the electrode potential obtained from $Li_{1-\delta}NiO_2$. The potential dependence of the cell resistance determined from the linear relation between the initial current and the applied potential step showed a parabolic shape, which is similar to the results obtained by electrochemical impedance spectroscopy (EIS). Here, the values of the initial current were taken at 10 s to exclude the effect of the non-faradaic current due to the charging/discharging of the capacitive elements. It is noteworthy that the former internal resistances quantitatively coincided quite well with the latter resistances.

It is further noted that the cell resistance estimated from the slope of the instantaneous current versus potential drop plot in the course of lithium insertion proved to be higher than that determined by EIS. This slight discrepancy might be caused by the increase in the over-potential with increasing potential step (or increasing current level) and the effect of the diffusion resistance on the total cell resistance at a prolonged lithium insertion time, which is actually disregarded to estimate the cell resistances based on the linear relation between initial current level and applied potential drop, and impedance spectra.

On the other hand, the charge/discharge curves obtained at various applied currents can be utilized to roughly estimate the internal cell resistance. Since a higher current leads to a larger close-circuit potential drop on the charge/discharge curve and this typically follows the Ohmic relation, the cell resistance can be calculated from such a linear relation for specific amounts of charge transfer (Fig. 8.12).

The calculated cell resistance agreed well with those determined from the linear current-potential relation in the current transients (Fig. 8.13). The quantitative coincidence of the internal cell resistances obtained from the current transients with those obtained using the conventional independent techniques proves that lithium transport proceeds under the "cell-impedance-controlled" constraint, not the "diffusion-controlled" one.

Fig. 8.12 (**a**) Galvanostatic
discharge curves of
$Li_{1-\delta}CoO_2$ at different
current drains and (**b**) closed
circuit potential versus
applied current plots at
various cumulative charges
(Reprinted from Go et al.
[31], Copyright ©2002 with
permission from Elsevier
Science)
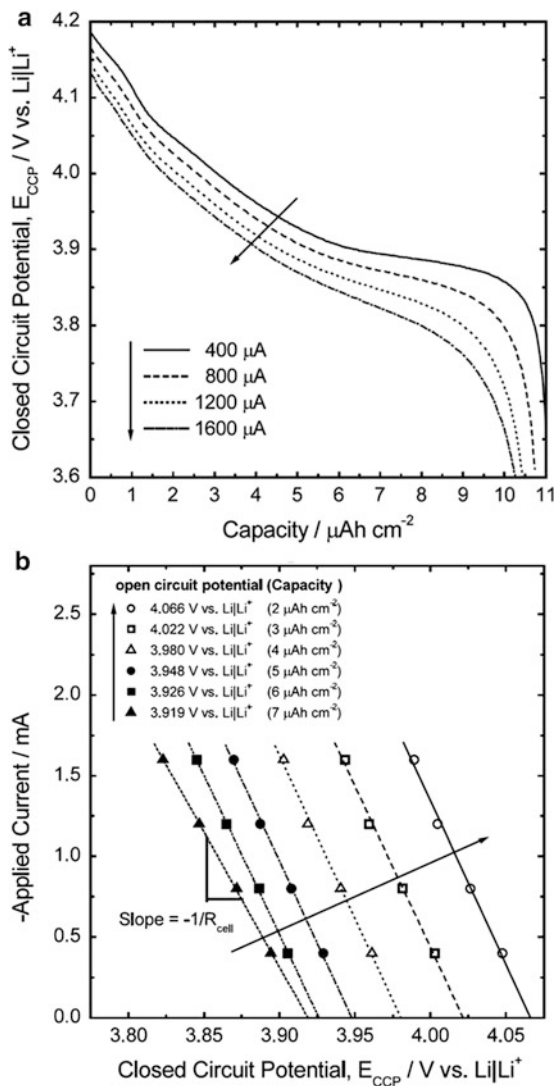
8.3   Theoretical Consideration of "Cell-Impedance-Controlled" Lithium Transport

8.3.1   Model for Chronoamperometry

As presented in the previous sections, the current flow is determined by the
potential difference between the instantaneous electrode potential $E(t;$ time$)$ or
$E(\delta;$ lithium content$)$ and the applied potential, E_{app}, divided by the internal cell

Fig. 8.13 Variation of internal cell resistance of $Li_{1-\delta}CoO_2$ with its electrode potential, determined from current transients (o), discharge curve (Δ), and electrochemical impedance spectroscopy ($\square$) (Reprinted from Go et al. [31], Copyright ©2002 with permission from Elsevier Science)
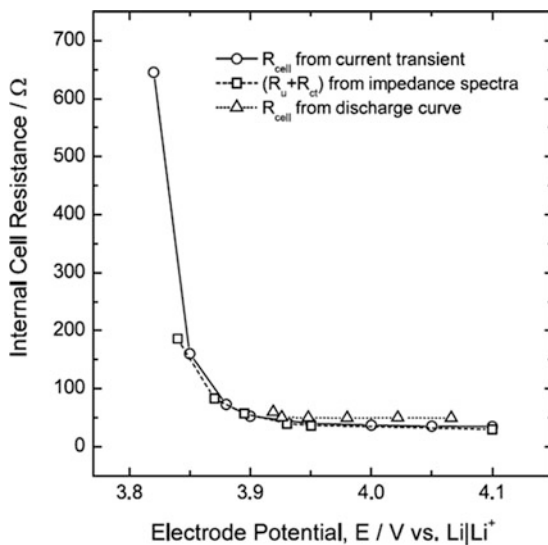
resistance, $R_{cell}(t)$ or $R_{cell}(\delta)$, i.e., $(E - E_{app})/R_{cell}$, which is accordingly the boundary condition at the electrode/electrolyte interface. The electrode/current collector interface or the center of the particle is under the typical impermeable boundary condition. Fick's diffusion equation is used as the governing equation to calculate the concentration gradient inside the electrode.

As a matter of fact, the diffusion process during the phase transition might not be properly modeled by the conventional diffusion equation, because the diffusion coefficient in each phase and the rate of phase boundary movement are expected to affect the lithium insertion rate and, thereby, the apparent diffusion coefficient. Nevertheless, it is suggested, from a number of comparative studies between the experimental and calculated current transients, that there is strong possibility that the presence of the phase boundary does not significantly affect the shape of the "cell-impedance-controlled" current transients. Rather, the boundary condition between the electrode/electrolyte interface determines their overall shape [24–30, 32]. However, further investigation is still needed to clarify the effect of the moving phase boundary on the solid-state diffusion and the current transients.

Among the model parameters, the instantaneous electrode potential E and the internal cell resistance R_{cell} are first experimentally determined as a function of the lithium content and then the functional relations of $E(\delta)$ and $R_{cell}(\delta)$ are obtained by the polynomial regression analysis of the corresponding experimental data. Since the relation $E(\delta)$ contains the information about the phase transition as a quasi-potential plateau, the theoretical current transients accordingly reflect the effect of the phase transition.

For the theoretical calculation of the "cell-impedance-controlled" current transients, the variation of the electrode potential with the lithium content $E(\delta)$ was assumed to follow the following equation [42]:
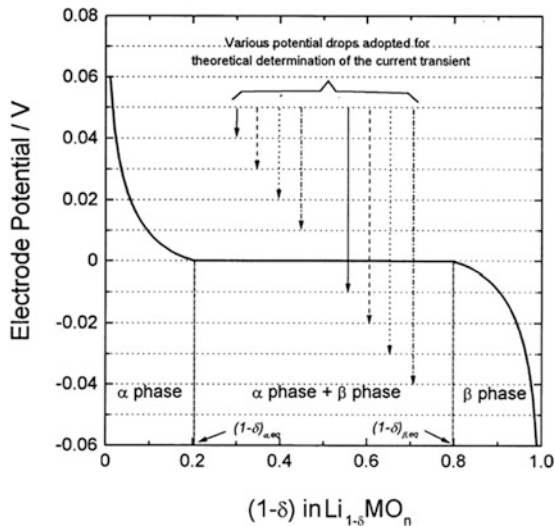
$$E = E_0 - \frac{z_i \phi}{F}[1 - 2\delta] - \frac{\alpha RT}{F} \ln\left[\frac{\delta}{1-\delta}\right] \tag{8.1}$$

where E_0 is the standard potential at $\delta = 0.5$; z_i, the number of neighboring sites; ϕ, the interaction energy; δ, the lithium content; and α, a parameter ($\alpha = 1$ or 2). We assumed that $E_0 = 0$ V, $z_i \phi = 0.059$ eV, $\alpha = 1$, and $T = 298$ K for constructing the hypothetical electrode potential curve (Fig. 8.14).

The electrode potential curve consists of three regions. One is the potential plateau region ($0.2 \leq \delta \leq 0.8$) and the other two are the potential sloping regions ($\delta < 0.2$ and $\delta > 0.8$). The potential plateau is ascribed to the phase transition (or the coexistence of two phases) and the potential slopes are due to the single-phase diffusion. The internal cell resistance was assumed to be independent of the lithium content, i.e., $R_{cell}(\delta) = $ constant. The current transients were theoretically obtained by applying eight different potential steps, as given in the figure. Four of these potential steps do not reach the plateau potential and, thus, lithium diffuses in the single phase while the other four go through the potential plateau where the phase transition occurs.

8.3.2 Lithium Transport in the Single-Phase Region

Figure 8.15a shows the current transients when the potential steps do not pass through the plateau potential, i.e., no phase transition occurs during the lithium insertion process. Unlike the "diffusion-controlled" curves, as discussed in Chap. 2, no remarkable shape change of the curves is observed except for a monotonic

Fig. 8.15 (**a**) Theoretical cathodic current transients obtained by hypothetically dropping the potential from 0.05 V to different potentials above the plateau potential 0 V, under the assumption of cell-impedance controlled lithium transport and (**b**) time dependence of lithium content profile across the active material at the potential drop from 0.05 to 0.04 V (Reprinted from Shin and Pyun [24], Copyright ©1999 with permission from Elsevier Science)
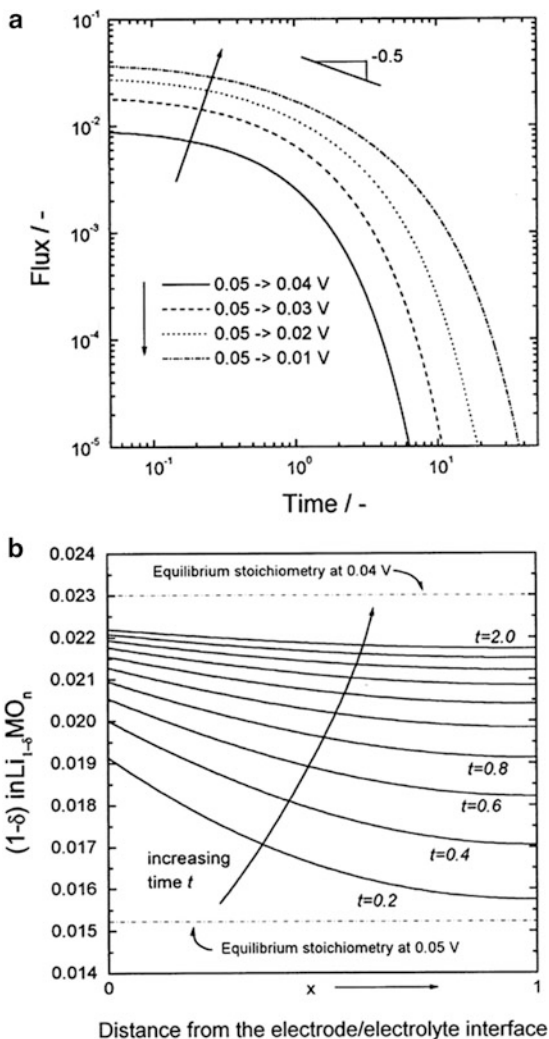

increase in its absolute slope with time: The transition point from the semi-infinite diffusion process to the finite-length diffusion process does not appear in the curves.

The concentration profile during the "cell-impedance-controlled" lithium transport is characterized by a variable surface lithium content (Fig. 8.15b). The instantaneous surface lithium content is determined by the amount of remaining surface lithium (i.e., the amount of lithium that does not diffuse inside the electrode) and the lithium flux at the electrode/electrolyte interface. Since the surface lithium content is not fixed and depends critically on the lithium insertion time, the lithium flux at the interface is basically smaller than that in the "diffusion-controlled" case, except at prolonged lithium insertion times. This implies that the rate of approach to the equilibrium lithium content in the former "cell-impedance-controlled" case is much lower than

that in the latter "diffusion-controlled" case. In the same context, it is noted that the concentration profile becomes quite flat, in spite of the fact that the overall lithium content is still far from the equilibrium value (please see the profile at $t = 2.0$ in Fig. 8.15b), strongly indicating that it takes a long time to reach the equilibrium concentration.

8.3.3 Lithium Transport with Phase Transition

Since the cell potential is basically invariable in the presence of two phases, the corresponding current transients are characterized by a constant current density, as long as there is no change in the cell resistance. Accordingly, the flux plateau regions in Fig. 8.16a certainly originate from the phase transition from the Li-poor

phase α to the Li-rich phase β (Fig. 8.14). The flux sloping regions on the left and right sides of the flux plateau are due to lithium diffusion through the single α and β phases, respectively.

Consistent with the above arguments, the calculated concentration profile of Fig. 8.16b shows that there are three steps of lithium transport with the phase transition: diffusion in the single α phase followed by the phase transition from α to β and finally diffusion in the single β phase. It is quite interesting to note that there is virtually no phase transition until the surface lithium content reaches the maximum solubility limit of the α phase. That is, in the course of "cell-impedance-controlled" lithium transport, the β phase might not be nucleated until the lithium content exceeds the solubility limit of the matrix α phase. Once the β phase nucleates, it gradually grows in the whole α phase.

This is quite different from the model suggested on the basis of "diffusion-controlled" lithium transport. The following is one example in which the moving phase boundary problem is numerically treated under the assumption of "diffusion-controlled" lithium transport. The basic concept is to simulate the growth of the new phase, β, in the preexisting matrix phase, α, by making the grids of the α and β phases contract and expand, respectively, during the phase transition. The concentration profile in each phase is determined by the following modified Fick's diffusion equations [43, 44].

$$\frac{\partial c_n^\beta}{\partial t} = \tilde{D}_{Li}^\beta \frac{\partial^2 c_n^\beta}{\partial x_n^2} + \frac{\partial c_n^\beta}{\partial x_n} \frac{x_n}{\xi} \frac{d\xi}{dt} \quad \text{(in } \beta \text{ phase, } 0 < x_n < \xi, n = 2, 3, .., r-1) \quad (8.2)$$

$$\frac{\partial c_n^\alpha}{\partial t} = \tilde{D}_{Li}^\alpha \frac{\partial^2 c_n^\alpha}{\partial x_n^2} + \frac{\partial c_n^\alpha}{\partial x_n} \frac{l - x_n}{l - \xi} \frac{d\xi}{dt} \quad \text{(in } \alpha \text{ phase, } \xi < x_n < l, n$$
$$= r+1, r+2, .., N) \quad (8.3)$$

The flux balance at the phase boundary is expressed as

$$(c_{\beta\alpha} - c_{\alpha\beta}) \frac{d\xi}{dt} = \tilde{D}_{Li}^\alpha \left(\frac{\partial c^\alpha}{\partial x}\right)_{x=\xi^+} - \tilde{D}_{Li}^\beta \left(\frac{\partial c^\beta}{\partial x}\right)_{x=\xi^-} \quad (8.4)$$

where $c_{\beta\alpha}$ and $c_{\alpha\beta}$ are the lithium contents of the β and α phase sides of the phase boundary, respectively.

The numerical solutions for Eqs. 8.2, 8.3, and 8.4 under the *potentiostatic* and *impermeable* boundary conditions lead to the current transients reflecting the "diffusion-controlled" phase transition and the results are presented in Fig. 8.17.

In contrast to the flux plateau of the "cell-impedance-controlled" phase transition, the flux monotonically decreases in the course of the "diffusion-controlled" phase transition. Moreover, the change in the concentration profile with time indicates that the Li-rich β phase completely covers the whole surface of the matrix α phase and then grows inside the electrode [44, 45].

The comparison of the changes in the concentration profile with time (Figs. 8.16b and 8.17b) implies that the growth pattern of the β phase occurs in a quite different way between the "cell-impedance-controlled" and "diffusion-controlled" processes. Schematically shown in Fig. 8.18 are the possible growth models of the Li-rich phase in the Li-poor matrix phase in each lithium transport mechanism.

8.4   Analysis of Lithium Transport Governed by Cell Impedance

8.4.1   Theoretical Reproduction of Experimental Current Transients

The time dependence of the concentration profile of real intercalation systems during chronoamperometry experiments (with applied potential E_{app}) can be obtained from a combination of the conventional Fick's diffusion equation and the following "cell-impedance-controlled" surface (boundary) flux equation.
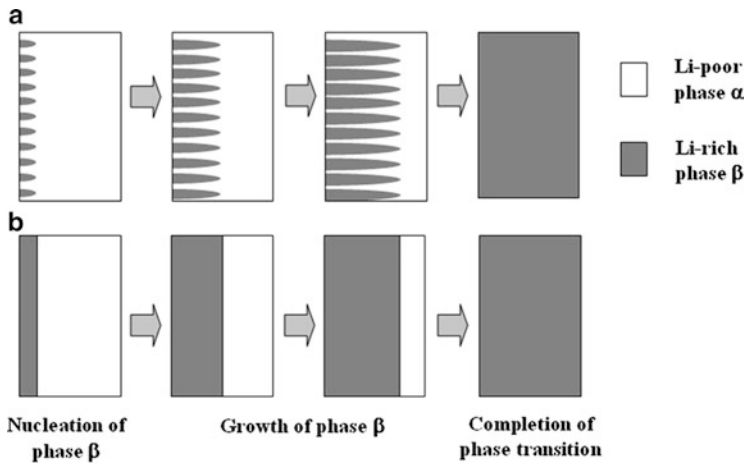
Fig. 8.18 Schematic illustrations of the possible second-phase growth models in the cases of (**a**) the "cell-impedance controlled" and (**b**) the "diffusion controlled" phase transitions

$$i = -nFA\tilde{D}_{Li}\left(\frac{\partial c(t)}{\partial x}\right)_{x=0} = \frac{E_{app} - E(t)}{R_{cell}} \qquad (8.5)$$

Here, the instantaneous surface potential, $E(t)$, is estimated from the calculated value of the surface lithium content at time t and the electrode potential curve. For the calculation, it is assumed that the cell resistance R_{cell} and chemical diffusion coefficients $\tilde{D}_{Li}$ were constant throughout the lithium transport (as a matter of fact, these assumptions possibly make the discrepancy between the experimental and calculated current transients, which will be discussed in Sect. 8.4.2). R_{cell} was estimated from the linear relationship between the initial current level and the applied potential step (Fig. 8.8) and $\tilde{D}_{Li}$ was determined as the value reported in the literatures [46–50]. The electrochemical active area A was roughly calculated from the particle size and active mass.

8.4.1.1 Non-Cottrell Character During the Entire Lithium Transport Process

Presented in Fig. 8.19 are the calculated current transients of lithium nickel oxide ($Li_{1-\delta}NiO_2$) and graphite. They show close resemblance to the corresponding experimental curves (Fig. 8.1) in terms of the non-Cottrell character at the initial stage of lithium transport and (quasi-) current plateaus.

Especially, Cottrell behavior is not observed in the lithium insertion/extraction process, as confirmed by the absence of any region with a constant value of $I(t) \cdot t^{1/2}$ in Fig. 8.20a, b. Rather, the $I(t) \cdot t^{1/2}$ versus $\ln t$ plots feature local maxima and shoulders, which are consistent with the corresponding experimental plots (Fig. 8.2).
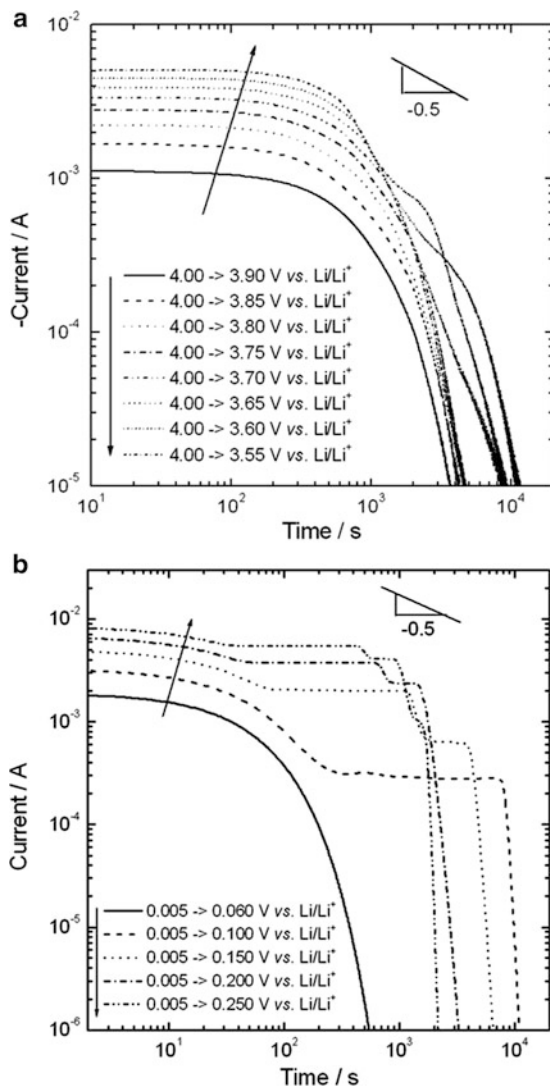
8.4.1.2   Intersection of Anodic and Cathodic Curves

The reproduced cathodic and anodic current transients of lithium cobalt dioxide
($Li_{1-\delta}CoO_2$) and lithium titanate ($Li_{1+\delta}[Ti_{5/3}Li_{1/3}]O_4$) (Fig. 8.21) are in substantial
agreement with the experimental results (Fig. 8.3) from the viewpoint of the
crossing of the cathodic and anodic curves during the lithium transport in the
single-phase region. This exceptional reproducibility proves that the shape of
the electrode potential curves plays a critical role in the interfacial lithium flux
during the "cell-impedance-controlled" lithium transport. That is, the rate of
cathodic and anodic current change is determined by the degree of electrode

Fig. 8.20 $I(t) \cdot t^{1/2}$ versus ln t plot reproduced from (**a**) Fig. 8.21a and (**b**) Fig. 8.21b, showing the non-Cottrell character of the current transients (Reprinted from Shin and Pyun [32], Copyright ©2003 with permission from Kluwer Academic/Plenum Publishers)
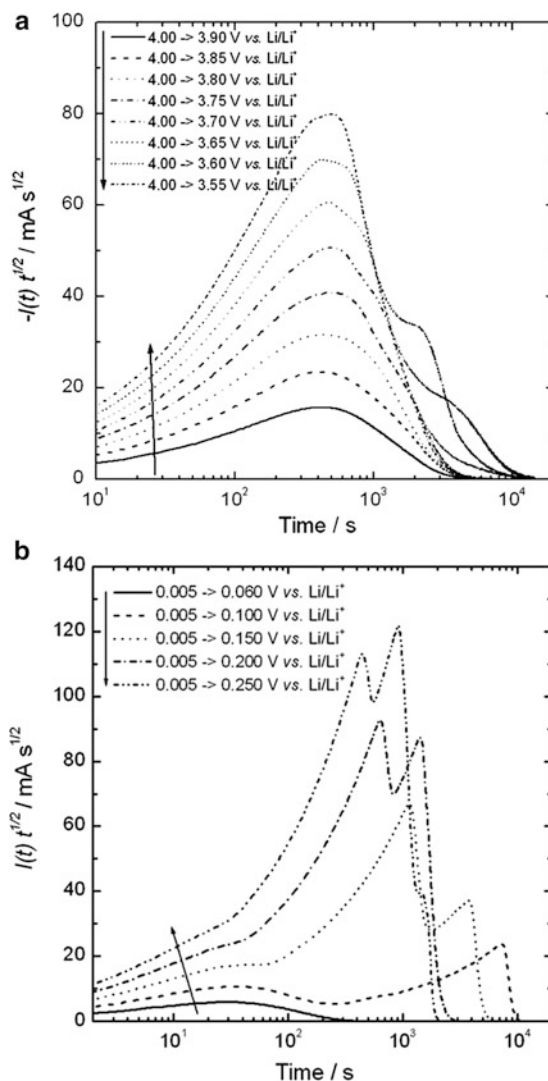
potential change (with the lithium content) in the cathodic and anodic directions, respectively. Then, the electrode potential curve with an upward concave shape in the single-phase region results in the mutual intersection of the cathodic and anodic current transients, as schematically demonstrated in Fig. 8.4.

8.4.1.3 Current Plateau During Phase Transition

In Sect. 8.1.3, it was explained that the charge transferred during the time span of the current plateau in the current transient is nearly equal to the charge in the potential plateau region of the electrode potential curve when the current plateau is

Fig. 8.21 Calculated
cathodic and anodic current
transients of (**a**) $Li_{1-\delta}CoO_2$
and (**b**) $Li_{1+\delta}[Ti_{5/3}Li_{1/3}]O_4$
under the assumption of the
"cell-impedance controlled"
lithium transport, showing
their mutual intersection in
the single phase region
(Reprinted from Shin and
Pyun [24], Copyright ©1999
and Shin et al. [27], Copyright
©2001, with permissions
from Elsevier Science)
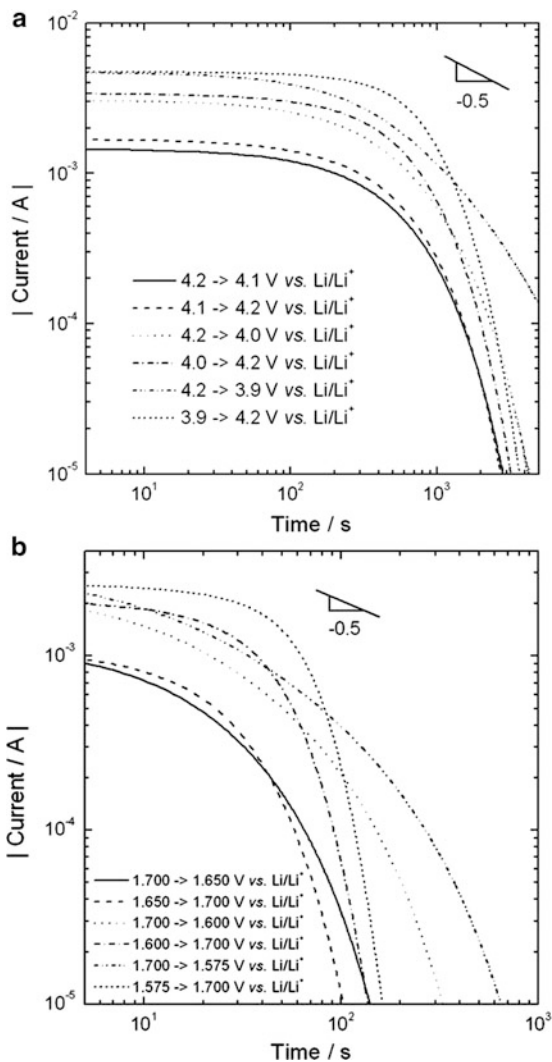
relatively clear, and the amount of charge transferred up to the inflexion point on the
quasi-current plateau falls to the potential plateau region when the time span of the
current plateau is unclear. This strongly implies that the (quasi-)current plateau is
ascribed to the phase transition. The above arguments are quite true for the "cell-
impedance-controlled" lithium transport, as discussed in Sect. 8.3.3: The calculated
flux is invariable in the course of the "cell-impedance-controlled" phase transition
in the case where there is no change in the cell resistance. The current plateaus and
inflection points in the experimental current transients of $Li_{1+\delta}[Ti_{5/3}Li_{1/3}]O_4$
(Fig. 8.5a) and $Li_\delta V_2O_5$ (Fig. 8.6a), respectively, are successfully reproduced in
the corresponding curves determined on the basis of "cell-impedance-controlled"
lithium transport, as presented in Fig. 8.22.

Fig. 8.22 Calculated cathodic current transients of (**a**) $Li_{1+\delta}[Ti_{5/3}Li_{1/3}]O_4$ and (**b**) $Li_\delta V_2O_5$ under the assumption of the "cell-impedance controlled" lithium transport, showing the current plateaus in the course of phase transition (Reprinted from Shin et al. [27], Copyright ©2001, with permission from Elsevier Science)
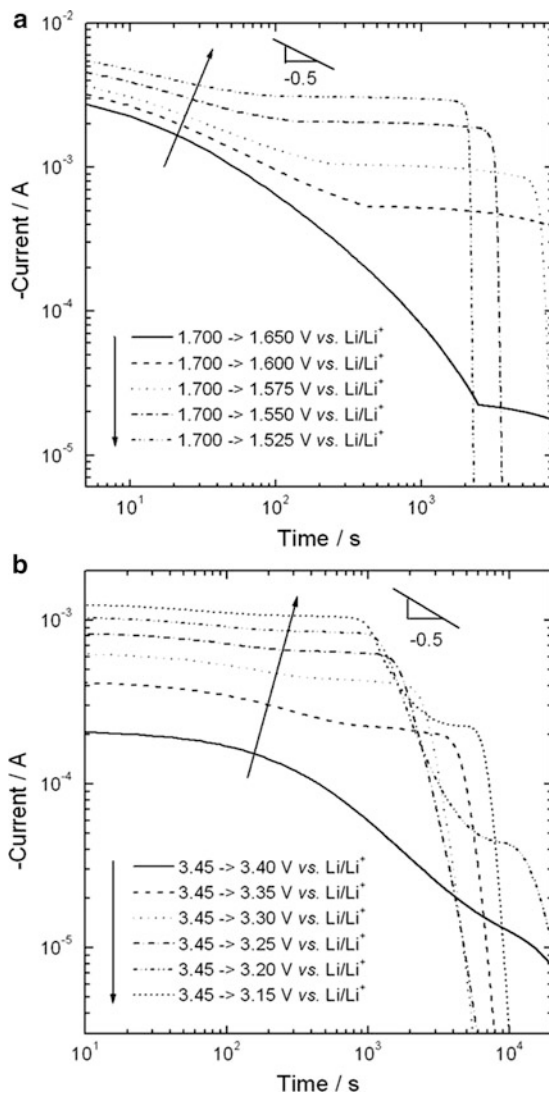
Nevertheless, two subtle differences are particularly noteworthy. One is the discrepancy in the plateau current level of the $Li_{1+\delta}[Ti_{5/3}Li_{1/3}]O_4$ system between the experimental and calculated curves, *especially* when the final potential is very close to the plateau potential (please compare the current plateaus in the curves of $Li_{1+\delta}[Ti_{5/3}Li_{1/3}]O_4$ where the final potential is 1.55 V vs. Li/Li$^+$). This does not appear to come from the intrinsic character of $Li_{1+\delta}[Ti_{5/3}Li_{1/3}]O_4$, but from the use of the closed circuit potential curve for the numerical calculation, instead of the open circuit potential curve. The closed circuit potential (during lithium insertion) is always found to be below the open circuit potential due to the (cathodic)

Fig. 8.23 Calculated anodic
current transients of
$Li_{1-\delta}NiO_2$ under the
assumption of the "cell-
impedance controlled" lithium
transport, showing the
depression of initial current
levels and their increase with
time (Reprinted from Lee et al.
[28], Copyright ©2001 with
permission from Elsevier
Science)
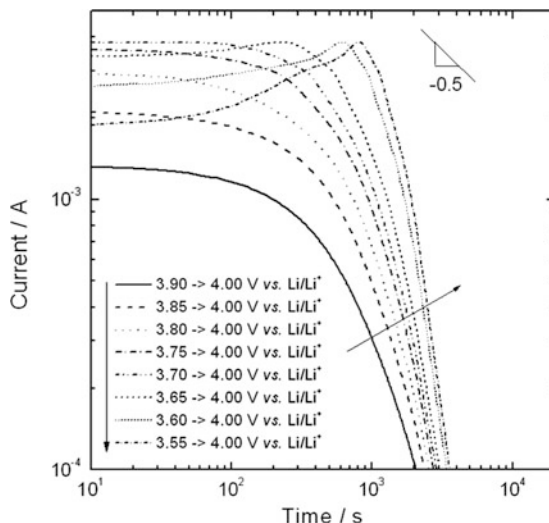
polarization. Accordingly, the $\left|E - E_{app}\right|$ value is underestimated, as compared to
what it should be and, thus, the calculated current level becomes much lower than
the experimental current level. The other difference is that the current plateaus
in the calculated curves are much clearer than those in the experimental curves.
The reason for this slight current slope observed during the phase transition in the
experimental curve has yet to be clarified. Nevertheless, the most plausible reason is
the increase in the cell resistance with increasing lithium content (Fig. 8.10a),
particle size distribution, etc.

8.4.1.4   Suppression of Initial Current Level and Current Increase with Time

The internal cell resistance of the $Li_{1-\delta}NiO_2$ system has a relatively stronger
dependence on the electrode potential (Fig. 8.11) than that of the other systems
previously mentioned. In this case, the time dependence of the cell resistance needs
to be considered for the reliable simulation of "cell-impedance-controlled" lithium
transport. The calculated current transients are shown in Fig. 8.23. It should be
mentioned that the curves are the result of the potential jumps (i.e., they are the
anodic current transients). Also, the initial potential is varied, while the final
potential is constant. This means that the cell impedances at the initial stage of
lithium transport are different from one another at all of the potential jumps. To be
precise, the lower the initial potential (or the larger the potential step), the larger the
cell resistance at the moment of the potential jump. The calculated curves appear to
exactly reveal the effect of the change in the cell resistance during the lithium

transport and reproduce fairly well the experimental curves (Fig. 8.7) in terms of the suppressed initial current and current increase with time. However, further clarification is needed as to why these features are more clearly seen in the calculated curves.

The cell impedance of $Li_{1-\delta}NiO_2$ increased sharply with decreasing electrode potential (Fig. 8.11), resulting in a reduction of the initial current level of the calculated curves with decreasing initial potential. The question is what makes the current suppression in the experimental curves much milder than that in the calculated ones (e.g., please compare the initial current levels of the calculated and experimental curves obtained at an initial potential of 3.55 V). To answer this question, the procedure employed for the chronoamperometry experiments and their limitation should be understood.

The time-dependent anodic current of the experimental curves was measured at a final potential of 4.00 V, immediately after maintaining the $Li_{1-\delta}NiO_2$ at the initial potential of 3.90, 3.85, ..., 3.60, or 3.55 V for 2×10^4 s. That is, the time required to cause the electrode to become equilibrated at a specific initial potential might be finite. Particularly, as the initial potential is lowered, it is more and more difficult to form a new equilibrium within several tens of thousands of seconds, due to the increased cell resistance and, thus, the real electrode potential is farther away from the initial potential that is tacitly admitted and considered for the calculation. As a result, the real values of both the driving force $E_{app} - E(t)$ and resistance R_{cell} at the initial stage are smaller than the values used for the numerical calculation. Furthermore, since R_{cell} is highly sensitive to the electrode potential in the low-potential region, as seen in Fig. 8.11, there is a greater underestimation of R_{cell} than of $E_{app} - E(t)$. Consequently, the measured current is higher than the calculated one at the initial stage of potential jumping, leading to the less suppressed initial current level of the experimental current transients.

The reason why the current increase in the calculated curves is much clearer than that in the experimental ones can be readily understood in the same context as the reason for the aforementioned current suppression. In the case of the "cell-impedance-controlled" lithium transport during the potential jump experiment for $Li_{1-\delta}NiO_2$, the current increase occurs when R_{cell} decreases more rapidly with time than $E_{app} - E(t)$. Let us take the case of the curve with an initial potential of 3.55 V. As explained above, it is quite unlikely that the equilibrium values of R_{cell} and $E(0)$ are attained, in spite of the prolonged time duration for equilibrating at 3.55 V. This indicates that the real potential is more than 3.55 V and, therefore, the real cell resistance is far less than $250 \, \Omega$ (Fig. 8.11). More importantly, the absolute value of the slope at the real electrode potential must be much smaller than that at 3.55 V (Fig. 8.11). This reduces the rate of decrease of R_{cell} during lithium extraction and eventually slows the current increase with time. The same argument holds in the curves with the initial potentials of 3.60 and 3.65 V, where R_{cell} is still quite susceptible to the electrode potential.

Fig. 8.24 Cathodic current transients of $Li_{1-\delta}NiO_2$ at different chemical diffusion coefficients, calculated by dropping the potential from 4.00 to 3.55 V versus Li/Li$^+$ under the assumption of the "cell-impedance controlled" lithium transport (Reprinted from Shin and Pyun [32], Copyright ©2003 with permission from Kluwer Academic/Plenum Publishers)
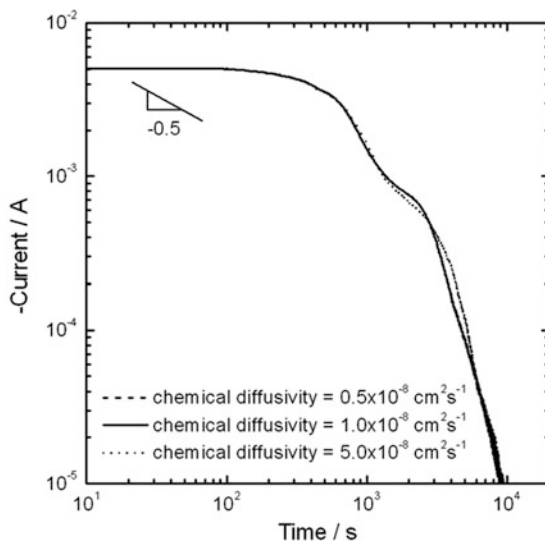
8.4.2 Parametric Dependence of Current Transients

8.4.2.1 Diffusion Coefficient

The current and its time dependence monitored during the chronoamperometry experiment contain the kinetic information of the overall reaction or, more specifically, the information on the rate-controlling step. Based on the tacit belief that the solid-state diffusion is the slowest step out of all of the reaction steps, the current transient has been widely used to estimate the diffusion coefficient of lithium. However, the several abnormal lithium transport behaviors observed in the chronoamperometry experiment (i.e., non-Cottrell character, current plateau, initial current depression, and current increase with time) make it quite unlikely that solid-state lithium diffusion governs the rate of the lithium insertion process. Instead, as discussed in previous sections, it looks like "cell-impedance-controlled" lithium transport is fairly promising as a new model to explain the curves and explain their abnormalities.

Then, does the rate of solid-state diffusion really have little effect on the shape and value of the "cell-impedance-controlled" current transients? Although the diffusion coefficient is not a crucial factor in determining the reaction rate in the model, it affects the instantaneous surface lithium content (please see Eq. 8.5) and content profile inside the electrode. To what extent does such an influence change the curves? The current transients calculated at different values of the diffusion coefficient (Fig. 8.24) shows that an order of magnitude increase in the diffusion coefficient causes small but discernible changes in the shape and value of the curves. This implies that the time (or lithium content)-dependent change in the diffusion coefficient needs to be considered even in the "cell-impedance-controlled" lithium transport, unless the change is trivial.
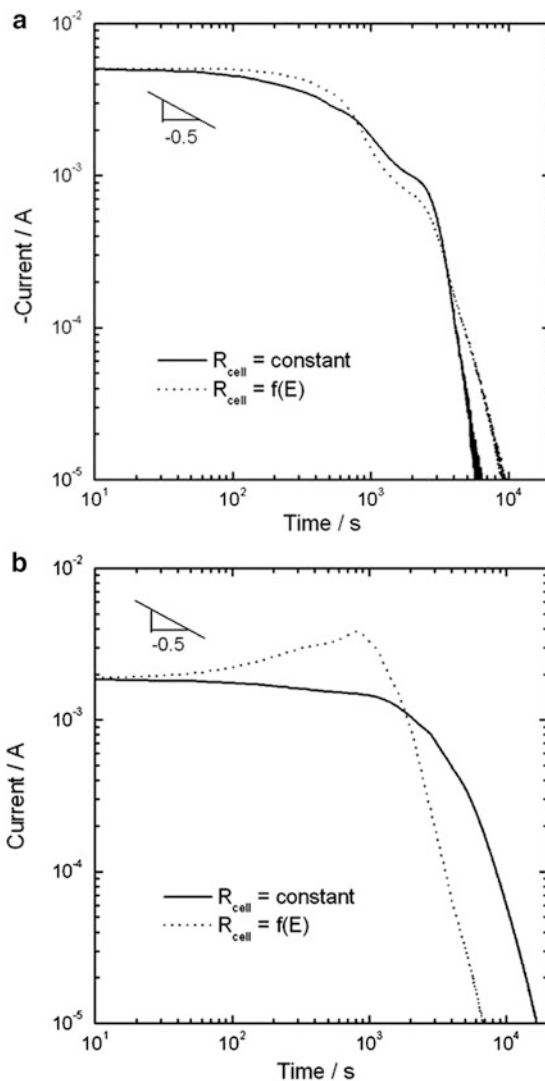
8.4.2.2   Cell Resistance

The effect of the cell resistance on the lithium transport (or the current transients) was already discussed in a relatively qualitative fashion when we set forth the reason for the suppressed initial current and time-dependent current increase of the current transients of $Li_{1-\delta}NiO_2$. Now, let us explore how much inaccuracy is introduced if the resistance change is not considered in the numerical calculation. Shown in Fig. 8.25 are the current transients calculated with and without considering the resistance change with time (or electrode potential), under the assumption of the "cell-impedance-controlled" lithium transport.

Regardless of the cathodic (lithium insertion, Fig. 8.25a) and anodic (lithium extraction, Fig. 8.25b) curves, there is a great discrepancy between the curves calculated with and without considering the resistance change with time. Especially, the two anodic curves might be considered to be completely different from each other in terms of their shape, while there are many parallels between the two cathodic curves – one inflection point, a mild decrease, and a subsequent abrupt drop in current. This considerable difference in the anodic curves is because the resistance drop is so large in the initial stage of the lithium extraction process that the anodic curve is seriously distorted from its normal monotonic decreasing tendency, as discussed in Fig. 8.23. This strongly implies that the change in the internal cell resistance must be critically considered for the reliable calculation of the "cell-impedance-controlled" lithium transport.

8.4.3   Theoretical Current-Time Relation

The theoretical equation for the "cell-impedance-controlled" current transient can be derived in a simplified case, with the assumptions that (1) the electrode potential is linearly dependent on the lithium content; (2) the phase transition does not take place during the insertion; (3) the double-layer charging current can be ignored; (4) the cell impedance R_{cell} and the chemical diffusivity of lithium $\tilde{D}_{Li}$ remain constant throughout the process. The current-time relation can be found from the solution of Fick's diffusion equation under the following initial and boundary conditions:

$$Initial\ condition\ :\ c = c^\circ\ \ for\ \ 0 \leq x \leq L\ \ at\ \ t = 0 \qquad (8.6)$$

$$Boundary\ \ condition\ :\ i = -nFA\tilde{D}_{Li}\left(\frac{\partial c(t)}{\partial x}\right)_{x=0} = \frac{E_{app}-E(t)}{R_{cell}} = \frac{V_m}{R_{cell}}\left(\frac{dE}{d\delta}\right)\left[c_{app} - c(t)\right]$$

$$for\ x = 0\ \ at\ \ t \geq 0$$
$$(8.7)$$

where c and c^o are the local and initial contents of lithium, respectively, c_{app} the lithium content at a potential of E_{app}, V_m the molar volume of the electrode, and $(dE/d\delta)$ the slope of the electrode potential versus lithium content curve at a given lithium content. Equation 8.7 indicates the cell-impedance-controlled interface condition under the assumption of a linear relationship between the electrode potential and the lithium content. When we apply the Laplace transform to the diffusion equation by considering the semi-infinite diffusion condition combined with Eqs. 8.6 and 8.7, we get the following current-time relation [51–54],

$$i = \left[\frac{E_{app} - E(0)}{R_{cell}}\right]\ \exp\left[\left(\frac{H}{R_{cell}}\right)^2 t\right]\ erfc\left[\left(\frac{H}{R_{cell}}\right)t^{1/2}\right]\ \ for\ t \ll \frac{L^2}{\tilde{D}_{Li}} \qquad (8.8)$$

Fig. 8.26 Electrode potential curve of the electrodeposited $Li_\delta V_2O_5$ film, determined by intermittently applying constant cathodic (lithium insertion) current (Reprinted from Lee and Pyun [54], Copyright ©2005 with permission from Elsevier Science)
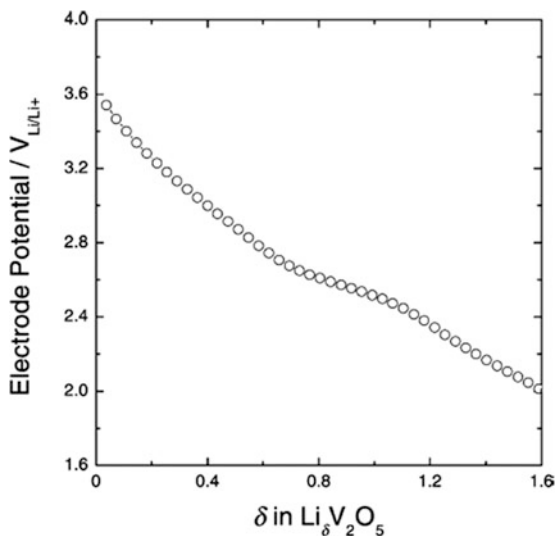
where

$$H = (V_m/F\tilde{D}_{Li}^{1/2}A)(dE/d\delta)$$

Although the derived current-time relation is of limited use due to the several assumptions to be made, it can be effectively used to systematically analyze the effect of the cell impedance R_{cell} and the chemical diffusivity of lithium $\tilde{D}_{Li}$ on current transient when we carefully control the experimental conditions, or to estimate their values from the "cell-impedance-controlled" current transient. The current transient of the electrodeposited $Li_\delta V_2O_5$ film electrode at a sufficiently early time (this makes the assumption (4) valid) gives a good example: Its electrode potential decreases monotonously without any potential plateau regions (i.e., the phase transition does not occur during lithium insertion) and the electrode potential versus lithium content curve is almost linear if we limit the potential interval to within *ca.* 0.1 V (Fig. 8.26). These satisfy the assumptions (1) and (2) used for the derivation of Eq. 8.8.

Figure 8.27a shows the experimental current transients (open symbols) and those calculated from Eq. 8.8 (dotted lines) by taking $E_{app} - E(0) = 0.1$ V. As can be seen in the figure, the experimentally measured current transients can be satisfactorily fitted to Eq. 8.8. For each transient, the parameters of R_{cell} and H (or $\tilde{D}_{Li}$) can be quantitatively estimated. When we collect the transient data in different potential ranges satisfying $E_{app} - E(0) = 0.1$ V and obtain the parameters by fitting them to Eq. 8.8, we can get the values of R_{cell} and $\tilde{D}_{Li}$ as a function of the electrode potential (Fig. 8.27b).

The use of Eq. 8.8 is much more suitable for the determination of R_{cell} than that of the initial current versus potential step plot (suggested in Fig. 8.8), because the

Fig. 8.27 (**a**) Typical experimental cathodic current transients (*symbols*) of the electrodeposited $Li_\delta V_2O_5$ and (**b**) the cell impedance R_{cell} and the chemical diffusivity of lithium $\tilde{D}_{Li}$ as a function of the electrode potential. *Dotted lines* in (a) were obtained by fitting the experimental current transients to Eq. 8.8, and R_{cell} and $\tilde{D}_{Li}$ were accordingly determined (Reprinted from Lee and Pyun [54], Copyright ©2005 with permission from Elsevier Science)
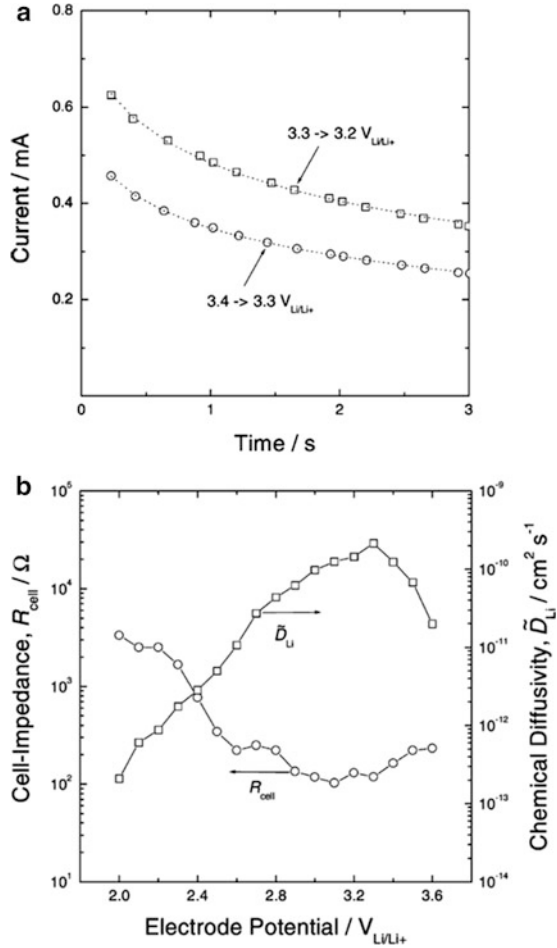
exact value of R_{cell} at a given potential is obtainable by extrapolating Eq. 8.8 to $t = 0$.

8.4.4 Cyclic Voltammograms

The variation in the current with the potential, i.e., the voltammogram, was discussed in Sect. 2.3 in the case of "diffusion-controlled" lithium transport, which is characterized by linearity between the peak current and the square root of the potential scan rate (the so-called Sevčik equation) for the semi-infinite diffusion process. However, such relationship is invalidated when the lithium transport is governed by the cell resistance. Actually, a number of studies have

reported abnormal voltammetric trends of lithium insertion compounds [55–60]. The "cell-impedance-controlled" model might shed light on their origin [61]. Figure 8.28a shows cyclic voltammograms of sputter-deposited $Li_{1-\delta}CoO_2$ at different potential scan rates, exhibiting continuous increase in peak shifts with scan rate. The deviation of the slope in the reproduced plot of peak current versus scan rate from the "Sevčik" relation, as seen in Fig. 8.28b, is also noteworthy. These are not typical from the viewpoint of the "diffusion-controlled" model (please see Fig. 2.12 for the typical shape of the "diffusion-controlled" cyclic voltammograms).
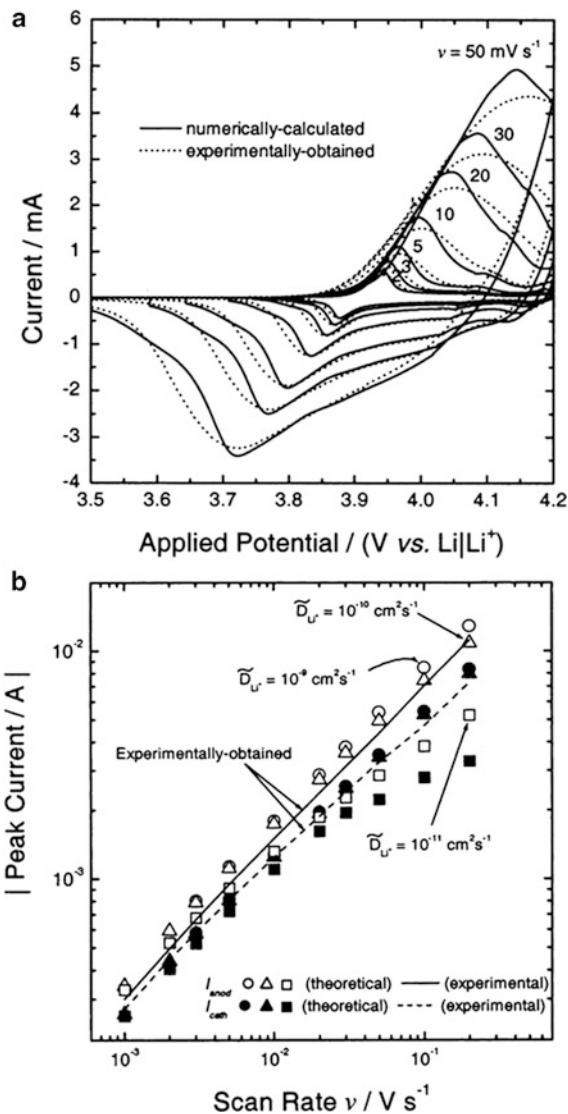
Now, it would be interesting to numerically calculate the cyclic voltammogram
under the assumption of "cell-impedance-controlled" lithium transport and
compare it with the experimental one. As shown in Fig. 8.29a, the experimental
and calculated voltammograms have high similarity with each other at different
scan rates. In particular, the shifts of the anodic and cathodic peaks with scan
rate are satisfactorily reproduced in the "cell-impedance-controlled" cyclic
voltammograms. The slope of peak current versus scan rate plot is matched well

with the experimental finding when the diffusion coefficient ranges from 10^{-9} to 10^{-10} cm^{2}s^{-1} (Fig. 8.29b).

References

1. Ohashi M, Gloffke W, Whittingham MS (1992) Iodine and lithium intercalation into the high-Tc superconducting oxide Bi$_2$Sr$_2$CaCu$_2$O$_y$. Solid State Ionics 57:183–187
2. Xu Q, Wan G (1993) Rechargeable Li/LiMn$_2$O$_4$ batteries with a polymeric solid electrolyte. J Power Sources 41:315–320
3. Barker J, Pynenburg R, Koksbang R (1994) Determination of thermodynamic, kinetic and interfacial properties for the Li//Li$_x$Mn$_2$O$_4$ system by electrochemical techniques. J Power Sources 52:185–192
4. Sato H, Takahashi D, Nishina T, Uchida I (1997) Electrochemical characterization of thin-film LiCoO$_2$ electrodes in propylene carbonate solutions. J Power Sources 68:540–544
5. De Albuquerque Maranhão SL, Torresi RM (1998) Electrochemical and chromogenics kinetics of lithium intercalation in anodic niobium oxide films. Electrochim Acta 43:257–264
6. McGraw JM, Bahn CS, Pariaal PA, Perkins JD, Reasey DW, Ginley DS (1999) Li ion diffusion measurements in V$_2$O$_5$ and Li(Co$_{1-x}$Al$_x$)O$_2$ thin-film battery cathodes. Electrochim Acta 45:187–196
7. Nishizawa M, Koshika H, Hashitani R, Itoh T, Abe T, Uchida I (1999) Ion- and electron-transport properties of a single particle of disordered carbon during the lithium insertion reaction. J Phys Chem B 103:4933–4936
8. Martos M, Morales J, Sánchez L (2000) Cation-deficient Mo$_y$Sn$_x$O$_2$ oxides as anodes for lithium ion batteries. Electrochim Acta 46:83–89
9. Fu ZW, Qin QZ (2000) Lithium intercalation and transport behavior in a Ta$_2$O$_5$ film fabricated by pulsed laser deposition. J Electrochem Soc 147:4610–4614
10. Waki S, Dokko K, Itoh T, Nishizawa M, Abe T, Uchida I (2000) High-speed voltammetry of Mn-doped LiCoO$_2$ using a microelectrode technique. J Solid State Electrochem 4:205–209
11. Isidorsson J, Strømme M, Gahlin R, Niklasson GA, Granqvist CG (1996) Solid State Commun 99:109–111
12. Mattsson MS, Niklasson GA, Granqvist CG (1996) Fractal dimension of Li insertion electrodes studied by diffusion-controlled voltammetry and impedance spectroscopy. Phys Rev B 54:2968–2971
13. Bae JS, Pyun SI (1996) Electrochemical lithium intercalation into and deintercalation from vanadium oxide electrode by using potentiostatic current transient technique. Solid State Ionics 90:251–260
14. Pyun SI, Choi YM (1997) Electrochemical lithium intercalation into and de-intercalation from porous LiCoO$_2$ electrode by using potentiostatic current transient technique. J Power Sources 68:524–529
15. Pyun SI, Ryu YG (1998) Lithium transport through graphite electrodes that contain two stage phases. J Power Sources 70:34–39
16. Pyun SI (1999) Lithium intercalation into and deintercalation from Li$_{1-\delta}$Al$_{1/4}$Ni$_{3/4}$O$_2$ electrode: current transient analysis. J Power Sources 81–82:442–447
17. Funabiki A, Inaba M, Abe T, Ogumi Z (1999) Nucleation and phase-boundary movement upon stage transformation in lithium-graphite intercalation compounds. Electrochim Acta 45:865–871
18. Levi MD, Aurbach D (1999) Frumkin intercalation isotherm – a tool for the description of lithium insertion into host materials: a review. Electrochim Acta 45:167–185

19. Levi MD, Salitra G, Markovsky B, Teller H, Aurbach D, Heider U, Heider L (1999) Solid-state electrochemical kinetics of Li-Ion intercalation into $Li_{1-x}CoO_2$: simultaneous application of electroanalytical techniques SSCV, PITT, and EIS. J Electrochem Soc 146:1279–1289
20. Mattsson MS, Isidorsson J, Lindström T (1999) Theoretical analysis of chronoamperometric electrochemical ion intercalation. J Electrochem Soc 146:2613–2615
21. Noel M, Rajendran V (2000) A comprehensive model for cyclic voltammetric study of intercalation/de-intercalation process incorporating charge transfer, ion transport and thin layer phenomena. J Power Sources 88:243–249
22. Hjelm AK, Lindbergh G, Lundqvist A (2001) Investigation of $LiMn_2O_4$ cathodes for use in rechargeable lithium batteries by linear sweep voltammetry (LSV): part II. Experimental study using thin films, single particles and composite electrodes. J Electroanal Chem 509:139–147
23. Krtil P, Fattakhova D (2001) Li Insertion into Li-Ti-O spinels: voltammetric and electrochemical impedance spectroscopy study. J Electrochem Soc 148:A1045–A1050
24. Shin HC, Pyun SI (1999) The kinetics of lithium transport through $Li_{1-\delta}CoO_2$ by theoretical analysis of current transient. Electrochim Acta 45:489–501
25. Pyun SI, Shin HC (2001) The kinetics of lithium transport through $Li_{1-\delta}CoO_2$ thin film electrode by theoretical analysis of current transient and cyclic voltammogram. J Power Sources 97–98:277–281
26. Pyun SI, Lee MH, Shin HC (2001) The kinetics of lithium transport through vanadium pentoxide composite and film electrodes by current transient analysis. J Power Sources 97–98:473–477
27. Shin HC, Pyun SI, Kim SW, Lee MH (2001) Mechanisms of lithium transport through transition metal oxides studied by analysis of current transients. Electrochim Acta 46:897–906
28. Lee MH, Pyun SI, Shin HC (2001) The kinetics of lithium transport through $LiNiO_2$ by current transient analysis. Solid State Ionics 140:35–43
29. Pyun SI, Kim SW (2001) Lithium transport through $Li_{1-\delta}Mn_2O_4$ electrode involving the ordering of lithium ion by numerical analysis of current transient. J Power Sources 97–98:371–376
30. Kim SW, Pyun SI (2002) Lithium transport through a sol–gel derived $LiMn_2O_4$ film electrode: analyses of potentiostatic current transient and linear sweep voltammogram by Monte Carlo simulation. Electrochim Acta 47:2843–2855
31. Go JY, Pyun SI, Shin HC (2002) Lithium transport through the $Li_{1-\delta}CoO_2$ film electrode prepared by rf magnetron sputtering. J Electroanal Chem 527:93–102
32. Shin HC, Pyun SI (2003) Chapter 5 mechanisms of lithium transport through transition metal oxides and carbonaceous materials. In: Vayenas CG, Conway BE, White RE (eds) Modern aspects of electrochemistry, vol 36. Kluwer Academic/Plenum Publishers, New York
33. Lee JW, Pyun SI (2004) Investigation of lithium transport through $LiMn_2O_4$ film electrode in aqueous $LiNO_3$ solution. Electrochim Acta 49:753–761
34. Jung KN, Pyun SI (2006) The cell-impedance-controlled lithium transport through $LiMn_2O_4$ film electrode with fractal surface by analyses of ac-impedance spectra, potentiostatic current transient and linear sweep voltammogram. Electrochim Acta 51:4649–4658
35. Jung KN, Pyun SI (2007) Theoretical approach to cell-impedance-controlled lithium transport through $Li_{1-\delta}Mn_2O_4$ film electrode with partially inactive fractal surface by analyses of potentiostatic current transient and linear sweep voltammogram. Electrochim Acta 52:2009–2017
36. Markovsky B, Levi MD, Aurbach D (1998) The basic electroanalytical behavior of practical graphite–lithium intercalation electrodes. Electrochim Acta 43:2287–2304
37. Yang W, Zhang G, Lu S, Xie J, Liu Q (1999) Electrochemical studies of Li/LixMn2O4 by using powder microelectrode. Solid State Ionics 121:85–89
38. Lu Z, Levi MD, Salitra G, Gofer Y, Levi E, Aurbach D (2000) Basic electroanalytical characterization of lithium insertion into thin, well-crystallized V_2O_5 films. J Electroanal Chem 491:211–221

39. Varsano F, Decker F, Masetti E, Croce F (2001) Lithium diffusion in cerium–vanadium mixed oxide thin films: a systematic study. Electrochim Acta 46:2069–2075

40. Funabiki A, Inaba M, Abe T, Ogumi Z (1999) Influence of defects on the phase-boundary movement in a stage transformation of lithium-graphite intercalation compounds. Carbon 37:1591–1598

41. Funabiki A, Inaba M, Abe T, Ogumi Z (1999) Stage transformation of lithium-graphite intercalation compounds caused by electrochemical lithium intercalation. J Electrochem Soc 146:2443–2448

42. Ohzuku T, Ueda A (1997) Phenomenological expression of solid-state redox potentials of $LiCoO_2$, $LiCo_{1/2}Ni_{1/2}O_2$, and $LiNiO_2$ insertion electrodes. J Electrochem Soc 144:2780–2785

43. Murray WD, Landis F (1959) Numerical and machine solutions of transient heat conduction problems involving phase change. Trans ASME Ser C J Heat Transfer 81:106–112

44. Shin HC, Pyun SI (1999) An investigation of the electrochemical intercalation of lithium into a $Li_{1-\delta}CoO_2$ electrode based upon numerical analysis of potentiostatic current transients. Electrochim Acta 44:2235–2244

45. Choi YM, Pyun SI, Paulsen JM (1998) Lithium transport through porous $Li_{1-\delta}CoO_2$ electrode: analysis of current transient. Electrochim Acta 44:623–632

46. Dickens PG, Reynolds GJ (1981) Transport and equilibrium properties of some oxide insertion compounds. Solid State Ionics 5:331–334

47. Takami N, Satoh A, Hara M, Ohsaka T (1995) Structural and kinetic characterization of lithium intercalation into carbon anodes for secondary lithium batteries. J Electrochem Soc 142:371–379

48. Choi YM, Pyun SI, Moon SI (1996) Effects of cation mixing on the electrochemical lithium intercalation reaction into porous $Li_{1-\delta}Ni_{1-y}Co_yO_2$ electrodes. Solid State Ionics 89:43–52

49. Choi YM, Pyun SI (1997) Effects of intercalation-induced stress on lithium transport through porous $LiCoO_2$ electrode. Solid State Ionics 99:173–183

50. Zaghib K, Simoneau M, Armand M, Gauthier M (1999) Electrochemical study of $Li_4Ti_5O_{12}$ as negative electrode for Li-ion polymer rechargeable batteries. J Power Sources 81–82:300–305

51. Crank J (1975) The mathematics of diffusion. Oxford University Press, London

52. Raistrick ID, Huggins RA (1982) The transient electrical response of electrochemical systems containing insertion reaction electrodes. Solid State Ionics 7:213–218

53. Montella C (2002) Discussion of the potential step method for the determination of the diffusion coefficients of guest species in host materials: part I. Influence of charge transfer kinetics and ohmic potential drop. J Electroanal Chem 518:61–83

54. Lee JW, Pyun SI (2003) Investigation of lithium transport through an electrodeposited vanadium pentoxide film electrode. J Power Sources 119–121:760–765

55. Peres PCD, de Paoli M, Panero S, Scrosati B (1992) A new electrode for a poly(pyrrole)-based rechargeable battery. J Power Sources 40:299–305

56. Kanoh H, Feng Q, Miyai Y, Ooi K (1995) Kinetic properties of a Pt/Lambda-MnO_2 electrode for the electroinsertion of lithium ions in an aqueous phase. J Electrochem Soc 142:702–707

57. Uchida I, Sato H (1995) Preparation of binder-free, thin film $LiCoO_2$ and its electrochemical responses in a propylene carbonate solution. J Electrochem Soc 142:L139–L141

58. Uchida I, Fujiyoshi H, Waki S (1997) Microvoltammetric studies on single particles of battery active materials. J Power Sources 68:139–144

59. Morcrette M, Barboux P, Perrière J, Brousse T, Traverse A, Boilot JP (2001) Non-stoichiometry in $LiMn_2O_4$ thin films by laser ablation. Solid State Ionics 138:213–219

60. Striebel KA, Deng CZ, Wen SJ, Cairns EJ (1996) Electrochemical behavior of $LiMn_2O_4$ and $LiCoO_2$ thin films produced with pulsed laser deposition. J Electrochem Soc 143:1821–1827

61. Shin HC, Pyun SI (2001) Investigation of lithium transport through lithium cobalt dioxide thin film sputter-deposited by analysis of cyclic voltammogram. Electrochim Acta 46:2477–2485

Chapter 9
Lithium Transport Through Electrode with Irregular/Partially Inactive Interfaces

9.1 Quantification of the Surface Irregularity/Inactiveness Based on Fractal Geometry

9.1.1 Introduction to Fractal Geometry

Fractal geometry is a tool employed to define real objects in nature which cannot be characterized by Euclidean geometry. It was conceptualized by Mandelbrot [1] and has been widely used in various fields such as science, art [2–4], economics [5–8], etc. Especially, in science, the secret of the anomalous phenomena which take place on rough and irregular surfaces has been unlocked with the help of fractal geometry.

Rough and irregular surfaces are created by electrodeposition [9–23], fracture [24–29], vapor deposition [18, 30–43], corrosion [44–51], surface modification such as machining and plasma irradiation [52–57], etc. These surfaces can be characterized by fractal geometry according to their own scaling properties: self-similar or self-affine. Self-similar fractals show isotropic scaling behavior in all directions, whereas self-affine fractals show asymmetric scaling behavior perpendicular to the surface. Self-affine fractals are more complex than self-similar fractals and most rough and irregular surfaces belong to the category of self-affine fractals.

The methods employed for the determination of the surface fractal dimension should be clarified according to the scaling property of the surface before using them. When we consider lithium transport through electrode with irregular/partially inactive interfaces, the characterization of these interfaces with the proper fractal dimension [58] is the first step and then the effect of the irregularity on the lithium transport could be analyzed [59]. Here, self-similar and self-affine fractals will be introduced in detail in order to get them well understood [60, 61].
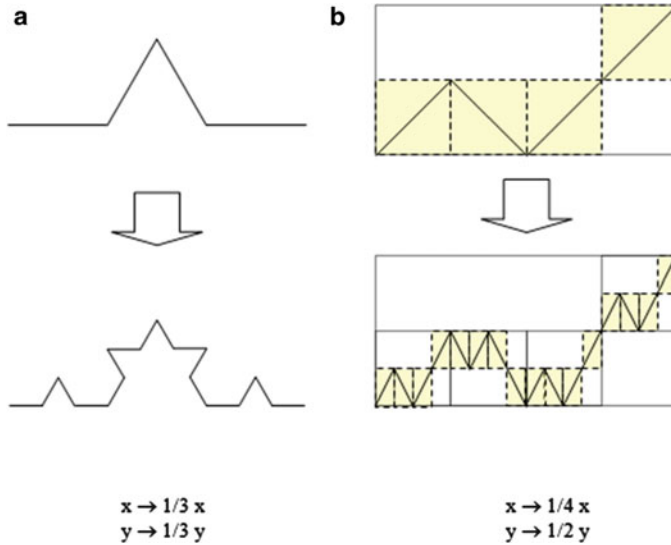
Fig. 9.1 (**a**) A deterministic self-similar fractal, i.e., the triadic Koch curve, generated by the similarity transformation with the scaling ratio $r = 1/3$ and (**b**) a deterministic self-affine fractal generated by the affine transformation with the scaling ratio vector $\mathbf{r} = (1/4, 1/2)$ (Reprinted from Go and Pyun [58], Copyright © 2005 with permission from Kluwer Academic/Plenum Publishers)

9.1.1.1   Self-similar Fractal

When a set of points S at position $\mathbf{x} = (x_1, ..., x_E)$ in Euclidean E-dimensional space is transformed into a new set of points $r(S)$ at position $\mathbf{x}' = (rx_1, ..., rx_E)$ with the scaling ratio $0 < r < 1$, we call it the similarity transformation. A bounded set S is self-similar with respect to a scaling ratio r if S is the union of N nonoverlapping subsets $S_1, ..., S_N$, each of which is congruent to the set $r(S)$. Here, congruent means that the set of points S_i is identical to the set of points $r(S)$ after possible translations and/or rotations.

For a deterministic self-similar fractal, the self-similar fractal dimension $d_{F,ss}$ is uniquely defined by the similarity dimension $d_{F,S}$ given by

$$d_{F,S} = \frac{\ln N}{\ln 1/r} \tag{9.1}$$

The triadic Koch curve is a representative deterministic self-similar fractal. Figure 9.1a depicts that it is generated by a similarity transformation with scaling ratio $r = 1/3$. In this case, the resulting curve is the union of four nonoverlapping curves and is congruent to the curve obtained from the original one by the similarity transformation. Therefore, $d_{F,ss}$ of this curve is determined to be $d_{F,S} = \ln 4/\ln 3 \cong 1.26$ by Eq. 9.1.

The set S is statistically self-similar when S is the union of N distinct subsets, each of which is scaled down by r from the original and is congruent to $r(S)$ in all statistical respects. For such sets, the box-counting method is useful in estimating $d_{F,ss}$ of the set [1, 60–64]. The box dimension $d_{F,B}$ is equal to $d_{F,S}$.

9.1.1.2   Self-affine Fractal

When a set of points S at position $\mathbf{x} = (x_1, ..., x_E)$ in Euclidean E-dimensional space is transformed into a new set of points $\mathbf{r}(S)$ at position $\mathbf{x}' = (r_1 x_1, ..., r_E x_E)$ with different scaling ratios $0 < r_1, ..., r_E < 1$, we call it the affine transformation. A bounded set S is self-affine with respect to a scaling ratio vector $\mathbf{r} = (r_1, ..., r_E)$ if S is the union of N nonoverlapping subsets $S_1, ..., S_N$, each of which is congruent to the set $\mathbf{r}(S)$. A deterministic self-affine fractal generated by the affine transformation with scaling ratio vector $\mathbf{r} = (1/4, 1/2)$ is demonstrated in Fig. 9.1b. The resulting curve is the union of four nonoverlapping curves and is congruent to the curve obtained from the original one by the affine transformation.

The set S is statistically self-affine when S is the union of N nonoverlapping subsets, each of which is scaled down by $\mathbf{r}$ from the original and is congruent to $\mathbf{r}(S)$ in all statistical respects.

The dimension of the self-similar fractal is simply defined as the similarity dimension $d_{F,S}$. However, the dimension of self-affine fractal $d_{F,sa}$ is not uniquely defined [60, 61, 65], i.e., there are two different dimensions: a global dimension and a local dimension [60–62, 65–67]. The global dimension is observed above a certain crossover scale. It is simply defined as $d_E - 1$, where d_E represents the topological dimension of the Euclidean space where the set is embedded. The self-affine fractal looks essentially smooth for large sizes.

Therefore, the local dimension describes the irregularity of the self-affine fractal. The local dimension can be determined by such methods as the box-counting method [1, 60–64] and the divider-walking method [60, 65]. $d_{F,B}$ for the self-affine fractal is defined by the Hurst exponent H which is a power exponent observed in the power law between the root mean square (*rms*) roughness σ_{rms} and the horizontal length L of the self-affine fractal according to the following equation:

$$d_{F,B} = d_E - H \qquad 0 < H < 1 \tag{9.2}$$

H defines divider dimension $d_{F,D}$ also as follows:

$$d_{F,D} = \frac{1}{H} \, 0 < H < 1 \tag{9.3}$$

As indicated in Eqs. 9.2 and 9.3, $d_{F,B}$ and $d_{F,D}$ do not coincide in value. Therefore, H is a unique parameter to characterize the self-affine fractal.

9.1.2   Characterization of Surface Using Fractal Geometry

The surface roughness is usually quantified using surface profiler or imaging equipment, such as a scanning electron microscope (*SEM*), transmission electron microscope (*TEM*), and scanning probe microscope (*SPM*). The digitized surface profile or image is used to determine the statistical roughness parameter like the rms roughness σ_{rms}. It describes only the vertical amplitude in a certain lateral direction so it is rather inadequate to provide a complete description of the three-dimensional surface. However, the surface fractal dimension represents both the vertical and lateral information of the three-dimensional surface over a significant range of length scales.

SPM would be a more adequate technique than *SEM* and *TEM* for the fractal analysis of the surface morphology. It has its high three-dimensional resolution and nondestructive character. Scanning tunneling microscope (*STM*) and atomic force microscope (*AFM*) provide the direct digitized height data with a resolution down to the atomic scale, whereas *SEM* and *TEM* produce the two-dimensional cross section of the surface morphology which can be described by only binary digits.

There are several algorithms used to determine the surface fractal dimension from *SPM* images, e.g., the power-spectrum method [1, 2, 68–71], the triangulation method [34, 40, 42, 60, 65, 72–76], the perimeter-area method [15–18, 20, 22, 24, 60, 61, 71, 77–79], the structure function method [2, 53, 54, 70, 77, 80, 81], the variance method [53, 54], and the box-counting method [1, 60–64]. Among these algorithms, the triangulation method and perimeter-area method are more popular so they are introduced in this chapter as useful tools to determine the self-similar and self-affine fractal dimensions, respectively.

9.1.2.1   Triangulation Method

The triangulation method, which is analogous to the Richardson method for a profile, is used to determine the self-similar fractal dimension $d_{F,ss}$ of three-dimensional self-similar fractal surface [1]. For this, the three-dimensional digitized image of the surface should be prepared.

Figure 9.2 describes schematically the algorithm used for the determination of $d_{F,ss}$ by the triangulation method. The square (x,y) plane with a cell size L^2 is first divided into N^2 equal squares. This defines the location of the vertices of a number of triangles. Then, the electrode surface is covered by $2N^2$ triangles inclined at various angles with respect to the (x,y) plane. These $2N^2$ triangles have equal projected triangle sizes, *TS* ($=L/N$), although their real areas are different.

The scaled surface area, *SSA*, *i.e.*, the measured surface area covered by the $2N^2$ triangles, is estimated to be the sum of the areas of all of the $2N^2$ triangles. This measurement is iterated with decreasing projected triangle size, *TS*, until every pixel in the *AFM* image serves as the vertices of the $2N^2$ triangles. Then, $d_{F,ss}$ of the surface is given by:
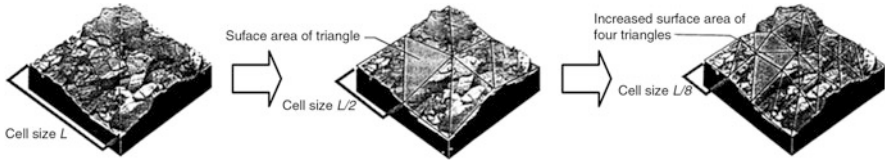
Fig. 9.2 Process of determination of the self-similar fractal dimension of the three-dimensional surface by the triangulation method (Reprinted from Go and Pyun [58], Copyright © 2005 with permission from Kluwer Academic/Plenum Publishers)
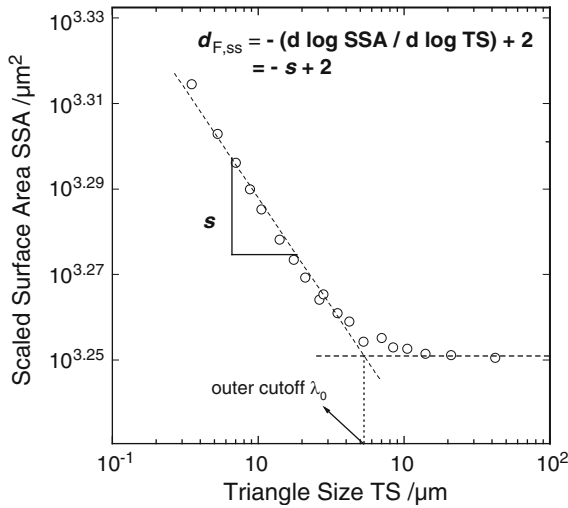
**Fig. 9.3** Dependence of the scaled surface area *SSA* on the projected triangle size *TS* on a logarithmic scale obtained from the three-dimensional *AFM* image of the rough surface (Reprinted from Go and Pyun [58], Copyright © 2005 with permission from Kluwer Academic/Plenum Publishers)

$$d_{\mathrm{F,ss}} = -\frac{\mathrm{d}\log SSA}{\mathrm{d}\log TS} + 2 \qquad (9.4)$$

Figure 9.3 shows the resulting *SSA*s plotted as a function of the projected *TS* on a logarithmic scale obtained from the three-dimensional *AFM* image of the rough surface. The linear relationship between the logarithm of the *SSA* and the logarithm of the projected *TS* is clearly displayed up to the *TS* less than around 5 μm, so $d_{\mathrm{F,ss}}$ of the surface can be determined using Eq. 9.4 within this length scale.

However, the logarithm of the *SSA* becomes constant over 5 μm of the *TS*. It means the rough surface shows fractal behavior within the certain length-scale range between the inner and outer cutoffs. In Fig. 9.3, the value of *TS* for which the linear line with a slope of *s* and the horizontal line intersect is the spatial outer (upper) cutoff λ_{o}. Due to the limitation in the resolution of the equipment, we cannot evaluate the spatial inner (lower) cutoff λ_{i} in this case.

a

b
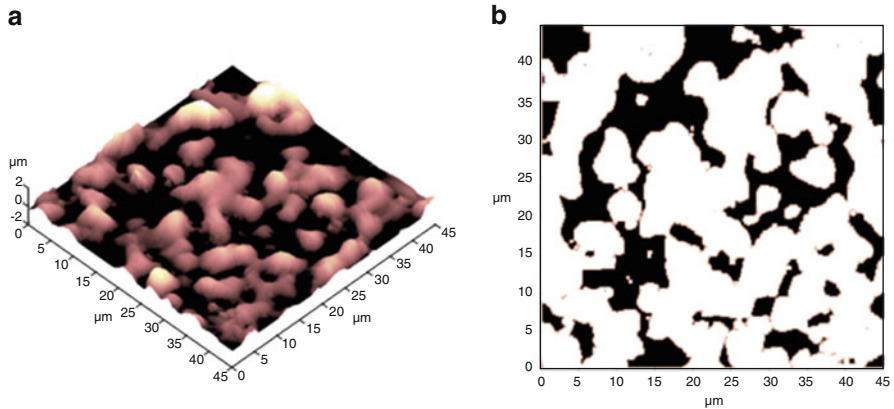
Fig. 9.4 (**a**) Three-dimensional *AFM* image of the rough surface filled with water (*black pixels*) up to a height corresponding to 40% of the maximum height and (**b**) corresponding two-dimensional description of the perimeters (*gray pixels*) and areas (*gray* and *black pixels*) of the lakes (Reprinted from Go and Pyun [58], Copyright © 2005 with permission from Kluwer Academic/Plenum Publishers)

9.1.2.2   Perimeter-Area Method

The perimeter-area method is based on the fact that the intersection of a plane with a self-affine fractal surface generates self-similar lakes. It usually used to characterize the self-affine fractal surface as $d_{\mathrm{F,sa}}$. To employ this method, the surface image obtained using tools such as *SEM*, *TEM*, and *STM* should be digitized and then the two-dimensional cross section of the surface at a certain height should be generated. The area A and perimeter P of self-similar lakes in the cross section of the fractal surface shows the relation with its fractal dimension $d_{\mathrm{F,ss}}^{\mathrm{L}}$ by

$$P = \beta\, d_{\mathrm{F,ss}}^{\mathrm{L}}\, A^{d_{\mathrm{F,ss}}^{\mathrm{L}}/2} \tag{9.5}$$

where β is a proportionality constant [60, 77]. Then, $d_{\mathrm{F,sa}}$ of the original surface is

$$d_{\mathrm{F,sa}} = d_{\mathrm{F,ss}}^{\mathrm{L}} + 1 \tag{9.6}$$

Figure 9.4a, b shows the example of application of the perimeter-area method. Figure 9.4a is the three-dimensional *AFM* images of the rough surface filled with water (black pixels) up to a height corresponding to 40% of the maximum height of the surface, and Fig. 9.4b is the corresponding two-dimensional description of P (gray pixels) along with A (black pixels + gray pixels) of the self-similar lakes. Here, the gray pixels in Fig. 9.4b are defined as the black pixels neighboring white pixels. The value of P is the numbers of gray pixels of each lake and the value of A is the number of both the black pixels and gray pixels for each lake.

Fig. 9.5 Dependence of the perimeter P on the area A for the self-similar lakes generated by the intersection of the three-dimensional *AFM* image of the rough surface with a plane at a height corresponding to 40% of the maximum height (Reprinted from Go and Pyun [58], Copyright © 2005 with permission from Kluwer Academic/Plenum Publishers)
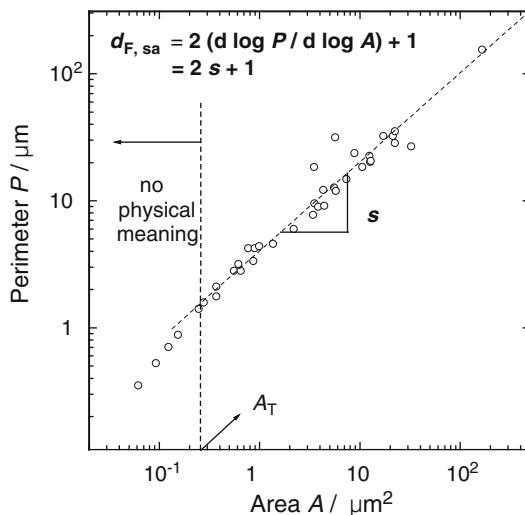
Figure 9.5 shows the plot of P against A of each self-similar lake on a logarithmic scale. It is clearly shown that the linear relation between $\log P$ and $\log A$ above the threshold area, $A_T \approx 2.6 \times 10^{-13} \, \text{m}^2$. From this linear line, the self-similar dimension of the two-dimensional lakes $d_{F,ss}^L$ and the self-affine fractal dimension of the three-dimensional surface $d_{F,sa}$ are determined using Eqs. 9.5 and 9.6, respectively. The other linear relation below A_T is physically meaningless, due to the limitation of the *AFM* measurement [17].

9.2   Theory of the Diffusion toward and from a Fractal Electrode

The diffusion toward and from a fractal electrode has been theoretically analyzed by using fractional derivatives [82]. Here, the generalized diffusion equation (*GDE*) is introduced with its historical background in Sect. 9.2.1 and, then, its analytical solutions are summarized under the various boundary conditions in Sects. 9.2.2 and 9.2.3.

9.2.1   Mathematical Equations

Le Mehaute [83, 84] proposed the *TEISI* (Transfert d'Energie sur Interface à Similitude Interne) model, which treats the thermodynamics of irreversible processes, in order to describe the transfer processes across a fractal interface in the sense of Mandelbrot [1]. In the linear approximation of the thermodynamics of

irreversible processes, the macroscopic flow of an extensive quantity across the fractal interface $J(t)$ is described by a generalized transfer equation which is expressed as

$$\frac{\mathrm{d}^{(1/d_F)-1}}{\mathrm{d}t^{(1/d_F)-1}}J(t) = K_0\Delta X(t) \tag{9.7}$$

where d_F is the fractal dimension, K_0 a constant, and $\Delta X(t)$ the local driving force.

The *GDE* involving the fractional derivative was explicitly introduced in physics by Nigmatullin [85] to describe the diffusion across a surface with fractal geometry and was mathematically studied by Wyss [86, 87] and Mainardi [88]. In the simplest case of spatially one-dimensional diffusion, it is expressed as [89]

$$\frac{\partial^{3-d_F}c(x,t)}{\partial t^{3-d_F}} = \tilde{D}^* \frac{\partial^2 c(x,t)}{\partial x^2} \quad (2 \leqslant d_F < 3) \tag{9.8}$$

where $c(x,t)$ is the local concentration of diffusing species, x the distance from the fractal interface, $\tilde{D}^*$ the fractional diffusivity defined as $K^{4-2d_F}A_{ea}^{d_F-2}\tilde{D}^{3-d_F}$ (K is a constant related to d_F of the fractal interface, A_{ea} the time-independent electrochemically active area of the flat interface, $\tilde{D}$ the chemical diffusivity of diffusing species), and $\partial^v / \partial t^v$ the Riemann-Liouville mathematical operator of the fractional derivative:

$$\frac{\partial^v y}{\partial t^v} = \frac{1}{\Gamma(1-v)}\frac{\mathrm{d}}{\mathrm{d}t}\int_0^t \frac{y(\xi)}{(t-\xi)^v}\mathrm{d}\xi \tag{9.9}$$

where $\Gamma(1-v)$ is the gamma function of $(1-v)$.

The procedure of the mathematical derivation of Eq. 9.8 was rigorously checked by Dassas and Duby [89]. Based upon the concept of the generalized transfer equation (Eq. 9.7), the flow at the fractal interface $J_F(x,t)$ is given as

$$J_F(x,t) = \frac{\partial}{\partial t}\left[\{\tilde{D}_F(t)^* \frac{\partial c(x,t)}{\partial x}\}\right] \tag{9.10}$$

where * is the convolution operator and $\tilde{D}_F(t)$ represents the time-dependent diffusivity defined as

$$\tilde{D}_F(t) = \tilde{D}^* \frac{t^{2-d_F}}{\Gamma(3-d_F)} \tag{9.11}$$

By using Eq. 9.10, the diffusion toward and from the fractal electrode is mapped to a one-dimensional diffusion in Euclidean space as follows:

$$A_{ea}J_F(x,t) = A_F(t)J_E(x,t) \tag{9.12}$$

where $A_F(t)$ is the time-dependent area of the fractal interface defined as $k^{2-d_F}A_{ea}^{d_F/2}$ $(\tilde{D}t)^{(2-d_F)/2}$ (k is a dimensionless constant) and $J_E(x,t)$ represents the flow at the planar interface given by Fick's first law. Consequently, this mapping process leads to the generalization of Fick's second law (Eq. 9.8) by the substitution of $\partial^{3-d_F}/\partial t^{3-d_F}$ and $\tilde{D}^*$ for $\partial/\partial t$ and $\tilde{D}$, respectively. When d_F equals two, Eq. 9.8 becomes the usual Fick's second law for diffusion toward and from a flat electrode/electrolyte interface.

9.2.2   Diffusion toward and from a Fractal Interface Coupled with a Facile Charge-Transfer Reaction

The mathematical derivation of the analytical solutions to the diffusion equations, i.e., Fick's first and second laws, is a very well-known approach to understanding the features of diffusion-controlled reactions at a flat electrode. The diffusion-controlled reactions are simply described as the semi-infinite diffusion coupled with facile charge-transfer reaction. Here, to understand the features of diffusion toward and from the fractal interface coupled with the facile charge-transfer reaction, the derivation of the analytical solutions to the *GDE* of Eq. 9.8 will be introduced under the boundary condition of the diffusion control for potentiostatic, galvanostatic, linear sweep/cyclic voltammetric, and ac-impedance experiments. These four analytical solutions refer to the generalized Cottrell, Sand, Randles-Sevčik, and Warburg equations, respectively. Their derivation was rigorously checked by Dassas and Duby [89] using the Laplace transform of the fractional derivative.

For the derivation, the initial condition (*IC*) and the boundary condition (*BC*) for the semi-infinite diffusion are given as

$$IC : c(x,0) = c^b \quad \text{for } 0 \leq x < \infty \tag{9.13}$$

$$BC : \ c(\infty,t) = c^b \text{ at } t \geq 0 \, (\text{semi} - \text{infinite constraint}) \tag{9.14}$$

where c^b is the bulk concentration of the diffusing species.

9.2.2.1   Generalized Cottrell Equation

The generalized Cottrell equation describes the response of the current I on the potential step ΔE applied to the electrode under the diffusion-controlled condition. The *BC* at the electrode/electrolyte interface for this situation is given as

$$BC : c(0,t) = 0 \quad \text{at} \quad t > 0 \quad (\text{potentiostatic constraint}) \tag{9.15}$$

As a result of the Laplace transforms of Eqs. 9.8, 9.13, 9.14, and 9.15, the generalized Cottrell equation is obtained by [89]

$$I(t) = \frac{zFA_{ea}\sqrt{\tilde{D}^*}c^b}{\Gamma\left(\frac{3-d_F}{2}\right)}t^{-(d_F-1)/2} = \frac{zFA_{ea}^{d_F/2}K^{2-d_F}\tilde{D}^{(3-d_F)/2}c^b}{\Gamma\left(\frac{3-d_F}{2}\right)}t^{-(d_F-1)/2} \qquad (9.16)$$

where $I(t)$ is the current as a function of t, z the valence of the diffusing species, and F the Faraday constant (= 96,487 C mol^{-1}). For $d_F = 2$, Eq. 9.16 shows the Cottrell equation for ordinary diffusion. The logarithmic plot of the current versus time, called the potentiostatic current transient (PCT), exhibits a linear line with a slope of $-(d_F - 1)/2$, which is the power exponent of Eq. 9.16.

9.2.2.2   Generalized Sand Equation

The generalized Sand equation describes the relationship between the constant current applied to the electrode I_{app} and the transition time τ, which is the time needed for the concentration of diffusing species to drop to zero at the electrode/electrolyte interface under the diffusion-controlled condition. The BC at the electrode/electrolyte interface for this situation is given as

$$BC : \left(\frac{\partial c(x,t)}{\partial x}\right)_{x=0} = -\frac{I_{app}}{zFA_{ea}\tilde{D}_F(t)} \text{at} t > 0 (\text{galvanostatic constraint}) \qquad (9.17)$$

As a result of the Laplace transforms of Eqs. 9.8, 9.13, 9.14, and 9.17, the generalized Sand equation is obtained by [89]

$$\begin{aligned} I_{app} &= zFA_{ea}\sqrt{\tilde{D}^*}c^b\Gamma\left(\frac{d_F+1}{2}\right)\tau^{-(d_F-1)/2} \\ &= zFA_{ea}^{d_F/2}K^{2-d_F}\tilde{D}^{(3-d_F)/2}c^b\Gamma\left(\frac{d_F+1}{2}\right)\tau^{-(d_F-1)/2} \end{aligned} \qquad (9.18)$$

For $d_F = 2$, Eq. 9.18 shows the Sand equation for ordinary diffusion. The logarithmic plot of I_{app} versus τ shows a linear line with a slope of $-(d_F - 1)/2$, which is the power exponent of Eq. 9.18.

9.2.2.3   Generalized Randles-Sevčik Equation

The generalized Randles-Sevčik equation explains the power dependence of the peak current I_{peak} on the potential scan rate v during the linear sweep/cyclic voltammetric experiments under the diffusion-controlled condition. For a solution containing only the oxidized species Ox with a concentration of c^b, the electrode is

subjected to an initial electrode potential E_{ini} where no reaction takes place. The redox reaction $Ox + ze = Red$ begins to occur when the potential is linearly increased or decreased with $E(t) = E_{ini} \pm v\,t$ ($E(t)$ is the electrode potential as a function of t, and the signs "+" and "−" represent the anodic and cathodic scans, respectively.). Under the assumption that the redox couple is reversible, the surface concentrations of Ox and Red, i.e., $c_{Ox}(0, t)$ and $c_{Red}(0, t)$, respectively, are always determined by the electrode potential E expressed as the following equation, which is derived from the Nernst equation,

$$E = E_{1/2} + \frac{RT}{zF} \ln\left(\frac{c_{Ox}(0, t)}{c_{Red}(0, t)}\right) \tag{9.19}$$

where $E_{1/2}$ means the half-wave potential, i.e., the potential bisecting the distance between the anodic and cathodic peaks in a cyclic voltammogram, R the gas constant ($= 8.314$ J mol^{-1} K^{-1}), and T the absolute temperature. (It is assumed that the diffusivities of Ox and Red are equal, i.e., $\tilde{D} = \tilde{D}_{Ox} = \tilde{D}_{Red}$.)

Under this circumstance, the generalized Randles-Sevčik equation can be derived from Eq. 9.8 as follows [89]:

$$
\begin{aligned}
I_{peak} &= \frac{0.2518(zF)^{3/2} A_{ea} \sqrt{\tilde{D}^*} c^b}{(RT)^{1/2}} \Gamma\left(\frac{d_F - 1}{2}\right) v^{(d_F-1)/2} \\
&= \frac{0.2518(zF)^{3/2} A_{ea}^{d_F/2} K^{2-d_F} \tilde{D}^{(3-d_F)/2} c^b}{(RT)^{1/2}} \Gamma\left(\frac{d_F - 1}{2}\right) v^{(d_F-1)/2}
\end{aligned}
\tag{9.20}
$$

For $d_F = 2$, Eq. 9.20 shows the Randles-Sevčik equation for ordinary diffusion. The power exponent of $(d_F - 1)/2$ in Eq. 9.20 is the slope of the linear line for the logarithmic plot of I_{peak} versus v called the linear sweep voltammogram (LSV).

9.2.2.4 Generalized Warburg Equation

The generalized Warburg equation describes the constant phase element (CPE) behavior of the diffusion impedance $Z_d(\omega)$ in a spatially restricted layer under the impermeable boundary condition. $Z_d(\omega)$ has been used as a tool for the electrochemical characterization of intercalation electrodes of which one side is impermeable [90–95].

Electrochemical impedance spectroscopy (EIS) superimposes the small sinusoidal signal of $E(t)$ onto the electrode with reversible potential E_{rev} given as

$$E(t) = E_{rev} + \varepsilon \sin \omega t \tag{9.21}$$
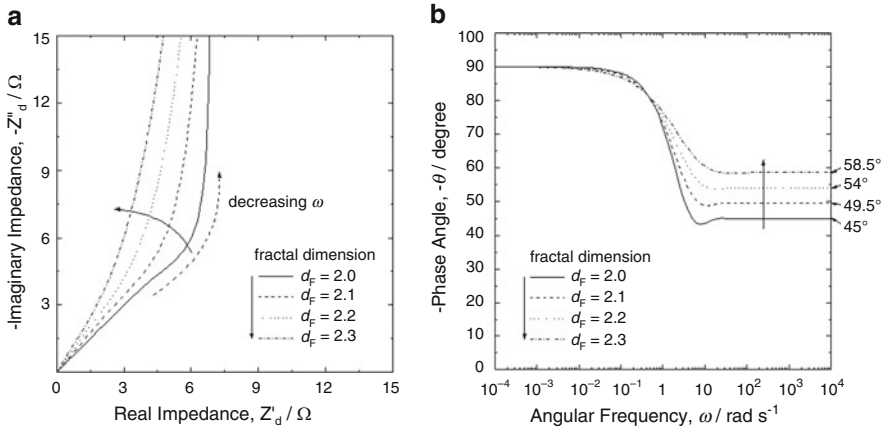
Fig. 9.6 (**a**) Nyquist plots of the ac-impedance spectrum and (**b**) Bode plots of the phase angle θ versus the logarithm of angular frequency log ω theoretically determined from Eq. 9.22 as a function of the fractal dimension d_F for diffusion in the fractal electrode during the ac potential oscillation experiment. The values of the parameters involved in Eq. 9.22 were taken as $L = 1 \times 10^{-5}$ cm, $z = 1$, $A = 1$ cm^2, $\tilde{D} = 1 \times 10^{-10}$ cm^2 s^{-1} and $(dE/dc) = 20$ V cm^3 mol^{-1} (Reprinted from Lee and Pyun [90], Copyright © 2005 with permission from Carl Hanser Verlag)

where ε is a constant which represents the perturbation amplitude and ω means the angular frequency.

Under the impermeable boundary condition, $Z_d(\omega)$ can be derived from Eq. 9.8 as follows [90–95]:

$$Z_d(\omega) = \frac{L}{zFA_{ea}\tilde{D}^*}\left(\frac{dE}{dc}\right)\frac{\coth\left[(j\omega)^{(3-d_F)}L^2/\tilde{D}^*\right]^{1/2}}{\left[(j\omega)^{(d_F-1)}L^2/\tilde{D}^*\right]^{1/2}} \tag{9.22}$$

where L is the thickness of the electrode. For $d_F = 2$, $Z_d(\omega)$ explains the Warburg equation for a planar electrode with a flat surface.

Figure 9.6a, b gives the typical ac-impedance spectra in Nyquist representation and the variations of the phase angle θ with log ω, respectively. Figure 9.6a shows that the ac-impedance spectrum obtained from the fractal electrode deviates more considerably from ideal behavior for $d_F = 2$ with increasing d_F. In Fig. 9.6b, $Z_d(\omega)$ clearly shows the Warburg impedance in the high-frequency range $\omega \gg \tilde{D}/L^2$. When we consider the high frequencies, Eq. 9.22 reduces to the generalized Warburg equation given as [89]

$$Z_d(\omega) = \frac{1}{zFA_{ea}\sqrt{\tilde{D}^*}}\left(\frac{dE}{dc}\right)(j\omega)^{-(d_F-1)/2}. \tag{9.23}$$

9.2.3 Diffusion toward and from a Fractal Interface Coupled with a Sluggish Charge-Transfer Reaction

When the diffusion is coupled with a sluggish charge-transfer reaction, the reaction rate of the system cannot be clearly determined and it is called a mixed-controlled system. Even though most electrochemical systems, including diffusion, are usually assumed to be diffusion-controlled ones, there are many systems which show different features from diffusion-controlled systems [96–104].

Several theoretical attempts have been made to obtain a clear understanding of the mixed-controlled system at the fractal electrode/electrolyte interface, as follows: de Levie and Vogt [105] derived explicit equations for the current response to a potential step, i.e., the *PCT*, at a fractal interface with self-similar scaling property, by employing the Laplace transform method, in the case where a sluggish charge-transfer process is operative. Furthermore, Kant and Rangarajan [106] formulated kinetic theories of the diffusion process involving finite charge-transfer rates using the perturbation approach and, especially, they provided analytical expressions for the *PCT* at fractal interfaces with various morphological features. However, the above work is oversimplified [105] or quite theoretically oriented [106], so that it is very difficult to completely or straightforwardly grasp the behaviors of the *PCT* at the fractal interfaces when diffusion is coupled with a sluggish charge-transfer reaction.

In this circumstance, the works of Pyun and his coworkers attracted the attention of researchers interested in investigating the kinetics of transfer processes in various systems, because they were the first to describe the fractal to flat transition and vice versa under the constraint of mixed control [107] and they gave a guideline to analyze the electrochemical responses at the fractal interface in a realistic regime [108].

Here, a numerical solution to the *GDE* based upon the fractional calculus [82] will be introduced, which was firstly derived by Go and Pyun [108]. Before exploring their work, it should be recognized that when diffusion in the fractal media is governed by the *GDE*, the fractal-to-flat transition never occurs during atom transport, even though the film thickness is long enough for semi-infinite diffusion to occur.

Go and Pyun [108] theoretically computed the *PCT* and *LSV* from the flat and fractal electrodes by using the numerical solution to the *GDE* under the cell-impedance-controlled constraint at the electrode/electrolyte interface, along with the impermeable constraint at the electrode/current collector interface.

The cell-impedance-controlled constraint at the electrode/electrolyte interface and the impermeable constraint at the electrode/current collector interface used in the calculation of the *PCT* and *LSV* are given as

$$BC : -zFA_{ea}\tilde{D}_F(t)\left(\frac{\partial c(x,t)}{\partial x}\right)_{x=0} = \frac{(E_{app} - E(t))}{R_{cell}} \text{ at } t > 0$$

$$(cell - impedance - controlled \text{ constraint})$$

(9.24)

$$BC : \left(\frac{\partial c(x,t)}{\partial x}\right)_{x=L} = 0 \text{ at } t > 0 \text{ (impermeable constraint)}$$

(9.25)

The current across the interface between the electrode/electrolyte, $I(t)$, was calculated from the following equation, which was obtained from the numerical analysis of Eq. 9.10

$$I(t) = -zFA_{ea}\tilde{D}_F(t)\left(\frac{\partial c(x,t)}{\partial x}\right)_{x=0} = zFA_{ea}\tilde{D}_F(t)\frac{c(0,t) - c(\Delta x,t)}{\Delta x}$$

(9.26)

Figure 9.7 shows the logarithmic $PCTs$ calculated from the flat and fractal electrodes. All of the $PCTs$ exhibited three-stage behavior: The logarithm of the current decreased first slowly with the logarithm of time, then proportionally to the logarithm of time with a constant negative slope, and finally it decayed exponentially. In the second stage, the linear relationship between the logarithms of current and time showed the absolute value of the slope increases with increasing d_F. The nonlinear relationship in the first and third stages did not obey the generalized Cottrell equation presented in Eq. 9.16. In addition, as d_F increased, the values of I during the first and second stages and the time to transition of the second stage to the third stage increased and decreased, respectively.

Figure 9.8 gives the values of I_{peak}, which were obtained from the $LSVs$ calculated from the fractal electrodes with different d_F values, as a function of v on a logarithmic scale.

All electrodes showed the power dependence of I_{peak} on v in the region of v higher than a certain critical scan rate. However, this power dependence deviated negatively from the generalized Randles-Sevčik relation expressed in Eq. 9.20. As d_F increased, I_{peak} and the critical scan rate, as well as the power exponent, just increased in value.

The time to transition t_{ch} of the second stage to the third stage in the PCT of Fig. 9.7 and the critical scan rate v_{ch} of the plots of I_{peak} versus v in Fig. 9.8 are caused by the transition from semi-infinite diffusion to finite diffusion and vice versa, respectively. It was suggested based on the analysis of the concentration profile transients of the diffusion species across the electrode that was under the constraint of mixed control.

As d_F increased, the value of t_{ch} in the PCT decreased and I increased up to t_{ch}, while the values of I_{peak} and v_{ch} in the LSV just increased. From this result, it is concluded that the surface roughness enhances the cell-impedance-controlled lithium transport as expected from Eq. 9.11: The surface roughness would result in a marked increase in $\tilde{D}_F(t)$.
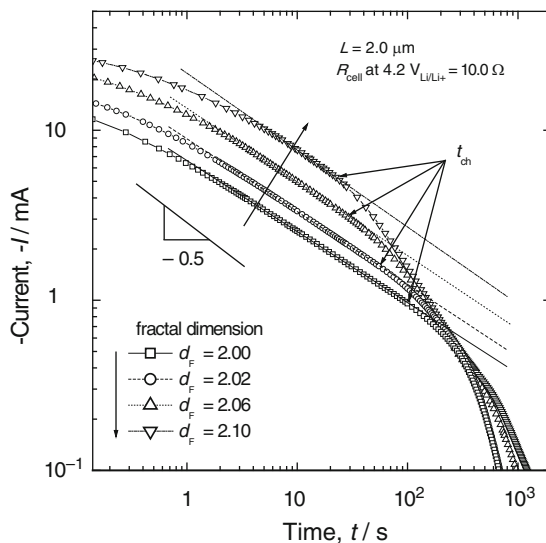
Fig. 9.7 Potentiostatic current transients calculated from the flat electrode with $d_F = 2.0$ and the fractal electrodes with $d_F = 2.02$, 2.06 and 2.10 by dropping the electrode potential of 4.2–3.9 V under the cell-impedance-controlled constraint at the electrode/electrolyte interface along with the impermeable constraint at the electrode/current collector interface. The values of the electrode thickness L and the internal cell resistance R_{cell} at 4.2 V are fixed as 2.0 μm and 10.0 Ω, respectively (Reprinted from Go and Pyun [108], Copyright © 2005 with permission from Elsevier Science)

   Regarding the effect of R_{cell} on the cell-impedance-controlled lithium transport, contrary to the effect of d_F on the lithium transport, as R_{cell} increased, the value of t_{ch} in the *PCT* increased and I decreased up to t_{ch}, while the values of I_{peak} and v_{ch} in the *LSV* just decreased. From this fact, it can be noted that the beneficial contribution of the surface roughness to the cell-impedance-controlled lithium transport counterbalances the detrimental contribution of the internal cell resistance.

9.3   Application of Fractal Geometry to the Analysis of Lithium Transport

9.3.1   Lithium Transport through Irregular Interface

Based on the theoretical studies of the diffusion toward and from the fractal interface, as described in the previous sections, Pyun and his coworkers tried intensively to provide experimental proof of the effect of the surface roughness on the lithium transport through intercalation compounds, i.e., $Li_{1-\delta}CoO_2$ [40, 42, 43, 109], V_2O_5 [110], $Li_{1-\delta}Mn_2O_4$ [111], and carbonaceous materials [112]. From their works, it is experimentally confirmed that the lithium intercalation through the
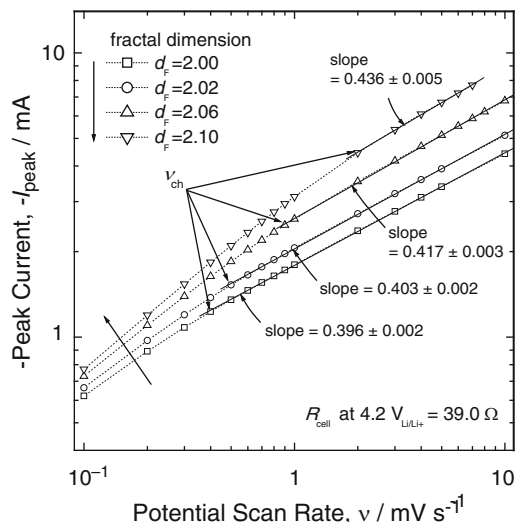
Fig. 9.8 Plots of the peak current I_{peak} versus the potential scan rate v theoretically calculated from the flat electrode with $d_F = 2.0$ and the fractal electrodes with $d_F = 2.02$, 2.06 and 2.10 by scanning the applied potential from 4.3 to 3.5 V at various v from 0.1 to 10 mV s^{-1} under the cell-impedance-controlled constraint at the electrode/electrolyte interface along with the impermeable constraint at the electrode/current collector interface. The values of the electrode thickness L and the internal cell resistance R_{cell} at 4.2 V are fixed as 5.0 μm and 39.0 Ω, respectively (Reprinted from Go and Pyun [108], Copyright © 2005 with permission from Elsevier Science)

intercalation compounds is a cell-impedance-controlled reaction and is crucially influenced by the irregularity of the reaction surface.

For dense film electrodes of $Li_{1-\delta}CoO_2$ and $Li_{1-\delta}Mn_2O_4$, the surface roughness was varied by adopting different Al_2O_3 substrates with flat and rough surfaces. Since the thickness of the *rf*-sputtered film was very thin compared to that of the Al_2O_3 substrate, the surface roughness of the Al_2O_3 substrate directly reflected that of the intercalation films. Their fractal dimension was characterized by image analysis using *AFM* and their spatial cutoff was several hundreds of nanometers, which is coincident with the ionic diffusion length scale. Under the cell-impedance-controlled lithium transport boundary conditions, Pyun and his coworkers provided the real *PCT* and *LSV*, which were experimentally measured from these film electrodes. The representative behaviors of *PCT* and *LSV* predicted from the theoretical studies (see Figs. 9.7 and 9.8) were clearly shown in the real *PCT* and *LSV* [109, 111].

For porous electrodes of V_2O_5 and carbonaceous materials, the pore structure was differentiated by the polymer surfactant template method and heat treatment, respectively. The single-probe gas adsorption method [58, 110, 112] was used to determine the fractal dimension of their surface with a spatial cutoff of several tens of nanometers. Due to the molecular scale spatial cutoff, the fractal scaling property of their surface characterized by this gas adsorption method was meaningful to the

charge-transfer reaction at the electrolyte/electrode interface, but not to the diffusion process [110]. This was the first attempt to differentiate the fractal scaling properties according to the spatial cutoff range of each method and to provide clear evidence of the following points: (1) the charge-transfer reaction at the fractal surface in the molecular length scale results in the interfacial capacitance dispersion of the ac-impedance spectra and (2) the diffusion reaction through the fractal surface in the hundreds of nanometers scale results in the frequency dispersion of the diffusion impedance of the *ac*-impedance spectra.

9.3.2   Lithium Transport through Partially Inactive Interface

In the previous chapters, the surface roughness was discussed in the case of a fully active interface. However, the composite electrodes used in electrochemical processes are often partially active, since they are composed of an active powder material and inactive binder and conductor. A partially blocked active electrode can be characterized by a contiguous fractal with $d_F < 2.0$. And electrodes composed of active islands on an inactive support are belonging to a noncontiguous fractal with $d_F < 2.0$ [113].

For a contiguous fractal with $d_F < 2.0$ under the diffusion-controlled constraint, Pajkossy and Nyikos gave the experimental evidence of the validity of the generalized Cottrell equation [113]. Two kinds of partially active electrodes: a regular fractal pattern with $d_F = (\log 8)/(\log 3) \cong 1.893$ and a Sierpinski gasket [1] with $d_F = (\log 3)/(\log 2) \cong 1.585$ were prepared, and then a *PCT* was obtained from the experiment on two partially active electrodes using the diffusion-limited redox couple of $K_3[Fe(CN)_6]$ and $K_4[Fe(CN)_6]$. For both electrodes, the *PCT* showed the generalized Cottrell behavior of Eq. 9.16.

Subsequently, Dassas and Duby [89] demonstrated experimentally (1) the transition time versus current relationship under galvanostatic experiment, (2) the peak current versus potential scan rate relationship in a voltammetric experiment, and (3) the current versus time relationship under potentiostatic experiment using a Sierpinski gasket in a gel electrolyte containing 0.02 M $K_4[Fe(CN)_6]$ + 0.5 M Na_2SO_4 solution. All followed power laws with a power exponent of $-(d_F - 1)/2$ according to the analytical solutions to the generalized diffusion equation involving the fractional derivative operator of Eq. 9.8.

Lee and Pyun [114] characterized the morphology of the surface groups formed on and polyvinylidene fluoride (*PVDF*)-binder materials dispersed on a graphite composite electrode as a contiguous fractal with $d_F < 2.0$. Two kinds of electrodes: (1) the as-received SLX50 graphite electrode composed of graphite and PVDF, and (2) the surface-modified SLX50 graphite electrode composed of heat-treated graphite, *PVDF*, and surface groups on the graphite were prepared, and then they were investigated using Kelvin probe force microscopy (*KFM*).

Figure 9.9a, b shows the surface potential profiles of the as-received SLX50 graphite electrode and the surface-modified SLX50 graphite electrode.
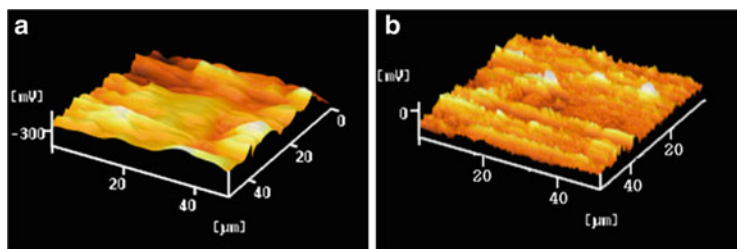
Fig. 9.9 *KFM* images obtained from the *PVDF*-bonded composite made from (**a**) the as-received SFG50 graphite and from (**b**) the surface-modified SFG50 graphite (Reprinted from Lee and Pyun [114], Copyright © 2003 with permission from Elsevier Science)

The as-received one showed a smooth surface with a few broad peaks, whereas the surface-modified one showed a rough surface with many sharp peaks with a lower surface potential and some broad peaks with a higher surface potential. Since the surface potential of the *PVDF* is much higher than that of the surface groups, they assigned the broad peaks to *PVDF* and the sharp peaks to the surface groups.

The three-dimensional *KFM* images were cross-sectioned into planes having a constant surface potential to determine the fractal dimension of the inactive site distribution. The resulting self-similar distributions of the *PVDF*s on the as-received one and on the surface-modified one are given in Fig. 9.10a, b, respectively. The self-similar complex distribution of the surface groups and *PVDF* on the surface-modified one is shown in Fig. 9.10c.

These cross-sectional images were analyzed by the perimeter-area method. As a result, the fractal dimensions of *PVDF* and the surface groups on the surface-modified SLX50 graphite were distinguished by using *KFM*. However, the fractal dimension determined by the peak-current method was just the average of the two individual fractal dimensions determined by the *KFM* analysis. From these results, it was concluded that the surface-modified SLX50 graphite has multi-fractal geometry [72].

For a noncontiguous fractal with $d_F < 2.0$, Pajkossy and Nyikos theoretically showed that the current response to a potential step obeys the generalized Cottrell equation by the random walk simulation of particles toward a Cantor-like boundary [113]. On the other hand, Strømme et al. experimentally elucidated that the surfaces of conducting oxide specimens, i.e. In oxide [115] and Sn oxyfluoride [38, 115], are noncontiguous fractals with $d_F < 2.0$ (Fig. 9.11).

Based on this background information, Jung and Pyun [116] conducted a theoretical study on the cell-impedance-controlled lithium transport through an $Li_{1-\delta}Mn_2O_4$ film electrode with a partially inactive fractal surface. They modeled the $Li_{1-\delta}Mn_2O_4$ film with partially inactive sites as a Cantor set, as shown in Fig. 9.11 [60, 72, 113], ran a kinetic Monte Carlo simulation using the random walk approach, and finally calculated the *PCT* and *LSV*.

They calculated the *PCT*s and *LSV*s for both the fully active and partially active fractal electrodes under the cell-impedance-controlled constraint and then
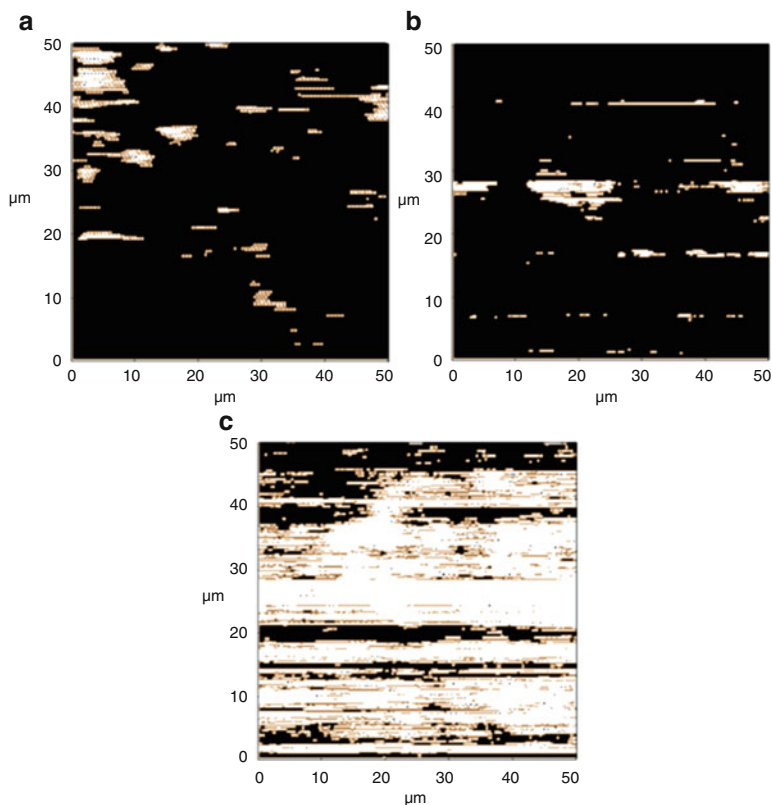
Fig. 9.10 Cross-sectional view of the three-dimensional *KFM* image (**a**) for the as-received SFG50 graphite by cross-sectioning with the plane of the height value in 50% of the maximum height of the surface potential, (**b**) for the surface-modified SFG50 graphite by cross-sectioning with 80% of the maximum height of the surface potential, and (**c**) for the surface-modified SFG50 graphite by cross-sectioning with 50% of the maximum height of the surface potential (Reprinted from Lee and Pyun [114], Copyright © 2003 with permission from Elsevier Science)

compared them with each other. Neither the *PCT*s calculated for the totally active nor partially inactive fractal electrodes exhibited generalized Cottrell behavior and their shape was significantly affected by the interfacial charge-transfer kinetics. In the case of the *LSV*s determined from both the totally active and partially inactive fractal electrodes, the power dependence of the peak current on the scan rate above the characteristic scan rate deviated from the generalized Randles-Sevčik behavior.

It was further recognized that the cell-impedance-controlled lithium transport through the partially inactive fractal $Li_{1-\delta}Mn_2O_4$ film electrode strongly deviates from the generalized diffusion-controlled transport behavior of the electrode with the totally active surface. This is attributed to the impeded interfacial charge-transfer kinetics governed by the surface inhomogeneities, including the fractal dimension of the surface and the surface coverage by active sites, and by the kinetic parameters including the internal cell resistance.

Fig. 9.11 Schematic diagram of producing the Cantor set fractal profile by iterative removal of the central part of a line segment (Reprinted from Jung and Pyun [116], Copyright © 2007 with permission from Elsevier Science)
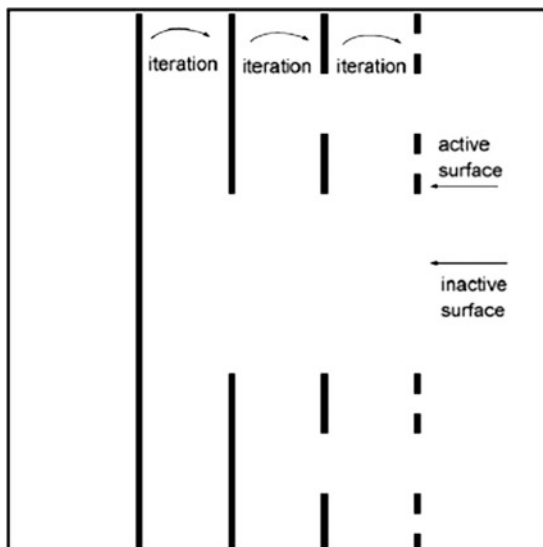
References

1. Mandelbrot BB (1983) The fractal geometry of nature. W.H. Freeman and Company, New York
2. Peitgen HO, Saupe D (1988) The science of fractal images. Springer, New York
3. Pickover CA (1990) Computers, pattern, chaos and beauty. St. Martin's Press, New York
4. Peitgen HO, Jürgens H, Saupe D (1992) Fractals for the classroom: introduction to fractals and chaos. Springer, New York
5. Mantegna RN, Stanley HE (1995) Scaling behaviour in the dynamics of an economic index. Nature 376:46–48
6. Stanley MHR, Amaral LAN, Buldyrev SV, Havlin S, Leschhorn H, Maass P, Salinger MA, Stanley HE (1996) Scaling behaviour in the growth of companies. Nature 379:804–806
7. Takayasu H, Okuyama K (1998) Country dependence on company size distributions and a numerical model based on competition and cooperation. Fractals 6:67–80
8. Takayasu H, Takayasu M, Okazaki MP, Marumo K, Shimizu T (2000) In: Novak MN (ed) Paradigms of complexity: fractals and structures in the sciences. World Scientific, Singapore
9. Brady RM, Ball RC (1984) Fractal growth of copper electrodeposits. Nature 309:225–229
10. Matsushita M, Sano M, Hayakawa Y, Honjo H, Sawada Y (1984) Fractal structures of zinc metal leaves grown by electrodeposition. Phys Rev Lett 53:286–289
11. Grier D, Ben-Jacob E, Clarke R, Sander LM (1986) Morphology and microstructure in electrochemical deposition of zinc. Phys Rev Lett 56:1264–1267
12. Meakin P (1986) Fractal scaling in thin film condensation and material surfaces. Crit Rev Solid State Mater Sci 13:143–189
13. de Levie R (1990) Fractals and rough electrodes. J Electroanal Chem 281:1–21
14. Sagues F, Mas F, Vilarrasa M, Costa JM (1990) Fractal electrodeposits of zinc and copper. J Electroanal Chem 278:351–360
15. Gómez-Rodríguez JM, Baró AM, Salvarezza RC (1991) Fractal characterization of gold deposits by scanning tunneling microscopy. J Vac Sci Technol B 9:495–499
16. Ocon P, Herrasti P, Vázquez L, Salvarezza RC, Vara JM, Arvia AJ (1991) Fractal characterisation of electrodispersed gold electrodes. J Electroanal Chem 319:101–110

17. Gómez-Rodríguez JM, Baró AM, Vázquez L, Salvarezza RC, Vara JM, Arvia AJ (1992) Fractal surfaces of gold and platinum electrodeposits: dimensionality determination by scanning tunneling microscopy. J Phys Chem 96:347–350

18. Herrasti P, Ocón P, Salvarezza RC, Vara JM, Viázquez L, Arvia AJ (1992) A comparative study of electrodeposited and vapour deposited gold films: fractal surface characterization through scanning tunnelling microscopy. Electrochim Acta 37:2209–2214

19. Vázquez L, Salvarezza RC, Ocón P, Herrasti P, Vara JM, Arvia AJ (1994) Self-affine fractal electrodeposited gold surfaces: characterization by scanning tunneling microscopy. Phys Rev E 49:1507–1511

20. Antonucci PL, Barberi R, Aricò AS, Amoddeo A, Antonucci V (1996) Fractal surface characterization of chalcogenide electrodeposits. Mater Sci Eng B 38:9–15

21. Huang W, Brynn Hibbert D (1996) Fast fractal growth with diffusion, convection and migration by computer simulation: effects of voltage on probability, morphology and fractal dimension of electrochemical growth in a rectangular cell. Phys A 233:888–896

22. Kessler T, Visintin A, Bolzan AE, Andreasen G, Salvarezza RC, Triaca WE, Arvia AJ (1996) Electrochemical and scanning force microscopy characterization of fractal palladium surfaces resulting from the electroreduction of palladium oxide layers. Langmuir 12:6587–6596

23. Gobal F, Malek K, Mahjani MG, Jafarian M, Safarnavadeh V (2000) A study of the fractal dimensions of the electrodeposited poly-ortho-aminophenol films in presence of different anions. Synth Met 108:15–19

24. Mandelbrot BB, Passoja DE, Paullay AJ (1984) Fractal character of fracture surfaces of metals. Nature 308:721–722

25. Underwood EE, Banerji K (1986) Fractals in fractography. Mat Sci Eng 80:1–14

26. Pande CS, Richards LE, Louat N, Dempsey BD, Schwoeble AJ (1987) Fractal characterization of fractured surfaces. Acta Metall 35:1633–1637

27. Wang ZG, Chen DL, Jiang XX, Ai SH, Shih CH (1988) Relationship between fractal dimension and fatigue threshold value in dual-phase steels. Scripta Metall 22:827–832

28. Lung CW, Zhang SZ (1989) Fractal dimension of the fractured surface of materials. Phys D 38:242–245

29. Imre A, Pajkossy T, Nyikos L (1992) Electrochemical determination of the fractal dimension of fractured surfaces. Acta Metall Mater 40:1819–1826

30. Voss RF, Laibowitz RB, Allessandrini EI (1982) Fractal (scaling) clusters in thin gold films near the percolation threshold. Phys Rev Lett 49:1441–1444

31. Gómez-Rodríguez JM, Asenjo A, Salvarezza RC, Baró AM (1992) Measuring the fractal dimension with STM: application to vacuum-evaporated gold. Ultramicroscopy 42–44:1321–1328

32. Rao MVH, Mathur BK, Chopra KL (1994) Evaluation of the scaling exponent of self-affine fractal surface from a single scanning probe microscope image. Appl Phys Lett 65:124–126

33. Spanos L, Irene EA (1994) Investigation of roughened silicon surfaces using fractal analysis. I. Two-dimensional variation method. J Vac Sci Technol A 12:2646–2652

34. Douketis C, Wang Z, Haslett TL, Moskovits M (1995) Fractal character of cold-deposited silver films determined by low-temperature scanning tunneling microscopy. Phys Rev B 51:11022–11031

35. Mbise GW, Niklasson GA, Granqvist CG (1996) Scaling of surface roughness in evaporated calcium fluoride films. Solid State Commun 97:965–969

36. Salvadori MC, Silveira MG, Cattani M (1998) Measurement of critical exponents of diamond films by atomic force microscopy imaging. Phys Rev E 58:6814–6816

37. Kleinke MU, Davalos J, Polo da Fonseca C, Gorenstein A (1999) Scaling laws in annealed LiCoO$_x$ films. Appl Phys Lett 74:1683–1685

38. Niklasson GA, Rönnow D, Strømme M, Kullman L, Nilsson H, Roos A (2000) Surface roughness of pyrolytic tin dioxide films evaluated by different methods. Thin Solid Films 359:203–209

39. Silva LLG, Ferreira NG, Dotto MER, Kleinke MU (2001) The fractal dimension of boron-doped diamond films. Appl Surf Sci 181:327–330

40. Shin HC, Pyun SI, Go JY (2002) A Study on the simulated diffusion-limited current transient of a self-affine fractal electrode based upon the scaling property. J Electroanal Chem 531:101–109

41. Sun X, Fu Z, Wu Z (2002) Fractal processing of AFM images of rough ZnO films. Mater Charact 48:169–175

42. Go JY, Pyun SI, Hahn YD (2003) A study on ionic diffusion towards self-affine fractal electrode by cyclic voltammetry and atomic force microscopy. J Electroanal Chem 549:49–59

43. Go JY, Pyun SI (2004) A study on lithium transport through fractal $Li_{1-\delta}CoO_2$ film electrode by analysis of current transient based upon fractal theory. Electrochim Acta 49:2551–2562

44. Costa JM, Sagués F, Vilarrasa M (1991) Fractal patterns from corrosion pitting. Corros Sci 32:665–668

45. Jøssang T, Feder J (1992) The fractal characterization of rough surfaces. Phys Scripta T 44:9–14

46. Holten T, Jøssang T, Meakin P, Feder J (1994) Fractal characterization of two-dimensional aluminum corrosion fronts. Phys Rev E 50:754–759

47. Balázs L, Gouyet JF (1995) Two-dimensional pitting corrosion of aluminium thin layers. Phys A 217:319–338

48. Park JJ, Pyun SI (2003) Pit formation and growth of alloy 600 in Cl^- ion-containing thiosulfate solution at temperatures 298–573 K using fractal geometry. Corros Sci 45:995–1010

49. Park JJ, Pyun SI (2003) Analysis of impedance spectra of a pitted Inconel Alloy 600 electrode in chloride ion-containing thiosulfate solution at temperatures of 298–573 K. J Solid State Electrochem 7:380–288

50. Park JJ, Pyun SI (2004) Stochastic approach to the pit growth kinetics of Inconel Alloy 600 in Cl^- ion-containing thiosulphate solution at temperatures 25–150°C by analysis of the potentiostatic current transients. Corros Sci 46:285–296

51. Pyun SI, Park JJ (2004) Fractal analysis of pit morphology of Inconel Alloy 600 in sulphate, nitrate and bicarbonate ion-containing sodium chloride solution at temperatures 25–100°C. J Solid State Electrochem 8:296–307

52. Almqvist N, Rubel M, Franconi E (1995) Surface characterization of SiC composites exposed to deuterium ions, using atomic force microscopy. Mater Sci Eng A 201:277–285

53. Almqvist N, Rubel M, Wienhold P, Fredriksson S (1995) Roughness determination of plasma-modified surface layers with atomic force microscopy. Thin Solid Films 270:426–430

54. Almqvist N (1996) Fractal analysis of scanning probe microscopy images. Surf Sci 355:221–228

55. Arnault JC, Knoll A, Smigiel E, Cornet A (2001) Roughness fractal approach of oxidised surfaces by AFM and diffuse X-ray reflectometry measurements. Appl Surf Sci 171:189–196

56. Kirbs A, Lange R, Nebe B, Rychly J, Müller P, Beck U (2003) On the description of the fractal nature of microstructured surfaces of titanium implants. Mater Sci Eng C 23:413–418

57. Kirbs A, Lange R, Nebe B, Rychly R, Baumann A, Neumann HG, Beck U (2003) Methods for the physical and chemical characterisation of surfaces of titanium implants. Mater Sci Eng C 23:425–429

58. Go JY, Pyun SI (2005) Chapter 4 Fractal approach to rough surfaces and interfaces in electrochemistry. In: Vayenas CG, White RE, Gamboa-adelco ME (eds) Modern aspects of electrochemistry, vol 39. Kluwer Academic/Plenum, New York, pp 167–229

59. Go JY, Pyun SI (2007) A review of anomalous diffusion phenomena at fractal interface for diffusion-controlled and non-diffusion-controlled transfer processes. J Solid State Electrochem 11:323–334

60. Feder J (1988) Fractals. Plenum, New York

61. Voss RF (1991) Dynamics of fractal surfaces. In: Family F, Vicsek T (eds) Randon fractals: characterization and measurement. World Scientific, New Jersey
62. Gouyet JF (1995) Physics and fractal structures. Springer, New York
63. So P, Barreto E, Hunt BR (1999) Box-counting dimension without boxes: computing D0 from average expansion rates. Phys Rev E 60:378–385
64. Bisoi AK, Mishra J (2001) On calculation of fractal dimension of images. Pattern Recognit Lett 22:631–637
65. Mandelbrot BB (1986) In: Pietronero L, Tosatti E (eds) Fractals in physics. North-Holland, Amsterdam
66. Gouyet JF, Rosso M, Sapoval B (1996) In: Bunde A, Havlin S (eds) Fractals and disordered systems. Springer, New York
67. Vicsek T (1991) Fractal growth phenomena, 2nd edn. World Scientific, Singapore
68. Majumdar A, Bhushan B (1990) Role of fractal geometry in roughness characterization and contact mechanics of surfaces. J Tribol 112:205–216
69. Majumdar A, Tien CL (1990) Fractal characterization and simulation of rough surfaces. Wear 136:313–327
70. Majumdar A, Bhushan B (1999) Characterization and modeling of surface roughness and contact mechanics. In: Bhushan B (ed) Handbook of micro/nano tribology, 2nd edn. CRC Press, New York
71. Silk T, Hong Q, Tamm J, Compton RG (1998) AFM studies of polypyrrole film surface morphology – II. Roughness characterization by the fractal dimension analysis. Synth Met 93:65–69
72. Russ JC (1994) Fractal surfaces. Plenum, New York
73. Clark KC (1986) Computation of the fractal dimension of topographic surfaces using the tricangular prism surface area. Comput Geosci 12:713–722
74. Liu J, Furuno T (2001) The fractal evaluation of wood texture by the triangular prism surface area method. Wood Fiber Sci 33:213–222
75. Liu J, Furuno T (2002) The fractal estimation of wood color variation by the triangular prism surface area method. Wood Sci Technol 36:385–397
76. Kim CH, Pyun SI, Kim JH (2003) An investigation of the capacitance dispersion on the fractal carbon electrode with edge and basal orientations. Electrochim Acta 48:3455–3463
77. Mandelbrot BB (1985) Self-affine fractals and fractal dimension. Phys Scripta 32:257–260
78. Salavarezza RC, Arvia AJ (1995) Chapter 5 A modern approach to surface roughness applied to electrochemical systems. In: Conway BE, Bockris JO'M, White RE (eds) Modern aspects of electrochemistry, vol 28. Plenum, New York
79. Lakshminarayanan V, Srinivasan R, Chu D, Gilman S (1997) Area determination in fractal surfaces of Pt and PtRu electrodes. Surf Sci 392:44–51
80. Majumdar A, Bhushan B, Tien CL (1991) Role of fractal geometry in tribology. Adv Inf Storage Syst 1:231–266
81. Oden PI, Majumdar A, Bhushan B, Padmanabhan A, Graham JJ (1992) AFM imaging, roughness analysis and contact mechanics of magnetic tape and head surfaces. J Tribol 114:666–674
82. Podlubny I (1999) Fractional differential equations: an introduction to fractional derivatives, fractional differential equations, to methods of their solution and some of their applications. Academic, San Diego
83. Le Mehaute A, Crepy G (1983) Introduction to transfer and motion in fractal media: the geometry of kinetics. Solid State Ion 9&10:17–30
84. Le Mehaute A (1984) Transfer processes in fractal media. J Stat Phys 36:665–676
85. Nigmatullin RR (1986) The realization of the generalized transfer equation in a medium with fractal geometry. Phys Status Solidi B 133:425–430
86. Wyss W (1986) The fractional diffusion equation. J Math Phys 27:2782–2785
87. Schneider WR, Wyss W (1989) Fractional diffusion and wave equations. J Math Phys 30:134–144

88. Mainardi F (1996) The fundamental solutions for the fractional diffusion – wave equation. Appl Math Lett 9:23–28
89. Dassas Y, Duby P (1995) Diffusion toward fractal interfaces: potentiostatics, galvanostatic, and linear sweep voltammetric techniques. J Electrochem Soc 142:4175–4180
90. Lee JW, Pyun SI (2005) Anomalous behaviour in diffusion impedance of intercalation electrodes. Z Metallkd 96:117–123
91. Ho C, Raistrick ID, Huggins RA (1980) Application of a-c techniques to the study of lithium diffusion in tungsten trioxide thin films. J Electrochem Soc 127:343–349
92. Jacobsen T, West K (1995) Diffusion impedance in planar, cylindrical and spherical symmetry. Electrochim Acta 40:255–262
93. Ding S, Petuskey WT (1998) Solutions to Fick's second law of diffusion with a sinusoidal excitation. Solid State Ion 109:101–110
94. Diard JP, Le Gorrec B, Montella C (1999) Linear diffusion impedance. General expression and applications. J Electroanal Chem 471:126–131
95. Bisquert J, Compte A (2001) Theory of the electrochemical impedance of anomalous diffusion. J Electroanal Chem 499:112–120
96. Han JN, Seo M, Pyun SI (2001) Analysis of anodic current transient and beam deflection transient simultaneously measured from Pd foil electrode pre-charged with hydrogen. J Electroanal Chem 499:152–160
97. Han JN, Lee JW, Seo M, Pyun SI (2001) Analysis of stresses generated during hydrogen transport through a Pd foil electrode under potential sweep conditions. J Electroanal Chem 506:1–10
98. Pyun SI, Lee JW, Han JN (2002) The kinetics of hydrogen transport through Pd foil electrode in the coexistence of two hydride phases by analysis of anodic current transient. J New Mater Electrochem Syst 5:243–249
99. Lee SJ, Pyun SI, Lee JW (2005) Investigation of hydrogen transport through Mm $(Ni_{3.6}Co_{0.7}Mn_{0.4}Al_{0.3})_{1.12}$ and $Zr_{0.65}Ti_{0.35}Ni_{1.2}V_{0.4}Mn_{0.4}$ hydride electrodes by analysis of anodic current transient. Electrochim Acta 50:1121–1130
100. Lee JW, Pyun SI (2005) Anomalous behaviour of hydrogen extraction from hydride-forming metals and alloys under impermeable boundary conditions. Electrochim Acta 50:1777–1805
101. Shin HC, Pyun SI (1999) The kinetics of lithium transport through $Li_{1-\delta}CoO_2$ by theoretical analysis of current transient. Electrochim Acta 45:489–501
102. Go JY, Pyun SI, Shin HC (2002) Lithium transport through the $Li_{1-\delta}CoO_2$ film electrode prepared by rf magnetron sputtering. J Electroanal Chem 527:93–102
103. Shin HC, Pyun SI (2003) Chapter 5 Mechanisms of lithium transport through transition metal oxides and carbonaceous materials. In: Vayenas CG, Conway BE, White RE (eds) Modern aspects of electrochemistry, vol 36. Kluwer Academic/Plenum, New York
104. Lee JW, Pyun SI (2004) Investigation of lithium transport through $LiMn_2O_4$ film electrode in aqueous $LiNO_3$ solution. Electrochim Acta 49:753–761
105. de Levie R, Vogt A (1990) On the electrochemical response of rough electrodes: Part II. The transient response in the presence of slow faradaic processes. J Electroanal Chem 281:23–28
106. Kant R, Rangarajan SK (1995) Diffusion to rough interfaces: finite charge transfer rates. J Electroanal Chem 396:285–301
107. Lee JW, Pyun SI (2005) A study on the potentiostatic current transient and linear sweep voltammogram simulated from fractal intercalation electrode: diffusion coupled with interfacial charge transfer. Electrochim Acta 50:1947–1955
108. Go JY, Pyun SI (2005) Theoretical approach to cell-impedance-controlled lithium transport through $Li_{1-\delta}CoO_2$ film electrode with fractal surface: numerical analysis of generalised diffusion equation. Electrochim Acta 50:3479–3487
109. Go JY, Pyun SI, Cho SI (2005) An experimental study on cell-impedance-controlled lithium transport through $Li_{1-\delta}CoO_2$ film electrode with fractal surface by analyses of potentiostatic current transient and linear sweep voltammogram. Electrochim Acta 50:5435–5443

110. Jung KN, Pyun SI (2006) Effect of pore structure on anomalous behaviour of the lithium intercalation into porous V_2O_5 film electrode using fractal geometry concept. Electrochim Acta 51:2646–2655
111. Jung KN, Pyun SI (2006) The cell-impedance-controlled lithium transport through $LiMn_2O_4$ film electrode with fractal surface by analyses of ac-impedance spectra, potentiostatic current transient and linear sweep voltammogram. Electrochim Acta 51:4649–4658
112. Lee SB, Pyun SI, Rhee CK (2003) Determination of the fractal dimensions of green MCMB and MCMB heat-treated at 800–1200°C by using gas adsorption method. Carbon 41:2446–2451
113. Pajkossy T, Nyikos L (1989) Diffusion to fractal surfaces – II. Verification of theory. Electrochim Acta 34:171–179
114. Lee SB, Pyun SI (2003) Determination of the morphology of surface groups formed and pvdf-binder materials dispersed on the graphite composite electrodes in terms of fractal geometry. J Electroanal Chem 556:75–82
115. Strømme M, Niklasson GA, Granqvist CG (1996) Fractal surface dimension from cyclic I-V studies and atomic-force microscopy: role of noncontiguous reaction sites. Phys Rev B 54:17884–17887
116. Jung KN, Pyun SI (2007) Theoretical approach to cell-impedance-controlled lithium transport through $Li_{1-\delta}Mn_2O_4$ film electrode with partially inactive fractal surface by analyses of potentiostatic current transient and linear sweep voltammogram. Electrochim Acta 52:2009–2017

About the Authors

Su-Il Pyun

Su-Il Pyun (born in 1942) is Professor Emeritus at Korea Advanced Institute of Science and Technology (KAIST) and Distinguished Professor at Jeju National University, Korea. After having obtained the Bachelor of Science degree in Physics at Seoul National University (1963), he moved to Rheinisch-Westfaelische Technische Hochschule (RWTH), Aachen (1966) as a recipient of the scholarship from the Government of "Nordrhein-Westfalen where he received the Diplom-Ingenieur degree (1970) under the supervision of Prof. O. Knacke and Doktor-Ingenieur degree (1975) at Prof. F. Mueller's research group in metallurgy and materials science. Having returned home to KAIST as professor (1976) he continued to work there until 2012 and also to work from 2012 on at Jeju National University until further notice. He also worked in the period of time between 1978 and 2004 as visiting Professor at Case Western Reserve University, University of Minnesota, USA, with Prof. R.A. Oriani; Max-Planck-Institut fuer Eisenforschung, Germany, with Prof. H.-J. Engell as Max-Planck Fellow; Universitaet des Saarlandes, Technische Universitaet Clausthal-Zellerfeld, Germany, with Prof. K.-E. Heusler; RWTH Aachen with Prof. E. Lugscheider with aid of the research grant from Volkswagen Stiftung; Hokkaido University, Japan; and Polish Academy of Science, Poland. He served as a member of the International Corrosion Council between 1991 and 2006. He has been serving now as Topical Editor for Metal Deposition and Corrosion of Journal of Solid State Electrochemistry (JOSSEC) (Springer, Germany) from 2007 on as well as acting as a member of the Editorial Board of the same journal since 2000.

He was honored with the "outstanding Professor" award for his great academic achievement in electrochemistry and materials science by KAIST two times, in

1996 and 1999, and the 50th Prize in recognition of advances in his electrochemistry and materials science research by SAM-IL Cultural Foundation 2009.

His research covers a wide spectrum of electrochemistry and materials science perspectives including high-temperature solid-state electrochemistry, sintering of metal oxides, cathodic and anodic corrosion of metals, passivation and repassivation kinetics, hydrogen insertion into and desertion from Pd alloys and metal hydrides, lithium intercalation into and deintercalation from transition metal oxide–based lithium intercalation compounds in the absence and presence of fractals as well as two phases in equilibrium, and oxygen reduction at gas diffusion electrode. His recent interest is in biological electrochemistry, in particular in hydrogen ion transfer during the reduction of carbon dioxide of photosynthetic processes and also sodium ion transport within neurons during the pulse propagation in the nervous system.

He has published 314 scientific articles in international journals as well as 109 scientific papers in domestic journals. He has also published five book chapters of *Modern Aspects of Electrochemistry* (MAE), Springer, New York; *Corrosion Research Trends*, Nova Science Publishers, New York; and *Solid State Electrochemistry*, Wiley-VCH Verlag, Germany; as well as four textbooks about thermodynamics in non-hydrostatic system, electrochemistry of such energy storage system as batteries, fuel cells and supercapacitors, electrochemistry at materials, and corrosion science in domestic publications. He is the editor of two volumes of MAE, Springer, New York, and one special issue on *Hybrid Materials and Design in Electrochemistry* in JOSSEC (Springer, Germany).

Heon-Cheol Shin

Heon-Cheol Shin (born in 1972) has been a professor of materials science and engineering at Pusan National University in Busan Metropolitan city, Republic of Korea, since 2006 and is presently an associate professor. He received his B.S. (1995) in Metallurgical Engineering at Yonsei University (Korea) and his M.Sc. (1997) and Ph.D. (2001) on lithium transport mechanism in rechargeable lithium battery in Materials Science and Engineering at Korea Advanced Institute of Science and Technology. He worked as a post-doc at Georgia Institute of Technology (USA) from 2002 to 2004 and worked as a senior researcher at Samsung SDI. He joined the Pusan National University in 2006.

His primary concern lies in fundamental understanding of the interfacial and transport phenomena, leading to next-generation functional electrochemical devices, particularly in high-power lithium secondary batteries. He also has a special interest and expertise on the electrochemical preparation of porous structures based on electroplating, anodization, and electrochemical etching

process. He is a member of the Editorial Board of the *Metals and Materials, International* and a topical editor in electrochemistry for the *Journal of the Korean Electrochemical Society*.

He has published about 40 research papers on nanomaterials for journals like *Advanced Materials*, *Chemistry of Materials*; on lithium battery operation mechanism for *Journal of Electrochemical Society*, *Electrochimica Acta*, etc., which have totally received more than 750 citations; and authored or coauthored three book chapters for *Modern Aspects of Electrochemistry* and *Lithium Batteries: Research, Technology and Applications*.

Jong-Won Lee

Jong-Won Lee (born in 1977) is a Senior Research Scientist at Korea Institute of Energy Research (KIER), South Korea. He received his B.S. (1999) in Materials and Metallurgical Engineering from Hanyang University (Seoul, South Korea), and M.S. (2001) and Ph.D. (2005) in Materials Science from Korea Advanced Institute of Science and Technology (Daejeon, South Korea). His M.S. and Ph.D. work was carried out under the supervision of Prof. Su-Il Pyun. Lee then worked with Prof. Branko N. Popov as a Postdoctoral Researcher (2005) and as a Research Assistant Professor (2006–2008) in the Department of Chemical Engineering at the University of South Carolina (Columbia, USA). From 2008 to 2010, he was an R&D staff member at Samsung Advanced Institute of Technology (Yongin, South Korea) before joining KIER in 2010.

His research interest is in the area of materials science and interfacial electrochemistry with specific emphasis on the preparation of electrode materials and the characterization of materials and electrochemical properties. The electrochemically active materials of interest include Pt-free electrocatalysts and mixed oxides for PEMFCs and SOFCs as well as transition metal oxides and metal-hydrides for rechargeable batteries. Numerical simulations are also used to gain fundamental insight into the electrochemical process. He has published more than 40 refereed papers in international journals and served as a coeditor (with Prof. S.-I. Pyun) of two volumes of *Modern Aspects of Electrochemistry* (Springer), *Progress in Corrosion Science and Engineering I* and *II*.

Joo-Young Go

Joo-Young Go (born in 1977) has been an engineer at SB LiMotive, in Giheung, South Korea, since 2009. She attained her B.S. (1999), M.S. (2001), and Ph.D. degrees (2005) in Materials Science from Korea Advanced Institute of Science and Technology (Daejeon, South Korea). Her M.S. and Ph.D. work was carried out under the supervision of Prof. Su-Il Pyun. From 2005 to 2009, she worked as an engineer at Samsung SDI before joining SB LiMotive in 2009.

She has carried out research and development of secondary lithium-ion batteries for mobile and xEV applications. She has a lot of experience in the electrochemical characterizations of intercalation compounds, numerical modeling, and degradation mechanism analysis of lithium-ion batteries.

About the Editor

Fritz Scholz

Fritz Scholz is Professor at the University of Greifswald, Germany. Following studies of chemistry at Humboldt University, Berlin, he obtained a Dr. rer. nat. and a Dr. sc. nat. (habilitation) from that university. In 1987 and 1989, he worked with Alan Bond in Australia. His main interest is in electrochemistry and electroanalysis. He has published more than 280 scientific papers, and he is editor and coauthor of the book "Electroanalytical Methods" (Springer, 2002, 2005, 2010, and Russian Edition: BINOM, 2006), coauthor of the book "Electrochemistry of Immobilized Particles and Droplets" (Springer 2005), coeditor of the "Electrochemical Dictionary" (Springer, 2008), and coeditor of volumes 7a and 7b of the "Encyclopedia of Electrochemistry" (Wiley-VCH 2006). In 1997, he founded the *Journal of Solid State Electrochemistry* (Springer) and serves as Editor-in-Chief since that time. He is the editor of the series "Monographs in Electrochemistry" (Springer) in which modern topics of electrochemistry are presented. Scholz introduced the technique "Voltammetry of Immobilized Microparticles" for studying the electrochemistry of solid compounds and materials, he introduced three-phase electrodes to determine the Gibbs energies of ion transfer between immiscible liquids, and currently he is studying the interaction of free oxygen radicals with metal surfaces, as well as the interaction of liposomes with the surface of mercury electrodes in order to assess membrane properties.

Index